David Jorge Ligeiro Peitinho

Licenciado em Bioquímica

Interaction between Gold Nanoparticles and Blood Proteins to define Disease states

Dissertação para obtenção do Grau de Mestre em Bioquímica

Supervisor: Prof. Doutor José Ricardo Franco Tavares, UCIBIO, REQUIMTE, Departamento de Química, Faculdade de Ciências e Tecnologia, Universidade NOVA de Lisboa

Co-Supervisor: Prof. Doutor Ludwig Krippahl, NOVA LINCS, Departamento de Informática, Faculdade de Ciências e Tecnologia, Universidade NOVA de Lisboa

Júri:

Presidente: Prof. Dr. Pedro António de Brito Tavares

Arguente: Prof. Dr. Nuno Correia Santos

Vogais: Prof. Dr. José Ricardo Ramos Franco Tavares

Outubro 2018

FACULDADE DE CIÊNCIAS E TECNOLOGIA
UNIVERSIDADE NOVA DE LISBOA

Interaction between Gold Nanoparticles and Blood Proteins to define Disease states

David Peitinho

=

Interaction between Gold Nanoparticles and Blood Proteins to define Disease states

Acknowledgements

Ao Professor Ricardo Franco pela oportunidade de trabalhar no seu laboratório bem como a sua constante disponibilidade para me ajudar com qualquer dificuldade que experienciei durante este trabalho. Também pela oportunidade do contacto direto com a componente de ensino, que de certa forma me fez crescer e ver o lado de um Professor após ter vivido grande parte da minha vida como estudante. Por consequência, agradeço aos alunos a que dei apoio pois aprendi muito mais do que esperava ao ensinar.

Ao Professor Ludwig Krippahl por dar o toque da minha segunda paixão, a informática, a problemas e ambições deste trabalho. Toda a dedicação e habilidade de um código em texto que leva a novas possibilidades, bem como a proposta de ideias e abordagens para passar por cima de um obstáculo.

Ao Mestre Miguel Peixoto de Almeida e à Professora Eulália Pereira, da Faculdade de Ciências da Universidade do Porto, pela sua disponibilidade para responder às minhas questões e fornecer amostras e resultados aos quais contribuíram para o meu conhecimento e valorizaram o conteúdo desta dissertação.

A todo o grupo do laboratório 603, desde dos momentos de mentor-aprendiz com a Mafalda Pinto e Maria "Mary Jones" João Oliveira, aos momentos de alegria que tornaram qualquer mau resultado numa onda de positivismo. Especial agradecimento à Marina Bento que conseguiu me tolerar durante um ano inteiro, me ajudou bastante nesta fase de trabalho e me levou à ocasional viagem ao *shopping*. Aos pombos que de certa forma, como convidados indesejados, estiveram lá sempre nos bons e maus momentos a espreitar pela janela.

A toda a turma do Mestrado em Bioquímica, em especial o Bruno Guerreiro e a Lígia Coelho, ambos que contribuíram bastante para a minha integração nesta turma e talvez uma das maiores razões para me manter feliz e motivado durante todo o processo. Pessoas que me provaram ser muito especiais por pequenos gestos e atitudes e que os considero como meus *buddies*. Fico à espera da mítica e prometida saída à noite!

Aos meus pais, que todo o investimento económico e emocional foi imensurável. Uma fase que finaliza em que a distância só me fez aproximar ao máximo dos dois. Família não se escolhe, mas não poderia estar mais feliz com o que me calhou. Espero os fazer orgulhosos como me fizeram sentir amado.

À Milene Sousa, por ser a minha melhor amiga, namorada e companheira de vídeo jogos, tudo num único pacote. Que a tua chama, característica do signo Carneiro, me faça continuar a ser curioso, ambicioso e positivo. Os dois contra tudo o que vier, como prometido. Amo-te.

"Everything could have been anything else

and it would have just as much meaning."

Mr. Nobody (2013)

Abstract

One of the most studied subjects in Bionanotechnology is the application of Gold Nanoparticles (AuNPs). These have unique optical and chemical properties and interact with proteins and other biomolecules forming dynamic (Protein-Corona) layers at the surface. These protein coronas are responsible for increased *in vivo* biocompatibility, and can be studied by multiple techniques, tracking for disease-specific protein profiles.

In this work, 15 nm AuNPs were synthesized by the Turkevich method, and 40 nm AuNPs were provided. Sample concentration and size were determined by UV-Vis spectroscopy, exploiting the Surface Plasmon Resonance (SPR) effect. Successful surface functionalization was performed with the alkanethiol 11-mercaptoundecanoic acid (MUA) or a pentapeptide (CALNN), maintaining a negative global net charge and increasing overall stability.

Bionanoconjugation with Bovine Serum Albumin (BSA) and Fibrinogen (Fib), with molecular weights of 66 and 340 kDa respectively, was performed and characterized by Agarose Gel Electrophoresis (AGE). Electrophoretic mobility was determined using image and video analysis performed by the eReuss software.

Adsorption affinity constant were determined using the conjugation curves obtained in the AGE results, fitted using the Langmuir Isotherm, and resulted in $(1.5 \pm 0.1) \times 10^{-2}$ (AuNP-MUA) for BSA conjugation, and $(51.2 \pm 4.7) \times 10^{-2}$ (AuNP-CALNN) and $(34.3 \pm 1.2) \times 10^{-2}$ (AuNP-MUA) for Fib conjugation. Bioconjugation of AuNP-CALNN with BSA was inconclusive. Competitive scenarios of a protein mixture favored Fib adsorption over BSA. Fib conjugation of 40 nm AuNPs showed multiple adsorption constants of $(3 \pm 0.7) \times 10^{-2}$ and $(9.7 \pm 2.2) \times 10^{-4}$ respectively.

The eReuss software proved to be a powerful tool to analyze image results from electrophoretic runs, and the video analysis feature gives way to an innovative way of analyzing these experiments and extract further information on the Protein Corona stability.

Fergusson Plot analysis and Light scattering techniques (DLS, NTA and ELS) were performed to determine hydrodynamic sizes and Zeta-Potential of bionanoconjugated samples.

Keywords: Gold nanoparticles, Surface Plasmon Resonance, Electrophoresis, Light Scattering, Protein-Corona, Plasma Proteins.

Resumo

Uma das mais estudadas áreas em Bionanotecnologia é a aplicação de Nanopartículas de Ouro (AuNPs). Estas possuem propriedades óticas e químicas únicas e interagem com proteínas e outras biomoléculas, formando camadas dinâmicas a superfícies (Coroa Proteica). Estas coroas são responsáveis pelo aumento da biocompatibilidade *in vivo*, e podem ser estudadas com múltiplas técnicas, podendo identificar perfis de doença específicos.

Neste trabalho, AuNPs de 15 nm foram sintetizadas pelo método de Turkevich, e AuNPs de 40 nm foram fornecidas. Concentração e tamanho das nanopartículas foram determinadas por espectroscopia UV-Vis, usando o efeito de Ressonância Plasmónica de Superfície (SPR). Funcionalização da superfície foi executada com adição de ácido 11-mercaptoundecanoico (MUA) e um penta-péptido (CALNN), mantendo a carga global negative e aumentando a estabilidade.

Bioconjugação com Albumina (BSA) e Fibrinogénio (Fib) de soro bovino, com pesos moleculares de 66 e 340 kDa, respetivamente, foi executada e caracterizada por Eletroforese em Gel de Agarose (AGE). Mobilidade eletroforética foi determinada usando análise de imagem e vídeo com o programa eReuss.

As constantes de afinidade de adsorção foram determinadas usando as curvas de conjugação pelos resultados de AGE, com a equação do modelo de adsorção de Langmuir, e resultou em $(1.5 \pm 0.1) \times 10^{-2}$ (AuNP-MUA) para a conjugação com BSA, e $(51.2 \pm 4.7) \times 10^{-2}$ (AuNP-CALNN) e $(34.3 \pm 1.2) \times 10^{-2}$ (AuNP-MUA) para a conjugação com Fib. Bioconjugação de AuNP-CALNN com BSA foi inconclusiva. Cenários de competição numa mistura de proteínas favoreceu o Fib sobre a BSA. A conjugação de AuNPs de 40 nm mostrou múltiplas constantes de adsorção de $(3 \pm 0.7) \times 10^{-2}$ e $(9.7 \pm 2.2) \times 10^{-4}$ respetivamente.

O programa eReuss provou ser uma poderosa ferramenta de análise de imagens das corridas eletroforéticas, e a componente de análise de vídeo sugere uma forma inovadora de analisar estas experiências e extrair informação adicional sobre a estabilidade da Coroa Proteica.

A análise de Fergusson e técnicas de dispersão de luz (DLS, NTA e ELS) foram executadas para determinar o tamanho hidrodinâmico e o Potencial-Zeta de bionanoconjugados.

Palavras-Chave: Nanopartículas de Ouro, Ressonância Plasmónica de Superfície, Electroforese, Dispersão de Luz, Coroa Proteica, Proteínas plasmáticas.

Table of Contents

Acknowledgements V

Abstract VII

Resumo IX

Table of Contents XI

Index of Figures XV

Index of Tables XXI

Index of Formulas and Equations XXIII

Abbreviations XXV

1 INTRODUCTION 1

1.1 Blood Proteins 1
1.1.1 Disease-specific protein profiles 1
1.1.2 Adsorption to surfaces and the Vroman Effect 2
1.1.3 Albumin 6
1.1.4 Fibrinogen 6

1.2 Bionanotechnology 8
1.2.1 Colloidal Suspensions 8
1.2.1.1 Light Scattering and Surface Plasmons 9
1.2.1.1.1 Dynamic Light Scattering 9
1.2.1.1.2 Nanoparticle Tracking Analysis 11
1.2.1.1.3 Surface Plasmon Resonance 12
1.2.1.2 Surface Potential 13
1.2.1.2.1 Electrical Double Layer and Zeta-Potential 13
1.2.1.2.2 DLVO Theory 14
1.2.1.3 Electrophoresis 19
1.2.1.4 Electrophoretic Light Scattering 21
1.2.1.5 Agarose Gel Electrophoresis 21
1.2.1.6 SDS-PAGE Electrophoresis 22
1.2.2 Gold Nanoparticles 24
1.2.2.1 Synthesis 25
1.2.2.2 Functionalization 26
1.2.2.2.1 Negative Surface Charge Functionalization 27
1.2.2.2.2 Positive Surface Charge Functionalization 28
1.2.2.3 Bioconjugation 28
1.2.2.3.1 Protein Corona 29

2 OBJECTIVES AND EXPERIMENTAL APPROACH 31

3 METHODS 33

3.1 Spherical Gold Nanoparticle Synthesis 33
3.1.1 Direct reaction method 33

3.1.2 Reverse reaction method 33
3.1.3 Gold Nanoparticle Characterization 34

3.2 Gold Nanoparticle Functionalization 35
3.2.1 MUA Functionalization 35
3.2.2 CALNN Functionalization 36
3.2.3 AUT Functionalization 36

3.3 Protein Concentration determination 37

3.4 Electrophoresis 37
3.4.1 Agarose Gel Electrophoresis 37
3.4.2 SDS-PAGE Electrophoresis 38
3.4.3 eReuss Image Analysis 39
3.4.3.1 Image Upload 40
3.4.3.2 Image Preprocessing 40
3.4.3.3 Image Clipping 40
3.4.3.4 Lane Identification 40
3.4.3.5 Band Profiling 41
3.4.3.6 Report 42
3.4.4 eReuss Data analysis 42
3.4.5 Fergusson Plot Analysis 42
3.4.6 eReuss Video Analysis 43
3.4.6.1 Frame extraction 43
3.4.6.2 Alignment and Clipping 43
3.4.6.3 Baseline 43
3.4.6.4 Final frames and Lane Selection 43
3.4.6.5 Report 44

3.5 UV-Vis Spectroscopy 44

3.6 Light Scattering techniques 44
3.6.1 Dynamic Light Scattering and Electrophoretic Light Scattering 44
3.6.2 Nanoparticle Tracking Analysis 44

3.7 Protein Homology 45

3.8 Molecular Visualization 45
3.8.1 Electrostatic Potential: Poisson-Boltzmann (APBS and PDB2PQR) 45
3.8.2 Solvent accessibility (Swiss-PDB viewer) 45

4 RESULTS 47

4.1 Synthesis and Characterization 47

4.2 Functionalization 48
4.2.1 Negative Charged Functionalization 49
4.2.2 Positive Charged Functionalization 50

4.3 AuNP colloidal stability assays 52
4.3.1 pH effect 54
4.3.2 Salt effect 57

4.4 Protein characterization and quantification 59
4.4.1 SDS-PAGE 60
4.4.2 Bicinchoninic Acid (BCA) Protein Assay 61

4.4.3 Human and Bovine Proteins Homologies 63
4.4.3.1 Fibrinogen 64
4.4.3.2 Albumin 67
4.4.4 Electrostatic properties 69
4.4.4.1 Fibrinogen 69
4.4.4.2 Albumin 71

4.5 BSA and Fibrinogen-AuNP Bionanoconjugates 73
4.5.1 Albumin-AuNP bionanoconjugate 76
4.5.1.1 Agarose Gel Electrophoresis 77
4.5.2 Fibrinogen-AuNP bionanoconjugate 80
4.5.2.1 Agarose Gel Electrophoresis 80
4.5.2.2 Dynamic Light Scattering and Nanoparticle Tracking Analysis 87
4.5.2.3 Electrophoretic Light Scattering 90
4.5.3 BSA and Fib conjugation competition 92

4.6 Fergusson Plot Analysis 96

4.7 Electrophoresis Video Analysis 107

5 CONCLUSION AND FUTURE PERSPECTIVES 111

6 REFERENCES 115

APPENDIX 121

Index of Figures

Figure 1.1. Relative protein abundance in Plasma. Representation of the twenty-two most abundant proteins. [1] 1
Figure 1.2. Histogram of the alterations in protein band intensities, in silver stained SDS-PAGE gel results, after incubation of polystyrene nanoparticles with plasma (50%) from different patients. [3] 2
Figure 1.3. Protein-Surface interaction types. a) Charge-dependent interaction, b) Size-dependent interaction, c) Conformation-dependent interaction. 3
Figure 1.4. Electrostatic interaction between Proteins and Surfaces. Depiction of surface Electrostatic attraction and Protein-Protein side Electrostatic repulsion. 3
Figure 1.5. Conformational changes due to an increase of protein concentration. [4] 4
Figure 1.6. Protein-Nanoparticle interaction. Protein side-on and end-on configurations. Adapted from [5]. 4
Figure 1.7. The structure of Human serum albumin (HSA) representing domains (I, II and III), subdomains (A and B). [7] 6
Figure 1.8. The structure of Human serum Fibrinogen representing the three pairs of chains $(\alpha, \beta, \gamma)_2$. The α-chain represented in blue, β-chain as green and γ-chain as red (A). The Fibrin polymerization process by Thrombin cleavage of the fibrinopeptides (B). [8] 7
Figure 1.9. Spherical Particle size assumption, as Hydrodynamic Diameter (D_h), by Dynamic Light Scattering. Adapted from [16]. 11
Figure 1.10. Surface Plasmon Resonance induced by incident light. Adapted from [27] 13
Figure 1.11. Schematic illustration of an Electric Double Layer (EDL) and an Electrical Potential curve for each plane. [32] 14
Figure 1.12. DLVO theory depiction on the interaction of two colloids of equal charge. Potential curves for repulsive forces (green) and attractive forces (blue) and resulting particle potential energy (black). [32]. 15
Figure 1.13. Energy barrier for colloids in an electrolytic medium, and Primary and Secondary electrical potential minimum. Adapted from [33]. 16
Figure 1.14. Influence of an increasing salt concentration (1 the lowest, and 5 the highest) on the repulsive electrical potential. [33]. 17
Figure 1.15. The influence of the potential energy of repulsive forces, Ψ_d, on the resultant total potential energy of the interaction between two particles. [30]. 18
Figure 1.16. Zeta-Potential values at a pH range of 2.0-12.0 for a particle with a surface isoelectric point around pH 6.0. [34] 19
Figure 1.17. The electrophoretic flow of a positively charged particle. Adapted from [39]. 20
Figure 1.18. Agarose gel electrophoresis method schematic. [41]. 21
Figure 1.19. Sodium Dodecyl Sulfate–Polyacrylamide Gel Electrophoresis (SDS-PAGE). [45] 23
Figure 1.20. Change of conformation and Charge of a Protein by Sodium Dodecyl Sulfate (SDS). [45]. 23
Figure 1.21. Shapes of Gold nanoparticles. Adapted from [49] 24
Figure 1.22. Gold clusters Au13, Au55, and Au147 and discrepancy in the number of gold atoms between quasi-sphere and regular icosahedron. The subscripted value is the number of gold atoms. Adapted from [50] 25
Figure 1.23. Gold nanoparticle Nucleation and Growth processes over time. [53] 26
Figure 1.24. Structure of Thiol molecule interacting with a substrate. [56] 27
Figure 1.25. Structural representation of MUA (top) and CALNN (bottom). 28
Figure 1.26. Structural representation of AUT. 28
Figure 1.27. Schematic illustration of soft and hard protein corona and the concept of the rate of adsorption and desorption. [63] 30

Figure 3.1. Morphological characterization by TEM of AuNPs synthesized by the Direct and Inverse (Reverse) methods with a Sodium citrate: Chloroauric acid ratios of 13.6 and 6.8. The correspondent size distributions are shown. [66] 35
Figure 3.2. eReuss Image clipping of the region of interest (in blue) and the lane start (yellow). 40
Figure 3.3. eReuss Band to Lane (horizontal) in pixels with correspondent band intensity (blue lines) and position (green lines). 41
Figure 3.4. eReuss Band Migration (vertical) in pixels with correspondent band intensity and Gaussian. Agarose Gel Electrophoresis Profile in the left and an SDS-PAGE Electrophoresis Profile in the right. 41

Figure 4.1. Synthesis of Gold Nanoparticles. Sequential change of color of the solution from a initial yellow to dark-red. 47
Figure 4.2. Post-synthesis. A diluted red colloidal solution of 15nm gold nanoparticles (left) and UV--Vis spectrum (right). 47
Figure 4.3. UV-Vis spectra of diluted AuNP colloidal solutions. Comparison of the SPR peaks of 15nm and 40nm sized nanoparticles. 48
Figure 4.4. Agarose Gel Electrophoresis (0.5%). AuNP-Citrate with increasing concentration ratios of BSA. 49
Figure 4.5 Agarose Gel Electrophoresis (0.5%). AuNP-MUA (Left) and AuNP-CALNN with increasing concentration ratios of the respective thiolated ligands. 49
Figure 4.6. UV-Vis spectra of AuNP colloidal solutions. Comparison of the SPR peaks of Citrate (Green), MUA (Red) and CALNN (Blue) functionalizations. 50
Figure 4.7. AUT-AuNP functionalization with different [AUT]/[AuNP] in the 100-10,000 range always leading to aggregation. 50
Figure 4.8. UV-Vis spectra of both AuNP-Citrate and AuNP-AUT colloidal solutions at the same concentration for direct comparison (left). Visible color change on the AUT-AuNP colloidal solution from a red to purple (right). 51
Figure 4.9. UV-Vis spectra of both AuNP-Citrate and AuNP-AUT colloidal solutions at the same concentration for comparison. 52
Figure 4.10. Increasing aggregation effects (left to right), leading to a change of color. 53
Figure 4.11. Aggregation ratio evolution of 2 nM AuNP-Citrate at pH 2.0 over a time lapse of several minutes. Vertical lines show the periods that manual sample homogenization was executed, and the red arrows indicate the highest increases in aggregation post-homogenization. 54
Figure 4.12. UV-Vis spectra of AuNP-Citrate at pH 6 (solid line) and for samples at increasing pH in the range 7.0-12.0 (dash lines). 54
Figure 4.13. UV-Vis spectra of AuNP-Citrate at pH 6 (solid line) and for samples at decreasing pH in the range 1.0-6.0 (dash lines). 55
Figure 4.14. Aggregation Ratios from the UV-Vis pH studies for citrate-AuNPs and Logistic fitting (red) to estimate aggregation mid-point. 56
Figure 4.15. UV-Vis spectra of MUA (red) and CALNN (blue) coated AuNPs at pH 6.5 (solid line) and 1.0 (dashed line) and correspondent SPR band before and after aggregation, respectively. 56
Figure 4.16. Variation of the normalized Aggregation Ratios as a function of pH for citrate-capped or MUA- or CALNN-functionalized AuNPs. 57
Figure 4.17. UV-Vis spectra of Citrate (black), MUA (red) and CALNN (blue) coated AuNPs. Different SPR and Aggregation peaks before (solid line) and after (dashed line) salt induced aggregation. 58
Figure 4.18. Variation of the normalized Aggregation Ratios as a function of NaCl concentration for citrate-capped or MUA- or CALNN-functionalized AuNPs. 59
Figure 4.19. SDS-PAGE gel for protein characterization of BSA and Fib, using Low Molecular Weight (LMW) Protein Markers. 60

Figure 4.20. SDS-PAGE gel processed by the eReuss software and respective band migration profile (left), and size-to-migration calibration curve and equation (right). 61
Figure 4.21. BCA calibration curve, using BSA standards, and resultant equation. 62
Figure 4.22. Measurement of different Protein concentration using the Bicinchoninic Acid Protocol. [83] 63
Figure 4.23. Schematic representing determination of protein homology determination, structural similarity and data integrity in this chapter. 64
Figure 4.24. Rigid Structural Alignment of Human Fibrinogen (blue) and Bovine Fibrinogen (orange). The structural zones in grey represent non-aligned regions. 66
Figure 4.25. Human (Red) and Bovine (Blue) Fibrinogen PDB superposition. 67
Figure 4.26. Rigid Structural Alignment of Human Serum Albumin (blue) and Bovine Serum Albumin (orange) PDB files. 68
Figure 4.27. Electrostatic Potential projected at a computed surface for the Human Fibrinogen (PDB 3GHG) at a pH range from 6.0 to 8.0. The color range indicates the estimated negative (red), neutral (white) and positive (blue) surface potential. The range varies between -5.0 and +5.0 (kb T e_c^{-1}). 70
Figure 4.28. Front (left) and Top (right) view of the Human Fibrinogen PDB at pH 7.4 and correspondent electrostatic potential surface below. 71
Figure 4.29. Electrostatic Potential projected at a computed surface for the Bovine Albumin (PDB 3V03) at a pH range from 5.0 to 8.0. The color range indicates the estimated negative (red), neutral (white) and positive (blue) surface potential. The range varies between -5.0 and +5.0 (kb T e_c^{-1}). 72
Figure 4.30. Representation of the BSA PDB file showing the Hydrophobic Pocket (Top-Left) and the correspondent Top-View (Top-Right). The electrostatic potential surfaces are shown below and were estimated at a pH 7.4. 73
Figure 4.31. UV-Vis spectroscopy depicting a red-shift upon nanoparticle conjugation. 74
Figure 4.32. Agarose gel (0.5%) electrophoresis of MUA functionalized AuNPs conjugated with BSA and Fib at indicated [Protein]/[AuNP] concentration ratios. 75
Figure 4.33. Average electrophoretic mobility for AuNP and fully conjugated AuNPs with Fib and BSA on a 0.5% agarose gel. 76
Figure 4.34. Agarose gel (0.5%) electrophoresis of MUA-AuNP conjugated with various [BSA]/[AuNP] ratios. Gel obtained after a 15-minute run at 150V. 77
Figure 4.35. Band migration profile, in pixels, obtained by eReuss (left) and normalized electrophoretic mobility variation with increasing BSA concentration fitted by the Hill and Langmuir equations (right). 78
Figure 4.36. Agarose gel electrophoresis results of fourteen individual essays of AuNP bionanoconjugation with BSA. AuNP concentrations varied between 1 and 3 nM while maintaining the same bioconjugation ratios. 79
Figure 4.37. Agarose Gel Electrophoresis of BSA conjugated samples, functionalized with MUA and CALNN (top), and respective band migration profiles (bottom). 80
Figure 4.38. Agarose Gel Electrophoresis of Fib conjugated samples, functionalized with MUA and CALNN (top), and respective band migration profiles (bottom). 81
Figure 4.39. Agarose gel electrophoresis results of Fib conjugation of 15nm MUA and CALNN AuNPs. A) Fib conjugation of AuNP-MUA original image, B) Fib conjugation of AuNP-MUA augmented contrast eReuss image, C) Fib conjugation of AuNP-CALNN original image, B) Fib conjugation of AuNP-CALNN augmented contrast eReuss image. 82
Figure 4.40. Agarose gel electrophoresis results of the Fib conjugation of 15nm, 19nm and 23nm AuNP-MUA samples (top) and first four ratios zoomed (bottom) for each sample. 83
Figure 4.41. Agarose gel electrophoresis results of the Fib conjugation of 40nm AuNP-MUA. 84
Figure 4.42. Normalized electrophoretic mobility of two AGE results, composed of Low and high ratio ranges, with increasing Fib conjugation of 40nm AuNP-MUA, fitted by the Hill Equation. 84

Figure 4.43. Agarose gel electrophoresis results of the Fib conjugation of 40nm AuNP-MUA samples at increased conjugation ratios (0 – 20,000) at 0.5% agarose (left) and 1.0% agarose gel (right). 85
Figure 4.44. Bionanoconjugation of 40 nm AuNP-MUA with Fib. Lower ratio (0-500) conjugation curve (left) and higher ratio (100-20000) conjugation curve (right). The two curves correspond to the 1.0% agarose gel results. 86
Figure 4.45. AGE results, of a 10 min run at 150V, of the tested samples (Left), Bar chart of the size distribution by DLS (Mean) and NTA (Mean and Highest Concentrated) results (Right). 87
Figure 4.46. Nanoparticle Tracking Analysis results, tested five times for each sample (1-4), showing size distributions. 88
Figure 4.47. DLS results for the 40 nm AuNP bioconjugation with Fib with values of the mean Diameters. 89
Figure 4.48. NTA results for the 40 nm AuNP bioconjugation with Fib with values of the mean Diameters. The ratios of 40, 60, 100 and 30000 were ignored due to high errors and deviations. 90
Figure 4.49. AGE (left) and ELS (right) results of bionanoconjugated samples with increasing [Fib]/[AuNP] ratios. 91
Figure 4.50. Zeta-Potential values, obtained by ELS, of the bioconjugated samples of 40 nm AuNPs with Fib. 91
Figure 4.51. Agarose gel electrophoresis results of MUA-AuNP samples conjugated with BSA and Fib in various orders. Arrows indicate band migration variation relative to the correspondent conjugation with the first introduced protein. 92
Figure 4.52. Agarose gel electrophoresis results of Citrate-AuNP samples conjugated with BSA and Fib in various orders. Arrow indicates band migration variation relative to the correspondent conjugation with the first introduced protein. 94
Figure 4.53. Solvent accessibility of amino acids. Accessibility color scale relative to maximum accessibility possible in the extended pentapeptide GGXGG environment. All amino acid (A and C) and Cysteine-only coloration (B and D) are represented. The structures on top (A and B) derive from the BSA PDB file (3V03) and the structures on the bottom (C and D) derive from the Fib PDB file (3GHG). 95
Figure 4.54. AGE results for BSA conjugation of AuNP-MUA samples at a concentration ratio range between 0 and 2000. Agarose Gel concentrations variated between 0.5% and 2.0%. 97
Figure 4.55. Fergusson plot analysis of multiple samples of AuNP-MUA conjugated to increasing ratios of [BSA]/[AuNP] ranging from 0 to 2000:1. 98
Figure 4.56. Estimated Zeta-Potential values for different molar ratios for BSA conjugation of AuNP-MUA samples. 99
Figure 4.57. Agarose gel electrophoresis results of different sized (15-39 nm) AuNP-MUA and fully conjugated 15 nm AuNP samples with BSA and Fib at different gel concentrations (0.5-2.0%). 101
Figure 4.58. Fergusson plot analysis of AGE results. Multiple sized samples of AuNP-MUA (left) and comparison with fully conjugated 15 nm AuNP-MUA with Fib and BSA (right). 102
Figure 4.59. Size determination calibration equation derived from the Fergusson Plot Analysis 103
Figure 4.60. Ball depiction of AuNP-MUA and BSA conjugation. 104
Figure 4.61. Semi-Collapsed formation of Fibrinogen at physiological conditions. The lower positive arms correspond to the extension of the alpha-chain. Adapted from [10]. 105
Figure 4.62. Image depiction of AuNP-MUA and Semi-collapsed Fib conjugation. 105
Figure 4.63. Image depiction of two AuNP-MUA and Semi-collapsed Fib conjugation. 106
Figure 4.64. Image depiction of an AuNP-MUA and two Semi-collapsed Fib conjugation. 106
Figure 4.65. Zeta-Potential values for the different sized (15-39 nm) AuNP-MUA samples and the fully conjugated 15 nm AuNP-MUA samples (BSA and Fib). 107

Figure 4.66. Intensity values for each Lane (1-12) along the recorded duration. Results past the 20-minute mark have been omitted due to video quality issues. 108
Figure 4.67. Dilution optimization for eReuss Video Analysis. Intensity various dilutions corresponding to 1:1 (Lane 1), 1:2 (Lane 2), 1:4 (Lane 3), 1:8 (Lane 4) and 1:16 (Lane 5). 108
Figure 4.68. eReuss video analysis of the dilution optimization step. Band intensity of each lane captured in specific time frames from the whole video duration. 109
Figure 4.69. Total Intensity values for each Lane (1-10) along the recorded duration for the diluted samples. 109
Figure 4.70. eReuss video analysis of the diluted samples. Band intensity of each lane captured in specific time frames from the whole video duration. Only the Lanes 1, 3, 5 and 7 were selected for this representation out of the ten total lanes. 110

Index of Tables

Table 1.1. Rate of Arrival of the highest concentrated plasma proteins based on diffusion coefficient values for a short time scenario. Adapted from [4]. 5
Table 1.2. Predicted Conformations of the Fibrinogen Molecule depending on the solution conditions. Adapted from [10]. 8
Table 1.3. Types of Colloids. Adapted from [11]. 9

Table 3.1. Handcasted Polyacrylamide Gels Protocol by Bio-Rad Laboratories, Inc. Reagents colored in green are the polymerization reaction inducers, being the last ones added. 38

Table 4.1. Estimated values of the SPR and Aggregation peaks. 58
Table 4.2. Average Protein Molecular Weight estimated values from SDS-PAGE electrophoresis. 61
Table 4.3. Sequence length (in number of aa residues) of Bovine and Human Fibrinogen by Chain. 65
Table 4.4. Sequence alignment of Human and Bovine Fibrinogen. 65
Table 4.5 Structural Similarity for Human and Bovine Fibrinogen. 66
Table 4.6.Data integrity for the Bovine and Human Fibrinogen PDB files compared to the correspondent UniProt sequences by Global alignment. 67
Table 4.7. Sequence length of Bovine and Human Serum Albumin. 67
Table 4.8. Sequence alignment of Human and Bovine Serum Albumin. 68
Table 4.9. Human and Bovine PDB Structural Similarity. 68
Table 4.10. Data integrity of the Human and Bovine PDB files. 69
Table 4.11. Isoelectric point (pI) and Molecular Weight (MW) data of Human (3GHG) and Bovine (1DEQ) PDB files for Fibrinogen. 71
Table 4.12. Isoelectric point (pI) and Molecular Weight (MW) data of Human and Bovine Albumin. 73
Table 4.13. Summary of the previous DLS and NTA results. 87
Table 4.14. Electrophoretic Mobility results from the Fib and BSA conjugation competition study for MUA functionalized AuNPs. 93
Table 4.15. Electrophoretic Mobility results from the Fib and BSA conjugation competition study for non-functionalized AuNPs. 94
Table 4.16. Results from the Fergusson plot analysis. The 15-39 nm AuNPs used for the size calibration in blue, and the fully conjugated with BSA and Fib samples in green. 102
Table 4.17. Diameter estimation of conjugated samples of 15nm AuNP-MUA with BSA and Fib. 103

Index of Formulas and Equations

Equation 1.1 5
Equation 1.2 5
Equation 1.3 10
Equation 1.4 10
Equation 1.5 10
Equation 1.6 10
Equation 1.7 11
Equation 1.8 12
Equation 1.9 15
Equation 1.10 15
Equation 1.11 15
Equation 1.12 16
Equation 1.13 19
Equation 1.14 19
Equation 1.15 20
Equation 1.16 25
Equation 1.17 25
Equation 1.18 26
Equation 1.19 26

Equation 3.1 34
Equation 3.2 34
Equation 3.3 34
Equation 3.4 34
Equation 3.5 42

Equation 4.1 53
Equation 4.2 55
Equation 4.3 76
Equation 4.4 97
Equation 4.5 98
Equation 4.6 100
Equation 4.7 100

Abbreviations

Abs	Absorbance
AGE	Agarose Gel Electrophoresis
APBS	Adaptive Poisson-Boltzmann Solver
AuNP	Gold Nanoparticle
AUT	11-Amino-1-undecanethiol
BSA	Bovine Serum Albumin
CALNN	Cysteine-Alanine-Leucine-Asparagine-Asparagine
DLS	Dynamic Light Scattering
DLVO	Derjaguin–Landau–Verwey–Overbeek
ELS	Electrophoretic Light Scattering
ExPASy	Expert Protein Analysis System
Fib	Fibrinogen
HSA	Human Serum Albumin
MUA	11-Mercaptoundecanoic acid
PDB	Protein Data Bank
PEI	Polyethylenimine
pI	Isoelectric Point
SDS-PAGE	Sodium Dodecyl Sulfate Polyacrylamide Gel Electrophoresis
SPR	Surface Plasmon Resonance
UniProt	Universal Protein (Resource)
UV-Vis	Ultraviolet-Visible
μ	Electrophoretic Mobility

1 Introduction

1.1 Blood Proteins

Blood is a complex mixture of components circulating throughout the organism responsible for materials transportation, immune response, wound sealing and body temperature. It can be divided in Blood Cells (45%) and Blood Plasma (55%), the latter being the fraction containing the Blood Proteins. The most abundant circulating plasma protein is Albumin, overshadowing in concentration any other protein in Figure 1.1. [1]

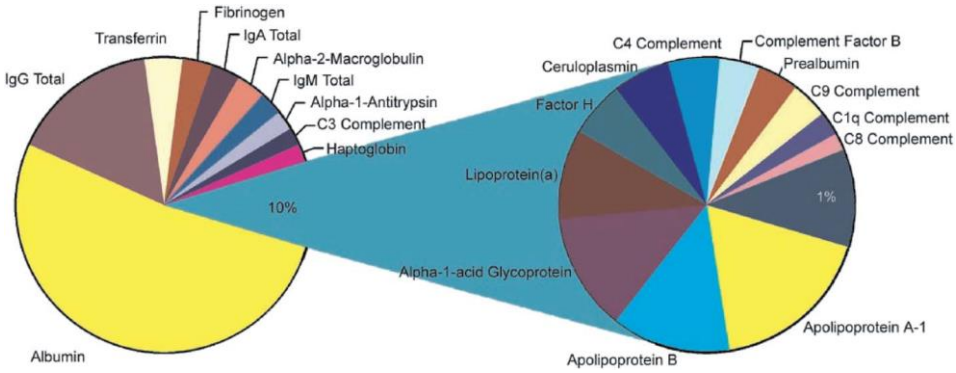

Figure 1.1. Relative protein abundance in Plasma. Representation of the twenty-two most abundant proteins. [1]

1.1.1 Disease-specific protein profiles

Protein composition is dependent on the genetic background, life style and health status, and could be assigned as biomarkers to study abnormalities of an individual. Previous studies have indicated that different types of diseases affect the plasmatic protein composition in different ways, leading to increased concentration levels of certain low abundant proteins.[2] As disease states induce specific plasma protein compositions, possible diagnostics can be developed in order to detect the presence and distinguish these profiles. A well-known issue is the concentration difference between abundant proteins, such as albumin, and less abundant ones, such as Fibrinogen, that complicates the detection of specific lower concentration proteins. Previous studies indicated that the adsorption effect of blood proteins to surfaces bypasses, to some extent, this problem by allowing detection of lower concentrated proteins after a long incubation period as seen in Figure 1.2. The so obtained protein profiles, included three size ranges (>100 kDa, 40-100 kDa and <40 kDa), with relative abundances varying depending on the health status of the individual. [3]

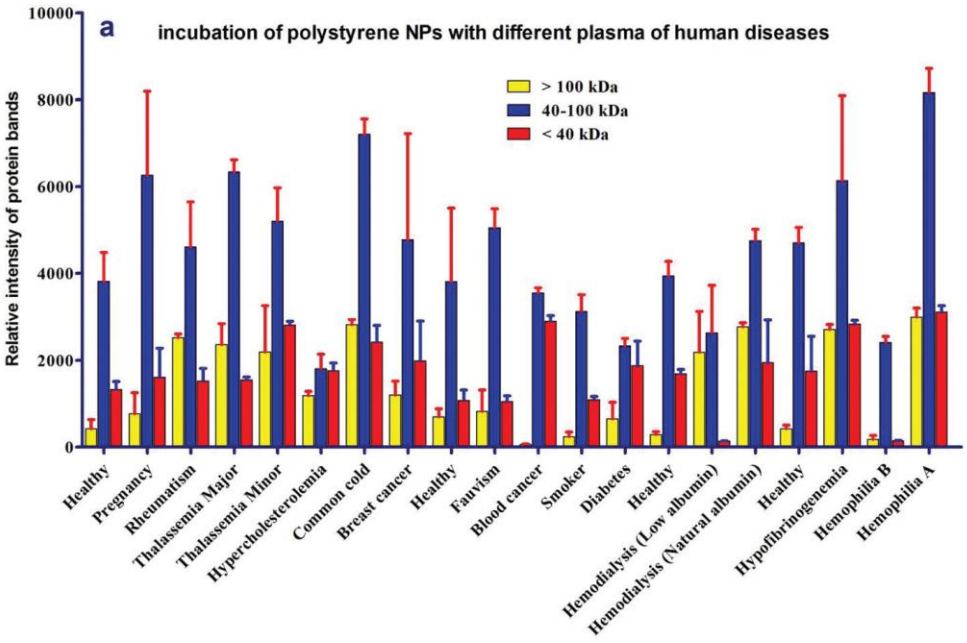

Figure 1.2. Histogram of the alterations in protein band intensities, in silver stained SDS-PAGE gel results, after incubation of polystyrene nanoparticles with plasma (50%) from different patients. [3]

1.1.2 Adsorption to surfaces and the Vroman Effect

Protein interaction with surfaces is a valuable information as blood coagulation, complement activation, and surface biocompatibility are affected by the surface chemistry of the nanostructure, and composition and conformation of the adsorbed biomolecules. Proteins will interact differently to surfaces depending on the chemical interaction forces involved, a stronger adsorption occurring for proteins that exhibit surface charges (Figure 1.3.a), resulting from the exposed residues. These different exposed charges depend on the pH of the solution, and on the size of the interacting protein (Figure 1.3.b), as an increase in size allows more contact points to the adsorbed surface. Structural properties also influence surface adsorption as unstable, higher unfolding rates, and elongated structures, allow more contact points between the protein and the surface (Figure 1.3.c), as for an example the higher adsorption by the elongated Fibrinogen compared to the globular BSA. Also, for example, exposure of internal hydrophobic residues that might interact with hydrophobic surfaces is also to be considered.

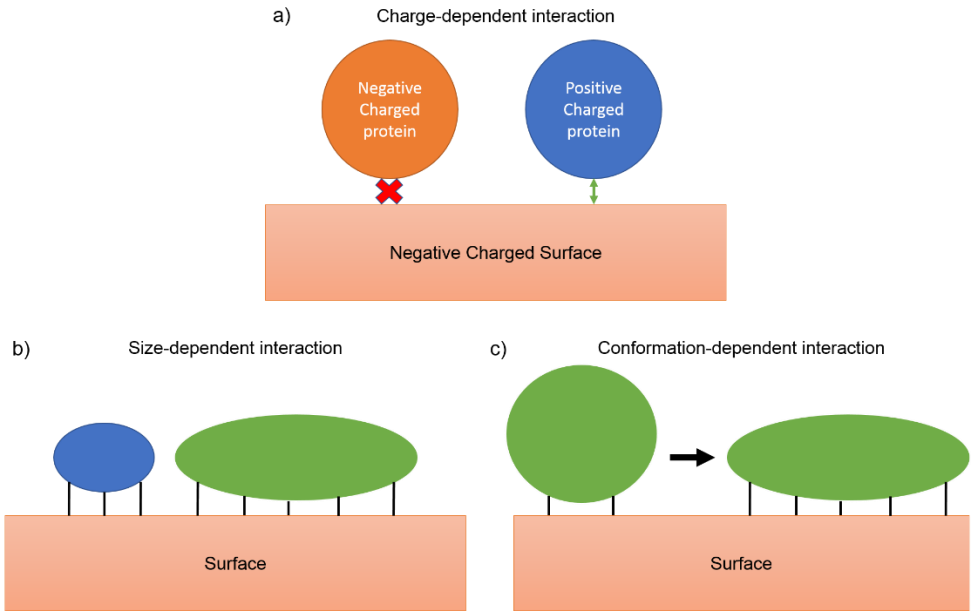

Figure 1.3. Protein-Surface interaction types. a) Charge-dependent interaction, b) Size-dependent interaction, c) Conformation-dependent interaction.

Electrostatic attraction between the surface and the protein is one of the main causes to cause the adsorption effect, suggesting that positively charged proteins (pH < pI) will mainly adsorb to negative charged surfaces, and vice-versa. However, it is theorized that a solution pH near the isoelectric point (pI) of a protein, allowing a near neutral global net charge, is ideal in order to maximize protein adsorption due to the minimization of side-by-side repulsion between adjacent adsorbed proteins as seen in Figure 1.4. This type of repulsion is common in single-protein solutions.

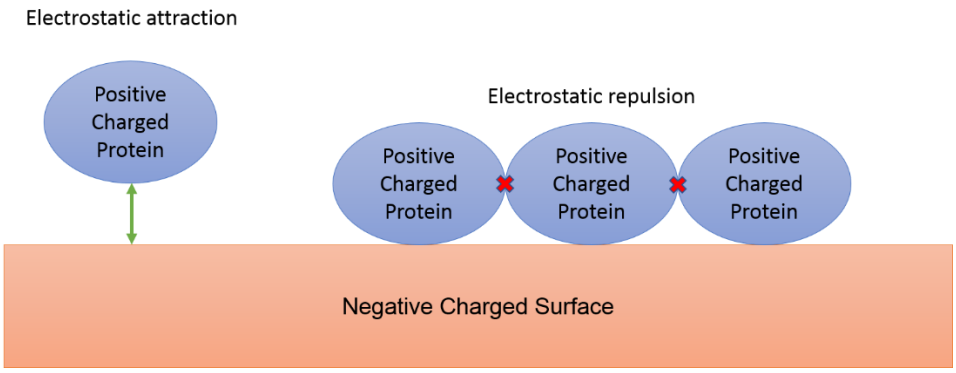

Figure 1.4. Electrostatic interaction between Proteins and Surfaces. Depiction of surface Electrostatic attraction and Protein-Protein side Electrostatic repulsion.

The adsorption effect usually proceeds in a two-step process, first by a fast-electrostatic attraction, where structural integrity and bioactivity are preserved, and secondly by a slow protein conformation rearrangement, that might compromise protein functionality. As protein

concentration increases, the adsorptive space availability will decrease, and protein-protein side repulsion increases, leading to a protein saturation at the surface. The previously referred contact point maximization step will then become impossible (Figure 1.5), as all available space is occupied by other proteins and a more compact layer is formed. [4]

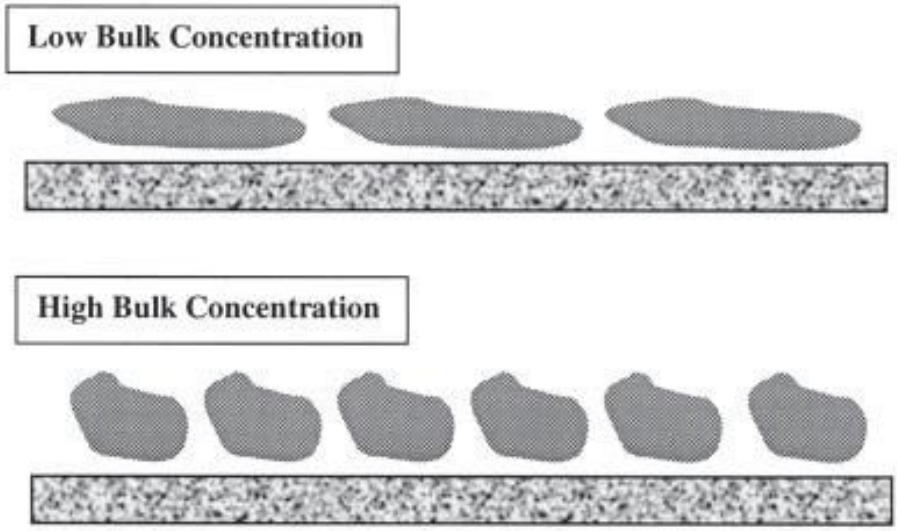

Figure 1.5. Conformational changes due to an increase of protein concentration. [4]

Another possible protein conformation can be adopted, as concentration increases, to augment the number of adsorbed proteins converting from a side-on to an end-on configuration as shown in Figure 1.6. As for surfaces, many aspects affect the adsorption effect such as texture, chemistry, curvature and surface potential. [5]

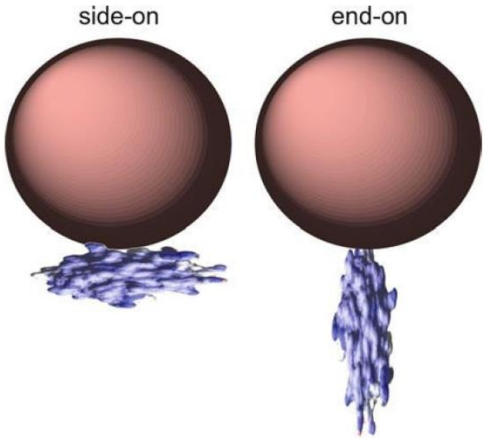

Figure 1.6. Protein-Nanoparticle interaction. Protein side-on and end-on configurations. Adapted from [5].

The plasma is composed of a great variety of proteins, and when these come in contact with a surface, layers are formed. However, the protein composition of these layers changes over time in a process known as the Vroman Effect.

Highly concentrated proteins, such as Albumin (606 x 10^{-6} M), adsorb first, relatively to less abundant proteins like Fibrinogen (9 x 10^{-6} M). These adsorptions are fast due to large diffusion coefficients of highly abundant circulating proteins, as for the previous example of 6.1 x 10^{-7} cm^2 s^{-1} and 2 x 10^{-7} cm^2 s^{-1} for Albumin and Fibrinogen respectively.

For better understanding the early adsorption process, the diffusion effect can be described using Equation 1.1:

$$\frac{\delta C}{\delta t} = D \frac{\delta^2 C}{\delta x^2}$$

Equation 1.1

where C is the protein concentration, D is the diffusion coefficient, and x is the distance travelled by the protein. For short time points, the rate of adsorption equals the rate of diffusion:

$$\frac{dn}{dt} = C_0 \left(\frac{D}{\pi t}\right)^{1/2}$$

Equation 1.2

where n is the surface concentration of protein, C_0 is the bulk concentration of protein, and t is the time, Equation 1.2 shows that bulk concentration and diffusion coefficient will directly influence the surface coverage.

Table 1.1. Rate of Arrival of the highest concentrated plasma proteins based on diffusion coefficient values for a short time scenario. Adapted from [4].

Protein	C (μM)	D (10^{-7} cm^2/s)	$C\sqrt{D}$
Albumin	606	6.1	1,497
IgG	100	4	200
α_1-Antitrypsin	56	5.2	127
Transferrin	34	5	76
α_2-Haptoglobins	20	4.7	43
IgA	14	3.4	26
High-density lipoprotein (HDL)	10	4.6	22
Complement 3	9	4.5	19
Fibrinogen	9	2	12
α_2-Macroglobulin	4	2.4	6
Low-density lipoprotein (LDL)	1	5.4	1

From the values of $C\sqrt{D}$ presented in Table 1.1, assumed as the protein rate of arrival at a surface, it is seen a clear advantage for Albumin in the early adsorption stages.

Low concentrated proteins with higher surface binding affinity (size, chemistry, structural properties), such as Fibrinogen, will then slowly replace the previously adsorbed proteins. This step is slower since the diffusion coefficients are lower, which delays the arrival to the target surface, and protein detachment is required by binding site competition. [4]

1.1.3 Albumin

Albumin is the most abundant circulating plasma protein and has a globular structure (66 kDa). The protein main functions are regulating osmotic blood pressure and transportation of molecules to a target site via the bloodstream. Structurally, this protein is composed of three homologous domains (I, II and III), each subdivided into two subdomains (A and B) (Figure 1.7). Most of its secondary structure is composed of α-chains (67%) crosslinked by 17 internal disulfide bridges which form a triangular shape, denominated the N-Form. This form is maintained in a pH range from 4.5 to 8 and has a single free thiol group (Cys-34) which promotes dimerization of aged protein solutions. [6, 7]

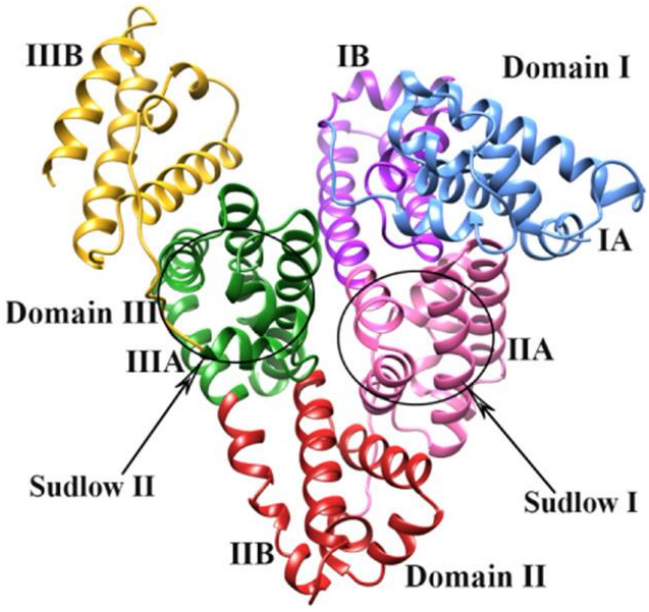

Figure 1.7. The structure of Human serum albumin (HSA) representing domains (I, II and III), subdomains (A and B). [7]

1.1.4 Fibrinogen

Fibrinogen is a rod-shaped Glycoprotein (340 kDa) and one of the most abundant plasma proteins. As an acute-phase protein, participates in blood coagulation in response to inflammation. As seen in Figure 1.8.A, Fibrinogen is composed of three symmetrical pairs of

chains (A*α, Bβ, γ*), and presents two distinct regions, the central domain (E) where all chains connect by the amino termini and the Distal globular regions (D) which contain the carboxylic-terminal regions of the *β and γ*-chains. As for the *α*-chain, the carboxylic-terminal region has no contact with either region. In the fibrin polymerization process, Thrombin cleaves fibrinogen into the fibrinopeptides A and B, as shown in Figure 1.8.B, the former being connect to a polymerization site in the *γ*-chain in order to form a protofibril, and the latter promoting lateral polymerization. [8, 9]

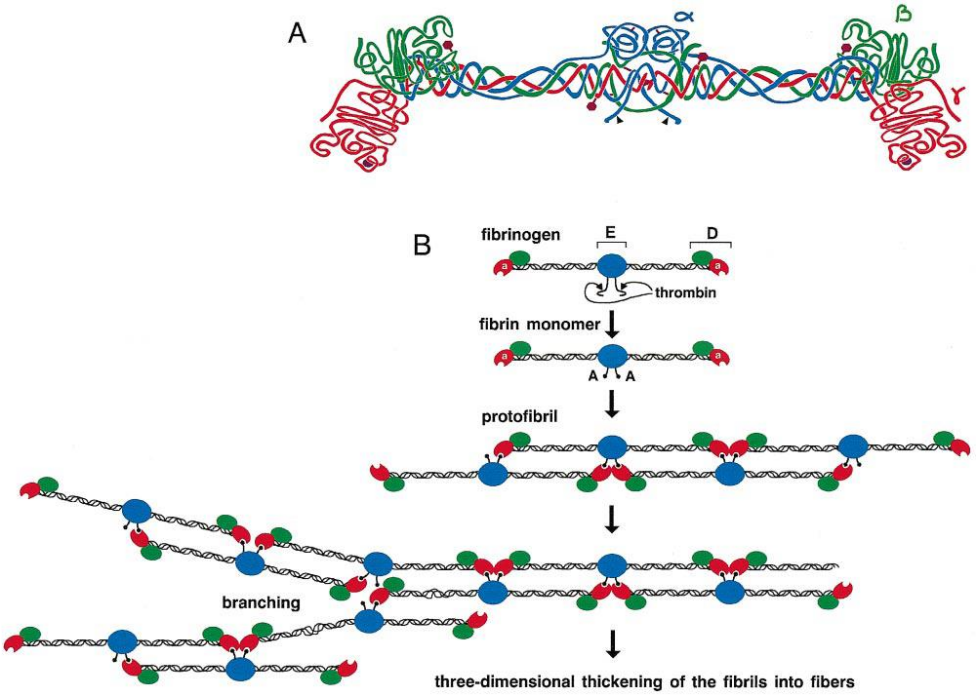

Figure 1.8. The structure of Human serum Fibrinogen representing the three pairs of chains (Aα, Bβ, γ)$_2$. The Aα-chain represented in blue, Bβ-chain as green and γ-chain as red (A). The Fibrin polymerization process by Thrombin cleavage of the fibrinopeptides (B). [8]

The protein conformation is dependent on the solution conditions. Although an overall flexibility is present, the free carboxylic-terminal region of the *α*-chains changes its conformation based on the pH and ionic force of a solution. In Table 1.2, three predicted conformations are presented, in which the localized electrostatic potentials influence the position of the A*α*-chains relative to the structure. In physiological conditions, a semi-collapsed state is most probable due to the electrostatic attraction between the E and D regions (negatively charged) and the Carboxylic-terminal of the A*α*-chains (positively charged). [10]

Table 1.2. Predicted Conformations of the Fibrinogen Molecule depending on the solution conditions. Adapted from [10].

Conformation	Remarks
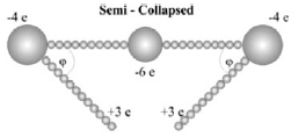	Attractive energy $\phi_0 \sim -4$ kT, Occurs for physiological conditions pH = 7.4, I = 0.15 M
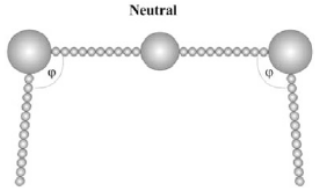	Zero energy $\phi_0 = 0$ kT, Most probable for pH > 9
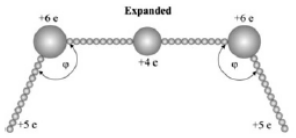	Repulsive energy between arms and body $\phi_0 \sim 4$ kT, Effective length L_e > 15 nm Most probable for pH < 4, or pH > 10, $I < 10^{-3}$ M

1.2 Bionanotechnology

Bionanotechnology is a booming field of study that combines the unique properties of nanoscale materials with the specificity and uniqueness of biomolecules, to surpass the limitations of conventional Medicine and Biotechnology, especially in the field of diagnostics and treatment. Since materials can vary in chemical composition, size, shape, charge and other properties, the research opportunities are numerous. As many nanoscale effects are being studied but are still not well understood, every piece of information is highly appreciated in order to develop theoretical models to explain the observed effects and envisage possible applications. [5]

1.2.1 Colloidal Suspensions

One of the main topics in Bionanotechnology is the application and study of Colloidal Suspensions. These are heterogeneous mixtures of a dispersion of particles, of a substance, in a dispersive medium of another substance, in different physical states. These particles are larger than the common solutes, with sizes varying between 1-1000 nanometers (nm). As for the dispersion and the dispersive medium, both components can be in various combinations of physical states of matter (Liquid, Solid, and Gas). As for the combination studied in this work, a dispersion of Solid Noble Metal particles in a Dispersive Liquid medium is called a Sol (Table 1.3) [11]

Table 1.3. Types of Colloids. Adapted from [11].

Dispersive Medium	Dispersion	Name
Gas	Liquid	Aerosol
Gas	Solid	Aerosol
Liquid	Gas	Foam
Liquid	Liquid	Emulsion
Liquid	Solid	Sol
Solid	Gas	Foam
Solid	Liquid	Gel
Solid	Solid	Solid Sol

1.2.1.1 Light Scattering and Surface Plasmons

Colloids are composed nanoscale sized particles, and the interaction with light has distinct effects from the macroscale bulk counterparts. One of the main defining properties of colloidal suspensions is the Rayleigh effect, which occurs as small sized particles interact with electromagnetic radiation, at longer wavelengths. Upon exposure to the incident light source, it induces polarization of the particle, which in turn results in light scattering. [12, 13] This effect can be exploited to determine valuable information such as the hydrodynamic size of particles in a colloid based on the scattered light. Some of these techniques are the Dynamic Light Scattering (DLS) and Nanoparticle Tracking Analysis (NTA). In the case of the DLS, a second technique can be used at the same time, which is the Electrophoretic light scattering that will be referred in section 1.2.1.4.

As for metallic nanoparticles, after induced polarization by the incident light, delocalized electrons circulate along the metallic surface. These electrons, or Surface Plasmons, resonate at a specific frequency, the Surface Plasmon Resonance (SPR), which leads to the absorption of light at a specific wavelength. The SPR band can be measured by UV-Vis spectroscopy and is commonly used in for metallic nanoparticle characterization as it is sensible to size and surface chemistry. [14] This effect in specific will be discussed in further detail below in Surface Plasmon Resonance chapter (1.2.1.1.3).

1.2.1.1.1 Dynamic Light Scattering

When light interacts with a sample of particles, oscillating dipoles are formed that reemit radiation. As particles are in movement, the Brownian motion, the scattered light suffers intensity fluctuations from the passing particles. These are influenced by the correspondent particle size as the particles acquire velocity and direction relative to the detector, where smaller sized particles have higher frequency fluctuations, while the bigger sized particles have lower frequency

fluctuations, the Doppler effect. Dynamic Light Scattering (DLS) evaluates particle size distributions based the scattered light monitored at a microsecond time range

As the erratically moving particles scatter light, the instrument uses a Correlation Function:

$$G(t) = A\left[1 + B\, e^{(-2\Gamma t)}\right]$$

Equation 1.3

where *t* is the time difference of the correlator, *A* is the baseline of the correlation function, *B* is intercept of the correlation function and Γ is the decay rate (the reciprocal of the decay time). Assuming the decay rate and the translational diffusion coefficient relate as:

$$\Gamma = Dq^2$$

Equation 1.4

Knowing that:

$$q = \left(\frac{4\,\pi\, n}{\lambda_0}\right) sin\left(\frac{\theta}{2}\right)$$

Equation 1.5

where *n* is the refractive index of dispersant, λ_0 is the wavelength of the laser, and θ is the scattering angle. From this data, radius of the particles can be estimated and using the Stokes-Einstein equation:

$$D = \frac{k_B T}{6\,\pi\,\eta\,\mathrm{r}}$$

Equation 1.6

where *D* is the translational diffusion coefficient, k_B is Boltzmann's constant, *T* is the temperature in Kelvin, η is the viscosity of the liquid and *r* is the radius of the particles. [15]

This technique is, however, less effective as size heterogeneity is present, as larger particles tend to affect the light intensity at a greater magnitude than smaller particles, and can be explained using the following equation:

$$\%I_a = \frac{100(a^6 N_a)}{N_a\ a^6 + N_b\ b^6}$$

Equation 1.7

where $\%I_a$ is the intensity-weighted distribution for particles with size *a,* N_a and N_b are the respective number of *a*-sized and *b*-sized molecules. The intensity is therefore influenced by the size of the particle at an order of magnitude of 6 (size^6). [15]

This problem leads to unaccounted small sized particles, and in many situations not being detected at all. A second issue with this technique is the particle concentration, as larger sized particles affect the light scattering effect, at a higher magnitude than smaller sized particles, upon analyzing highly concentrated colloidal solutions, the high proximity of neighboring particles leads to an irregular light scattering, misleading the instrument into assuming the results as bigger sized particles as seen in Figure 1.9. Particle aggregation also misleads the instrumentation as the high concentration issue. [14, 16]

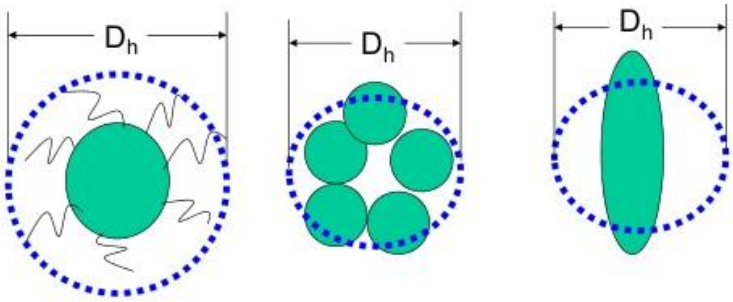

Figure 1.9. Spherical Particle size assumption, as Hydrodynamic Diameter (D_h), by Dynamic Light Scattering. Adapted from [16].

As for irregular shaped structures, like the elongated shape in the previous figure, different strategies are recommended to estimate the dimensions, like the use of the gyration radius and diffusion coefficient to estimate length and side radius. [17]

1.2.1.1.2 Nanoparticle Tracking Analysis

Nanoparticle Tracking Analysis (NTA), as DLS, uses the light scattering effect and the Brownian motion of nanoparticles to characterize them. But, whereas in the case of DLS, hydrodynamic sizes are determined for the bulk, in the case of NTA, individual nanoparticles can be tracked. In fact, NTA uses video recording to track individual particles in a colloidal solution under optical darkfield conditions. This analytical strategy allows to obtain a better and more accurate size distribution in polydisperse solutions. Using a similar equation to Equation 1.6 the hydrodynamic diameter, d_h, can be estimated:

$$d_h = \frac{4\, k_B\, T\, \Delta t}{3\, \pi\, \eta < (x,y)^2 >}$$

Equation 1.8

where k_B is Boltzmann's constant, Δt is the recording time, T is the temperature in Kelvin, η is the viscosity of the liquid and $<(x,y)^2>$ is the mean-squared displacement in two dimensions. [18]

Although NTA presents other important advantages over DLS, such as the possibility to determine exact concentrations for colloidal solutions of nanoparticles with any morphology, many disadvantages relatively to the DLS technique are also present. The latter include a lower size range, limited concentration range, lower reproducibility, higher complexity, longer measurement times. Since both techniques have advantages and disadvantages, the application of both as complementary methods is recommended. [19, 20, 21]

1.2.1.1.3 Surface Plasmon Resonance

As previously stated, colloidal solutions upon irradiation, scatter light in all directions. Metallic nanostructures however have additional conductive properties and noble metals in particular, such as Gold (Au) with an electronic configuration of [Xe] $4f^{14}$ $5d^{10}$ $6s^1$, have valence electrons, in the valence band, which overlap the energy level of the conduction band. These free electrons, move freely at the gold nanostructure surface, producing an electrical current. [22]

As gold nanostructures interact with electromagnetic waves and the incident electric field, a dipole is created, as seen in Figure 1.10, due to charge separation. The oscillating delocalized electrons resonate at the same frequency as the alternating electrical field and this effect is the Surface Plasmon Resonance (SPR), leading to an absorption band in the visible spectrum. Gold nanoparticles of 15 nm in diameter have the SPR absorption peak at around 520 nm, which corresponds to a transmitted red color (620-750 nm). UV-Visible Spectroscopy is commonly used to measure these optical properties, which have been exploited in the development of biosensors by chemical modifications at the surface. [23, 24, 25] A 450 nm (blue color) absorption peak is also visible due to d-s transition (interband) of electrons. [26]

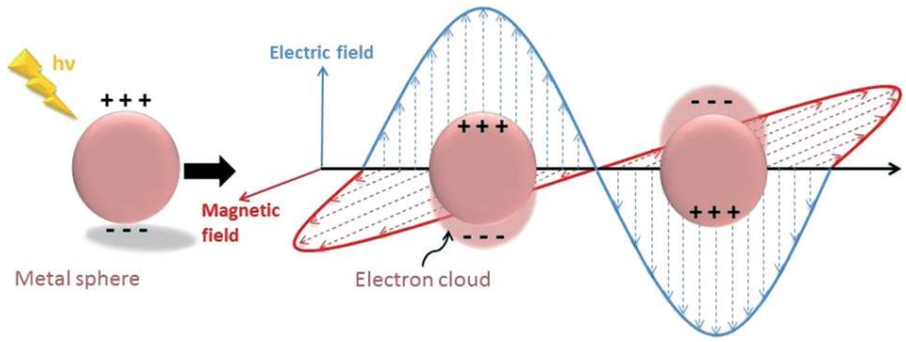

Figure 1.10. Surface Plasmon Resonance induced by incident light. Adapted from [27]

The resonance frequency depends on the dielectric properties of the metal and the medium, and the electric field strength. These effects are also influenced by particle size, shape, chemistry, concentration, and the refractive index of the medium. [28] The SPR effect is used to characterize the AuNPs in terms of size and surface modifications. Sample size and concentration is obtained by using empirical data from previous studies that accurately relate the SPR and 450 nm absorbance peaks to the correspondent particle size, and then estimate sample concentration. [29]

1.2.1.2 Surface Potential

Colloids, as previously stated, are small solid particles dispersed in a liquid and, upon interaction with other electrolytes present in the aqueous medium, gain a net surface charge. These charged particles, possess a differential electric potential at the surface relative to the medium, thus creating an electric double-layer (EDL) which can be explained by the Stern Model. [30]

1.2.1.2.1 Electrical Double Layer and Zeta-Potential

The EDL, which thickness highly depends on the electrolyte concentration and chemistry, can be divided into two different layers, the Stern layer and the Diffuse layer (Figure 1.11).

The Stern layer is composed of charges from the interacting surface and ions of opposite charge from the medium, here the electrical potential is maximum. The Diffuse Layer is composed of free ions in the medium that are affected by the electrostatic forces of the particle and random thermal motion, and in this layer, distance greatly affects the electrical potential value. The ζ-Potential (Zeta-potential) is the only obtainable value of an electrical potential and is used as the value of the EDL potential to explain some of the particle properties and interaction phenomena. One of such properties is the colloidal stability in which the DLVO theory explains how electrolyte

concentration and other variables affect the particle-particle interaction in an aqueous medium and thus their stability. [30, 31]

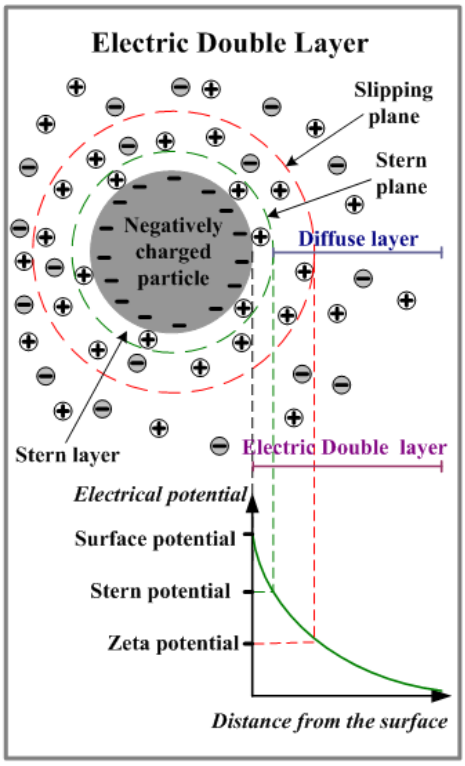

Figure 1.11. Schematic illustration of an Electric Double Layer (EDL) and an Electrical Potential curve for each plane. [32]

1.2.1.2.2 DLVO Theory

Assuming a colloidal dispersion of negatively charged particles in a polar medium, as two similar particles of equal charge approach, there are two main forces contributing to the total potential energy of the system: (i) the attractive intermolecular forces represented by the Van der Waals forces; and (ii) the repulsive forces from the Electrostatic effects of the EDL.

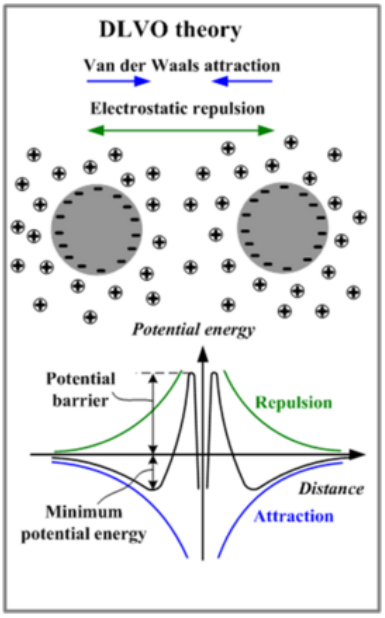

Figure 1.12. DLVO theory depiction on the interaction of two colloids of equal charge. Potential curves for repulsive forces (green) and attractive forces (blue) and resulting particle potential energy (black). [32].

As seen in Figure 1.12, as these two forces counter-act each other, a resulting potential energy is obtained. This potential energy (V_T) can be estimated by the following equation:

$$V_T = V_A - V_R \qquad \text{Equation 1.9}$$

where V_A is the potential energy of the attractive forces, and V_R is the potential energy of the repulsive forces. These potentials are given by:

$$V_A = -\frac{A\,r}{12\,x} \qquad \text{Equation 1.10}$$

$$V_R = 2\,\pi\,\varepsilon\,\varepsilon_0\,r\,\zeta^2\,e^{(-kx)} \qquad \text{Equation 1.11}$$

where A is the Hamaker constant, x is the distance between particles, ε is the permittivity of the solvent, ε_0 is the vacuum permittivity, r is the particle radius, ζ is the zeta-potential, k is an ionic

composition function (k^{-1} is the EDL thickness, also known as the Debye length). The Debye length is given by:

$$k^{-1} = \left(\frac{k_B T \varepsilon_0 \varepsilon}{2q^2 N_A I}\right)$$

Equation 1.12

where q is the elementary charge, N_A is the Avogadro number, I is the ionic strength, k_B is the Boltzmann constant, and T is the absolute temperature.

The resultant potential energy is nullified at large inter-particle distances as shown in Figure 1.13 and, as the distance decreases, an Energy Barrier is observed that impedes equally charged particle to strongly adhere. If, however, the two particles make contact, due to a collision or a decrease in the EDL thickness, the adhesion process is highly favored, and the particles will irreversibly aggregate. Two potential minima surround the energy barrier, the Secondary and Primary minima. These low potential energy zones correspond to the aggregation state of the particles and can be tuned by the electrolyte concentration present in the colloidal solution. The secondary minimum regulates weak-aggregation effects, also known as the Flocculation process, where reversible particle aggregation occurs, and at low electrolyte concentrations, this minimum potential is nullified. The Primary minimum however, is always present as the proximity of particles lead to irreversible aggregation, also known as Coagulation, caused by the full extent of attractive forces. This minimum is reached upon overcoming the energy barrier.

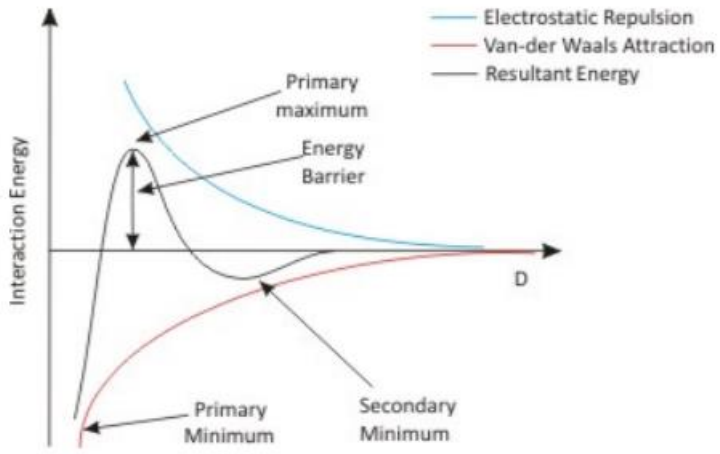

Figure 1.13. Energy barrier for colloids in an electrolytic medium, and Primary and Secondary electrical potential minimum. Adapted from [33].

The attractive forces, and correspondent electrical potential (V_A), mainly depend on the inter-particle distances. The repulsive forces, and electrical potential (V_R), however greatly depend, besides inter-particle distance, on the EDL thickness (Debye Length) and the Zeta-potential. Both

these values are affected by the electrolyte concentration, and thus the concentration of ions of opposing charges. Even though monovalent salts have an equal presence of anions and cations when introduced in a colloidal solution, upon entering the vicinity of charged particles, the opposing charged ions tend to concentrate around the particle. This will lead to a weakening of the EDL, and neutralization of the Zeta-Potential, and the respective repulsive electrostatic forces as seen in Figure 1.14.

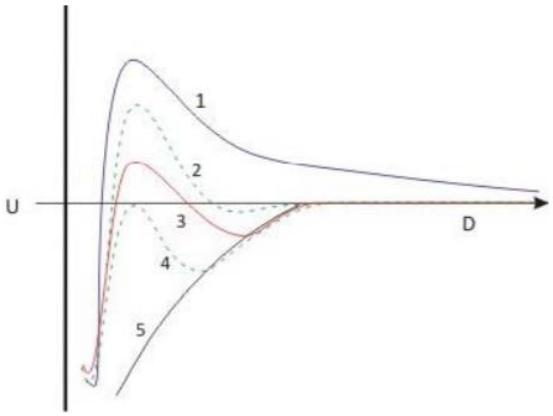

Figure 1.14. Influence of an increasing salt concentration (1 the lowest, and 5 the highest) on the repulsive electrical potential. [33].

As the repulsive forces are weakened by an increase in salt concentration, the resultant electrical potential is also lowered, as seen in Figure 1.15. As salt concentration increases, the energy barriers decrease, and at later stages are nullified. This will cause the particles to be fully affected by attractive forces and irreversibly aggregate. A way to overcome this issue is to coat the particles with a polymer or biomolecule, which thickness impedes the surfaces of the particles to interact due to steric repulsion. As the thickness of the coating increases, so does the inter-particle distance, passively mitigating the attractive forces.

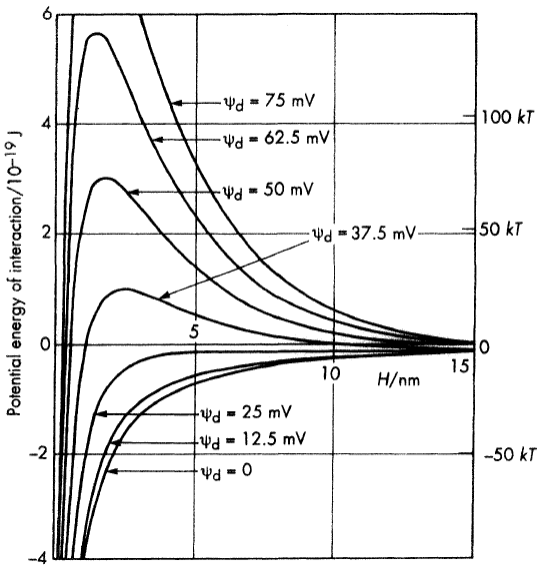

Figure 1.15. The influence of the potential energy of repulsive forces, Ψ_d, on the resultant total potential energy of the interaction between two particles. [30].

The EDL and Zeta-potential are also affected by ion valence, as colloids are more sensitive to multivalence ions, and pH, as negatively charged particles are introduced to acidic environments, positively charged ions interact with the surface leading to charge neutralization (and vice-versa). It is accepted that particles in a colloid are stable when their Zeta-Potential is outside the range of ± 30 mV. When in this range, Zeta-Potential values closer to neutrality, represent weaker repulsive forces and result in aggregation. An example of the pH effect is depicted in Figure 1.16, as the pH of the colloidal solution nears the isoelectric point of the particle, the Zeta-Potential is nullified and the particle aggregates, also pH values in the proximity of the isoelectric point are unstable. The only stable region is at the extreme values of pH. However, transitioning from a stable region to the opposite stable region of Zeta-Potential values may lead to irreversible aggregation by passing through the unstable region. [31]

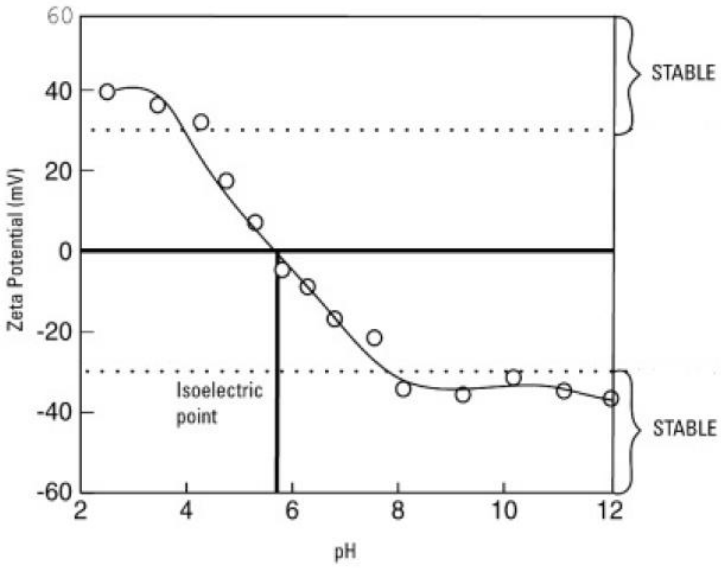

Figure 1.16. Zeta-Potential values at a pH range of 2.0-12.0 for a particle with a surface isoelectric point around pH 6.0. [34]

1.2.1.3 Electrophoresis

Electrically charged particles (and biomolecules) may acquire movement, in a solution, when an external electric field is applied. The electric field, assuming as a uniform field, can be characterized by the following equation:

$$E = \frac{P}{d}$$

Equation 1.13

where *E* is the Electric Field, *P* is the electric potential and *d* is the distance between electrodes. The charged particles, upon being affected by the external electrical potential move to the correspondent Electrode of opposite charge . The movement of charged particles, upon reaching maximum velocity, can be estimated as the Electrophoretic Mobility by the equation:

$$M = \frac{v}{E}$$

Equation 1.14

where *M* is the Electrophoretic Mobility, *v* is the electric charged particle velocity and *E* is the applied Electric Field. This phenomenon of movement of a charged specimen in an electric charged environment is an Electrokinetic effect denominated Electrophoresis. This effect can be exploited to obtain an important parameter that correlates to the Zeta-Potential, also known as the Electrokinetic Potential by using the following equation:

$$M_0 = \frac{\varepsilon\,\zeta}{\eta} f_H(ka)$$

Equation 1.15

where M_0 is the free Electrophoretic Mobility, ε and η are the dielectric constant and the viscosity of the medium respectively, ζ is the zeta-potential, and $f_H(ka)$ is Henry's function. Henry's function can be assumed to have a value between 1, the Huckel approximation for a non-polar medium, and 1.5, the Smoluchowski approximation for a polar medium. The electrophoresis however, is composed of two main acting forces that depend on the electric field and the EDL as seen in Figure 1.17. These are the Electrostatic Force (E_F), which is derived from the interaction between the surface charge of the particle and the electric field, and the Retardation Force (R_F), caused by the interaction between the diffuse layer of ions of opposing charges, and also by the charge from the surface of the particle, and the electric field. The longer the Debye Length (k^{-1}), also known as the ELD thickness, the weaker the Retardation Force will be. This is due to the lower number of counteracting ions at the diffuse layer as previously stated. [35, 36, 37, 38]

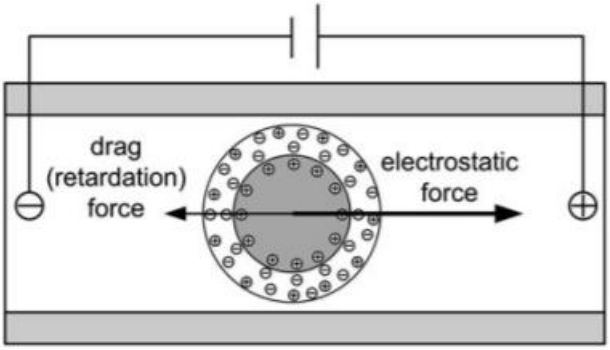

Figure 1.17. The electrophoretic flow of a positively charged particle. Adapted from [39].

Knowing this relationship between Electrophoretic Mobility and Zeta-Potential, techniques like Electrophoretic Light Scattering (ELS) and Agarose Gel Electrophoresis (AGE) are commonly applied to estimate the Zeta-Potential values of particles. Another technique that

uses the electrophoretic effect is the Sodium Dodecyl Sulfate–Polyacrylamide Gel Electrophoresis (SDS-PAGE), which can estimate the molecular weights of proteins.

1.2.1.4 Electrophoretic Light Scattering

This technique combines the previously mentioned properties of Light Scattering and Electrophoresis. Firstly, an electric field is applied, and the particles acquire movement. Afterwards, a light source is applied, where the subsequent scattering is evaluated, and the particle velocity is determined. Knowing the velocity and the applied electric field strength, the electrophoretic mobility is obtained. Finally, by using the relationship between the electrophoretic mobility and the Zeta-Potential, the latter value is obtained. [38, 40]

1.2.1.5 Agarose Gel Electrophoresis

Agarose Gel Electrophoresis is commonly used to study the electrophoretic mobility of DNA and RNA fragments, Proteins and Bionanoconjugates. Having two electrodes of opposing charge, an electric field is created which leads to sample migration as seen in Figure 1.18.

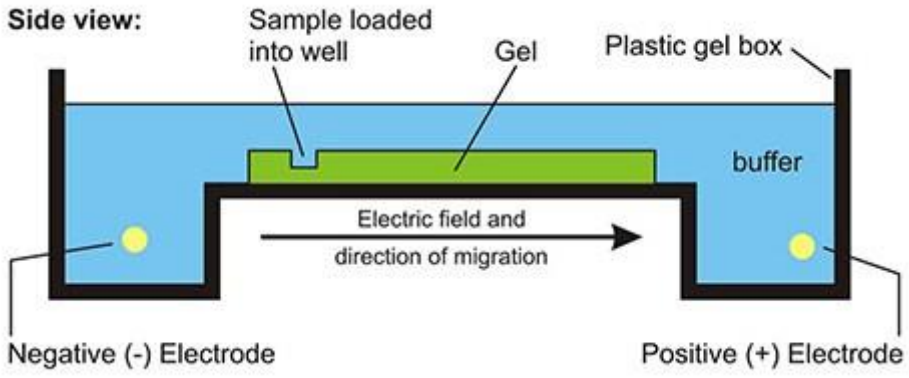

Figure 1.18. Agarose gel electrophoresis method schematic. [41].

This technique has a particularity of applying the samples, horizontally, in an Agarose Gel. The porosity, viscosity and conductivity of the gel can be tuned by choosing the desirable Agarose concentration and Buffer (type and concentration). After electrophoresis runs, samples are usually dyed in order to be detected and the migration quantified. However, in colored samples like nanoparticles and bionanoconjugates dyeing is not required. [41, 42, 43] Similar results can be obtained as the Electrophoretic Light Scattering technique, however, since a Gel matrix is used, the obtained electrophoretic mobility (M) is not the same that the free electrophoretic mobility (M_0) discussed previously, that can be exploited to obtain Zeta-Potential values. To estimate a free electrophoretic mobility, a Fergusson Plot Analysis procedure can be executed.

The Fergusson Plot Analysis is composed of the same electrophoretic experiment being performed at various Agarose Gel concentrations. After obtaining all the electrophoretic mobility profiles for each agarose concentration, an extrapolation to a condition of zero concentration of agarose is applied and the free electrophoretic mobility, and sample effective diameter (D_{eff}), can be obtained. The results obtained from this indirect procedure, as the free electrophoretic mobility (M_0) is extrapolated from the sample mobility variation between multiple agarose gels of differing concentrations and may lead to erroneous results. Furthermore, the tested AuNP sizes in the referenced study were between 4 and 20 nm and conjugated with DNA, while the samples in this work were between 15 and 40 nm and conjugated with BSA and Fib. [44] Although the low credibility of the estimated values, relative size and charge variations are still a precious source of information to augment the understanding of the biomolecule adsorption to the AuNPs. Other more direct methods, like DLS and ELS, should be always preferred to verify size and zeta-potential values.

1.2.1.6 SDS-PAGE Electrophoresis

Sodium Dodecyl Sulfate–Polyacrylamide Gel Electrophoresis (SDS-PAGE) resembles the Agarose Gel Electrophoresis (AGE) technique, as an electric field Is applied in order to promote movement of charged biomolecules. This technique however, varies due to the vertical position of the gel, the type and concentration of the gel matrix, the sample preparations, staining and decoloring steps, electrical potential and duration.

The gel matrix, composed of Polyacrylamide, has a tunable well-structured pore matrix depending on the concentration used, and has two differently concentrated sections, a more concentrated (7.5-15%) gel bellow, to promote band separation called the Resolving Gel, and a less concentrated (4%) on top, to allow the samples to concentrate in the wells called the Stacking Gel. When an electric field is applied, lower weight protein fragments migrate faster than higher weight protein fragments, allowing a protein weight profile based on electrophoretic movement as seen in Figure 1.19.

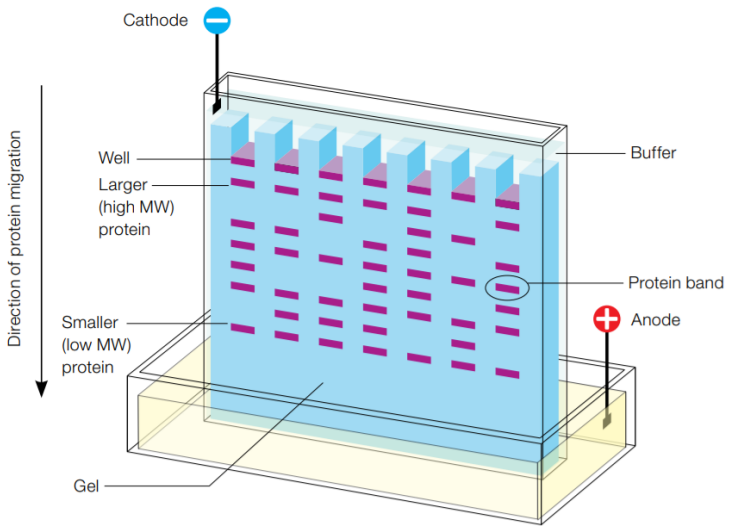

Figure 1.19. Sodium Dodecyl Sulfate–Polyacrylamide Gel Electrophoresis (SDS-PAGE). [45]

Compared to Agarose, Polyacrylamide allows a smaller pore size, and thus the separation of proteins, and a molecular weight resolution between 5-250 kDa. Due to the dense matrix, the technique is tuned to a lower electric potential (50-60V) and longer duration (1-2 hours).

As for samples, since different proteins have different electrostatic potentials, when applying an electric field, the migration would be affected by the correspondent surface charge and conformation. To eliminate these factors and make migration to depend exclusively on the mass of the protein, Sodium Dodecyl Sulfate is used to fully denature the proteins in to an elongated form, as seen in Figure 1.20, and to confer an overall uniform negative charge to all protein fragments. By applying this denaturing step, all migrations are dependent on fragment size. [3, 45, 46]

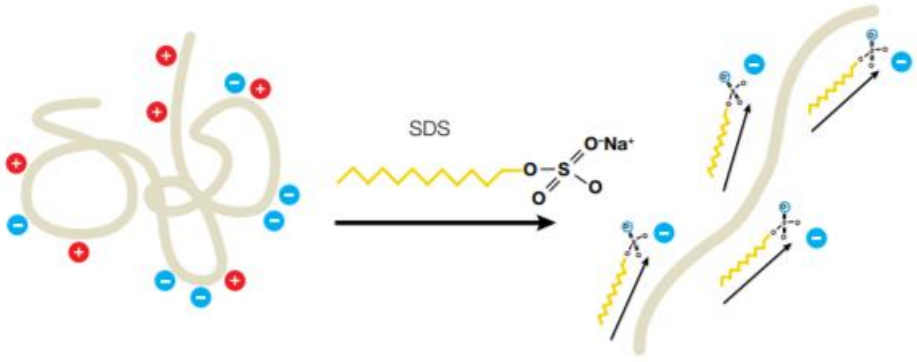

Figure 1.20. Change of conformation and Charge of a Protein by Sodium Dodecyl Sulfate (SDS). [45].

1.2.2 Gold Nanoparticles

Gold nanoparticles (AuNPs) are one of the most common types of nanostructures used in biomedical research due to their low toxicity, easy and fast synthesis methods, and relative stability. As for the inherent chemical and physical properties, such as surface plasmon resonance (SPR), conductivity and others, and the innumerous types of Functionalization and Bioconjugation make these particles versatile and popular. The nanoscale size allows a higher surface area to volume ratio and accessibility to biological tissues, relative to their bulk counterparts, while having distinct color, toughness and reactivity. Many applications are being designed to use the AuNPs to reach targets within tissues and perform tasks like imaging and drug delivering. The higher surface area allows better performance in terms of reactivity, serving as improved catalysts, diminishing the reaction times. As for optical and chemical properties at this size range, these particles have enhanced conductivity and sensitivity to chemical environment changes, which are extremely useful in the development of biosensors and other electrochemical applications. [47, 48]

As for the morphology, AuNPs are polyhedral nanostructures, have an atomic packing of a face-centered cubic (fcc) crystal system and may present various types of shapes depending on the synthesis method performed as seen in Figure 1.21. The multiple shapes allow different properties, having advantageous exploitable effects for more techniques and surface interactions. These shapes further can be further classified as Isotropic, which have the same physical and chemical properties in all directions, such as the Nanospheres, and Anisotropic, which have multiple properties due to the various crystallographic orientations, such as Nanorods and Nanostars. [49]

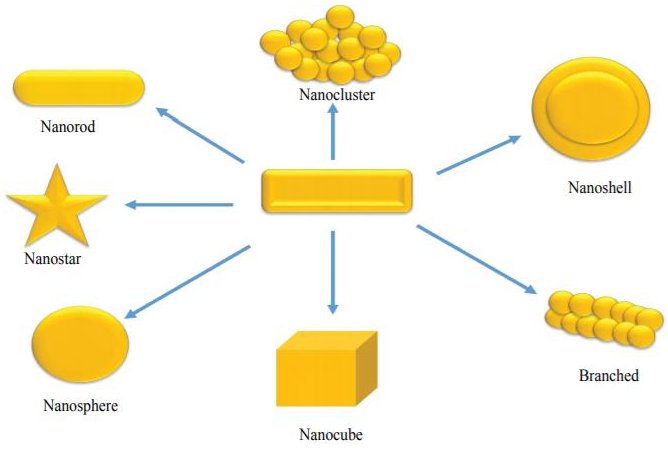

Figure 1.21. Shapes of Gold nanoparticles. Adapted from [49]

In this work only Nanospheres were used. Although called Nanospheres, the structure is, as stated before, polyhedral. The quasi-spherical classification is attributed to simplify AuNP molecular modelling. Assuming a perfect spherical shape, the number of gold atoms can be estimated from the AuNP size using the following equation:

$$N_{Au} = \frac{4\,\pi\,r^3}{3\,V_{Au}} = \frac{\pi\,D^3}{102}$$

Equation 1.16

where N_{Au} is the number of gold atoms, *r* and *D* are the radius and diameter, in angstroms, of the gold nanoparticle, respectively, and V_{Au} is the volume of a gold atom. The problem of assuming a spherical morphology, is the discrepancy of the number of atoms from the real polyhedral shape. This discrepancy increases as the particle size decreases as seen in Figure 1.22, where the number of gold atoms in a quasi-spherical, N_{cs}, and an icosahedron, N_{ico}, configuration have a difference of a factor of 1.7, and the icosahedron configuration has the closest number of gold atoms to reality. [50]

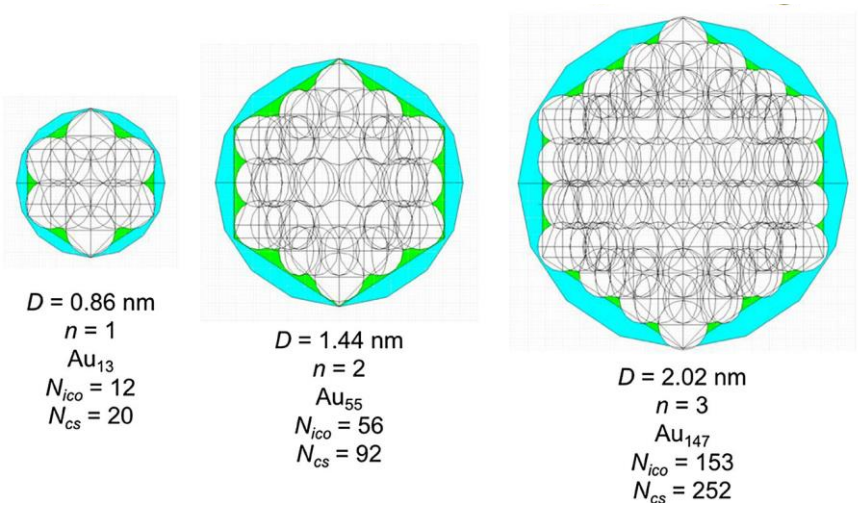

Figure 1.22. Gold clusters Au13, Au55, and Au147 and discrepancy in the number of gold atoms between quasi-sphere and regular icosahedron. The subscripted value is the number of gold atoms. Adapted from [50]

1.2.2.1 Synthesis

Spherical gold nanoparticles can be synthesized in multiple ways. The most common and practical one is the bottom-up synthesis by chemical reduction, in which the gold precursor is reduced by a reducing agent in a heated aqueous solution. The typical reagents used in this type of reaction are the chloroauric acid ($HAuCl_4$), as the gold precursor, and sodium citrate ($Na_3C_6H_5O_7$) as the reducing agent, as described in the Turkevich Method. [31]

First, the oxidation process of citrate to dicarboxy acetone is performed:

$$C_6H_5O_7 \rightarrow C_5H_6O_5 + CO_2 + H^+ + 2e^-$$

Equation 1.17

Secondly, the reduction of auric salt to aurous salt:

$$AuCl_3 + 2e^- \rightarrow AuCl + 2Cl^-$$

Equation 1.18

And finally, disproportionation of aurous salt to gold atoms:

$$3AuCl \rightarrow 2Au^0 + AuCl_3$$

Equation 1.19

Having the gold reduced from Au^{3+} to Au^0, the formation of individual gold atoms leads to saturation, where occurs binding of multiple gold atoms in the process called Nucleation as seen in Figure 1.23. During this process, dissolved gold atoms bind to these particles promoting their growth. The particle size can be tuned by modifying the reducing agent concentration. In fact, as the reducing agent is also a capping agent for the synthesized nanoparticles, having less reducing agent contributes to fewer ions to stabilize the particles surface, making the particles bigger. Constant stirring is necessary to minimize particle size distribution. After the synthesis, these gold particles can be used as seed particles, in which we can increase the particle size by further gold atom binding. [51, 52]

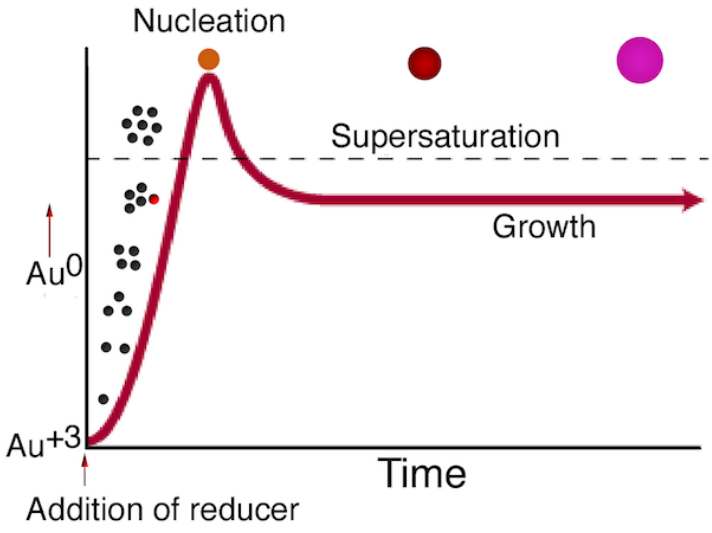

Figure 1.23. Gold nanoparticle Nucleation and Growth processes over time. [53]

1.2.2.2 Functionalization

Although the post-synthesis stabilization of the nanoparticle surface by citrate, the interaction is weak and can be easily disturbed. This type of interaction is denominated Physisorption and consists mostly of electrostatic forces. Due to surface instability, these particles tend to agglomerate and interact with other particles without stabilizing agents until they reach a stable size. A way to stabilize the surface of the particle is by using capping agents, which are molecules that interact by weak or strong bonds, depending on the type of agent, making an

intermediate monolayer between the solvent molecules and the nanoparticle. One of the most common types of capping agents are the Thiolates, which strongly interact with the Gold surface by chemisorption through their sulfur atom (S-Au). A monolayer can form by self-assembly (self-assembled monolayer or SAM), completely covering the particle. The molecular structure of these capping agents can be divided in three regions of interest as seen in Figure 1.24. The terminal group, constituted by the sulfur end that directly interacts with the gold surface, the intermediate hydrophobic spacer group, that promotes the self-assembly monolayer formation, and the head group, which determines the surface chemistry and surface charge of the functionalized particle. [54, 55]

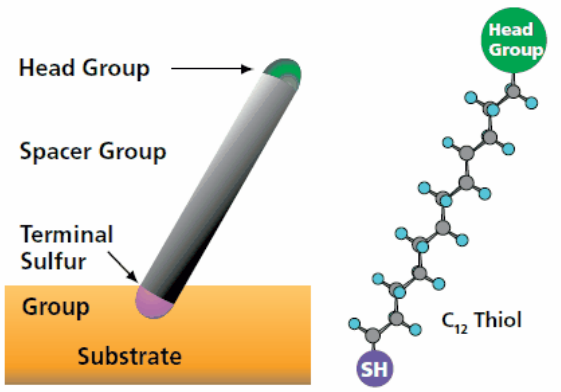

Figure 1.24. Structure of Thiol molecule interacting with a substrate. [56]

1.2.2.2.1 Negative Surface Charge Functionalization

In this work, two types of negative surface charge capping agents were studied, the 11-Mercaptoundecanoic acid (MUA) and the pentapeptide Cysteine-Alanine-Leucine-Asparagine-Asparagine (CALNN) as seen in Figure 1.25. Both have the three regions of interest, the sulfur terminal group, the self-assembly spacer group characterized by the alkane chain, in the case of MUA, and the Alanine-Leucine peptides, in the case of CALNN, and the head group that confers the functionalized surface identity, being the carboxylic (COOH) group for MUA, and the two Asparagine peptides for CALNN. Both these types of functionalization aim to electrostatically attract positively charged regions of biomolecules. [57, 58]

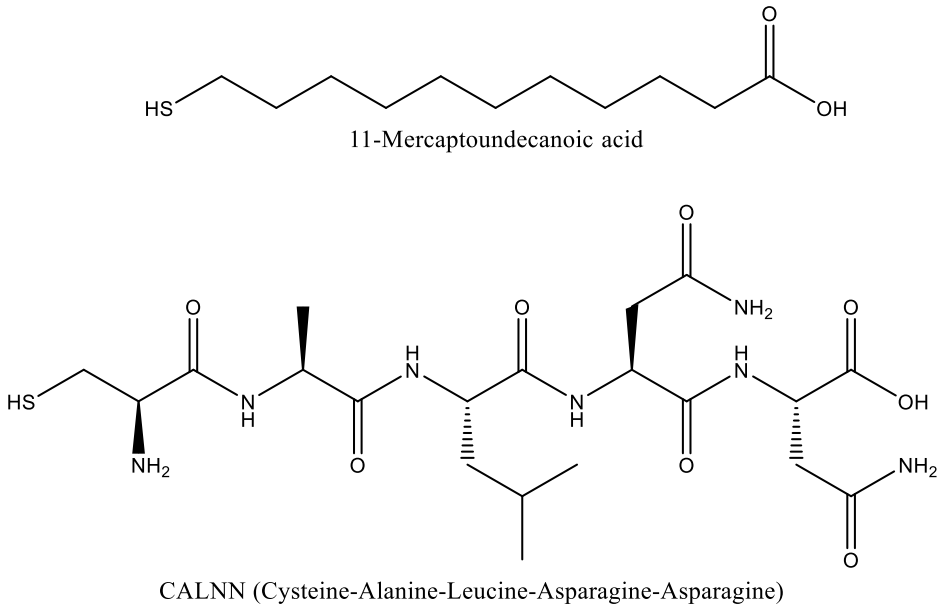

Figure 1.25. Structural representation of MUA (top) and CALNN (bottom).

1.2.2.2.2 Positive Surface Charge Functionalization

As for the positive surface charge functionalization, 11-Amino-1-undecanethiol (AUT) was selected as a capping agent candidate. The structural properties are closely similar to the MUA molecule, as seen in Figure 1.26, only varying on the head group composition. The carboxylic end group is replaced by the amino (NH_2) end group. This type of functionalization leads to a surface charge inversion from the negative charged post-synthesis AuNPs to positive charged. [59]

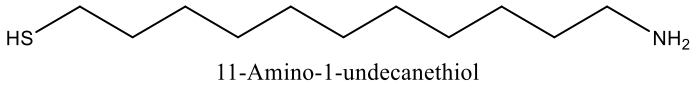

Figure 1.26. Structural representation of AUT.

1.2.2.3 Bioconjugation

The study of the interaction between biomolecules and metallic nanoparticles is essential to determine the applicability and safety displayed *in vivo*. The possibility of penetrating target tissues to perform a task is quite exciting, but the assurance that no damage is done and that is performed at maximum efficiency is preoccupying the scientific community. [60]

The immune system is programmed to eliminate foreign threats, and the nanoparticle presence might trigger a response followed by opsonization. Due to this, biocompatibility should be highly regarded by minimizing collateral hazardous effects and stealthily perform under the

immune system surveillance for a time period long enough before clearance. The adapted strategies were:

- Have the right size, not small enough to be captured by large biomolecules, and not too large to be detected by the immune system;
- Present colloidal stability to ensure that no aggregate formation is triggered;
- Have an outer layer that mimics the bio-setting.

For the first two strategies, sizes between 5 and 40 nm are preferred, and surface functionalization enhances overall stability. As for the last one, biomolecules such as proteins dynamically adsorb to the nanoparticle surface as discussed in the Vroman effect (chapter 1.1.2). [61]

1.2.2.3.1 Protein Corona

The adsorption of proteins at the nanoparticle surface is a dynamic process and leads to the formation of an outer layer called the Protein Corona. The composition and structure of this biological layer depends on the physicochemical properties of the nanoparticle (size, shape, surface charge, hydrophobicity, functionalization, etc.) and the physiological conditions. The protein content of the outer layer will determine the biological identity, the immune system response and the performance of these particles. [62]

The Protein Corona can be divided in two regions, as seen in Figure 1.27, the inner and strongly attached proteins that interact directly with the surface of the nanoparticle, forming the Hard Corona, and the loosely attached proteins in an outer layer, that interact weakly with the adsorbed proteins, frequently exchanging with other proteins that form the Soft Corona. Due to the weak interactions by proteins forming the Soft Corona, many techniques performed to analyze bionanoconjugated samples will inevitably lead to these protein's removal by physical or electrochemical effects. Consequently, alternative methods must be performed to differentiate the Hard and Soft Corona composition. As for this work, only the Hard corona should be considered since the used techniques (centrifugation and electrophoresis of the protein-AuNP conjugates) most likely are enough to detach the weakly bounded Soft Corona, as reported in the referenced study [63], although the two coronas are undistinguished in the obtained results.

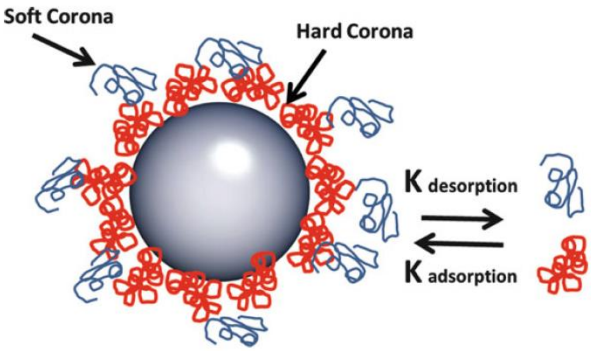

Figure 1.27. Schematic illustration of soft and hard protein corona and the concept of the rate of adsorption and desorption. [63]

2 Objectives and Experimental approach

The direct application of the Gold Nanoparticles has been one of the main focuses of biomedical research. This work aims to establish a foundation that allows better understanding of the properties of the different combinations of proteins, nanoparticles and functionalization types, and to possibly design a diagnostic protocol that allows the use of these particles to detect blood protein composition anomalies, that might be connected to specific diseases and conditions.

Some of the factors that affect the interaction Protein-Nanoparticle interaction, such as size, curvature, surface chemistry, the type and quantity of proteins, were tested and compared. The following experimental approach was designed:

1. **Nanoparticle**
    a. **Synthesis** – Direct and Inverse methods were tested to yield the target size with a narrow size distribution.
    b. **Characterization** – Surface Plasmon Resonance allowed, by UV-Vis Spectroscopy, to obtain values of concentration and size. Functionalization and Stability of AuNP and its bioconjugates were also tested by this method.
    c. **Functionalization** – Thiol-Au interactions between capping agents and the AuNP surface, forming self-assembling monolayers, to confer further stability and functionality. Negative charged functionalization with CALNN and MUA were performed, and Positive charged functionalization with AUT was attempted.
    d. **Stability** – Comparison of Ionic force and pH (acidic and basic) tolerance of functionalized and non-functionalized samples to determine the viability for *in vivo* applications.

2. **Protein**
    a. **Characterization** – SDS-PAGE was performed to analyze the molecular weights and to confirm the quality and purity of the protein samples.
    b. **Quantification** – BCA assays determined the protein concentration of the prepared samples, allowing to perform bioconjugation at varying Protein : AuNP molar ratios.
    c. **Human-Bovine Homology** – Comparison of the Human and Bovine sequential and structural homology, to check for possibility of similar effects, that were verified in this work on Bovine samples, on Human samples. The PDB files used in the protein structural representation were also tested for data integrity based on the sequential data.
    d. Electrostatic Potential – Based on Bioinformatic tools, the pH-dependent electrostatic potential maps were estimated to localize the positive charged structural regions with the highest probability of interacting with the negative charged nanoparticles. Giving insight on possible conformations adapted post adsorption.

3. **Nanoparticle-Protein**
    a. **Bioconjugation** – Progressive protein adsorption to the surface of AuNPs, by varying protein (BSA or Fib) concentration relative to AuNP concentration, allowing the establishment of the adsorptive equilibrium.
    b. **Protein-Protein Competition** – Competitive behavior of BSA *versus* Fib for AuNPs in a colloidal solution, suitable to study the Vroman effect and the protein exchanges in an *in vivo* environment. Hints on the Protein-Corona composition in complex protein mixtures.
    c. **Electrophoretic Analysis** – Successful functionalization confirmed by this method when bands presented gel migration. Electrophoretic mobility analysis of the bioconjugated samples to determine the [Fib]/[AuNP] ratio at which full surface conjugation can be obtained, and to estimate the relative binding affinity of the two tested proteins for AuNPs of various sizes. Effects of charge and size on electrophoretic mobility were observed.
    d. **Light Dispersion Analysis** – Hydrodynamic diameter (DLS and NTA) and Zeta-Potential (ELS) estimation of Fib conjugated samples, to further understand the multi-band effect verified in this type of conjugation on smaller sized AuNPs.

3 Methods

All reagents and instruments are documented in Appendix IV.

3.1 Spherical Gold Nanoparticle Synthesis

All glassware used in the synthesis process was previously cleansed of any contaminating residues using *aqua regia*, a 1:3 mixture of Nitric acid (HNO_3) and Hydrochloric acid (HCl). Any metallic residues quickly dissolve upon exposure to this solution and were further washed with Milli-Q water (18.2 MΩ cm) until any acidic remains were removed. After a few Milli-Q water wash steps, pH was measured using pH strips until a value of 7.0-8.0 was observed.

The synthesis follows the Turkevich Method reported by Turkevich et al. [64], by reduction of Chloroauric acid ($HAuCl_4$) by Trisodium citrate ($Na_3C_6H_5O_7$), with minor alterations by Kimling et al. [65].

Two types of synthesis were used, Direct and Reverse, both having the same reactive process differing on reagent concentration ratios and order of use in the reaction, in order to obtain different AuNP size ranges close to 15nm in diameter. The main difference between both methods is the smaller size of AuNP obtained by the reverse method. Both reactions have common features, use of a round-bottom flask in reflux system to maintain total volume and concentration and constant magnetic stirring.

3.1.1 Direct reaction method

This reaction is the standard Turkevich method, by adding 69.2 µL of Chloroauric acid (1.42 M) to 100 ml of Milli-Q water. The solution was then heated for a few minutes until boiling. At that point, 10ml of Trisodium citrate (38.8 mM) were added to the solution and the reduction reaction begins. After 15 minutes, heating was stopped, and the solution cooled down at room temperature for a few hours and then proceeded to be characterized. This reaction method yields spherical gold nanoparticle with 15-20 nm in diameter.

3.1.2 Reverse reaction method

Proposed by Ojea-Jiménez et al. [66] as an alternative to the conventional synthesis process, 2 ml of Trisodium citrate (343 mM) was added to 98 ml of Milli-Q and heated until boiling. The pre-heating of water is also a viable alternative. Then, 69.2 µL of Chloroauric acid (1.42 M) was added to start the reduction reaction. After 5 minutes the reaction was stopped, and the solution was cooled down to room temperature for a few hours. This reaction method allows a successful increase in Trisodium Citrate concentration without compromising the final product stability and yields spherical gold nanoparticle with 13-15 nm in diameter.

3.1.3 Gold Nanoparticle Characterization

Post-synthesis AuNPs are stored in glass recipients and covered with aluminum foil to avoid light exposure and possible colloid aggregation.

Characterization of the nanoparticle size and concentration was done using an empirical UV-Vis spectroscopy method discussed by Haiss et al. [29], where diluted (1:6) samples are analyzed in a 300-900nm wavelength. From a SPR peak absorbance and 450 nm absorbance ratio, Equation 3.1, an approximate AuNP diameter was estimated using Equation 3.2 and Equation 3.3.

$$\frac{A_{SPR}}{A_{450nm}} = y \qquad \text{Equation 3.1}$$

$$y = 0.335x + 0.7301 \qquad \text{Equation 3.2}$$

$$Diameter = e^{x} \qquad \text{Equation 3.3}$$

From the known size, the Lambert-Beer law, as in Equation 3.4, is applied which correlates the absorbance value at 450nm with the correspondent extinction coefficient, determining an approximate concentration value.

$$A_{450nm} = \varepsilon_{450nm}\, l\, c \qquad \text{Equation 3.4}$$

The constant ε is the molar extinction coefficient (M^{-1} cm^{-1}), l the optical path (cm) and c is the diluted AuNP concentration (M).

From that diameter, a size-specific molar extinction coefficient provided by Appendix I was used to estimate AuNP concentration. The concentration value was then multiplied by the dilution factor (6x).

The AuNPs from the Reverse reaction method seem to have better stability and narrower size distributions being primarily used in this study as shown in Figure 3.1.

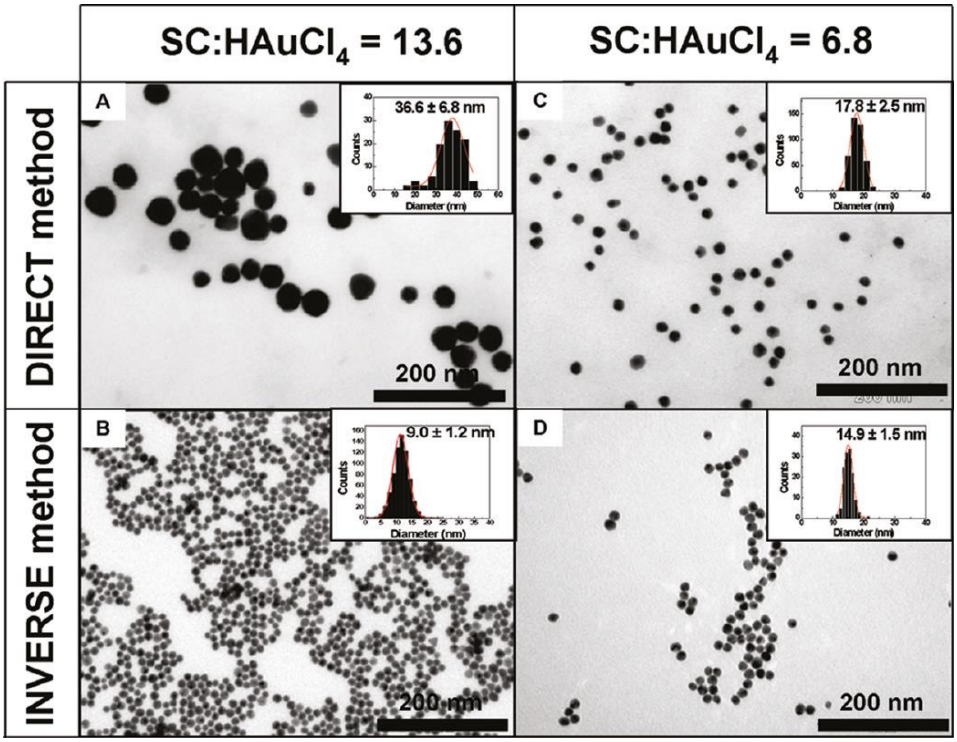

Figure 3.1. Morphological characterization by TEM of AuNPs synthesized by the Direct and Inverse (Reverse) methods with a Sodium citrate: Chloroauric acid ratios of 13.6 and 6.8. The correspondent size distributions are shown. [66]

3.2 Gold Nanoparticle Functionalization

Citrate-AuNPs were functionalized with capping agents, that function as an intermediate, “biofriendly” surface for protein bioconjugation of the Nanoparticle, and also increase colloid stability and allow samples to be used in Agarose Gel Electrophoresis studies without irreversible aggregation. Three capping agents were used, two that make the nanoparticles negatively charged, namely, CALNN (pentapeptide Cys-Alanine-Leucine-Asparagine-Asparagine) and MUA (11-Mercaptoundecanoic acid); and one that makes the nanoparticles positively charged, AUT (11-Amino-1-undecanethiol).

A successful functionalization process was confirmed by UV-Vis spectroscopy by a small 4-5 nm red-shift of the SPR peak. Before use of functionalized AuNPs, a UV-vis spectrum was performed to identify possible aggregation effects.

3.2.1 MUA Functionalization

A 10 mM MUA solution was prepared by adding 21.8 mg of 11-Mercaptoundecanoic acid to 10 ml Ethanol (absolute, HPLC grade). Citrate-capped AuNPs were diluted to a 1-3 nM

concentration in basic water (pH >7) and then added an amount of MUA solution for a 5000:1 ([MUA]/[AuNP]) concentration ratio to fully functionalize the nanoparticle surface with a self-assembly monolayer of MUA molecules. The colloidal solution was then stirred for 15 minutes and left to incubate at room temperature, overnight, for monolayer formation.

The AuNP-MUA colloidal solution was then centrifuged to remove excess MUA, and then quality checked for:

i. Color by naked eye, a red color is considered optimal, whereas a purple color is usually due to aggregation;
ii. UV-Vis spectroscopy, low absorption at the 600-900 nm wavelength range (corresponding to aggregated nanoparticles) is optimal;
iii. Agarose Gel Electrophoresis, uninterrupted electrophoretic mobility without any signs of aggregation or interaction in the sample wells.

3.2.2 CALNN Functionalization

A 5 mM CALNN solution was prepared by adding 1874 µL of potassium phosphate buffer at (pH = 7.4, 10 mM) to 5 mg of the commercial CALNN (Caslo, Denmark). Citrate-capped AuNPs were diluted to a 1-3 nM concentration in basic water (pH >7) and then added an amount of CALNN solution at a 1000:1 ([CALNN]/[AuNP]) concentration ratio to fully functionalize the nanoparticle surface with a self-assembly monolayer of CALNN molecules. The colloidal solution was then stirred for 15 minutes and incubated at room temperature, overnight, to allow complete monolayer formation.

The AuNP-CALNN colloidal solution was then centrifuged to remove excess CALNN, and then quality checked for the same issues as reported for MUA Functionalization.

3.2.3 AUT Functionalization

A 10 mM AUT solution was prepared by adding 23.9 mg of 11-Amino-1-undecanethiol hydrochloride to 10 ml Ethanol (absolute, HPLC grade).

A similar method to the MUA functionalization was applied and irreversible aggregation was observed, so an inverse method was proposed by coating a glass beaker with 1% (m/m) Polyethylenimine (PEI) and then added a diluted 1 mM AUT solution in constant stirring. The colloidal solution pH was set to pH 4.0 to stabilize positively charged AUT-AuNPs by adding HCl 0.1 M. Citrate-AuNPs were then introduced to the AUT colloidal solution in a drop-by-drop method to allow fast functionalization and minimal contact with non-functionalized AuNPs which are negatively charged and can trigger an irreversible aggregation reaction. The amount of AuNPs drops added varied with desired final concentration and multiple samples were tested in UV-Vis to report signs of aggregation along the various AuNP drop additions.

3.3 Protein Concentration determination

A bicinchoninic acid (BCA) protein concentration determination kit was used for the absorbance vs. concentration calibration curve by performing a series of dilutions of a 1.0 mg/ml BSA Standard solution into six Eppendorf tubes of different concentrations (0 to 1.0 mg/ml) in Milli-Q water. Each standard was used for the calibration curve and BSA and Fib solution absorbance determined the correspondent protein concentration using a linear fitting of the calibration curve. BSA and Fib solutions of 0.5 mg/ml were prepared by weighting 5 mg of each protein and dissolved in 10 ml of potassium phosphate buffer (pH = 7.4, 10 mM). A 49:1 (v/v) Bicinchoninic acid to copper (II) sulfate mixture was used as a Working reagent, and immediately protected from light with aluminum foil. 25 µL of each sample, standards and protein solutions, were added to Eppendorf tubes, having duplicates for each, 475 µL of the Working reagent was then added. Each sample was incubated at 37ºC for 30 minutes in a shaker covered by aluminum foil.

After a 30-minute incubation at room temperature, samples change from green to purple with increasing protein concentration due to Cu^{+2} reduction and formation of a Cu^{+} and BCA complex which is purple. This reduction is caused mainly by peptide bonds (but also by some aminoacid residues), as so color intensity is proportional to protein concentration.

3.4 Electrophoresis

Electrophoretic assays were performed under constant electric field by automatic modulation of current intensity by the power source (BioRad). Results were processed by the eReuss software to analyze individual band migration.

3.4.1 Agarose Gel Electrophoresis

Agarose gel 0.5% (w/v) was prepared by weighting 0.3 mg of Agarose and dissolving in 60 ml of TAE 0.125x (from subsequent dilutions of TAE 50x and 1x) for standard AGE studies, and ranges of 0.5-2.0% were used in the Fergusson Plot Analysis studies. Agarose solution were then heated to ~100ºC in constant stirring until translucid. The solution is then cooled down at room temperature and manual mixing the Erlenmeyer until a lower temperature is reached without triggering gelification.

The bioconjugation step was performed using AuNPs at an initial concentration of 1 nM. Samples were incubated overnight in a 4ºC refrigerator, and then centrifuged at 10,000 RPM (~9500 G) at 10 ºC for 10 minutes, and the supernatant was discarded. 13.5 µL of potassium phosphate buffer (pH = 7.4, 5 mM) was used to resuspend the pellet. Finally, 1.5 µL of glycerol was added to increase sample density and improve well deposition.

Agarose Gel Electrophoresis (AGE) was performed using TAE Buffer 0.125x, and under a voltage of 150 V (E = 10 V/cm) for standard AGE studies and 60 V (E = 4 V/cm) for Fergusson Plot analysis studies in a BIO-RAD MINI-SUB® CELL GT.

Although TAE buffer was highly diluted to prevent any aggregation of AuNP samples, lowering media conductivity, and therefore augmenting electric resistance, increases power consumption and temperature on the electrophoretic instruments. This required a low environmental temperature to prevent gel irregularities.

Standard 150 V AGE runs lasted 10-20 minutes depending on the type of test while Fergusson Plot Analysis runs lasted for 40-60 minutes.

3.4.2 SDS-PAGE Electrophoresis

SDS-PAGE was performed by casting two different gels, a Stacking Gel (4%) and a Resolving Gel (12%) composed by the reagents in Table 3.1.

Table 3.1. Handcasted Polyacrylamide Gels Protocol by Bio-Rad Laboratories, Inc. Reagents colored in green are the polymerization reaction inducers, being the last ones added.

	Stacking Gel (4%)	**Resolving Gel (12%)**
30% Acrylamide/Bis	1.98 ml	6 ml
0.5 M Tris-HCl, pH 6.8	3.78 ml	-
1.5 M Tris-HCl, pH 8.8	-	3.75 ml
10% SDS	150 µl	150 µl
Milli-Q H_2O	9 ml	5.03 ml
TEMED	15 µl	7.5 µl
10% APS	75 µl	75 µl
Total Volume	15 ml	15ml

TEMED (Tetramethylethylenediamine) and APS (Ammonium Persulfate) should be added immediately before adding the correspondent gel to the glass cast as the combination of both reagents triggers the polymerization reaction.

First the Resolving Gel is added and left to polymerize (~30-60 minutes) and only then the Stacking Gel is added and left to polymerize (~30-60 minutes) on top of the resolving gel. In this way a two-section gel is created allowing sample to concentrate in the Stacking Gel and increase band resolution on the Resolving Gel.

The resulting gel, trapped in the glass cast, is introduced in the BIO-RAD Mini-PROTEAN® Tetra System, entirely filled in the inner part of the gel with Running Buffer 1x, diluted from a 10x Running Buffer containing 0.025 M Tris 8.8, 0.192 M glycine and 0.1% SDS, and partially filled in the outer part to a marked level.

SDS-PAGE protein and marker samples need denaturing treatment by adding the Sample Buffer, containing 1% (w/v) Bromophenol blue, 10% (w/v) Glycerol 87%, 715 mM Beta-

mercaptoethanol, 10% (w/v) SDS and 0.5 M Tris-HCl (pH 6.8), and boiled at 100ºC for 10 minutes. Protein samples are composed of 20 µl protein solution and 10 µl Sample Buffer, and Marker samples are composed of 3 µl of marker solution (BIO-RAD Unstained Low Range SDS-PAGE six Standards of 4.4, 21.5, 31, 45, 66.2, and 97.4 kDa), 2 µl of Milli-Q water and 5 µl of Sample Buffer. After boiling, samples were centrifuged at 11700 RPM (~13000 G) for 2 minutes and then applied to the Stacking Gel wells, 15 µl of protein sample and 3 µl of marker samples.

SDS-PAGE Electrophoresis ran at 150 V for 60-80 minutes until the Sample Buffer line reached maximum distance of around 5 cm. The resulting gel was removed in Milli-Q water and then stored overnight in a plastic container with Staining Solution, composed of 10% (v/v) Glacial acetic acid, 2% (w/v) Coomassie Brilliant Blue R-250 Dye and 35% (v/v) Methanol. In the next day, several destaining steps were performed using a Destaining Solution composed of 7% (v/v) Glacial acetic acid and 5% (v/v) Methanol. The destained gel was then photographed and introduced in the eReuss plataform to determine relative marker band migrations, creating the Log (Molecular Weight) vs. Relative distance (Rf) calibration curve, allowing the estimation of the molecular weight for each protein monomer.

3.4.3 eReuss Image Analysis

AGE and SDS-PAGE image capturing allowed to process results using eReuss. eReuss is a free access web browser software (https://github.com/lkrippahl/eReuss) created by Prof. Dr. Ludwig Krippahl for Electrophoresis gel image processing. This software requires Python 2.7 and some associated libraries (Scipy, Numpy, Scikit-image, Matplotlib). For an easier installment, the Anaconda 2 package distributed by Continuum, Analytics™ should provide all the essential libraries and a platform to fully operate eReuss. Some conflicts with the Windows operating system might require the installation of an older version, the Anaconda2 v.4.2.0 found in the old repository list (https://repo.continuum.io/archive/).

When all files are extracted, and the required software and libraries installed, the webserver is started by opening the run.bat file or manually entering the command *python erserver.py*. A Command Prompt window should appear, and after a few seconds a warning on server status should appear, allowing the browser to connect to the eReuss server (http://127.0.0.1:8081/).

From the web browser, several steps will provide user-friendly guidance on how to process an image and obtain results:

i. Image Upload;
ii. Image Preprocessing;
iii. Image Clipping;
iv. Lane Identification;
v. Band Profiling;
vi. Report.

3.4.3.1 Image Upload

Here image uploading allows transfer of an image file (JPEG, BMP, PNG) to the web browser server. Image orientation should be considered since no rotation option is available, band migration should be vertical, starting from the top to bottom.

3.4.3.2 Image Preprocessing

Image are only processed by eReuss if the background is dark and the bands are bright, to do this an RGB (Red, Green and Blue) analysis took place in order to intensify a specific color from the desired bands. As bands originating from AuNPs are red, in AGE results the red color was chosen. For SDS-PAGE, since protein bands were dyed by Coomassie Blue, blue was chosen. Images are inverted as the software needs a dark background and bright bands to successfully operate.

3.4.3.3 Image Clipping

In this step, the ROI (Region of Interest) was clipped as shown in Figure 3.2. The number of wells and comb length determine how many samples the software accounts for and a pixel to centimeter conversion of the band migration. Comb length was determined by the distance between the start of the first well to the start of the last well, which is the same distance from the middle of the first well to the middle of the last well. This number is then divided by the number of samples, determined by the well number, and the area corresponding to each band is analyzed.

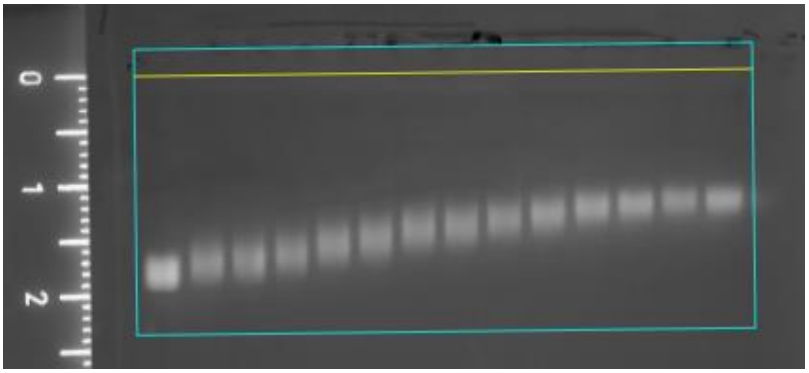

Figure 3.2. eReuss Image clipping of the region of interest (in blue) and the lane start (yellow).

3.4.3.4 Lane Identification

Automatic band to lane attribution was applied as seen in Figure 3.3. Manual attribution can be done if the software selects wrong lane lengths in pixels.

Each lane was then identified with the value of [Protein]/[AuNP] ratio to provide the XX-axis values of the Langmuir/Hill curve fitting to AGE results. SDS-PAGE results do not require lane identification since each lane is an independent sample.

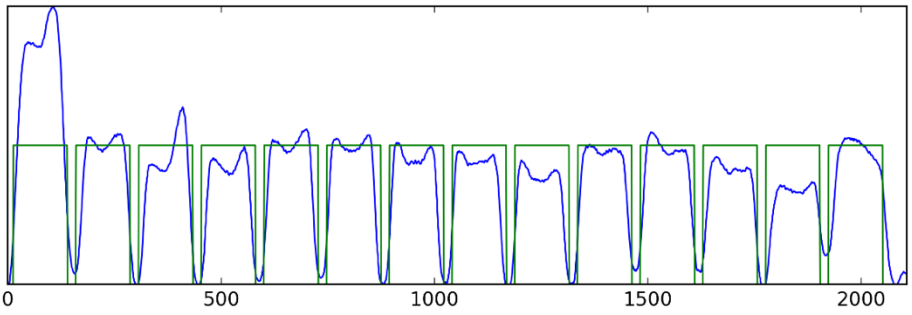

Figure 3.3. eReuss Band to Lane (horizontal) in pixels with correspondent band intensity (blue lines) and position (green lines).

3.4.3.5 Band Profiling

Band profiles were determined by a Gaussian distribution of band intensity in each lane. For single-band results like AGE, a single Gaussian was performed while in SDS-PAGE results, multiple Gaussians were performed to identify Protein marker migration in the same lane as well to identify the multiple bands of Fibrinogen as seen in Figure 3.4.

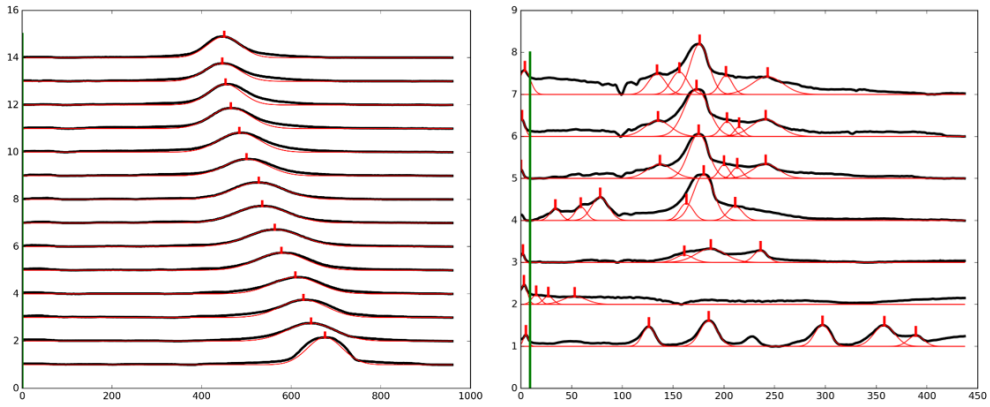

Figure 3.4. eReuss Band Migration (vertical) in pixels with correspondent band intensity and Gaussian. Agarose Gel Electrophoresis Profile in the left and an SDS-PAGE Electrophoresis Profile in the right.

Minimum weight was modulated to pass a certain band intensity threshold for less intense essential bands. And for AGE results, Langmuir and Hill plots were performed and compared to Excel Solver and OriginPRO fittings.

3.4.3.6 Report

The final step compiled the image treatment results into a compressed file composed of migrations, Langmuir and Hill parameters and other data. All eReuss inputted data and results are saved. Resulting graphs and images were also stored.

3.4.4 eReuss Data analysis

eReuss outputted individual band migrations which were converted to electrophoretic mobility from the respective electrophoresis duration and voltage. The loss of Electrophoretic mobility is used to plot with the increasing conjugation ratios, giving out the bioconjugation curve.

Electrophoretic mobility loss was plotted vs. Protein:Nanoparticle Concentration ratios and final protein concentration for determination of conjugation ratio and concentration mid-points respectively.

Two plot fittings were used, the Langmuir Isotherm and Hill Equation. The Langmuir Isotherm derivates from the Hill Equation when the cooperativity coefficient is equal to 1 (n = 1), assuming a non-cooperative conjugation. The fitting follows the formula on the following equation:

$$M = M_{max} \frac{Cp^n}{\left({}^{1}/_{K_{ad}}\right)^n + Cp^n}$$

Equation 3.5

where, M is the loss of electrophoretic mobility ($cm^2\ V^{-1}\ s^{-1}$), M_{max} is the maximum value of loss of electrophoretic mobility loss that the fitting tends to, *Cp* stands for the Protein Ratio or concentration and K_{ad} is the adsorption constant. K_{ad}^{-1} give information on the value of *Cp* at half value of M_{max}, assumed as the conjugation mid-point. In the Hill equation fitting the cooperativity coefficient is modulated to obtain maximum fitting.

3.4.5 Fergusson Plot Analysis

All AGE results for the Fergusson plot analysis were obtained by the eReuss software and converted to electrophoretic mobility. Lower voltage (60V) and longer electrophoretic runs (40-60 minutes) were chosen to avoid band irregularities at higher concentrations of agarose (>1.0%). Water constant values for permittivity (80.1 pF m^{-1}) and viscosity (1 x 10^{-3} Pa s) were used to estimate zeta-potential.

As for size calibrations, AuNPs of 15, 19, 23, 25, 37 and 39 nm fully-functionalized with MUA, were kindly provided by M.Sc. Miguel Peixoto de Almeida from the research group of Professor Eulália Pereira from LAQV, REQUIMTE, Faculdade de Ciências, Universidade do Porto, Portugal.

3.4.6 eReuss Video Analysis

AGE runs were filmed using a 12 Megapixel camera from a smartphone, secured in a tripod to further stabilization. For light optimization, the recording was made inside a white box with a filtered scattered light source. Results were then processed by the developing eReuss video processing features. Since no user interface is available, all video analysis settings are managed in an input text file divided in various steps:

i. Frame extraction
ii. Alignment and Clipping
iii. Baseline
iv. Final frames and Lane selection
v. Report

3.4.6.1 Frame extraction

Conversion of the video file to multiple frames, organized by the timeline, using the FFmpeg software. [67] Checking the obtained frames is advised and can be rotated in order to make the band migration in the vertical orientation, from top to bottom. After this process finishes, the eReuss image analysis component is used to identify the desired pixel coordinates for the alignment, clipping and lane selection.

3.4.6.2 Alignment and Clipping

For this step, two sets of coordinates are necessary. One for the frame alignment to mitigate video anomalies like movement or focusing issues. And another for the selection of the region of interest to be clipped.

3.4.6.3 Baseline

Although light optimization is performed, abnormalities are still observed due to the quality limitations of the camera, gel and instrument light reflection and others. To mitigate these effects, initial frames are used as a baseline reducing the undesired background visible effects.

3.4.6.4 Final frames and Lane Selection

The baseline is then subtracted to the obtained clipped frames, and the final frames are created which have a dark background and high contrast bands similar to the eReuss Image analysis steps. Similarly, to the Image Analysis, lanes are selected for each migration band.

3.4.6.5 Report

The outcome results, for each band, in the area and peaks of intensity along the video duration. This method allows a better understanding of individual profiles in a electrophoretic run compared to the limited final frame Image analysis.

3.5 UV-Vis Spectroscopy

All studies were conducted in a 300-900nm wavelength at medium velocity (600 nm/min). Absorbance spectra were obtained in a VARIAN, Cary 50 Bio, UV-Visible spectrophotometer, using Hellma quartz cells at room temperature.

For the colloidal stability studies, all samples were incubated for 30 minutes in Eppendorf tubes before reading, to allow the aggregation effect to stabilize. For pH measurements, a CRISON, pH-meter BASIC 20+, was used.

3.6 Light Scattering techniques

All light scattering techniques were performed, and data obtained was treated and provided, by M.Sc. Miguel Peixoto de Almeida from the research group of Professor Eulália Pereira from LAQV, REQUIMTE, Faculdade de Ciências, Universidade do Porto, Portugal.

3.6.1 Dynamic Light Scattering and Electrophoretic Light Scattering

Using a Malvern Panalytical Zetasizer ZS instrument, Dynamic light scattering (DLS) and Electrophoretic Light Scattering were performed at room temperature, with light detection at the angles of 173º for DLS and 17º, using the backscatter mode, for ELS. The data was analyzed using a cumulants method by the Malvern Zetasizer software (v.7.11). Non-diluted samples were injected in folded capillary cells Malvern DTS1070 and were measured 3-5 times at room temperature. Hydrodynamic sizes were obtained from number distributions, and zeta-potential values using the Henry equation with the Smoluchowski approximation ($f_H(ka)$ = 1.5).

3.6.2 Nanoparticle Tracking Analysis

Using a Malvern Panalytical Zetasizer NanoSight NS300 instrument, equipped with a 642 nm laser module, Nanoparticle Tracking Analysis (NTA) was performed. Hydrodynamic and concentration of particles were obtained by the NTA 3.3 software. Diluted samples, using ultrapure water, were tested using aliquots taken by a plastic syringe and injected into the flow cell. Post-focusing by the camera, five videos of 1 min duration were filmed at a flow rate of 2 µl/min at room temperature. The viscosity of the medium was considered that of water. The results were processed into a size distribution chart.

3.7 Protein Homology

For Bovine and Human protein homology determination, the UniProt (https://www.uniprot.org/) database [68] and the RCSB PDB (https://www.rcsb.org/) database [69] were used. Sequence alignments UniProt FASTA files were tested. Blast 2 Sequences [70] was used for Local alignments and the Needleman & Wunsch algorithm was used for the Global alignments. [70] As for structural alignments, the RCSB PDB files were used (1DEQ,3GHG, 3V03,1AO6). The jFATCAT java program was used for Rigid and Flexible structural alignments. [71]

3.8 Molecular Visualization

The PDB files were used in the representation of surface electrostatic potential and solvent accessibility (for Fib) to extend the structural understanding of these proteins and the interactions with the negative charged nanoparticles.

3.8.1 Electrostatic Potential: Poisson-Boltzmann (APBS and PDB2PQR)

The electrostatic potential representation on a molecular surface was performed first by converting the PDB to a PQR file. This new file has information on the partial charges and electrostatic radii of every atom. To create this file the PDB2PQR v2.0.0 web service (http://nbcr-222.ucsd.edu/pdb2pqr_2.0.0) was utilized, using a PARSE forcefield and pKa estimation of the residues and the isoelectric point for the whole protein by the PROPKA v3.0 web service, hosted at the PDB2PQR website. The PQR file is then processed by the APBS plugin in the Pymol software, using the PDB2PQR input file which determines the simulation conditions. The molecular surface is calculated by the Pymol software and then colored according to the electrostatic potential variation within a negative and positive range.

3.8.2 Solvent accessibility (Swiss-PDB viewer)

Solvent accessibility was performed by the Swiss-PDB viewer software, which estimates the accessibility for each residue individually based on a referenced molecule. The accessibility is represented in a color scheme varying from blue (less accessible) to red (fully accessible).

4 Results

4.1 Synthesis and Characterization

Gold nanoparticle synthesis was performed according to the Turkevich Method, allowing the production of approximate 15nm sized nanoparticles. From the Figure 4.1, at the start of the reaction, the solution had a yellow color due to the gold salt addition, and upon adding the citrate or, in the case of the Inverse method, upon adding the gold salt to the citrate solution, the yellow color turned to colorless immediately from the reduction reaction of gold. After a few seconds, the solution turns into a dark red color resulting from the nucleation process of gold atoms.

Figure 4.1. Synthesis of Gold Nanoparticles. Sequential change of color of the solution from a initial yellow to dark-red.

After synthesis, and the colloidal solution cooled down, samples were characterized by UV-Visible Spectroscopy. The resulting spectra, as seen in Figure 4.2, allowed the estimation of AuNP size and concentration. Multiple synthesis processes were performed due to the colloid instability over time and quantities necessary for the various tests performed.

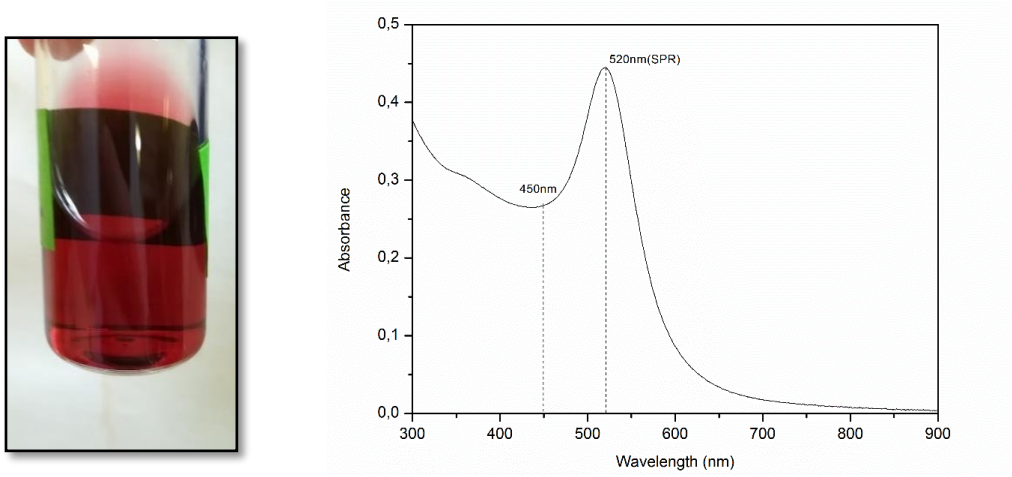

Figure 4.2. Post-synthesis. A diluted red colloidal solution of 15nm gold nanoparticles (left) and UV--Vis spectrum (right).

Two methods were tested, the Direct method and the Reverse method, which produce AuNPs with distinct diameter size distributions. The Direct method results in an AuNP diameter size

distribution around 15-20nm, whereas the Reverse method allowed a narrower diameter size distribution of around 13-15nm. The reverse method was preferably used. As for concentrations, larger sized AuNPs yielded lower concentrations of around 4-10 nM, while smaller sized AuNPs yielded higher concentrations of around 7-15 nM, due to the gold atom availability in which bigger AuNPs require more gold atoms leading to the formation of a smaller number of nanoparticles.

As for AuNP stability, low absorbance values at a 600-700nm were observed indicating insignificant effects of colloid aggregation.

Comparing a 15nm AuNP colloidal solution with a provided 39nm AuNP colloidal solution, in Figure 4.3, and ignoring absorbance values since the two sets of values were normalized, there is an evident change to the SPR peak wavelength, causing a red-shift, from 520nm to 527nm, to occur with increasing particle size.

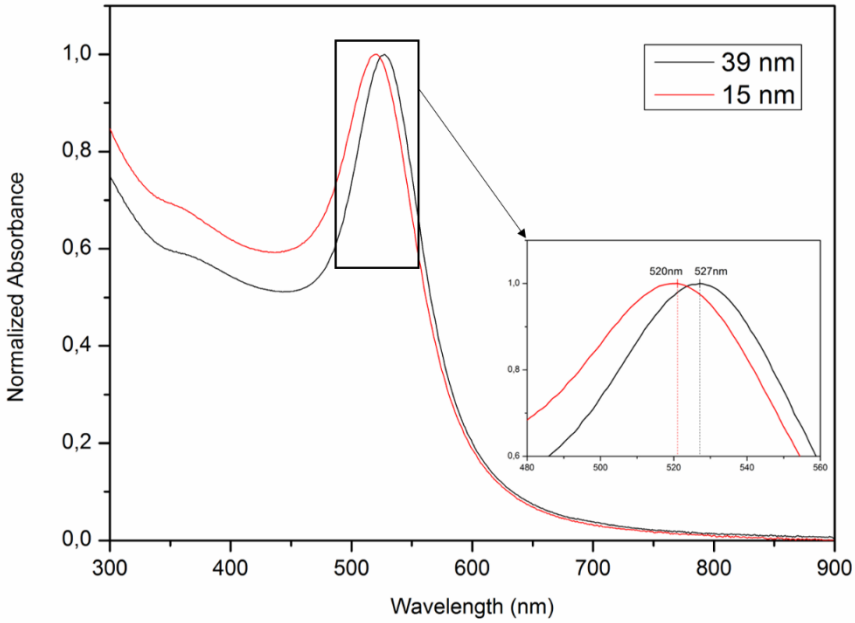

Figure 4.3. UV-Vis spectra of diluted AuNP colloidal solutions. Comparison of the SPR peaks of 15nm and 40nm sized nanoparticles.

4.2 Functionalization

After synthesis, Citrate-AuNPs were functionalized with CALNN, MUA, and AUT to further increase colloidal stability and functionality. Since citrate-functionalized AuNPs do not migrate in AGE, due to possible interactions between citrate and agarose, unless these are fully conjugated as shown in Figure 4.4, any attempts at studying the intermediate stages of the interaction between AuNPs and Blood Proteins is rendered impossible. So, to certify that all the AuNPs were properly functionalized and ready to be applied in the study, AGE runs were performed at zero protein concentrations, in order to find the ideal ratios of capping agents that would completely replace the citrate capping with the pretended one. The samples that performed maximum

electrophoretic mobility, without any aggregation signs, were selected as viable candidates for further testing.

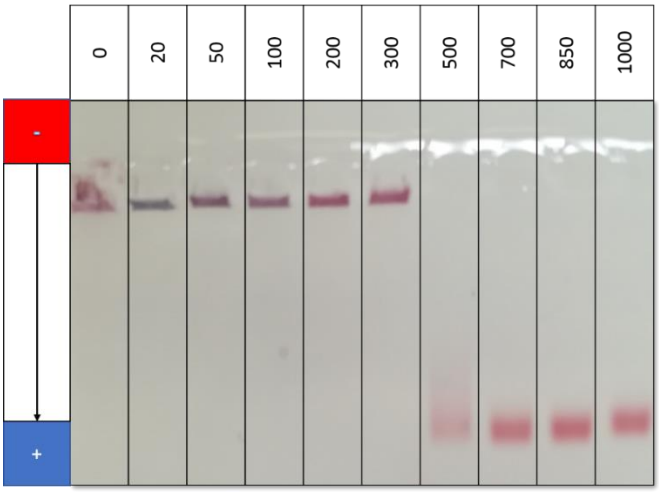

Figure 4.4. Agarose Gel Electrophoresis (0.5%). AuNP-Citrate with increasing concentration ratios of BSA.

4.2.1 Negative Charged Functionalization

Firstly, the quantity of thiol added to perform a full surface functionalization was tested by AGE. Similarly, to the previous test, only a fully functionalized surface migrates in the gel. From the Figure 4.5, a ratio of above 2000 for MUA and 500 for CALNN ensures full functionalization, but due to a possibility of lesser efficient coverage scenarios, experiments were done on a 5000 ratio for MUA and 1000 for CALNN to guarantee full stability through various experiments.

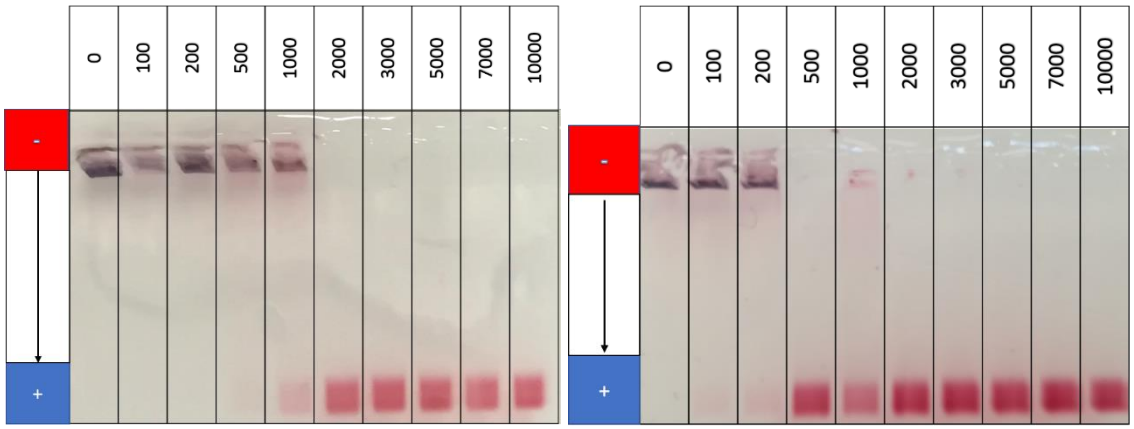

Figure 4.5 Agarose Gel Electrophoresis (0.5%). AuNP-MUA (Left) and AuNP-CALNN with increasing concentration ratios of the respective thiolated ligands.

UV-Vis spectroscopy can also be used to evaluate the quality of the functionalization process, by ensuring that the 600-700nm absorbance is minimal and a small red-shift of the SPR peak is visible due to the change of surface chemistry. From the spectra in Figure 4.6 both stability

and SPR peak red-shift, from 520nm to 523mm, are visible indicating a successful functionalization process.

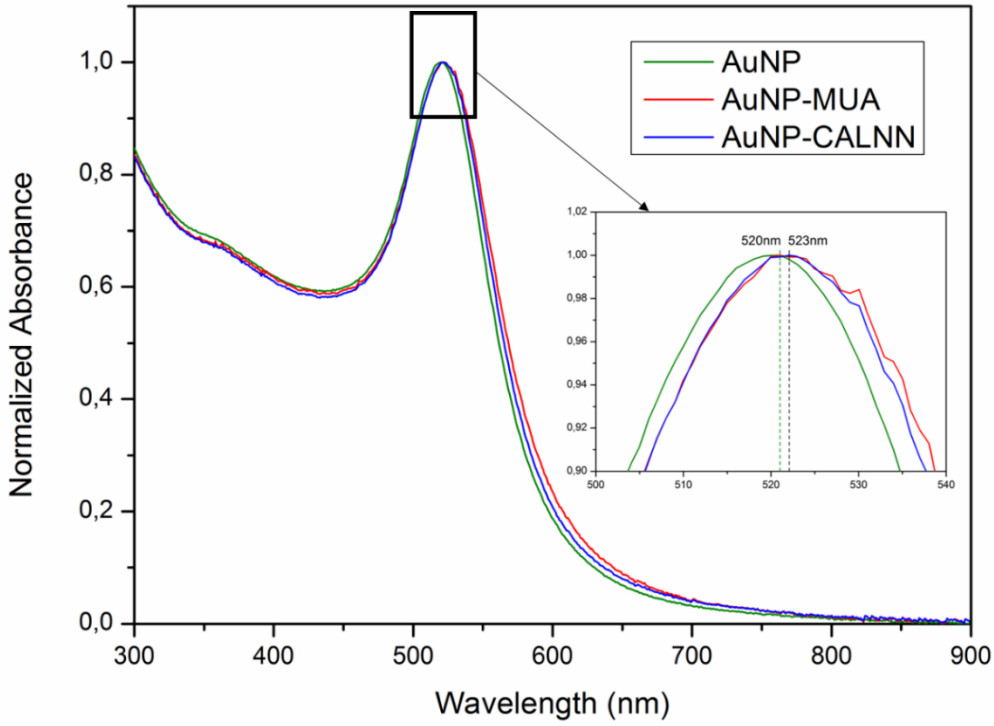

Figure 4.6. UV-Vis spectra of AuNP colloidal solutions. Comparison of the SPR peaks of Citrate (Green), MUA (Red) and CALNN (Blue) functionalizations.

4.2.2 Positive Charged Functionalization

In the case of AUT, a positive thiol functionalization, two different methods were applied regarding the solution addition order. In the first method, the process was similar to the CALNN and MUA methods, by adding a concentrated solution of AUT to the AuNPs. Unfortunately, this method leads to irreversible nanoparticle aggregation, as seen in Figure 4.7, at all the tested [AUT]/[AUNP] ratios in the range 100-10,000, resulting in a purple colored colloidal solution and upon adding more AUT the solution would turn gray and precipitate.

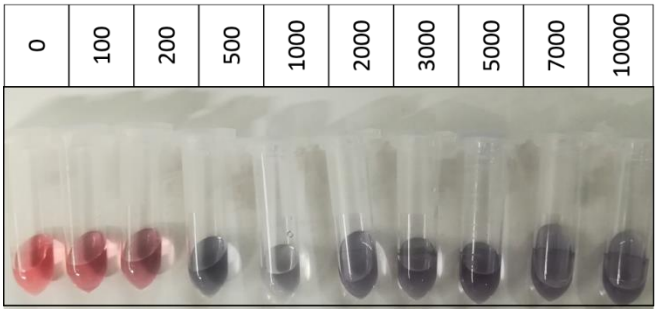

Figure 4.7. AUT-AuNP functionalization with different [AUT]/[AuNP] in the 100-10,000 range always leading to aggregation.

The second method was to reverse the order of addition. By having a larger volume of concentrated AUT and adding drops of AuNPs, the idea was to fully functionalize the nanoparticles immediately and, by not having large quantities of nanoparticles in solution, avoid aggregation.

Overall, this method seemed to outperform the previous one by ensuring a fast transition between the negative and positive global charge, although the final color was purplish and the spectra in Figure 4.8 shows some signs of aggregation. Also, after letting the vial containing solution stabilize overnight, there were signs of aggregation on the glass of the vial.

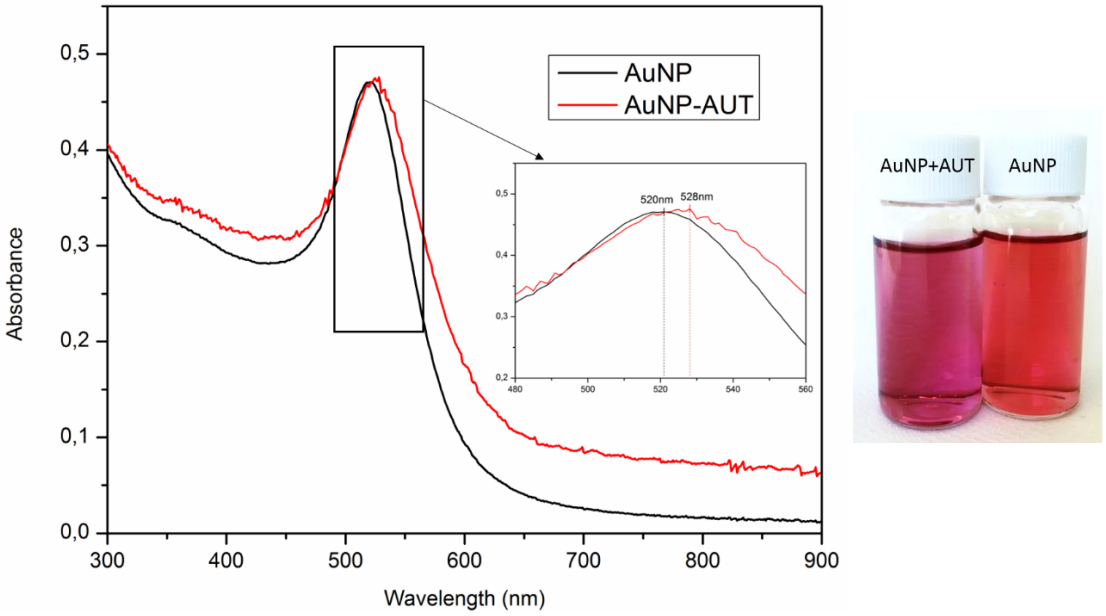

Figure 4.8. UV-Vis spectra of both AuNP-Citrate and AuNP-AUT colloidal solutions at the same concentration for direct comparison (left). Visible color change on the AUT-AuNP colloidal solution from a red to purple (right).

To minimize aggregation effects, the previous trial was repeated with Polyethylenimine (PEI) coating of the glass vial. According to the Figure 4.9 spectra, clear improvements were shown in the 700-900nm wavelength by decreasing any signs of aggregation, even though the color was purple in the end and a red-shift from 520nm to 535nm was observed in the respective UV-vis spectra.

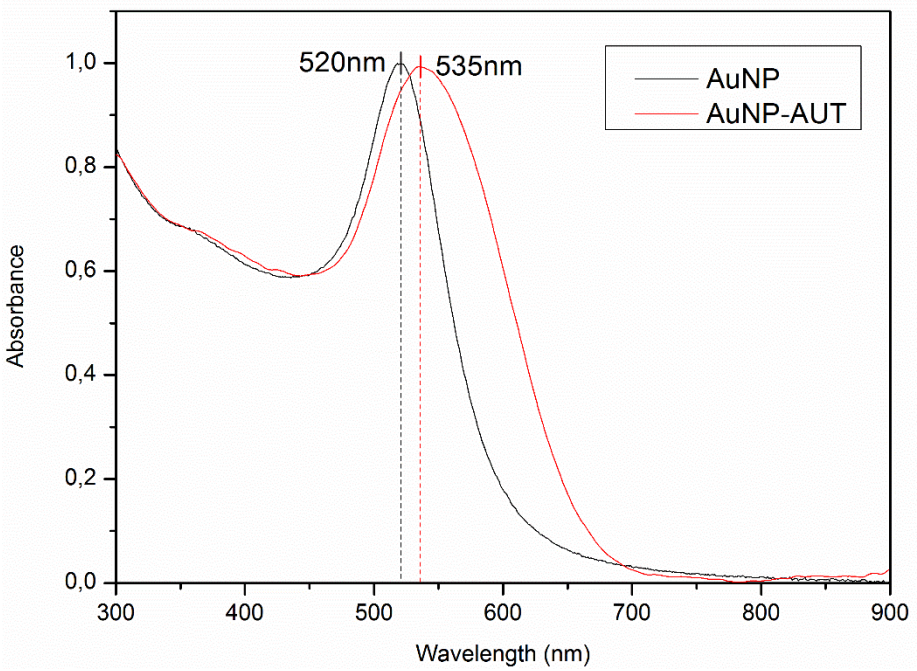

Figure 4.9. UV-Vis spectra of both AuNP-Citrate and AuNP-AUT colloidal solutions at the same concentration for comparison.

Although this method represented a clear improvement of the process, centrifugation or any attempts to conjugate further would result in loss of AuNPs, by aggregation and sedimentation. Also, due to the acidic pH requirement for this type of functionalization, any bionanoconjugation step would affect protein stability and defeat the purpose of comparing with the negatively charged nanoparticle assays since the proteins would be mostly protonated and positively charged and no common pH could be used to compare both sets of experiments.

A possible solution would be a two-step functionalization by transitioning to a neutral charged surface in an organic solvent and after stabilizing, attempt a positive charge functionalization. [72]

4.3 AuNP colloidal stability assays

Stability assays were conducted to evaluate the effects of pH and salt concentration, by UV-Vis spectroscopy. The SPR peak wavelength shifts towards longer wavelengths allowing to estimate the aggregation state. In this study, the 630nm wavelength was assumed as the aggregation peak, and the absorbance ratio of 630nm/initial SPR peak, the Equation 4.1 depicting the Aggregation Ratio (A_R), was analyzed to study the evolution of aggregation. The aggregation ratio mid-point only refers to the pH or concentration value when half of the maximum value of the A_R is reached, not assuming that any sample below this value threshold is stable and/or usable. Any small increase in the A_R should discourage further use of the samples in other studies or applications.

$$A_R = \frac{A_{630nm}}{A_{SPR}}$$

Equation 4.1

As the aggregation level increased, so did the color changed from red to purple, and in the end to a gray color as seen in Figure 4.10.

Figure 4.10. Increasing aggregation effects (left to right), leading to a change of color.

Each sample had a 30-minute incubation, to permit the system to reach equilibrium, allowing a more accurate study of the aggregation phenomena. This specific incubation time was determined by studying the aggregation ratio growth over time, as seen in Figure 4.11, by exposing a sample to a pH 2.0, which is a value around the estimated aggregation mid-point.

Although the aggregation effect seems to stabilize at an earlier stage, for these particular experimental conditions, it should be noted that during this analysis, the sample was manually stirred to promote sample homogenization hence the various spikes of increasing aggregation ratios in small time frames and so a 30-minute (1800 seconds) incubation minimum time and two manual homogenization procedures, one at the start of the reaction and one before UV-Vis spectroscopy sample reading, was stabilized for the stability study protocol. Also, depending on the type of aggregation, salt or pH, the salt concentration, pH value, total volume and AuNP concentration affects the equilibrium and the time needed to reach equilibrium, and so the incubation time was set to a specific time frame, as every different type of aggregation sample would have a different aggregation behavior and it would be difficult to test all the individual kinetic processes.

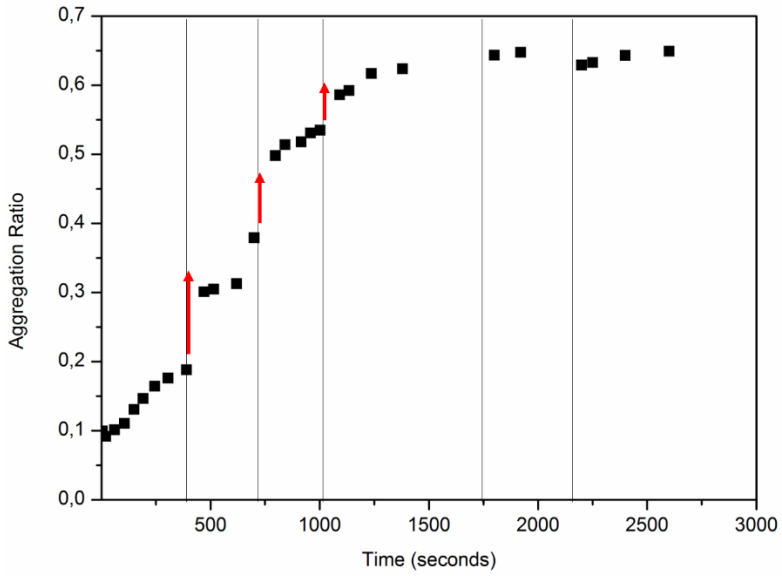

Figure 4.11. Aggregation ratio evolution of 2 nM AuNP-Citrate at pH 2.0 over a time lapse of several minutes. Vertical lines show the periods that manual sample homogenization was executed, and the red arrows indicate the highest increases in aggregation post-homogenization.

4.3.1 pH effect

The stability of the colloidal solution of Citrate-AuNPs was tested, both in an acidic (1.0–6.0) and a basic (7.0-12.0) pH ranges. No significant differences were observed for the basic pH samples as shown in Figure 4.12.

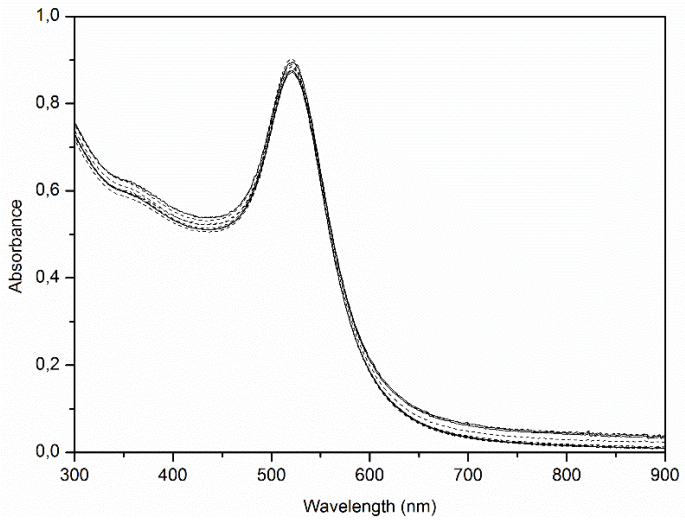

Figure 4.12. UV-Vis spectra of AuNP-Citrate at pH 6 (solid line) and for samples at increasing pH in the range 7.0-12.0 (dash lines).

The acidic pH ranges in Figure 4.13, however, show a red-shift and loss of absorbance in the SPR peak and red-shifts to the 600-800 nm range, showing clear signs of aggregation.

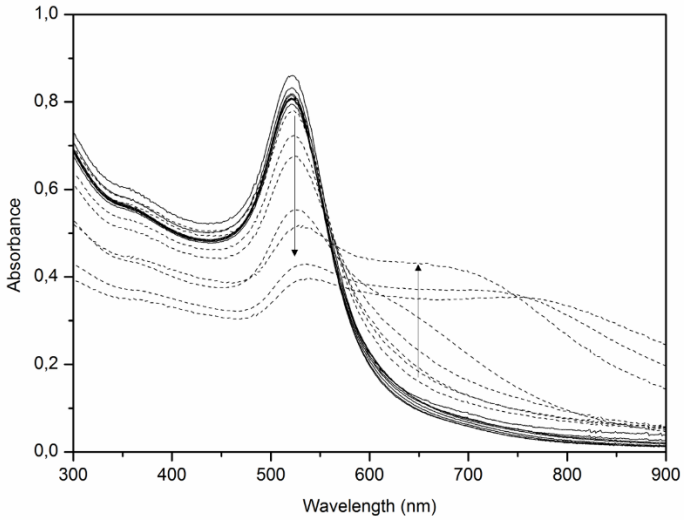

Figure 4.13. UV-Vis spectra of AuNP-Citrate at pH 6 (solid line) and for samples at decreasing pH in the range 1.0-6.0 (dash lines).

Pooling both sets of data as seen in Figure 4.14, and analyzing the shifted peak growth, an aggregation mid-point can be estimated by a logistic function fitting to the results. The Logistic Function commonly applied to sigmoidal curves to easily estimate curve mid-points, which in this case gives the approximate pKa value, is show in the equation below:

$$A_R = \frac{A_1 - A_2}{1 + (x/x_0)} + A_2$$

Equation 4.2

A_R is the aggregation ratio, A_1 and A_2 are constants used to adjust the fitting to the observed curve, x is the pH value and x_0 is the ph value at aggregation ratio mid-point.

The aggregation mid-point had a value of 2.7 which represents a good approximation for the literature value for the citrate pKa of 3.1. [73] The protonation of citrate leads to a neutral charge at the surface of the AuNP, leading to aggregation.

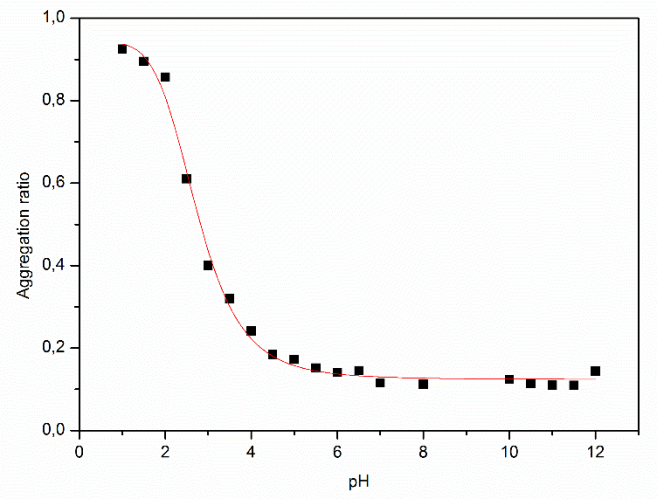

Figure 4.14. Aggregation Ratios from the UV-Vis pH studies for citrate-AuNPs and Logistic fitting (red) to estimate aggregation mid-point.

As for MUA and CALNN functionalized AuNPs, the same effect was observed for basic pH values in the range of 7.0-12.0, where no aggregation was visible. However, in acidic pH values in the range of 1.0-6.5, aggregation was observed, as seen in Figure 4.15. The MUA and CALNN samples red-shifted to 575 nm and 610 nm respectively.

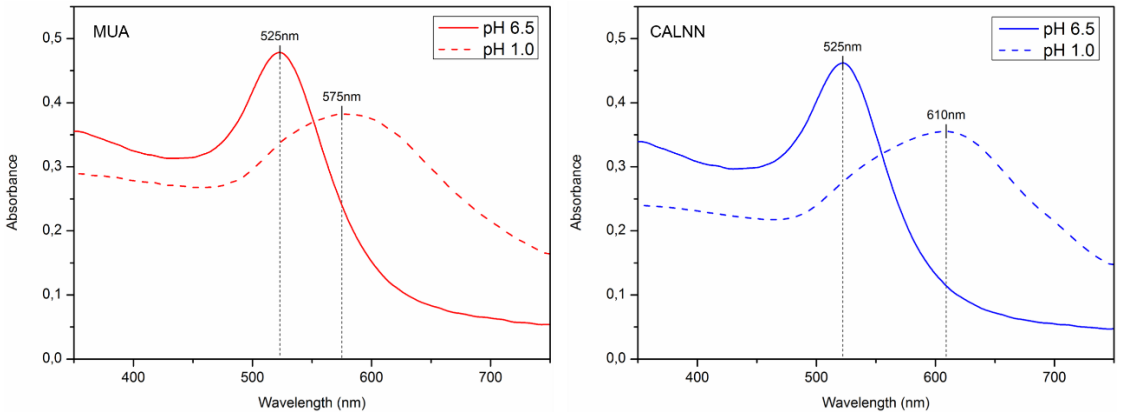

Figure 4.15. UV-Vis spectra of MUA (red) and CALNN (blue) coated AuNPs at pH 6.5 (solid line) and 1.0 (dashed line) and correspondent SPR band before and after aggregation, respectively.

From Figure 4.16, pKa values of 3.9 for MUA and 2.9 for CALNN were estimated, which according to the referenced values of apparent pKa values are 4.5 and 3.5 respectively. [74, 75] These pKa results differ for the estimated free molecule values, which are 4.9 for MUA [76] and 2.0 for the acidic terminal of Asparagine (N) in CALNN [77], the possible cause of this effect was previously discussed and theorized as the increased electrostatic repulsions, when these molecules attach to the surface of the AuNP, leads to a decreased fraction of charged molecules. [78]

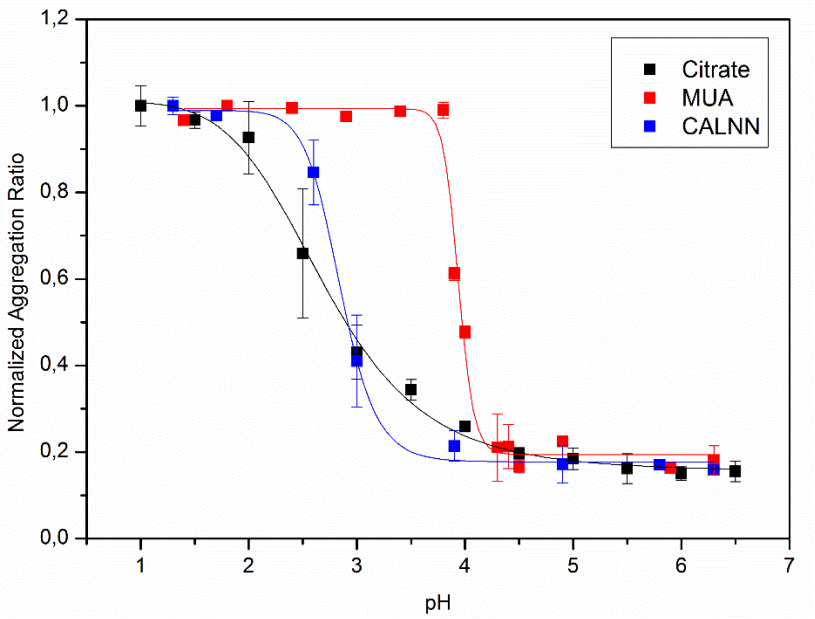

Figure 4.16. Variation of the normalized Aggregation Ratios as a function of pH for citrate-capped or MUA- or CALNN-functionalized AuNPs.

AuNP-CALNN functionalization seem to be as resistant to aggregation induced by acidic pH (1.0-6.0) as citrate-AuNPs, having a similar estimated aggregation mid-points of 2.9 and 2.7, while in the case of the AuNP-MUA functionalization, the aggregation mid-point is around 3.9. From these results, AuNP-CALNN and citrate-AuNPS seem to slightly outperform AuNP-MUA in stability at acidic pH conditions. However, since the application of the AuNPs are in physiological conditions (pH ~ 7.4), the three types seem to be ideal candidates for further tests.

4.3.2 Salt effect

Salt-induced aggregation was tested with a monovalent salt, NaCl, on Citrate-AuNPs and thiol-functionalized AuNPs. Some differences were observed in the SPR peak shifts and between the various nanoparticle coatings and can be checked in the Figure 4.17.

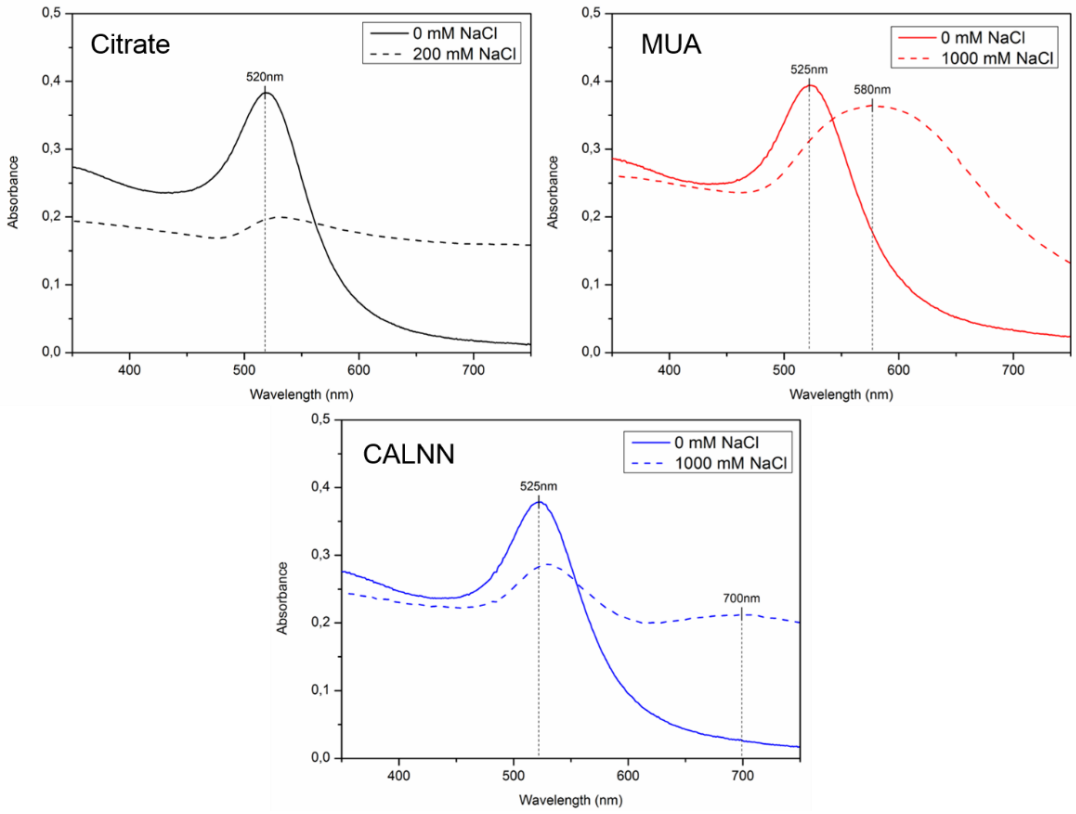

Figure 4.17. UV-Vis spectra of Citrate (black), MUA (red) and CALNN (blue) coated AuNPs. Different SPR and Aggregation peaks before (solid line) and after (dashed line) salt induced aggregation.

As the salt concentration increases, in the case of citrate-AuNPs, the absorbance of the SPR peak lowers and red-shits from 520nm to 535nm, while the 600-900nm absorbance increases at an even rate. In the case of the MUA-AuNPs the SPR peak at 525nm lowers in absorbance and red-shifts to 580nm. And for the CALNN-AuNPs, the SPR peak at 525nm also lowers in absorbance and red-shifts to 700nm. The different SPR shifts might reflect the different surface chemistries for each case. Table 4.1 gives a summarizing overlook at the initial peaks and shifted peaks observed.

Table 4.1. Estimated values of the SPR and Aggregation peaks.

Coating	SPR Peak (nm)	Shifted SPR Peak (nm)
Citrate	520	535
MUA	525	580
CALNN	525	700

As seen in Figure 4.18, a clear difference in salt concentration aggregation resistance can be detected for MUA-AuNPs and CALNN-AuNPs.

A value of the salt concentration, to reach the aggregation ratio mid-point, for each case was estimated, 28 mM for Citrate-AuNPs, 277 mM for MUA-AuNPs and 1080 mM for CALNN-AuNPs. A clear difference in salt concentration resistance is therefore visible making CALNN-AuNPs and MUA-AuNPs highly resistant to aggregation induced by an increase of ionic strength. As for the difference between the functionalized AuNPs, CALNN provides a considerable advantage towards MUA, most likely due to the charge distribution of the Asparagine (Asn-Asn) residues that surpass the performance of the single negative carboxylic group at the end of a MUA molecule.

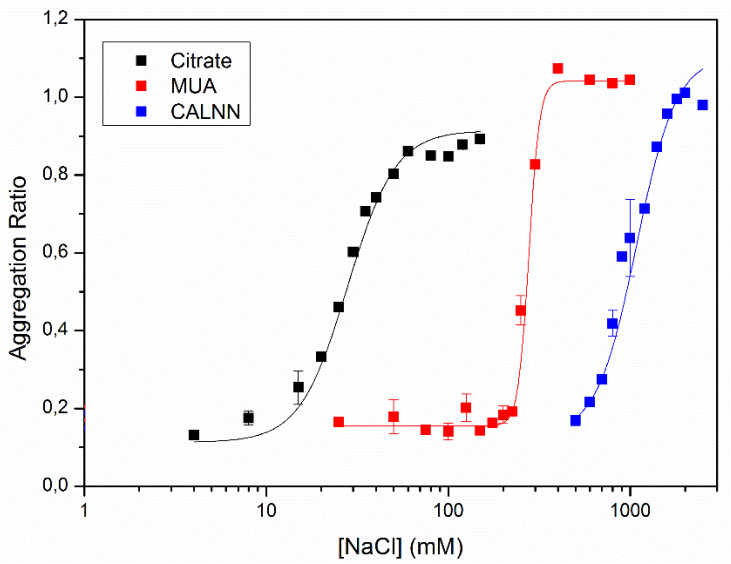

Figure 4.18. Variation of the normalized Aggregation Ratios as a function of NaCl concentration for citrate-capped or MUA- or CALNN-functionalized AuNPs.

Based solely on a concentration of 130-150 mM NaCl and a pH value of around 7.4 at physiological conditions [67], Citrate-AuNPs will irreversibly aggregate and will be rendered useless for any attempted studies. Overall, CALNN seems to confer resistance for both salt and pH effects to AuNPs, making it the most suited candidate for a *in vivo* case study. Even so, a low ionic strength buffer was used, to avoid possible aggregation scenarios.

4.4 Protein characterization and quantification

Bovine Serum Albumin (BSA) and Fibrinogen (Fib) have distinct Molecular Weights and structure. For instance, BSA is a globular-shaped protein, while FIB presents an elongated structure. Multiple techniques were thus used for their characterization before these proteins were used on Protein-Nanoparticle interaction studies.

4.4.1 SDS-PAGE

SDS-PAGE electrophoreses was performed to check the purity and confirm molecular weight of the proteins used in this work. The gel was analyzed by the image analysis software eReuss, and a correlation between band migration and molecular weight was determined for each sample, based on a calibration curve derived from the analysis of protein standards. Figure 4.19 shows that Fibrinogen has four bands, correspondent to the α and α', β and γ chains, while Albumin has a single band as expected from a monomeric protein. Fib presents two different isoforms of the α-chain, due to chain heterogeneity. [79]

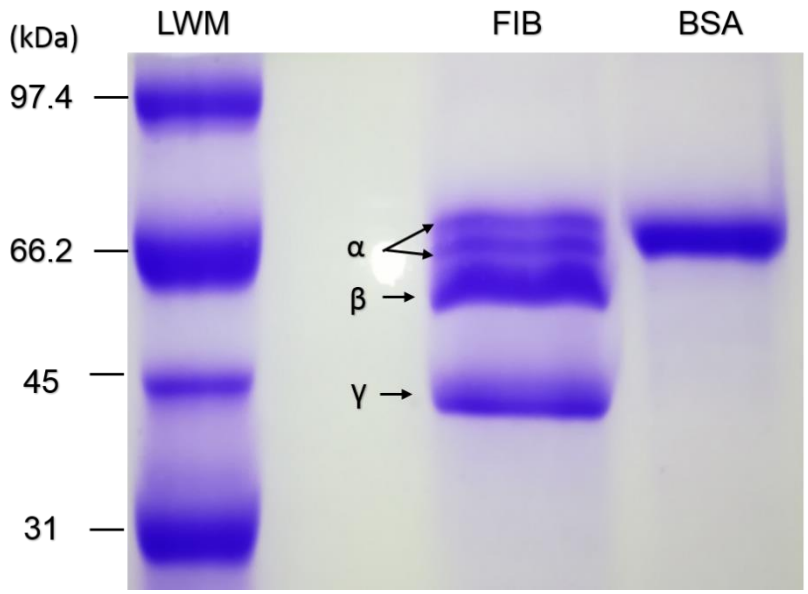

Figure 4.19. SDS-PAGE gel for protein characterization of BSA and Fib, using Low Molecular Weight (LMW) Protein Markers.

After eReuss image processing, as seen in Figure 4.20, a band profile is obtained allowing the determination of an approximate molecular weight value for each protein. Due to the limitations of this software several unwanted peaks are detected and then manually filtered to fit the bands seen in the gel. Each peak is associated with a gaussian curve that passes a certain intensity threshold. Only the four highest molecular weight bands were considered for the calibration curve due to the low resolution of the lower weight bands.

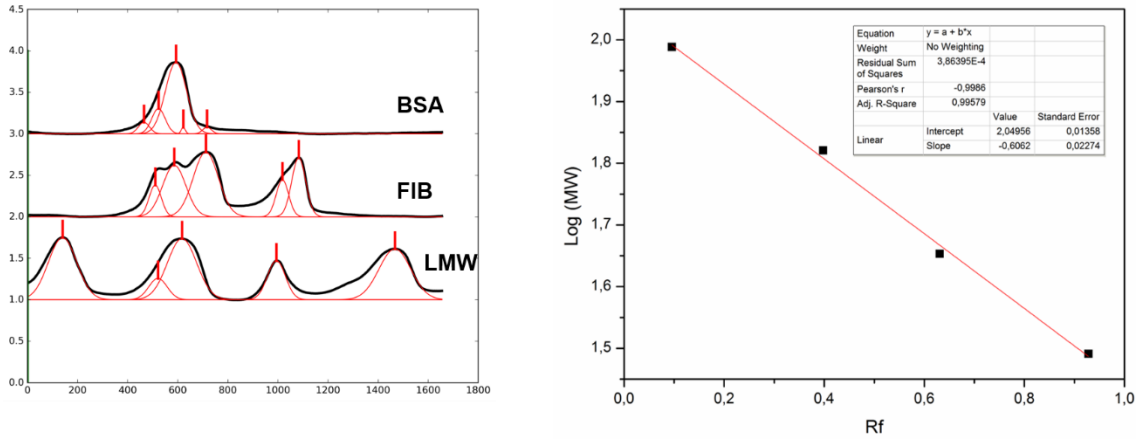

Figure 4.20. SDS-PAGE gel processed by the eReuss software and respective band migration profile (left), and size-to-migration calibration curve and equation (right).

Table 4.2. Average Protein Molecular Weight estimated values from SDS-PAGE electrophoresis.

Protein	Molecular Weight (kDa)	Reference Values (kDa)	Chain	Complete Structure (kDa)
Fibrinogen	72.2 ± 0.6	63.5	α	345 - 351 (2α, 2β, 2γ)
	67.7 ± 0.6		α'	
	61.6 ± 2.0	56	β	
	43.4 ± 0.5	47	γ	
Albumin	67.8 ± 0.9	66	Monomer	68.9

Comparing the experimental data, in Table 4.2, with the literature [80, 81], we can assume that the SDS-PAGE method resulted in similar Molecular Weight values for Albumin (BSA). As for the Fibrinogen (FIB), the values deviate from the reference by overestimation. The molecular weight errors were calculated in relation with data from two independent gel runs, and not from band smearing.

4.4.2 Bicinchoninic Acid (BCA) Protein Assay

The Bicinchoninic Acid (BCA) Protein Assay calibration used BSA standards for the construction of a calibration curve for protein concentration determination (Figure 4.21). Samples containing protein solutions were tested in the same conditions as the standards, and from the resulting absorbance, the respective concentration value was estimated from this calibration curve.

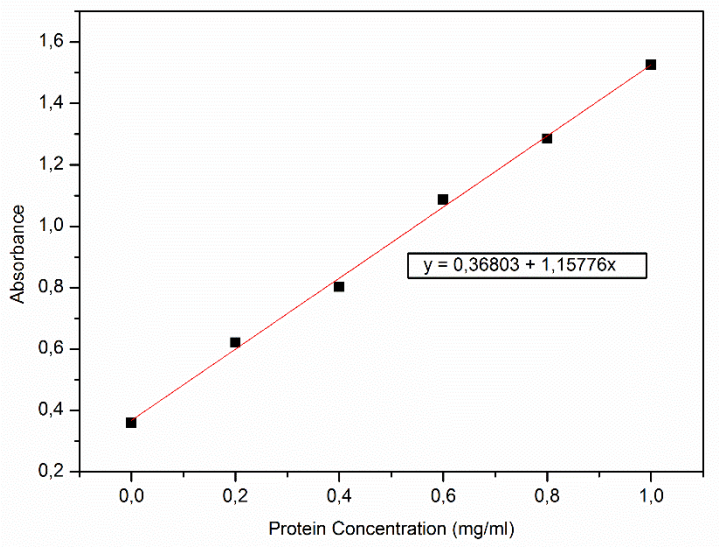

Figure 4.21. BCA calibration curve, using BSA standards, and resultant equation.

For BSA solution the accuracy of manual sample weighting and the concentration value reported by the BCA method was close to 100% (e.g. 1 mg of BSA in 1 ml of buffer would give a 1 mg/ml concentration by BCA), meaning that for each mg of BSA introduced in a volume of phosphate buffer, was accurately determined by BCA concentration determination. In the case of the Fib solution, a decreased value of 70-80% which corresponds to the product details, provided by the supplier, that exhibits an approximate of 65-85% total protein as it contains sodium citrate and sodium chloride.

Additionally, BSA standards were used to correlate the absorbance to protein concentration, which in the case of Fib might overestimate the concentration value. This method is based on copper reduction by the the peptide backbone and also by the amino acid residues cysteine (or cystine), tyrosine and tryptophan, but it should be taken into consideration that Fib and BSA have a difference of almost four times (234:59) on the amounts of these residues, in favor of Fib. If every residue was accessible to contribute to the copper reduction reaction, the resulting absorbance for Fib and BSA at the same concentration would be different. However, the peptide backbone also contributes to the absorbance increase which might mitigate the different amino acid composition of the proteins. [82]

As seen in the study shown in Figure 4.22, for the same amount of protein in a sample, a different absorbance value was observed. Protein conformation and residue accessibility might also have a role in the reduction reaction and affect the absorbance. [83]

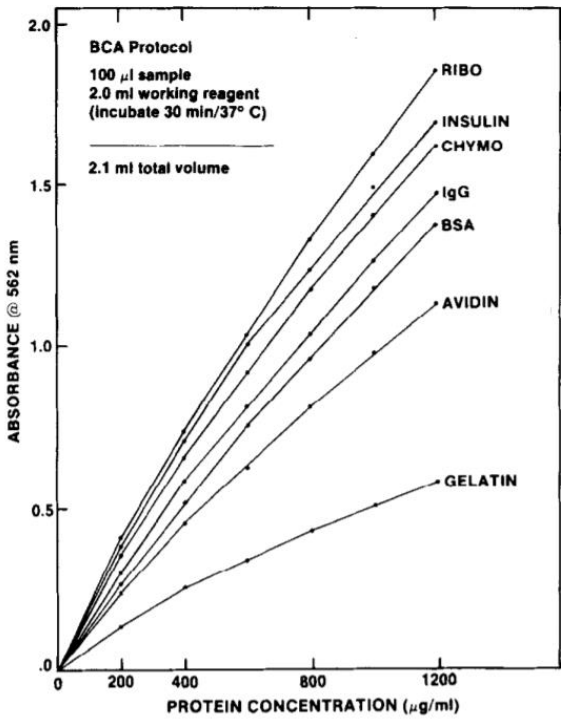

Figure 4.22. Measurement of different Protein concentration using the Bicinchoninic Acid Protocol. [83]

Using the protein concentration results, bionanoconjugation studies, with different molar ratios of Protein and AuNPs, were conducted.

4.4.3 Human and Bovine Proteins Homologies

To compare Human and Bovine proteins, various protein sequences and PDB files were selected to compare both structural and sequence homology. For human Fibrinogen, PDB 3GHG was selected and PDB 1DEQ for its bovine counterpart, for human Albumin PDB 1AO6 was chosen and PDB 3V03 for its bovine counterpart.

As for Alignment quality analysis, the parameters Identity, Similarity and Gaps were calculated. The Identity refers to a perfect alignment, when the same amino acid is present in both sequences and in the same order. Similarity only requires similar amino acids, which have similar biochemical properties like hydrophobicity and polarity (e.g. leucine and isoleucine), to be in the same sequential order and accounting for the sequential gaps, always scoring higher than Identity, which is more restrictive. As for Gaps, these refer the amount of amino acid deletions or insertions needed to align both sequences. [84]

Sequence Alignment was determined by Global (Needleman-Wunsch) and Local (blastp) Alignment. While Global Alignment seeks to fully align both sequences by the use of Gaps, Local Alignment focus on maximizing sequence homology in separated groups, allowing more freedom to the algorithm to fully explore regions with higher sequence similarity. [Appendix – II]

Structural Alignment was superimposed by Rigid and Flexible Alignments (jFATCAT) for each Chain. Rigid Structural Alignment, as the name suggests, aligns structures considering both as rigid molecules being ideal for equally sized proteins. As for Flexible Structural Alignment, the structure has more freedom to adjust in a 3D space allowing superposition of distant groups by changing protein conformation, which is ideal for differently sized proteins. [Appendix – II]

Finally, Data integrity is analyzed by comparing the sequential information of the UniProt database with the correspondent PDB files. All these steps are summarized in the Figure 4.23.

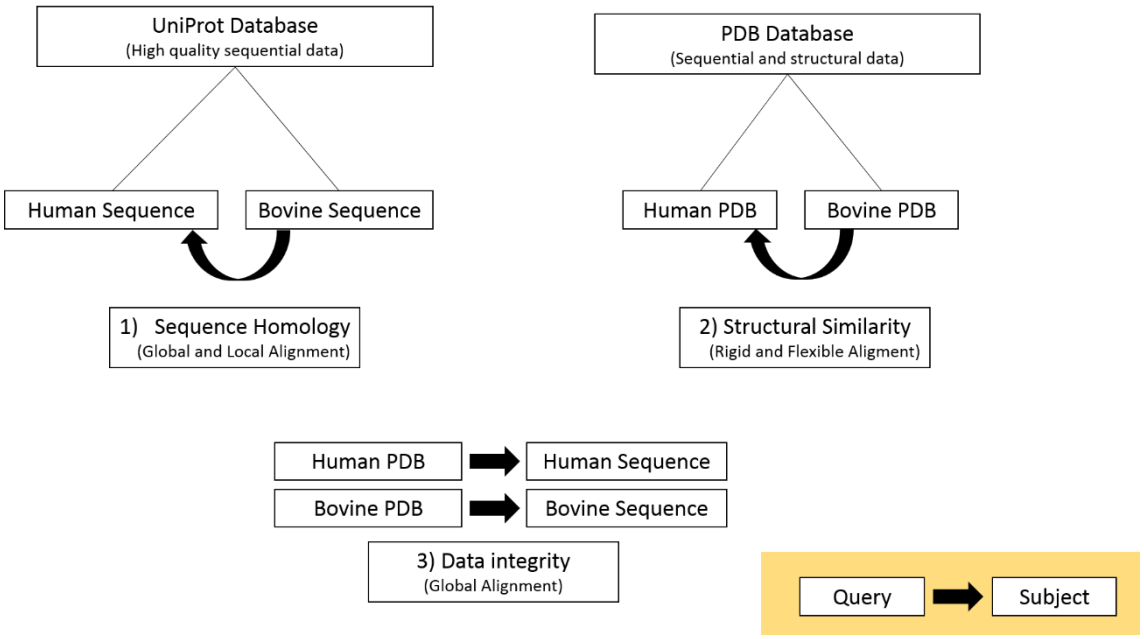

Figure 4.23. Schematic representing determination of protein homology determination, structural similarity and data integrity in this chapter.

4.4.3.1 Fibrinogen

Comparing protein sequence length for fibrinogen from human or bovine origins (Table 4.3), a clear difference in size in the α-chain and β-chain is noticeable, both in PDB and UniProt data, that will affect sequence and structural homologies between the Human and Bovine proteins.

Table 4.3. Sequence length (in number of aa residues) of Bovine and Human Fibrinogen by Chain.

	Sequence Size (# Residues)			
Chain	**Bovine PDB**	**Human PDB**	**Bovine Uniprot**	**Human Uniprot**
alpha	390	562	615	866
beta	408	461	468	491
gamma	411	411	444	453
Complete protein	2418	2868	3054	3620

Alignments of the PDB files with the correspondent protein sequences from the UniProt database, which have higher quality of sequential data, also reveals that the PDB sequences have incomplete chains, in particular the α-chains, and thus the relative difference in sequence sizes are observed between PDB and UniProt files. This is due to the difficulty in the crystallization of the native protein, which is a prerequisite for the construction of a PDB file, and so a proteolytic treatment was applied deleting sequential data.

Firstly, Uniprot sequence alignments were tested in order to obtain the maximum amount of information on sequence homology, subsequently PDB files were superimposed to check for structural similarity.

Analyzing Table 4.4, beta and gamma chains seem to have high homology (>60%), while the alpha chains seem to have less homology having around 40-50% Identity and Similarity on a Global Alignment. However, when compared locally, alpha chains seem to have higher homology (~60%) most likely due to conserved Domains.

Table 4.4. Sequence alignment of Human and Bovine Fibrinogen.

Human and Bovine Sequence Homology (UniProt)			
Global Alignment			
Chain	Identity (%)	Similarity (%)	Gaps (%)
alpha	44	51	31
beta	77	85	4
gamma	80	88	2
Local Alignment			
Chain	Identity (%)	Similarity (%)	Gaps (%)
alpha	58	68	10
beta	82	91	0
gamma	81	90	1

Structural similarity by superimposing both PDB files, based on rigid structural alignment, is presented in Figure 4.24, and shows a high degree of similarity

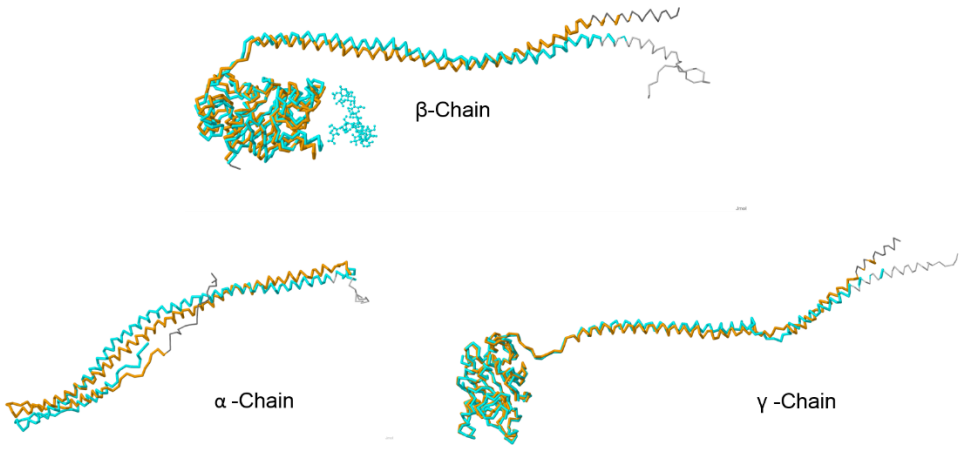

Figure 4.24. Rigid Structural Alignment of Human Fibrinogen (blue) and Bovine Fibrinogen (orange). The structural zones in grey represent non-aligned regions.

Checking Table 4.5, both rigid and flexible alignments have approximate values of chain similarity, allowing the assumption that protein functionality and chain three-dimensional structure should be similar and that the more complete PDB file of the Human Fibrinogen can be used as a reference structure for the Bovine counterpart.

Table 4.5 Structural Similarity for Human and Bovine Fibrinogen.

Human and Bovine Structural Similarity (PDB)		
Rigid Alignment		
Chain	**Similarity (%)**	**Gaps (%)**
alpha	82	3
beta	91	6
gamma	91	2
Flexible Alignment		
Chain	**Similarity (%)**	**Gaps (%)**
alpha	82	0
beta	93	0
gamma	91	0

Superposing both PDB structures the similarities in size and conformation can be observed as seen in Figure 4.25.

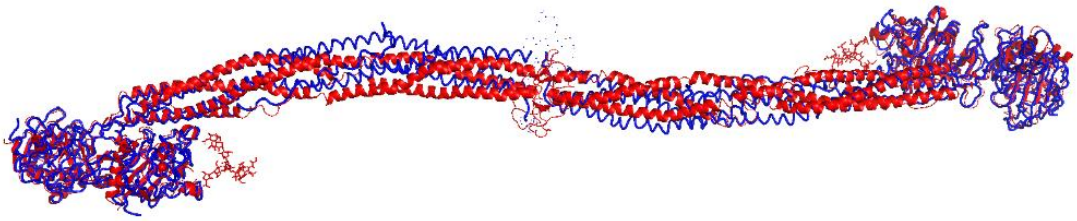

Figure 4.25. Human (Red) and Bovine (Blue) Fibrinogen PDB superposition.

As for the PDB data integrity, relatively to the correspondent sequential data of highest quality, both Human and Bovine Fibrinogens seem to lack a major part of the information of the alpha-chains, as seen in Table 4.6, corresponding to the diminished sequence sizes of these chains in the PDB files seen in Table 4.3.

Table 4.6.Data integrity for the Bovine and Human Fibrinogen PDB files compared to the correspondent UniProt sequences by Global alignment.

	PDB data integrity			
Organism	**Chains**	**Identity (%)**	**Similarity (%)**	**Gaps (%)**
Bovine	alpha	63	63	0
	beta	87	87	0
	gamma	91	91	0
Human	alpha	65	65	0
	beta	94	64	0
	gamma	90	90	3

4.4.3.2 Albumin

Albumin sequence size seems mostly preserved when comparing Uniprot sequence data and correspondent PDB files as seen in Table 4.7, giving an early hint that the PDB structures have high data integrity relatively to the UniProt sources.

Table 4.7. Sequence length of Bovine and Human Serum Albumin.

Sequence Size (# Residues)			
Bovine PDB	**Human PDB**	**Bovine Uniprot**	**Human Uniprot**
583	585	617	619

In Table 4.8, both Global and Local alignments score high levels of Identity and Similarity (>75%) and no gaps displaying high homology for Bovine and Human Albumin.

Table 4.8. Sequence alignment of Human and Bovine Serum Albumin.

Human and Bovine Sequence Homology (UniProt)		
Global Alignment		
Identity (%)	**Similarity (%)**	**Gaps (%)**
76%	88%	0%
Local Alignment		
Identity (%)	**Similarity (%)**	**Gaps (%)**
76%	88%	0%

As expected, since albumin protein sequences from bovine and human sources share 88% similarity and 76% identity, structural alignments depict similar structural features and superimposing the PDB files shows minimal variation as can be observed in Figure 4.26.

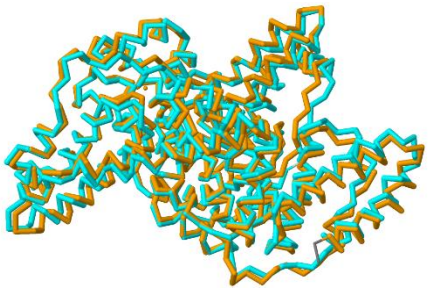

Figure 4.26. Rigid Structural Alignment of Human Serum Albumin (blue) and Bovine Serum Albumin (orange) PDB files.

An 88% similarity was estimated for both alignments (global and local) as tabulated in Table 4.9, showing no significant variation in the structural identity between the Human and Bovine proteins.

Table 4.9. Human and Bovine PDB Structural Similarity.

Human and Bovine Structural Similarity (PDB)	
Rigid Alignment	
Similarity (%)	**Gaps (%)**
88	0
Flexible Alignment	
Similarity (%)	**Gaps (%)**
88	0

As predicted by analyzing the low variance in the number of residues in Table 4.7, the above 95% in Identity and Similarity, seen in Table 4.10, acknowledge these PDB files with high preservation in sequence information.

Table 4.10. Data integrity of the Human and Bovine PDB files.

	Global alignment (PDB vs. UniProt)		
	Identity (%)	**Similarity (%)**	**Gaps (%)**
Bovine	96	95	0
Human	96	96	0

4.4.4 Electrostatic properties

To further the understanding of the Protein-NP interactions, the electrostatic properties of the studied proteins were analyzed. The estimated isoelectric point and electrostatic potential maps, at various pH ranges, are essential information to find the regions with the highest probability of adsorbing at the surface of a nanoparticle and understand how the pH influences the electrophoretic mobility of bioconjugated samples.

4.4.4.1 Fibrinogen

Electrostatic potential results have been omitted for the Bovine PDB file, since the bioinformatic tools used in this section require a degree of sequence completeness, which was not met by that file. Thus, only the Human PDB file was considered for analysis. As the isoelectric point, of the complete structure, estimated by the Propka and ExPASy tools, was around pH 6.5-6.6, the Poisson-Boltzmann equation was performed on a pH range between 6.0 and 8.0 in order to cover both the isoelectric point and the working pH (7.4), and analyze the variation in the electrostatic potential of the Fib protein. It is possible to verify, according to Figure 4.27, that the central region and part of the globular ends are the most electropositive parts of the protein, being candidates for the interaction between Fib and the negative charged AuNPs.

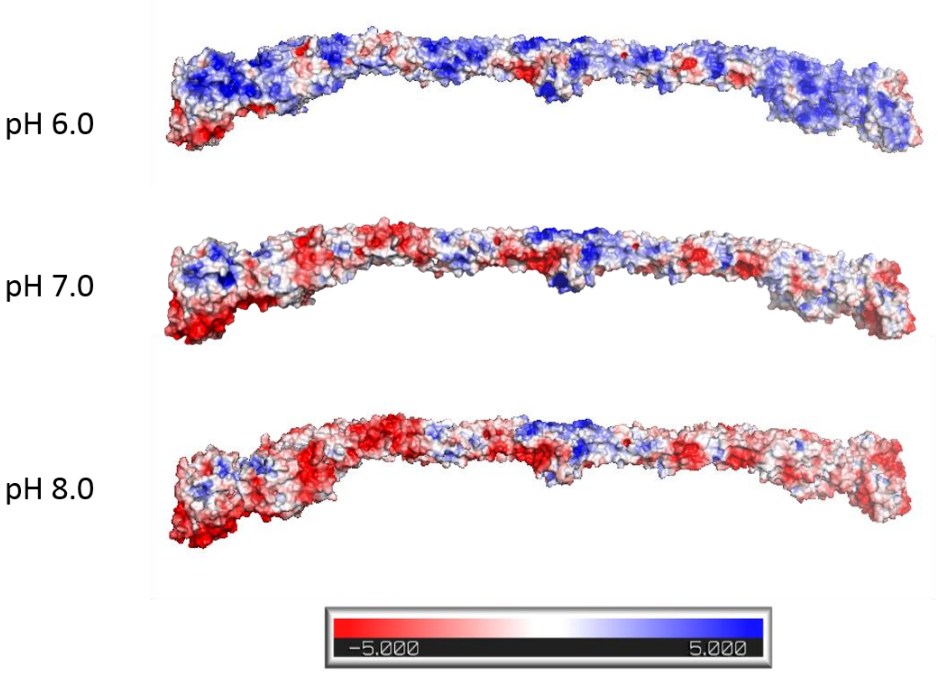

Figure 4.27. Electrostatic Potential projected at a computed surface for the Human Fibrinogen (PDB 3GHG) at a pH range from 6.0 to 8.0. The color range indicates the estimated negative (red), neutral (white) and positive (blue) surface potential. The range varies between -5.0 and +5.0 (kb T e_c^{-1}).

Focusing on the electrostatic potential map at pH 7.4, as it is the working and physiological pH, in Figure 4.28, viewing from the top side of the protein structure, the previously mentions zones, central and globular ends, might indicate how the protein folds around the AuNP or explain the possibility that one Fib molecule might conjugate multiple AuNPs, forming complex AuNP-Fib-AuNP nanostructures. This might give some insight on how Fib molecules adsorb to AuNPs of various sizes, requiring more flexibility in the case of smaller nanoparticles, like the 15 nm AuNPs, while in the case of larger sized AuNPs these electropositive regions will ensure that Fib will have favorable electrostatic interactions with negative nanoparticles.

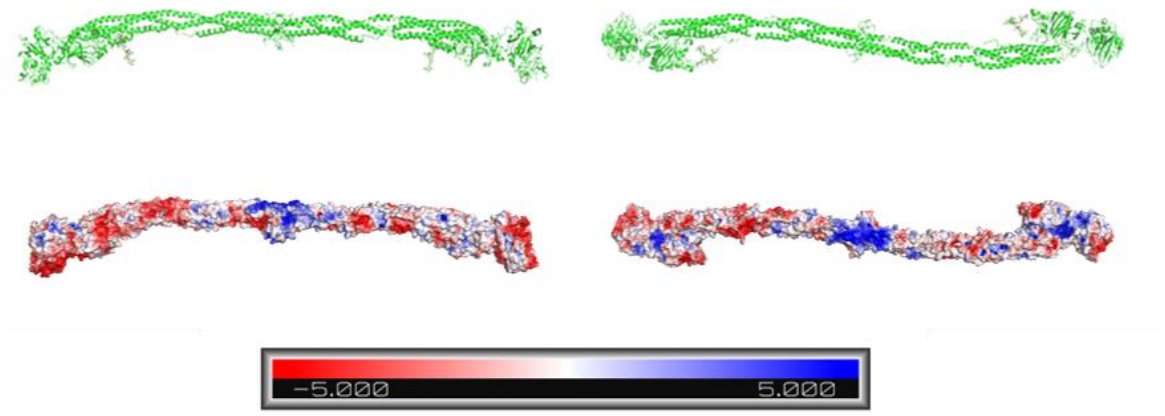

Figure 4.28. Front (left) and Top (right) view of the Human Fibrinogen PDB at pH 7.4 and correspondent electrostatic potential surface below.

All the isoelectric and molecular weight calculations, using various available Bioinformatic tools, were tabulated in Table 4.11.

Table 4.11. Isoelectric point (pI) and Molecular Weight (MW) data of Human (3GHG) and Bovine (1DEQ) PDB files for Fibrinogen.

	Fibrinogen							
	PDB	**pI (propka)**	**pI (H^{++})**	**pI (ExPASy)**	**MW (ExPASy)**	**Uniprot**	**pI (ExPASy)**	**MW (ExPASy)**
Bovine	1deq	-	>12	6.47	272 kDa	-	6.52	341
	1deq a	-	9.96	8.21	42 kDa	FGA	6.73	67
	1deq b	-	7.38	7.94	46.5 kDa	FGB	8.45	53
	1deq g	-	6.36	5.49	46.5 kDa	FGG	5.53	50
Human	3ghg	6.58	>12	6.36	319 kDa	-	5.97	404
	3ghg a	-	8.52	6.96	60.6 kDa	FGA	5.70	95
	3ghg b	-	6.13	7.15	52.3 kDa	FGB	8.54	56
	3ghg g	-	6.02	5.54	46.4 kDa	FGG	5.37	52

4.4.4.2 Albumin

Since the Bovine and Human Albumin share high sequence homology (>76% in Identity and Similarity), only the Bovine protein was considered here as it was the protein used in the bioconjugation studies. The isoelectric point estimated by the PROPKA and ExPASy tools, was around pH 5.0-6.0. The Poisson-Boltzmann equation was performed on a pH range between 5.0 and 8.0 in order to cover both the isoelectric point and the working pH (7.4). From the Figure 4.29, the central inner is the most electropositive part of the protein, being a possible candidate for the interaction between BSA and the negative charged AuNPs.

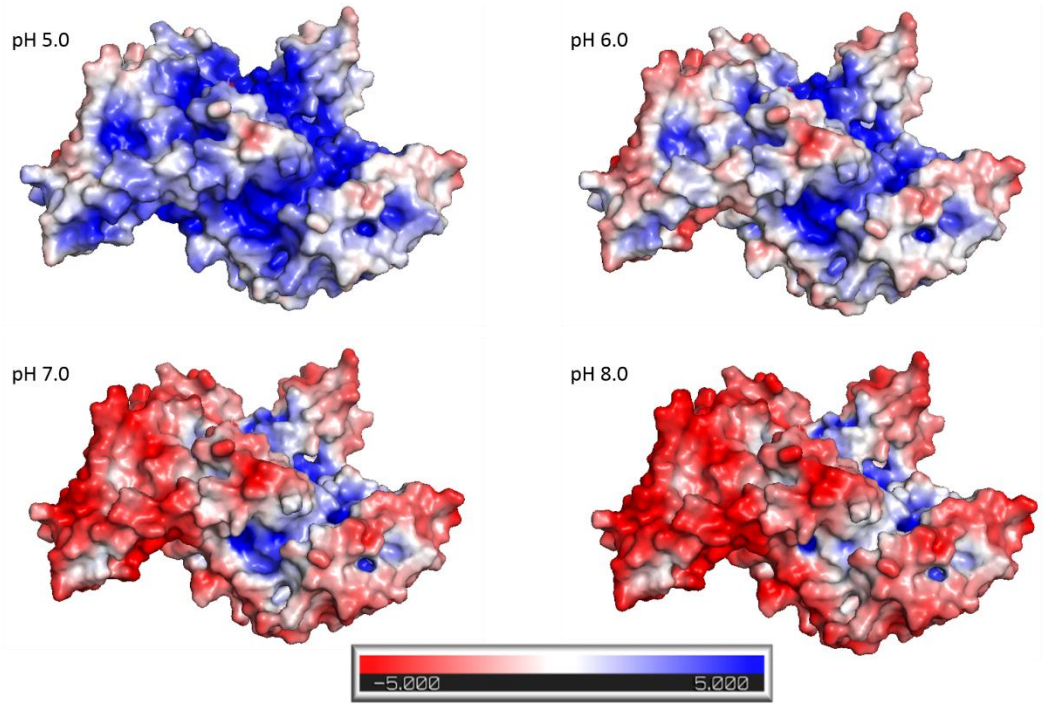

Figure 4.29. Electrostatic Potential projected at a computed surface for the Bovine Albumin (PDB 3V03) at a pH range from 5.0 to 8.0. The color range indicates the estimated negative (red), neutral (white) and positive (blue) surface potential. The range varies between -5.0 and +5.0 (kb T e_c^{-1}).

Although the software detected the central region as the most electropositive zone, it actually coincides with a reported hydrophobic pocket. [85] Centering the BSA PDB file, as previously seen in Figure 1.7, for a better understanding of the location of the electropositive and hydrophobic region is shown in Figure 4.30 at pH 7.4 as it is the working and physiological pH. If the inner region, has in fact an electropositive chemistry, it will be attracted to the negative nanoparticle, the conformation of the protein might change to maximize the exposition of these residues to the surface.

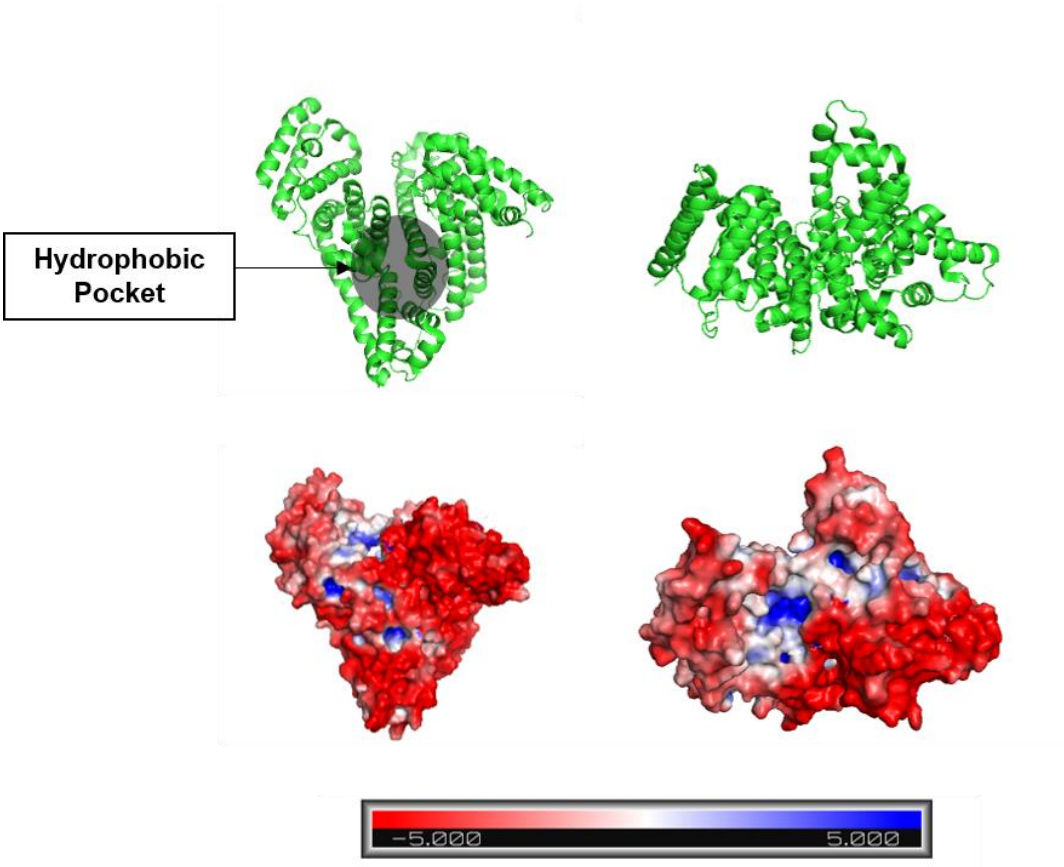

Figure 4.30. Representation of the BSA PDB file showing the Hydrophobic Pocket (Top-Left) and the correspondent Top-View (Top-Right). The electrostatic potential surfaces are shown below and were estimated at a pH 7.4.

The data summarized in the Table 4.12, obtained by various Bioinformatic tools, allows to predict the pH range that corresponds to the isoelectric point.

Table 4.12. Isoelectric point (pI) and Molecular Weight (MW) data of Human and Bovine Albumin.

	Albumin							
	PDB	**pI (propka)**	**pI (h++)**	**pI (expasy)**	**MW (expasy)**	**Uniprot**	**pI (expasy)**	**MW (expasy)**
Bovine	3V03	5.62	5.18	5.60	66 kDa	ALB	5.82	69 kDa
Human	1AO6	5.87	5.23	5.67	66 kDa	ALB	5.92	69 kDa

4.5 BSA and Fibrinogen-AuNP Bionanoconjugates

Gold nanoparticle surface interactions with blood proteins were studied using the previously prepared protein solutions and MUA- or CALNN- functionalized AuNPs. Each test was performed in similar conditions, maintaining the buffer and AuNP volumes and concentrations, and overnight incubation times for the formation of the AuNP-protein bionanoconjugates, even when complete

bioconjugation was observed after a few hours of incubation. For bionanoconjugation characterization, UV-Vis spectroscopy was used although conjugated samples differ only in a 3 nm red-shift from unconjugated AuNPs, shifting from 525nm to 528nm upon conjugation as shown in Figure 4.31Figure 4.31, for the case of BSA bioconjugation with MUA-functionalized AuNPs.

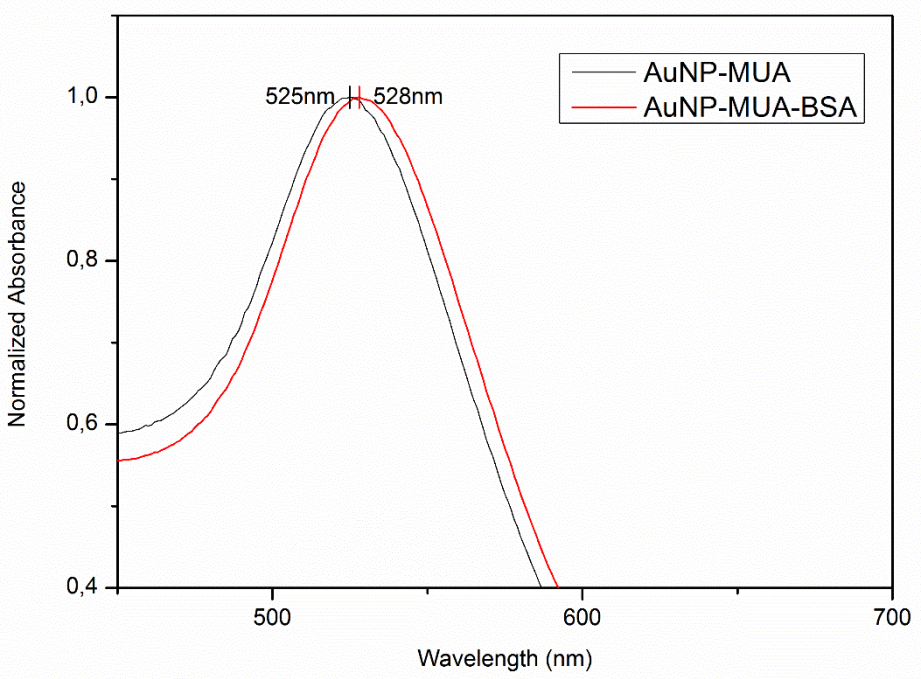

Figure 4.31. UV-Vis spectroscopy depicting a red-shift upon nanoparticle conjugation.

Agarose gel electrophoresis allowed to compare AuNP-BSA and AuNP-Fib protein corona formation for various protein concentration ratios, stabilizing at a higher concentration which is assumed to correspond the fully conjugated AuNP. In Figure 4.32 a direct comparison of both protein-nanoparticle conjugations is possible. The direction of band migration goes from top (negative pole) to bottom (positive pole). AuNP-MUA and AuNP-CALNN are, as stated before, negatively charged and so migrate to the positive pole. As for proteins, they have a more neutral or positive global net charge, at pH of 7.4, and upon adsorption on a negative charged surface, partially cancel this charge, causing AuNP-(MUA/CALNN)-protein bionanoconjugates to migrate less towards the positive pole. As protein concentration increases in the bionanoconjugate

incubation colloidal solution, a higher number of proteins will adsorb to the surface hence decreasing the total migration for increasing Protein/AuNP ratios.

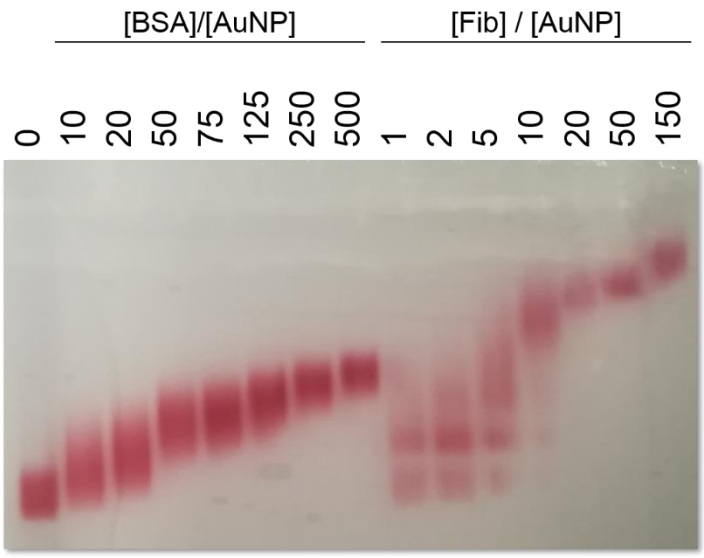

Figure 4.32. Agarose gel (0.5%) electrophoresis of MUA functionalized AuNPs conjugated with BSA and Fib at indicated [Protein]/[AuNP] concentration ratios.

BSA-AuNP conjugation follows a curve, where bands occupy a larger area (wider bands) at intermediate ratios due to the variability in conjugation stages and the effects of a dynamic adsorption equilibrium, not present at the ratio of stabilization where all AuNPs should be fully conjugated and variability is minimal since the equilibrium is shifted towards a total surface conjugation from protein saturation. In the case of Fib-AuNPs, a multi-band phenomenon is visible for smaller [Fib]/[AuNP] molar ratios (1:1 to 5:1), making difficult to choose which experimental points to include in the Langmuir/Hill curve fitting. However, at ratios from 10:1 to 150:1, the multi-band effect is not apparent, or the various bands are closer spaced, allowing determination of the migration distance. At the higher stages of conjugation, near the maximum surface coverage range, the bands reduce in size as for BSA bionanoconjugates.

As for total band migration, BSA-conjugated AuNPs, with an average electrophoretic mobility of (13 ± 2) x $10^{-5} cm^2 V^{-1} s^{-1}$ migrate more than Fib-conjugated AuNPs, that have an average of (6.5 ± 2.2) x10^{-5} $cm^2 V^{-1} s^{-1}$, possibly due to the global surface charge of Fib being more positive than BSA, making the surface of the resulting bioconjugate more positive. Size is also a promoter on the migration hindrance, which might indicate that the size of a Fib-conjugated AuNP is higher than the BSA-conjugated AuNP. These effects, charge and size, are further discussed in the Fergusson Plot Analysis section below. The average electrophoretic mobility for each case can be verified in Figure 4.33.

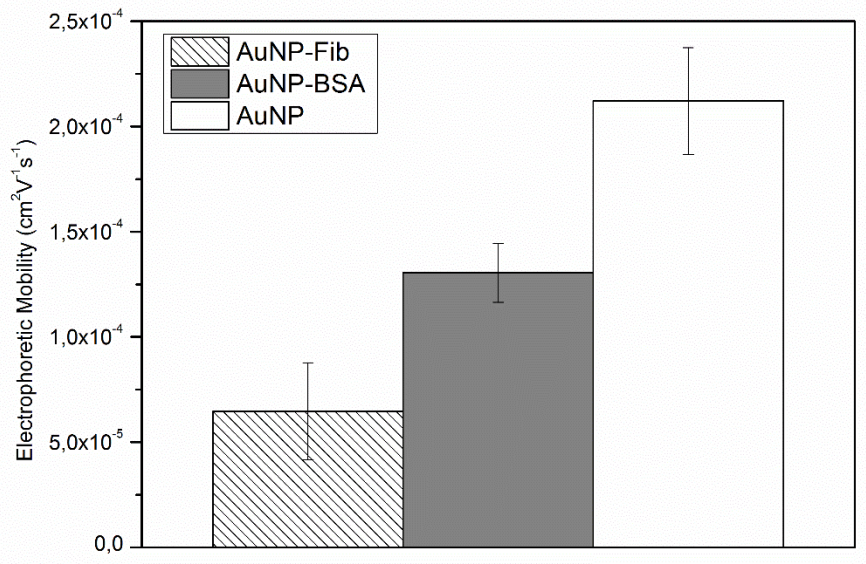

Figure 4.33. Average electrophoretic mobility for AuNP and fully conjugated AuNPs with Fib and BSA on a 0.5% agarose gel.

The migration distance for each band was obtained by using the image and video RGB analysis with the eReuss software. Using the distance, the electrophoretic mobility (μ) is calculated using Equation 4.3, which accounts for the band velocity (v) in the applied electric field (E).

$$\mu = \frac{v}{E}$$

Equation 4.3

AGE results with dissimilar parameters like electrophoresis duration and voltage can be compared since electrophoretic mobility normalizes these variations. Non-conjugated and fully conjugated 15nm AuNPs differ in mobility as seen in the previous figure.

4.5.1 Albumin-AuNP bionanoconjugate

For BSA-AuNP studies, several tests were performed to find the range of Protein/AuNP ratios where the conjugation curve would allow a better understanding of the protein interaction with the surface of the nanoparticle. Protein/AuNP ratios of up to 1000:1 were used to obtain the fully conjugated surface.

4.5.1.1 Agarose Gel Electrophoresis

Analyzing the AGE results of MUA-AuNP in Figure 4.34, a clear difference between non-conjugated and fully conjugated band migration is visible, stabilizing around the 300-600 ratio of [BSA]/[AuNP]. The maximum conjugation ratio does not correlate to the total protein at the nanoparticle surface, but the concentration needed in colloidal solution during the incubation period, to allow full surface conjugation to occur.

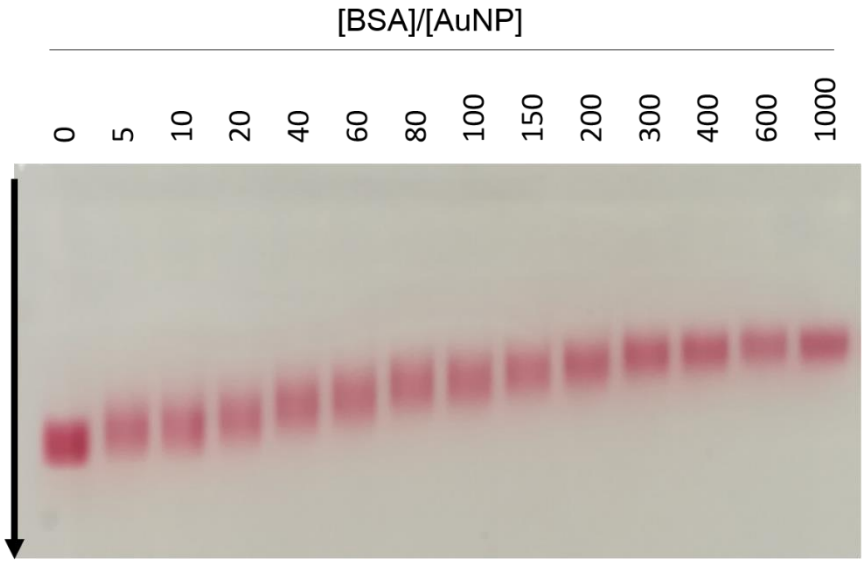

Figure 4.34. Agarose gel (0.5%) electrophoresis of MUA-AuNP conjugated with various [BSA]/[AuNP] ratios. Gel obtained after a 15-minute run at 150V.

Analysis of the gel by the eReuss software, allows a migration distance (cm) to be obtained for each sample, which divided by the electrophoresis duration, gives the band velocity (cm s^{-1}), that by knowing the electric field (E = 10 V cm^{-1}), can be converted into electrophoretic mobility (cm^2 V^{-1} s^{-1}) using Equation 4.3. Two possible fittings can be applied to these data, Hill Equation fitting and Langmuir Isotherm Fitting as seen in Figure 4.35. The Hill Equation modulates the value of the cooperativity coefficient (n) to better fit the curve, the value which can determine the type of cooperativity involved in the conjugation process. The Langmuir Isotherm derives from the Hill Equation assuming a non-cooperative conjugation (n = 1).

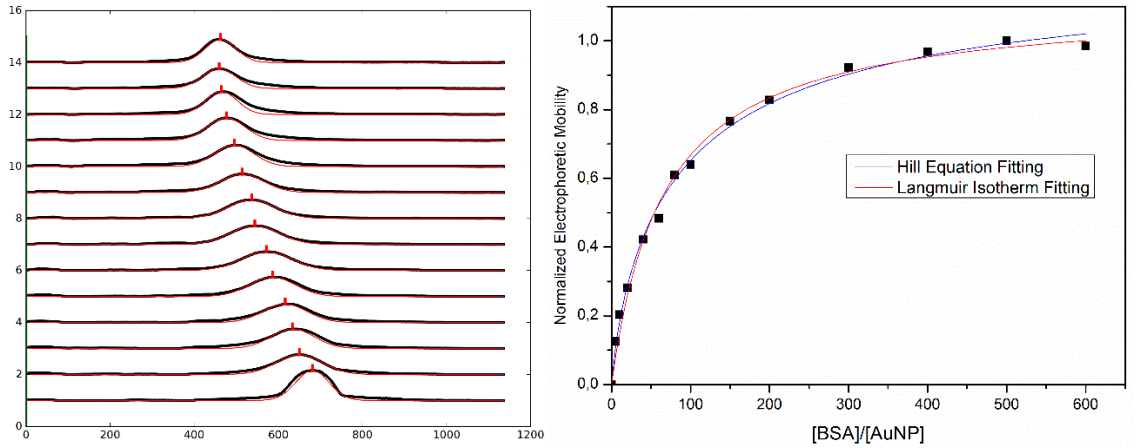

Figure 4.35. Band migration profile, in pixels, obtained by eReuss (left) and normalized electrophoretic mobility variation with increasing BSA concentration fitted by the Hill and Langmuir equations (right).

From the results for both fittings, adsorption constants (K_{ad}) were compared. Langmuir fitting, with a cooperativity coefficient of n = 1, resulted in a K_{ad} of (1.5 ± 0.1) x 10^{-2}, while the Hill fitting, with a cooperativity coefficient of n = 0.81, lead to a K_{ad} of (1.15 ± 0.1) x 10^{-2}. Both estimated constants were in the same order of magnitude, corresponding to a conjugation ratio value, at half of maximum band migration in the migration curve, in the range of 10:1 to 100:1 BSA:AuNP, as verified in all conjugation experiments of BSA to 15 nm AuNPs, with similar cooperativity coefficients, allowing to state that the flexible parameters of a Hill equation fitting are close to the adsorptive behavior of a non-cooperative adsorption as the Langmuir Isotherm. Although the curve fitting to the Langmuir Isotherm is acceptable, the resulting Hill coefficient, which is below 1 (n < 1), might hint to a negatively cooperative binding by electrostatic repulsion by the lateral adsorbed protein-protein interactions (as discussed in chapter 1.1.2).

Varying AuNP concentration, buffer and sample volume and other parameters not accounted for in the electrophoretic mobility equation, will affect the protein corona formation, caused by hydrodynamic effects and AuNP size differences (13-17 nm), and subsequently the gel migration. Also, different migration distances are verified due to gel concentration inconsistency from gel to gel, as the process of gelification is affected by conditions such as temperature, humidity and air exposure. These effects are predominant in the intermediate protein to nanoparticle conjugation ratios leading to a greater variety of the migration profile. As seen in Figure 4.36 the results form a well-defined conjugation curve with increasing BSA concentration that yielded an average K_{ad} of (3.86 ± 1.0) x 10^{-2} upon fitting to a Langmuir Isotherm.

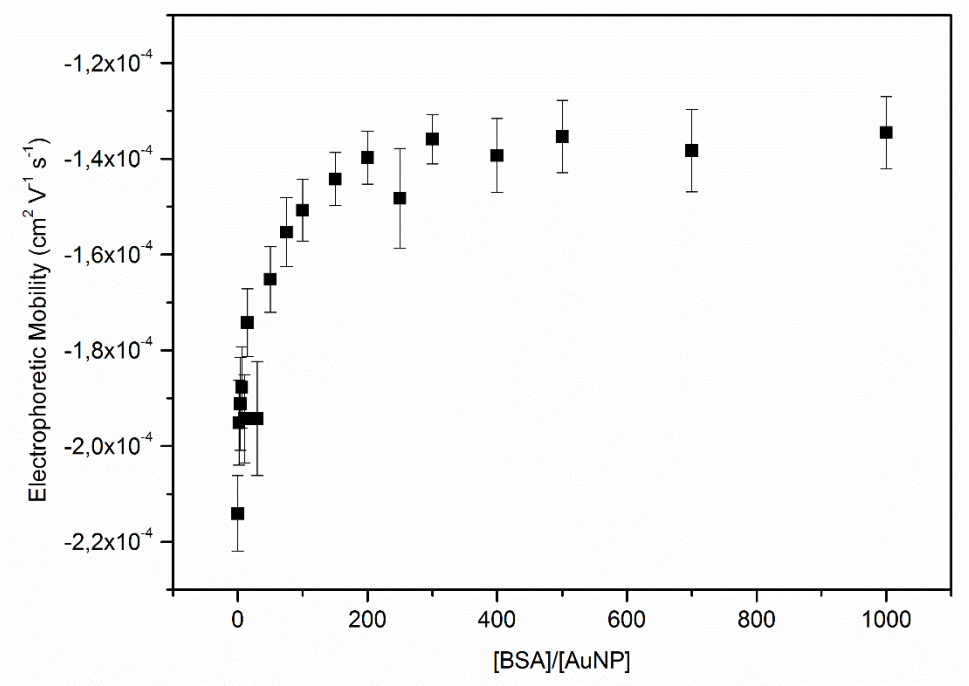

Figure 4.36. Agarose gel electrophoresis results of fourteen individual essays of AuNP bionanoconjugation with BSA. AuNP concentrations varied between 1 and 3 nM while maintaining the same bioconjugation ratios.

.

Comparing BSA bionanoconjugation with MUA-AuNP and CALNN-AuNP in Figure 4.37, band migration for non-conjugated and fully conjugated samples are the same for both functionalizations. Only for intermediate conjugation ratios a variation is observed, as AuNP-MUA samples have a well-defined curve, although with signs of band smearing, while AuNP-CALNN bands are too diffused across the gel, not allowing a distinction between increasing concentration ratios. Any attempt to estimate the band migration and calculate a possible K_{ad} for the adsorption of BSA to AuNP-CALNN is highly unrecommended due to band smearing and so the conjugation curve was not plotted. Other than parameter estimation from the gel, full conjugation of AuNP-CALNN was successful since the resulting bands migrated less than the non-conjugated counterparts, establishing a migration minimum close to the AuNP-MUA conjugated samples.

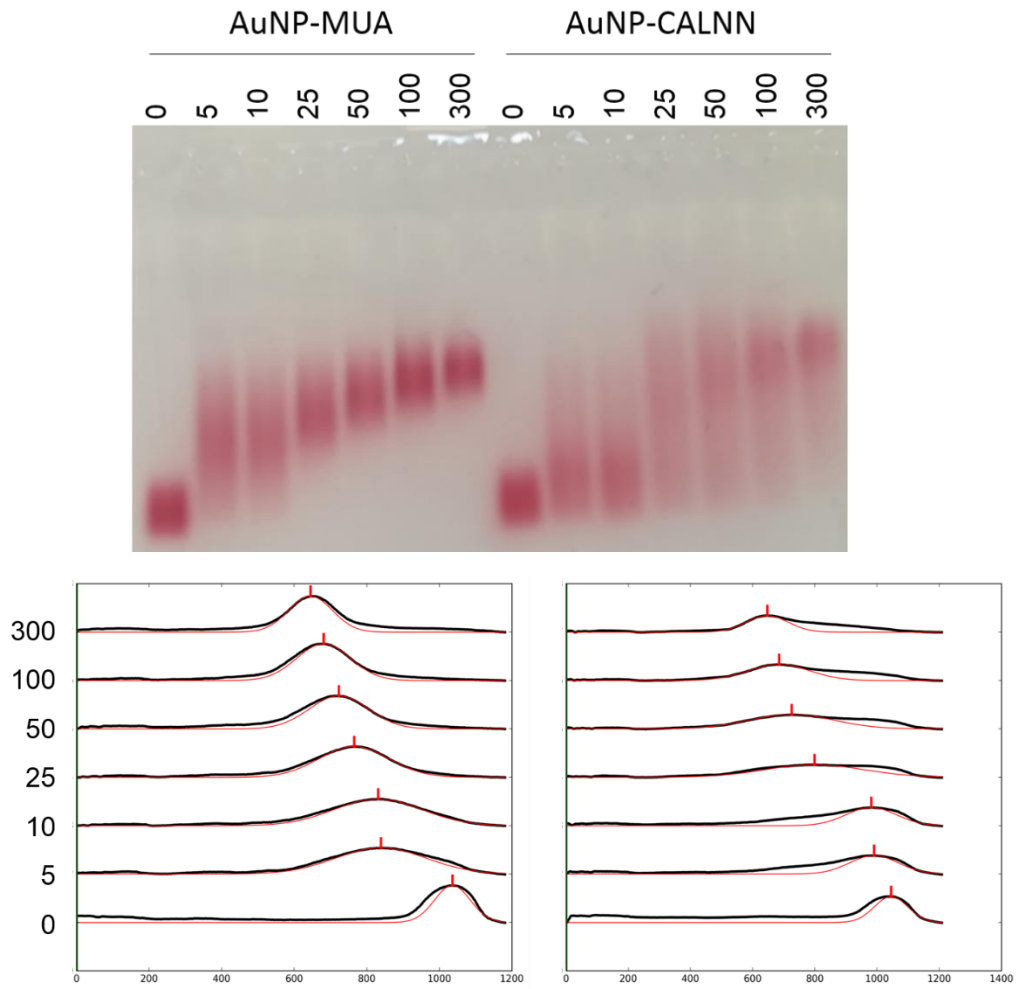

Figure 4.37. Agarose Gel Electrophoresis of BSA conjugated samples, functionalized with MUA and CALNN (top), and respective band migration profiles (bottom).

4.5.2 Fibrinogen-AuNP bionanoconjugate

For Fib-AuNP studies, ratios up to 1000:1 were used to obtain the fully conjugated surface as well as the intermediate states of conjugation.

4.5.2.1 Agarose Gel Electrophoresis

Analyzing the AGE results in Figure 4.38, MUA and CALNN functionalizations have similar migration profiles for fully conjugated samples. On the other hand, conjugates for 5 and 10 [Fib]/[AuNP] ratios show very dispersed bands and showing more than one band for the same lane. MUA results however, have a dispersed band behavior that allows an estimation of the band migration average by the software.

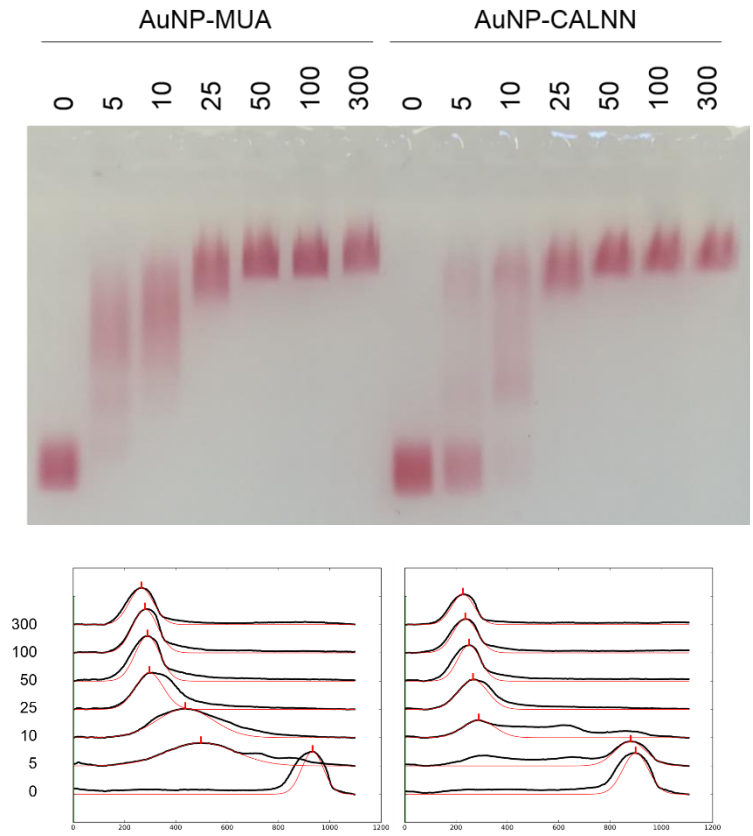

Figure 4.38. Agarose Gel Electrophoresis of Fib conjugated samples, functionalized with MUA and CALNN (top), and respective band migration profiles (bottom).

Further experiments tried to elucidate the behavior of lower than 5 [Fib]/[AuNP] ratios result for both MUA and CALNN functionalization and attempt to perform the same plot fittings as for the BSA results.

Results are presented, although estimated adsorption constants have a high degree of error as migration values for lower ratios, as these calculations can only consider the value of a single band migration for the multi-banded samples. And for the fitting, values from these ratios are used only if one of the bands has a relative higher contrast over the other or, if the bands seem smeared or equal in contrast, are completely ignored from the plot due to the inherent uncertainty.

Due to the multi-band effect at low Fib to AuNP ratios, an accurate analysis of the conjugation curve cannot be obtained. The software was assigned to determine the highest color intensive band, and in the case of the multiple bands, the color predominant band in the multi-band samples was used for the analysis. This assumption seems to calculate the migration profile for the conjugated AuNP-MUA early ratios by averaging the multi-bands as a unique smeared band allowing a possible fitting, while in the AuNP-CALNN results assuming a band out of the two visible bands is possible, but at an increased estimated parameter error. To avoid further fitting error, all bands that show a multi-band behavior are excluded from the parameter estimations.

Interestingly, all results (Figure 4.38 and Figure 4.39) show the same band separation on lower ratios, with increased separation for the CALNN functionalization as one example, is shown in Figure 4.39 using enhanced contrast images. While the smaller conjugation ratios for MUA functionalized AuNPs show a variety of bands for the same ratio, CALNN results demonstrate a clearer gap between non-conjugated and partially conjugated samples in the same sample lane.

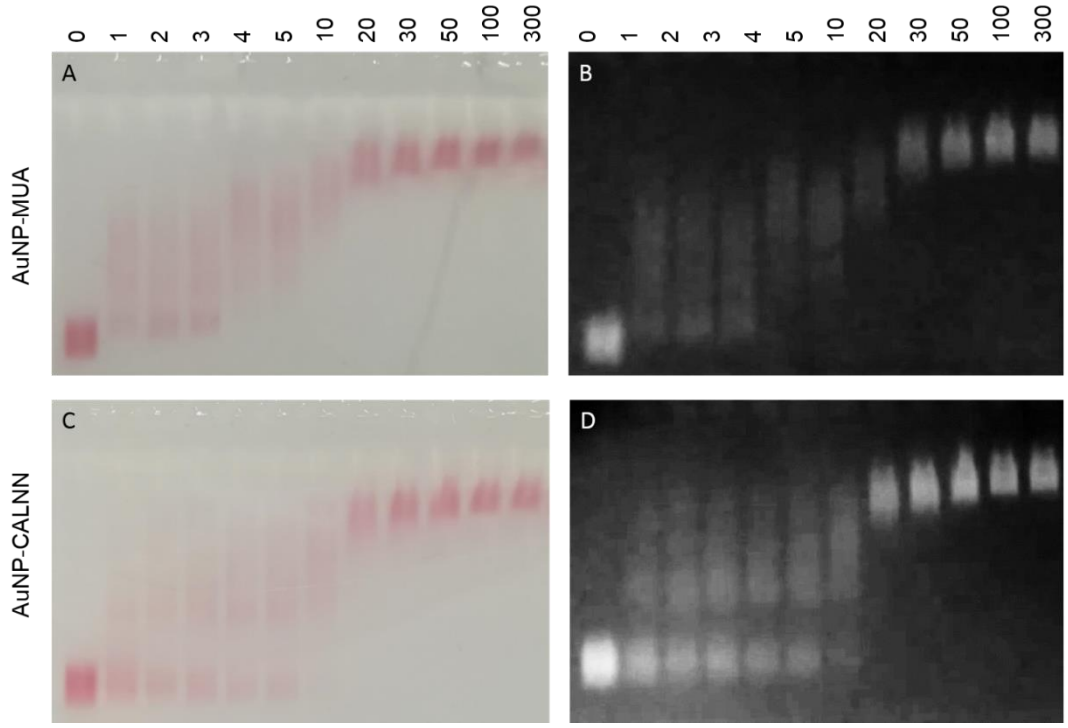

Figure 4.39. Agarose gel electrophoresis results of Fib conjugation of 15nm MUA and CALNN AuNPs. A) Fib conjugation of AuNP-MUA original image, B) Fib conjugation of AuNP-MUA augmented contrast eReuss image, C) Fib conjugation of AuNP-CALNN original image, B) Fib conjugation of AuNP-CALNN augmented contrast eReuss image.

As for the estimated K_{ad} values, by Langmuir Isotherm Fitting, for AuNP-CALNN results the ratios between 1 and 10 were not considered, while for AuNP-MUA samples ratios from 1 to 4 were not considered. Acknowledging the high associated error of the lower ratio migrations, the obtained K_{ad} for the association constant of Fib to AuNP with the two different functionalizations, was $(51.2 \pm 4.7) \times 10^{-2}$ for AuNP-CALNN and $(34.3 \pm 1.2) \times 10^{-2}$ for AuNP-MUA. Comparing with the estimated value for the BSA conjugation of $(1.5 \pm 0.1) \times 10^{-2}$ for AuNP-MUA, these results for the Fib conjugates are one order of magnitude higher, indicating a much higher affinity of Fib than BSA for the formation of conjugates with AuNP-MUA.

These binding constants results, however, do not explain what causes the multi-band phenomenon, so as an attempt to study this effect, complementary experiments were performed. Firstly, by varying the AuNP diameter, the purpose was to test if nanoparticle to protein ratio would affect surface adsorption of Fibrinogen and influence AGE results. Different [Fib]/[AuNP] ratios were used for each nanoparticle size due to the expect increase of surface area for AuNP with higher diameters.

As seen in Figure 4.40, the gap between the bands of lower ratio samples (for which the multi-band effect was observed for 15 nm AuNPs) diminishes with increasing nanoparticle diameter size, from 15 nm to 19nm and 23 nm.

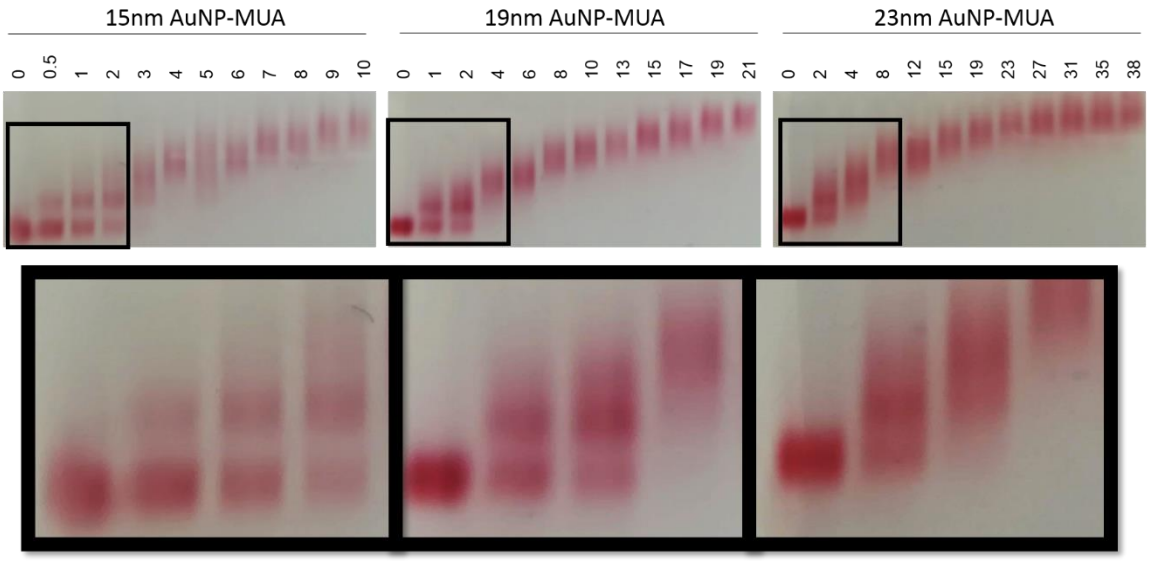

Figure 4.40. Agarose gel electrophoresis results of the Fib conjugation of 15nm, 19nm and 23nm AuNP-MUA samples (top) and first four ratios zoomed (bottom) for each sample.

Since the results seem to indicate a smaller multi-band separation with larger nanoparticles, even larger 40nm AuNPs were tested. As expected (Figure 4.41), the multi-band phenomenon is not present on these larger nanoparticles and a conjugation curve can be constructed, including all the experimental data. However, the observed conjugation behavior deviates from a simple Langmuir adsorption process, with a sigmoidal shaped curve suggesting cooperative adsorption. An alternative fitting can probably be obtained with two consecutive Langmuir adsorption processes, suggesting the formation of a second protein layer.

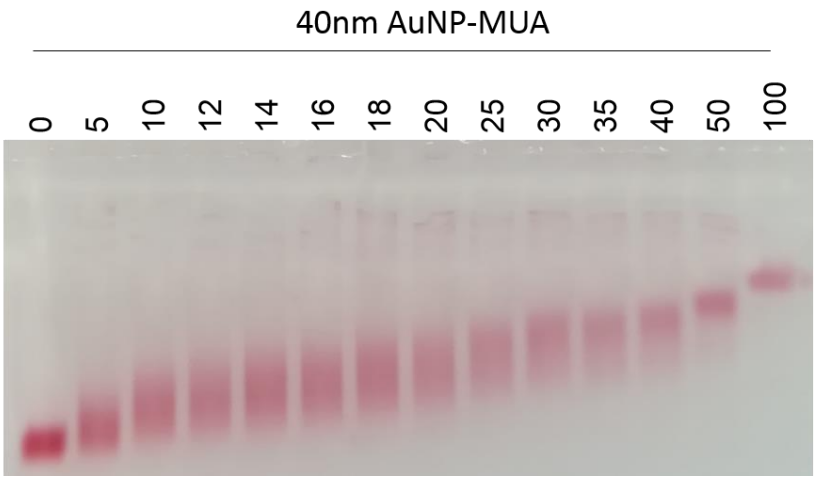

Figure 4.41. Agarose gel electrophoresis results of the Fib conjugation of 40nm AuNP-MUA.

Several AGE results of 40nm AuNP-MUA conjugated with Fib were analyzed in order to study the low and high ratios of conjugation as seen below in Figure 4.42. As the conjugation ratios increase, a plateau is reached soon after the 100 to 1, Fib to 40 nm AuNP-MUA ratio. However, past the 500:1 ratio, a new increase of the curve takes place. A Hill equation fitting was performed, yielding a cooperativity coefficient (n) of 1.8 and an estimated K_{ad} of 5.1 x 10^{-2} ± 0.2.

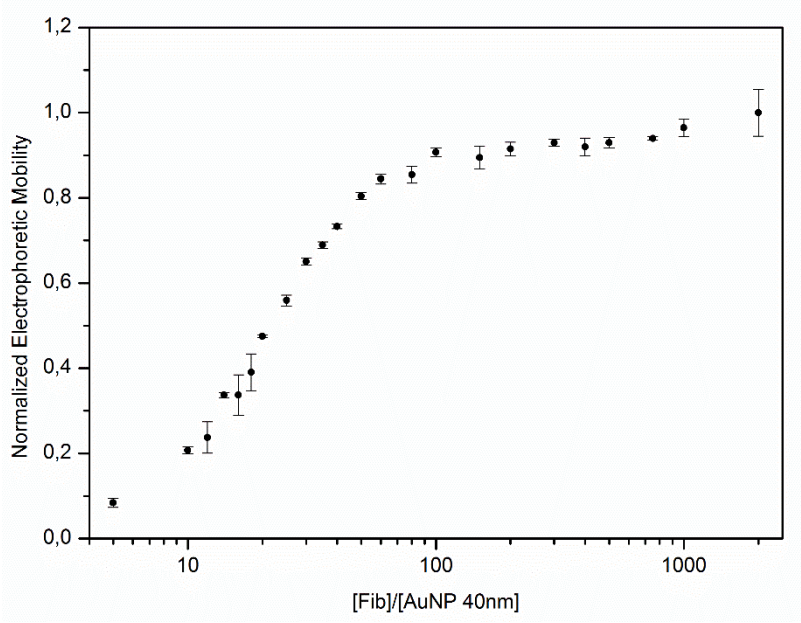

Figure 4.42. Normalized electrophoretic mobility of two AGE results, composed of Low and high ratio ranges, with increasing Fib conjugation of 40nm AuNP-MUA, fitted by the Hill Equation.

These results however would mislead into positive cooperativity (n = 2) adsorption behavior assumption. To clarify this, the conjugation ratios were increased past the ranges tested before to check for a possible second conjugation curve. From Figure 4.43, the 0.5% agarose gel

to the left, shows the previously observed full conjugation at the 100-500 ratio range, and then a second curve is seen past that range, for very high ratios (between 1,000 and 20,000). Since the migration distance on the second conjugation curve are too closely spaced, a new AGE was performed on a 1.0% agarose gel hoping to increase the migration difference for the highest conjugation ratios. Since sample (AuNP and Bioconjugate) size affects migration with agarose gel concentration, as is discussed further bellow in the Fergusson Plot Analysis, a curve with higher resolution is obtained. These results suggest that a possible second protein layer is formed and could give information on the protein corona, since the outer layer usually is classified as a soft-corona depending on the adsorption strength to the AuNP surface. However, a previous study indicated that the weak interactions between the soft-corona proteins and the AuNP, can be easily broken by physical effects like centrifugation and electrophoresis, so in the bioconjugates observed be AGE, the soft corona is probably not present. [86]

These results do not rule out other multi-layered behaviors from the smaller 15nm AuNPs with BSA and Fib, the migration retardation effect on AGE might be too difficult to detect. Even the 40nm AuNP conjugation with a relatively large protein as Fibrinogen gives only small effects on AGE results. However, a previous study refers that particle sizes below the 40 nm in diameter threshold are unlikely to form second layers of proteins. [87]

Further studies should be performed using techniques that minimize physical effects upon the Protein-Corona. DLS and NTA methods, accompanied with non-centrifugated and centrifugated samples to check for loss in protein content of the bioconjugates, might unveil hidden layers of proteins that are removed when checked under techniques likes AGE.

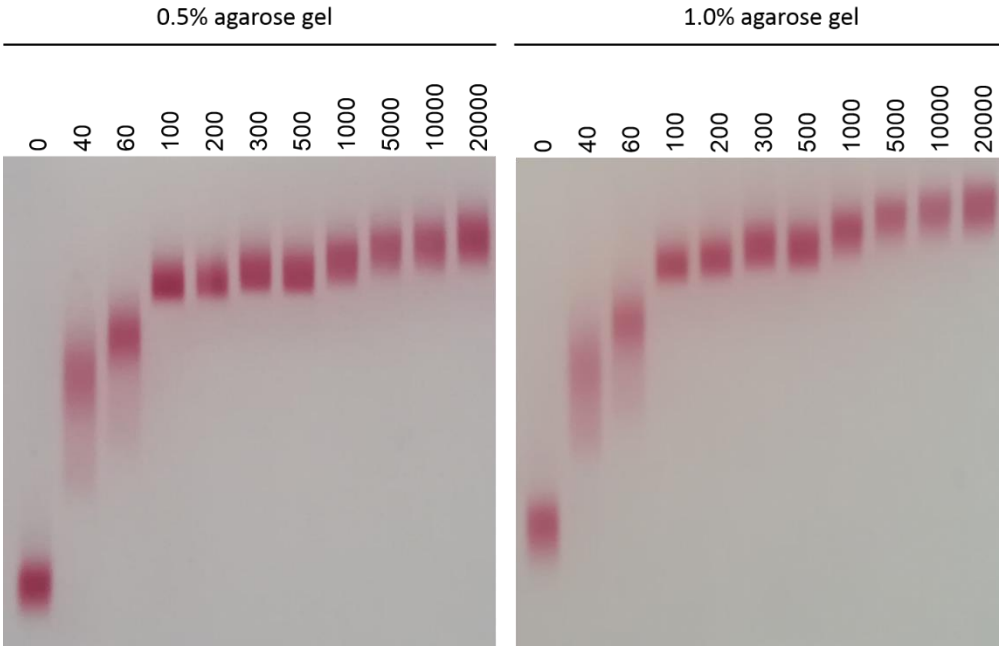

Figure 4.43. Agarose gel electrophoresis results of the Fib conjugation of 40nm AuNP-MUA samples at increased conjugation ratios (0 – 20,000) at 0.5% agarose (left) and 1.0% agarose gel (right).

Converting the migrations of the previous results into electrophoretic mobilities, two sets of data can be obtained, corresponding to the two curves. The first curve, between the ratios 0 to 500, and the second curve, between 100 to 20 000. In order to improve curve resolution, in the 500 to 20 000 ratio range, the 1.0% agarose gel was selected.

Each set of data is seen in Figure 4.44 was normalized from 0, the lowest conjugation ratio (0 for the first curve, 100:1 for the second curve), and 1, the highest conjugation ratio (500:1 for the first curve, and 20000 for the second curve).

Applying the Langmuir Isotherm fitting, the lower ratio curve had a conjugation mid-point at a ratio of 30:1, corresponding to a K_{ad} of (3 ± 0.7) x $10^{-2,}$ while the higher ratio curve had a conjugation mid-point at a ratio of 1100:1, corresponding to a K_{ad} of (9.7 ± 2.2) x 10^{-4}. All standard errors are from the fitting process since no replicated experiments were performed in similar conditions, although the behavior is noticeable in the two gels of different agarose concentrations.

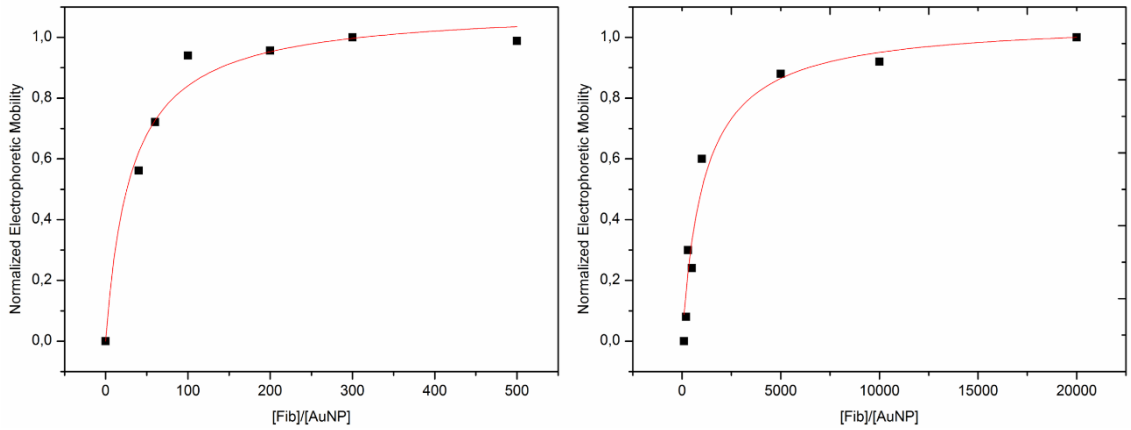

Figure 4.44. Bionanoconjugation of 40 nm AuNP-MUA with Fib. Lower ratio (0-500) conjugation curve (left) and higher ratio (100-20000) conjugation curve (right). The two curves correspond to the 1.0% agarose gel results.

These results are quite intriguing as the two adsorption binding constants differ in two orders of magnitude, making the formation of the supposed second layer quite difficult relatively to the first layer. The electrostatic attraction between the second outer layer of proteins should be weaker than the first inner layer proteins, hence the necessity of higher protein concentrations to force the adsorption equilibrium to shift towards a two-layered bioconjugate. Since the overall global net charge of the proteins are negative, at around pH 7, having only a small portion of positive residues (14.3% for Fib and 16.6% for BSA) to interact with the negative surface of the nanoparticle, the second layer of proteins should have none or minimal contact with the surface of the particle. This would explain the reason for such a low binding affinity and could be improved if the protein and the surface of the particle were of opposite global charges.

4.5.2.2 Dynamic Light Scattering and Nanoparticle Tracking Analysis

To study the multi-band phenomenon observed in AGE for AuNP-MUA-Fib conjugates with low Fib to AuNP ratios, DLS and NTA techniques were applied in trying to characterize these bionanoconjugate. Results are presented in Figure 4.45. The DLS results show a clear increase in the size of the bionanoconjugates for increasing Fib to AuNP ratios in the range of 1:1 to 10:1, from 35.2 ± 0.5 nm to 76.1 ± 0.4 nm, respectively, while the NTA mean results have increasing size values, as Fib concentration increases, from 113.1 ± 3.2 nm to 140.5 ± 10.6 nm, with the exception of the sample with a 3:1 ratio, that doesn´t seem to follow this trend. Nevertheless, the NTA highest results do follow the diameter increasing trend (Figure 4.45).

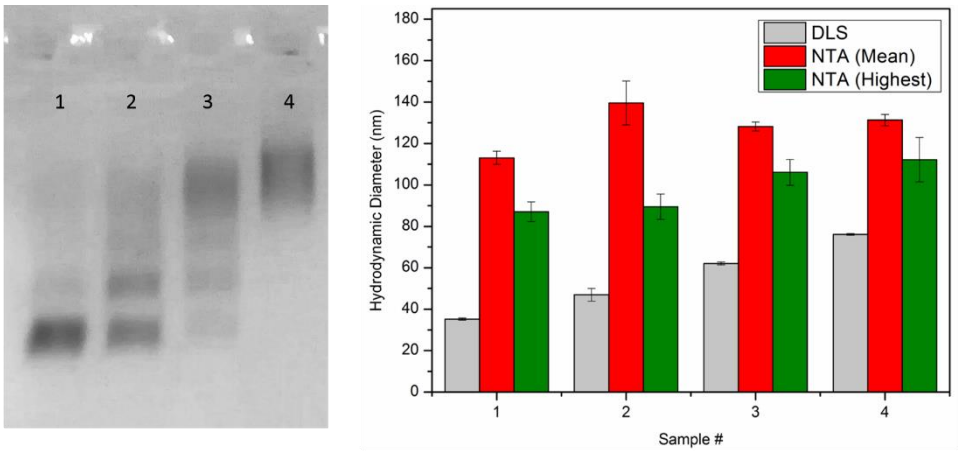

Figure 4.45. AGE results, of a 10 min run at 150V, of the tested samples (Left), Bar chart of the size distribution by DLS (Mean) and NTA (Mean and Highest Concentrated) results (Right).

Table 4.13. Summary of the previous DLS and NTA results.

Sample #	Initial Diameter (nm)	[Fib]/[AuNP]	DLS Results	NTA Results	
			Z-Average (nm)	Average (nm)	SD (nm)
1	15	1	35.2 ± 0.5	113.1 ± 3.2	62.8 ± 4.0
2	15	3	47.0 ± 3.1	140.5 ± 10.6	110.5 ± 12.4
3	15	5	62.1 ± 0.7	128.3 ± 2.2	55.8 ± 3.3
4	15	10	76.1 ± 0.4	131.1 ± 2.8	66.5 ± 5.8

Comparing the NTA mean and highest concentrated size values, in Table 4.13, there is an indication that size distributions vary across a large range of values. This is confirmed when checking the NTA size distributions for each sample individually as seen in Figure 4.46. Two simultaneous effects are verified as Fib concentration increases:

i. the increase in the average size, as the formation of a protein outer layer increases the bioconjugate diameter.

ii. decrease in the concentration of larger sized populations, being prominent in the sample #2, probably due to the initial low abundance in Fib molecules available to interact with AuNPs, that leads to multiple interactions of a small number of Fib molecules with many available AuNPs, making large bioconjugated structures. As Fib concentration and availability increases, every AuNP should be successfully conjugated, reducing the possibility of the large AuNP-Fib-AuNP nanostructures.

Another possible explanation is the presence of contaminating agglomerated Fib complexes or induced AuNP aggregation due to incomplete conjugation or other experimental issues from the sample transportation, which accounted for a longer period (> 48 hours) than the tested conjugation procedures. Longer conjugation times often resulted in unwanted sample effects like aggregation.

Further testing is required to address the cause of these larger structures of sizes above 150 nm and check the effect at larger particles, such as the 40 nm AuNPs. However, the available data allows to confirm that the size increase, of the highest concentration sample population, might correlate to the formation of the Protein corona by Fib molecules at the surface of AuNPs.

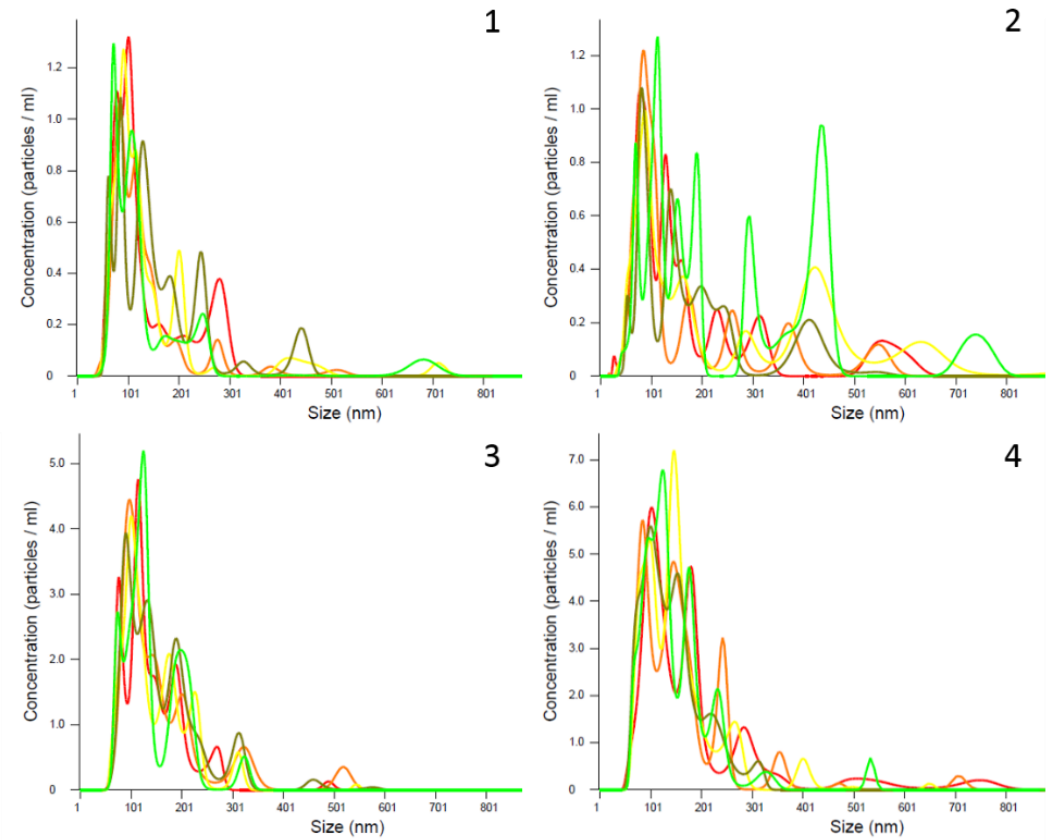

Figure 4.46. Nanoparticle Tracking Analysis results, tested five times for each sample (1-4), showing size distributions.

As for the result discrepancy between the two light dispersion techniques, it can be appointed to the DLS limited capacity at evaluating polydisperse samples and NTA limitations at obtaining meaningful data for nanoparticles with diameters smaller than 40 nm. Also, the presence of particles above 400 nm in diameter, in both techniques, might be due to AuNP aggregation or Fib agglomeration. Due to these experimental problems, the study of multi-band effect with Light scattering methods was inconclusive and require further testing or alternative methods.

Another set of experiments, using the Light scattering methods, were performed on 40 nm AuNPs to test the bioconjugation with Fib. A summary of the DLS and NTA results is shown in Appendix IV. Analyzing the DLS results in Figure 4.47, by both Intensity and Number distributions mean values, an increasing diameter is visible with increasing Fib concentration. Similarly, to the AGE results that showed two conjugation curves, these results also show a fast increase in diameter for the conjugation ratios between 0 and 1000:1, and second slower increase in diameter after the 5000:1 conjugation ratio. In this particular experiment the ratio of 30000:1 was added to extend the range of the AGE results, and shows an increased diameter compared to the 20000:1 ratio. This effect can also be attributed to sample aggregation.

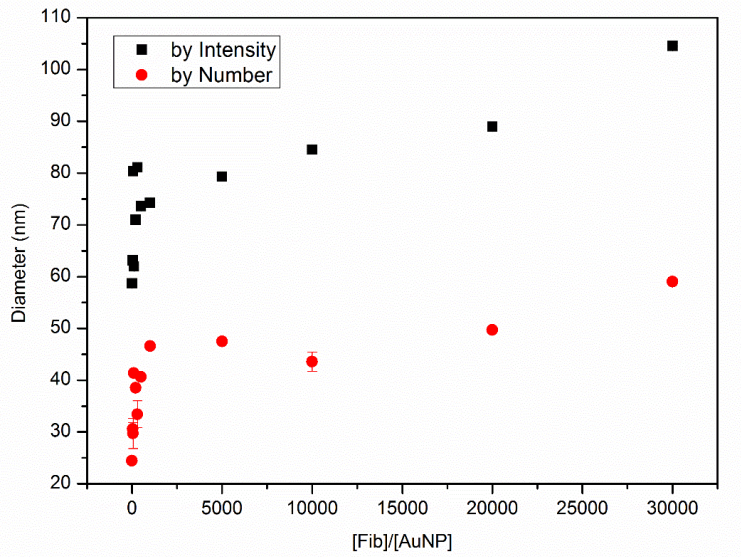

Figure 4.47. DLS results for the 40 nm AuNP bioconjugation with Fib with values of the mean Diameters.

The data obtained by NTA revealed high polydispersity, that showed a high standard error and standard deviation (SD) in some samples (40:1, 60:1, 100:1, 30000;1) which might be caused by the aggregation of the AuNPs and agglomeration of Fib molecules as was discussed in the previous NTA results. As for the NTA mean diameter, with acceptable error margins, the same behavior of increasing diameter with Fib concentration is verified as shown in Figure 4.48,

although no distinction of two different conjugation curves is visible. The NTA size distributions can be observed in Appendix IV.

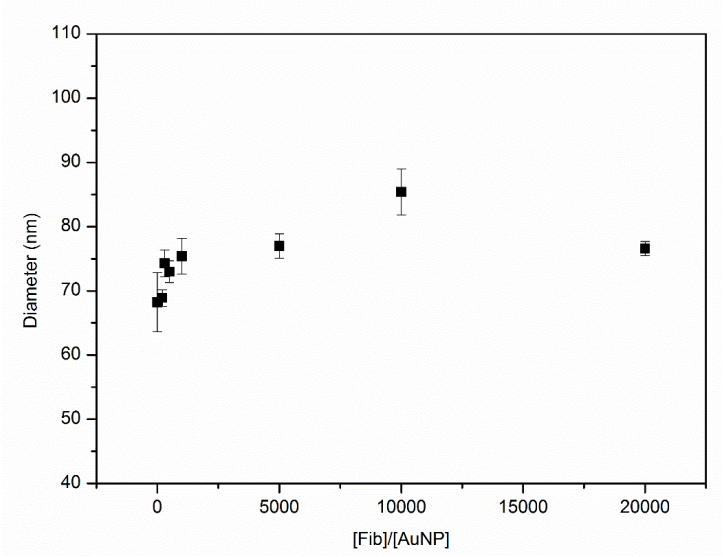

Figure 4.48. NTA results for the 40 nm AuNP bioconjugation with Fib with values of the mean Diameters. The ratios of 40, 60, 100 and 30000 were ignored due to high errors and deviations.

4.5.2.3 Electrophoretic Light Scattering

The protein corona formation by Fib on 15 nm AuNPs was also studied by the variation of the surface electrokinetic potential, or Zeta-Potential, as Fib concentration increases, by Electrophoretic Light Scattering (ELS). In Figure 4.49, the AGE results for the studied samples show the respective band migration due to a decrease of negative surface charge, and to some extent due to an increase of size, and then analyzed by ELS to determine the correspondent Zeta-Potential. The ratios at 0 and 1.5 have offsetting results, showing near neutral surface potentials when the Fib concentrations are null or low, which are impossible since the MUA functionalized AuNPs should have negatively charged surfaces. The ratios from 1 to 5 show a decrease in the negative values of Zeta-Potential, as expected since the adsorption of Fib molecules at the AuNP surface should decrease the global negative net charge. However, from the ratios 6 to 10 the Zeta-Potential decreases to values expected of non-conjugated samples. These are conflicting results, since the surface charge should stabilize at a certain conjugation ratio, and as such should be repeated with new samples in order to confirm this effect. Another possibility is that the cuvettes were reused and had damaged electrodes.

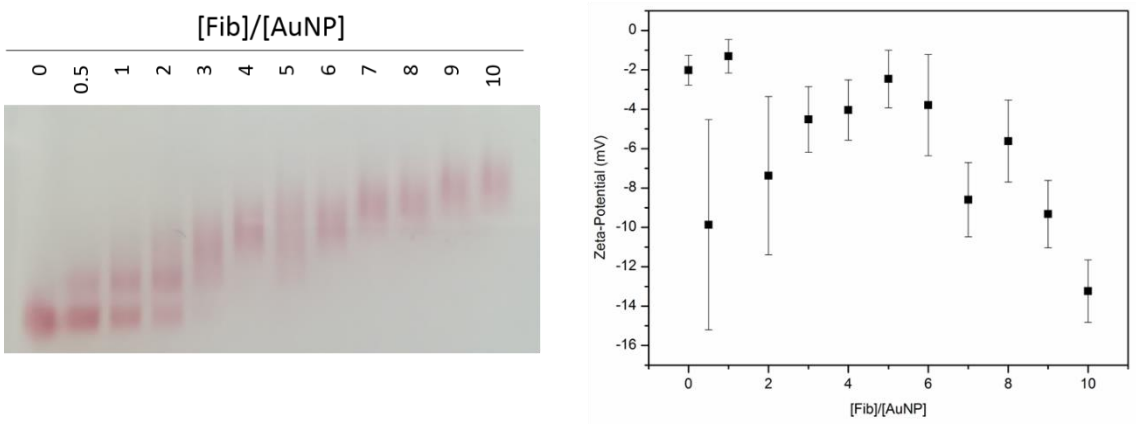

Figure 4.49. AGE (left) and ELS (right) results of bionanoconjugated samples with increasing [Fib]/[AuNP] ratios.

Better results were obtained for the bioconjugation of Fib with 40 nm AuNPs, as the Zeta-Potential increase, to more positive values, depicts a behavior similar to a bioconjugation curve, as seen in Figure 4.50. Surprisingly the non-conjugated sample has a value of -27.3 mV which can be compared to the values in the Fergusson analysis, as AuNPs of varying sizes share a Zeta-Potential value of around -24 mV.

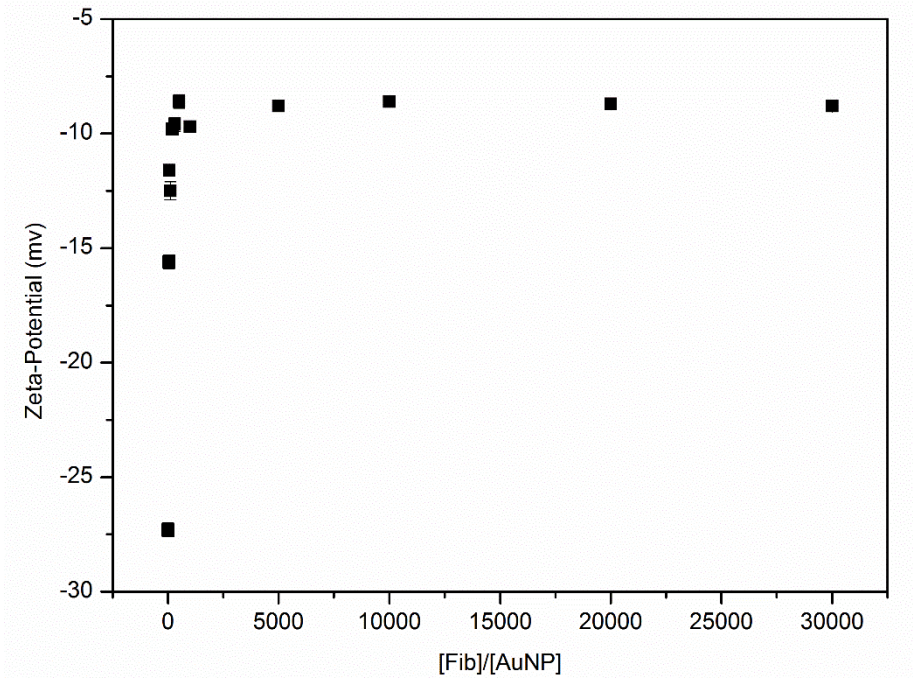

Figure 4.50. Zeta-Potential values, obtained by ELS, of the bioconjugated samples of 40 nm AuNPs with Fib.

4.5.3 BSA and Fib conjugation competition

Acknowledging the differences of BSA and Fib proteins in terms of size, shape and adsorption to the surface of AuNPs, competition between different proteins is inevitable in a mixture of two or more proteins or in a complex mixture such as plasma. This phenomenon occurs *in vivo* leading to different proteins to adsorb on a surface over time, which is denominated the Vroman effect, previously discussed on chapter 1.1.2.

Two different ways of testing this effect were applied, one by pre-incubating the nanoparticles with one protein, afterwards the sample is centrifuged and resuspended in buffer, followed by addition of a solution of another protein. The second method was by simply applying a mixture of both proteins, at a concentration that would cause a full surface conjugation, as previously determined, namely, 400:1 of Fib/AuNP and 1000:1 of BSA/AuNP

Firstly, MUA-AuNPs were tested due to the electrostatic interactions between surface and proteins. In Figure 4.51, as previously stated, different migration profiles are observed for non-conjugated (Lane 1) and BSA (Lane 2) and Fib (Figure 4.51Lane 3) conjugated samples. To test the competitive behavior of each protein, three different scenarios were tested, either the protein substitution of BSA by Fib (Lane 4), or the substitution of Fib by BSA (Lane 5) and a mixture of both proteins (Lane 6).

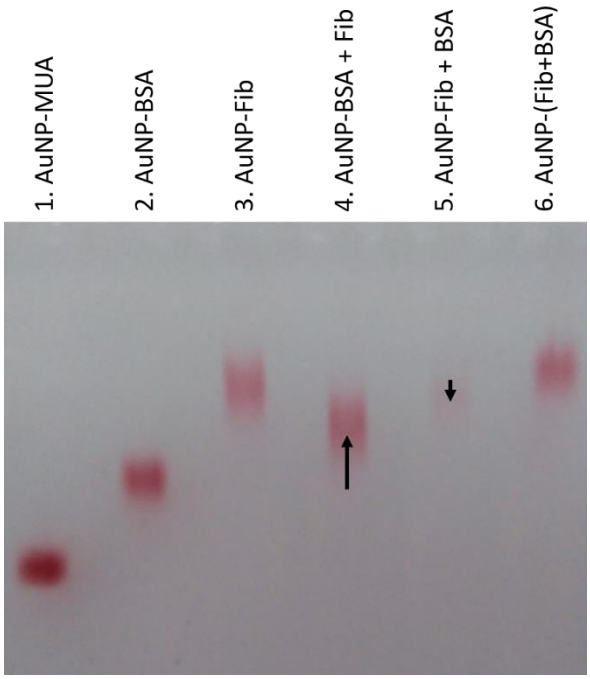

Figure 4.51. Agarose gel electrophoresis results of MUA-AuNP samples conjugated with BSA and Fib in various orders. Arrows indicate band migration variation relative to the correspondent conjugation with the first introduced protein.

As seen in Figure 4.51 and Table 4.15, BSA is clearly substituted by Fib as the band migration shifts towards the AuNP-Fib migration. Meanwhile, Fib seems to be substituted by BSA, although

this type of test leads to sample partial aggregation, resulting in a less visible band. The main doubt in these results is focused on quantifying the protein substitution by band migration variation, where visually Fib seems to be less prone to substitution than BSA.

In the case of a protein mixture, band migration maintains at the same value as the AuNP-Fib conjugation, indicating that in a mixture of both proteins, if incubation time is enough (>2hours), the protein corona will be mainly composed of fibrinogen. This correlates to the higher K_{ad}, for the 15 nm MUA functionalized AuNPs, of the Fib conjugation ($34.3 \times 10^{-2} \pm 1.2$) relative to the BSA conjugation ($1.5 \times 10^{-2} \pm 0.1$). However, when comparing the Electrophoretic Mobility data in Table 4.15, a migration difference between band 3, AuNP-Fib, and 6, AuNP-(Fib+BSA),is verified, showing a decrease in mobility in the protein mixture, suggesting perhaps a better surface coverage by having the two proteins competing, simultaneously, for the available space at the surface, always favoring the Fib conjugation but, at the same time, possibly filling surface gaps by BSA.

Table 4.14. Electrophoretic Mobility results from the Fib and BSA conjugation competition study for MUA functionalized AuNPs.

#	Sample	Electrophoretic Mobility ($\times 10^{-4}$ cm^2 V^{-1} s^{-1})
1	AuNP	1.9 ± 0.1
2	AuNP-BSA	1.4 ± 0.1
3	AuNP-Fib	0.9 ± 0.1
4	AuNP-BSA + Fib	1.1 ± 0.1
5	AuNP-Fib + BSA	0.9 ± 0.1
6	AuNP-(BSA+Fib)	0.8 ± 0.1

Considering that having a surface mediator as MUA affects the protein substitution due to the absorption being electrostatic-based, by physisorption, non-functionalized nanoparticles were tested (AuNP-Citrate) to analyze protein substitution on stronger interactive surface chemistries, by chemisorption, due to the interaction of sulfur, from the available Cysteine residues of both proteins, with the Gold surface, mimicking the S-Au interaction between the gold surface and the thiol capping agents like MUA, and replacing the stabilizing citrate molecules. The results can be observed in Figure 4.52 and Table 4.16.

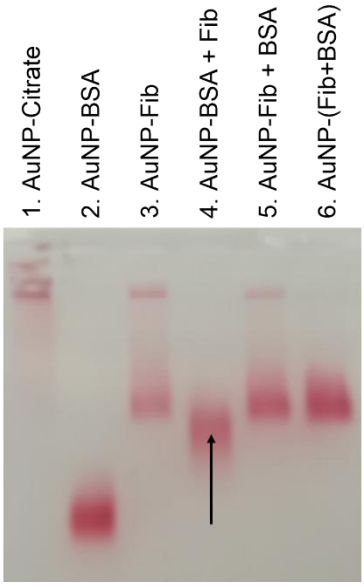

Figure 4.52. Agarose gel electrophoresis results of Citrate-AuNP samples conjugated with BSA and Fib in various orders. Arrow indicates band migration variation relative to the correspondent conjugation with the first introduced protein.

One major visual difference is observed which is the non-conjugated sample band migration, which in this case remains in the gel well, this is due to the possible interaction of citrate with the gel as previously studied in the functionalization chapter. In terms of protein substitution, as previously observed on the MUA-AuNPs, BSA seems to be partially substituted by Fib, but in this case, Fib seems to be less prone to substitution by BSA, with AuNP-Fib bionanoconjugates maintaining approximately the same band migration distance, after incubation with BSA.

Table 4.15. Electrophoretic Mobility results from the Fib and BSA conjugation competition study for non-functionalized AuNPs.

#	Sample	Electrophoretic Mobility ($x\ 10^{-4}\ cm^2\ V^{-1}\ s^{-1}$)
1	AuNP	0
2	AuNP-BSA	1.3 ± 0.1
3	AuNP-Fib	0.8 ± 0.1
4	AuNP-BSA + Fib	0.9 ± 0.1
5	AuNP-Fib + BSA	0.8 ± 0.1
6	AuNP-(BSA+Fib)	0.8 ± 0.1

The stronger interaction of Fib to the nanoparticle surface would be possible due to the amount of Cysteine residues available to create contact points all around the nanoparticle, which according to the Vroman effect, would make any attempts of BSA substitution harder than the previous electrostatic surface interactions. According to literature, BSA protein has 34 disulfide linked cysteines and one non-linked cysteine (Cys-34) [88], which is responsible for the

dimerization process of aged BSA molecules, while the Fib protein has all 58 cysteine residues disulfide linked to prevent dimerization with other Fib molecules. [89]

Analyzing Figure 4.53, the PDB files of BSA and Fib, 3GHG (human) and 3V03 (bovine) respectively, for amino acid solvent accessibility. The solvent accessibility calculations estimate that all Cysteine residues for both proteins are core amino acids, or of low solvent accessibility. These results suggest that, for Cysteine residues to interact with the gold surface on the AuNP, protein structure denaturation would have to occur in order to expose these residues. It should be noted that all cysteine residues are accounted for in the BSA PDB file while the Fib PDB file only 49 out of the 58 cysteine residues are represented.

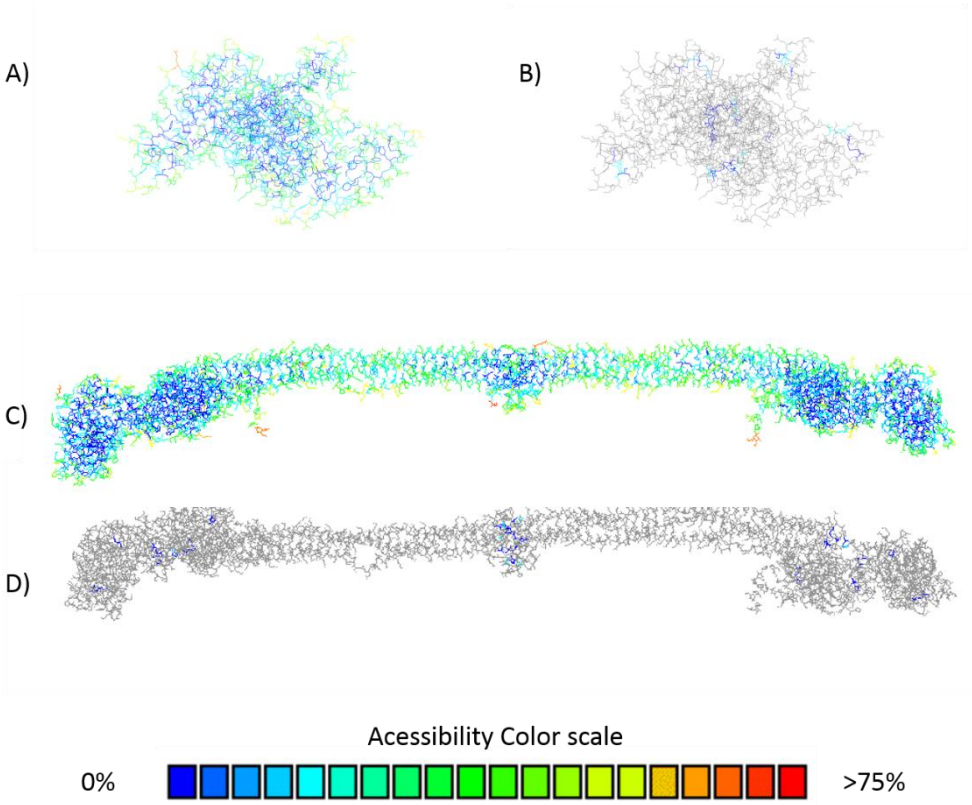

Figure 4.53. Solvent accessibility of amino acids. Accessibility color scale relative to maximum accessibility possible in the extended pentapeptide GGXGG environment. All amino acid (A and C) and Cysteine-only coloration (B and D) are represented. The structures on top (A and B) derive from the BSA PDB file (3V03) and the structures on the bottom (C and D) derive from the Fib PDB file (3GHG).

The interaction should be mostly electrostatic, as in the MUA functionalized samples, and the free thiol on BSA has no appreciable effect on the competitive scenario. However, if the disulfide bounds are exposed, leading to a Gold-Disulfide interaction, an increased adsorption strength of Fib relative to BSA is observed.

In a previous study [90], the dissociation of disulfide with the formation of strongly bound Au-S is favored. This would give Fib further advantages over BSA in adsorption to non-functionalized

AuNPs, due to the increased size, higher electrostatic attraction, and increased number of available cysteines, formed from the dissociation of disulfides, readily to interact strongly with the gold surface. This however, would compromise the structural integrity of the adsorbed proteins.

Another visible effect in the non-functionalized AuNPs is the induced aggregation of the conjugation with Fib. All initially conjugated samples with Fib display a band in the application well, indicating that part of the sample was either incompletely conjugated or that the conformation of adsorbed Fib exposes part of the AuNP surface leading to aggregation. This is not verified on the mixture of BSA an Fib possibly due to an optimal surface coverage by the two proteins, which is also verified in the BSA substituted by Fib sample. Comparing to the MUA functionalized AuNPs, the aggregation caused by a possible incomplete coverage by Fib might be mitigated due to the presence of the intermediate MUA layer that stabilizes the adsorption gaps, avoiding aggregation of samples as verified in the non-functionalized cases.

The hypothesis of Fib not totally covering the gold surface might be attributed to protein size relative to the AuNP. This protein, rod-shaped with reported lengths of 46 x 4 nm, when associating to the surface of a 15 nm AuNP, will require high degrees of flexibility to fully adsorb to the available surface area. [91] These high degrees of flexibility have been reported in previous studies [92] to denature the protein, on particles smaller than 30 nm, losing up to 12% of the helical structure and exposing hydrophobic regions to the solvent, turning into an aggregation inducer for the AuNP surface.

4.6 Fergusson Plot Analysis

Further zeta-potential data for the bionanoconjugates can be obtained from AGE by varying the agarose gel concentration (%w/v) as seen in Figure 4.54. In fact, electrophoretic mobility varies depending on gel concentration and sample characteristics.

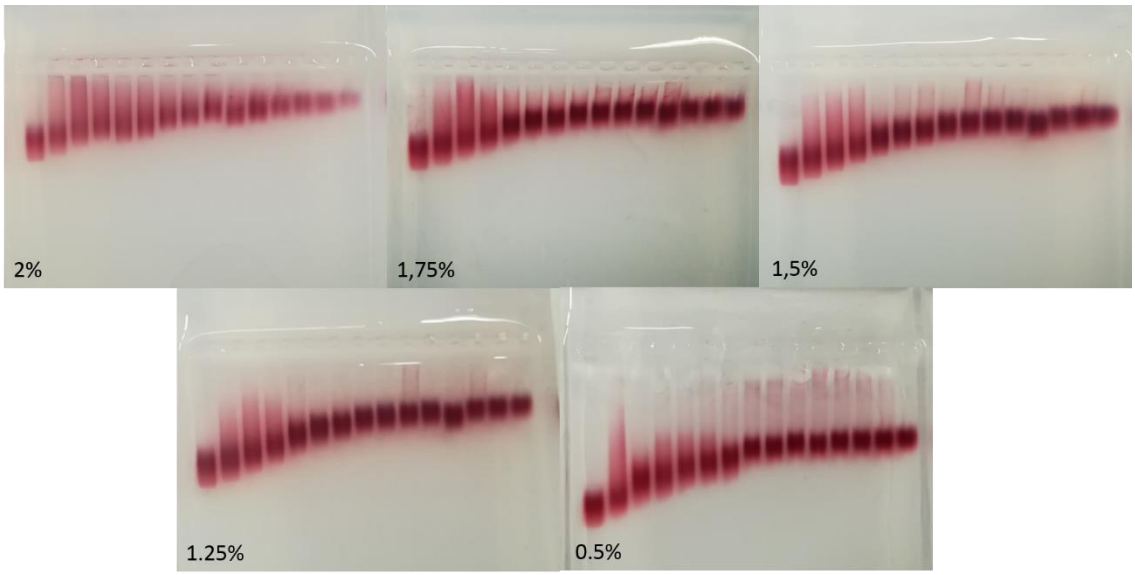

Figure 4.54. AGE results for BSA conjugation of AuNP-MUA samples at a concentration ratio range between 0 and 2000. Agarose Gel concentrations variated between 0.5% and 2.0%.

Values like zeta-potential and hydrodynamic size can be estimated as reported in the literature, by applying the Fergusson Plot Analysis. This method provides a sample size and surface charge relationship to band electrophoretic mobility in varying gel concentrations. [44] However, this study in particular was only tested for AuNP size ranges between 4-20 nm in diameter, while many samples, in this work, had sizes outside that range.

To apply this type of Ferguson analysis, all migration distances must be firstly converted to electrophoretic mobility (M) and logarithmized ($Log_{10}M$). Plotting $Log_{10}M$ vs. gel concentration (T), as seen in Equation 4.4, and linear fitting estimates two key parameters, logarithm of the free mobility (M_0) where the gel concentration is 0%, and the retardation coefficient (K_R).

$$\mathrm{Log_{10}M} = \mathrm{Log_{10}M_0} - \mathrm{K_R T}$$

Equation 4.4

Free mobility (M_0) gives information about sample migration in the absence of a gel. Without the migration hindrance of a gelatinous medium, any sample, regardless of size and shape, should be able to migrate in an electrophoretic run based only on the surface charge. From Figure 4.55, a $Log_{10}M$ vs. gel concentration plot is applied to multiple samples of AuNP-MUA conjugated to increasing ratios of [BSA]/[AuNP].

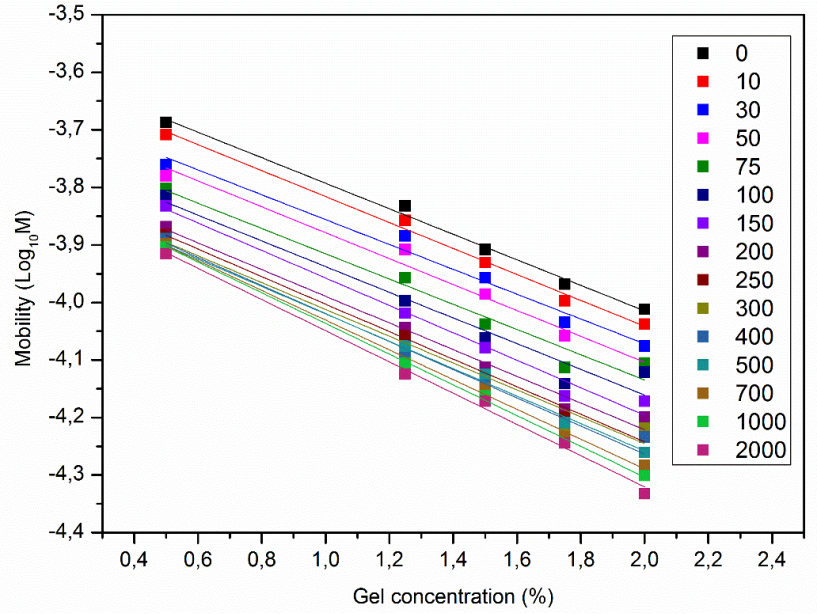

Figure 4.55. Fergusson plot analysis of multiple samples of AuNP-MUA conjugated to increasing ratios of [BSA]/[AuNP] ranging from 0 to 2000:1.

The linear equation fitting is applied to obtain the K_R and M_0 parameters as seen before in Equation 4.4. An increase in K_R, the equation slope, is observed as BSA conjugation increases from the resulting bionanoconjugate size (Appendix III). An increase in the $Log_{10}M_0$, the equation interception, suggests a decrease in free mobility as BSA concentration increases, indicating a loss of negative surface charge or, in other words, a more neutral Zeta-Potential.

From the previous results, M_0 is obtained for each sample and, by using Equation 4.5, Zeta-Potential (ζ-Potential) can be estimated.

$$M_0 = \frac{\varepsilon\zeta}{\eta} f(kR)$$

Equation 4.5

Assuming that $f(kR)$ is 1.5 for polar media (Smoluchowski approximation), and permittivity (ε) and the viscosity (η) are proximate of the water values since the buffer is highly diluted (1/8x TAE). Zeta-potential data can be represented in function of [BSA]/[AuNP] ratios, leading to a Langmuir-like conjugation curve representation (Figure 4.56).

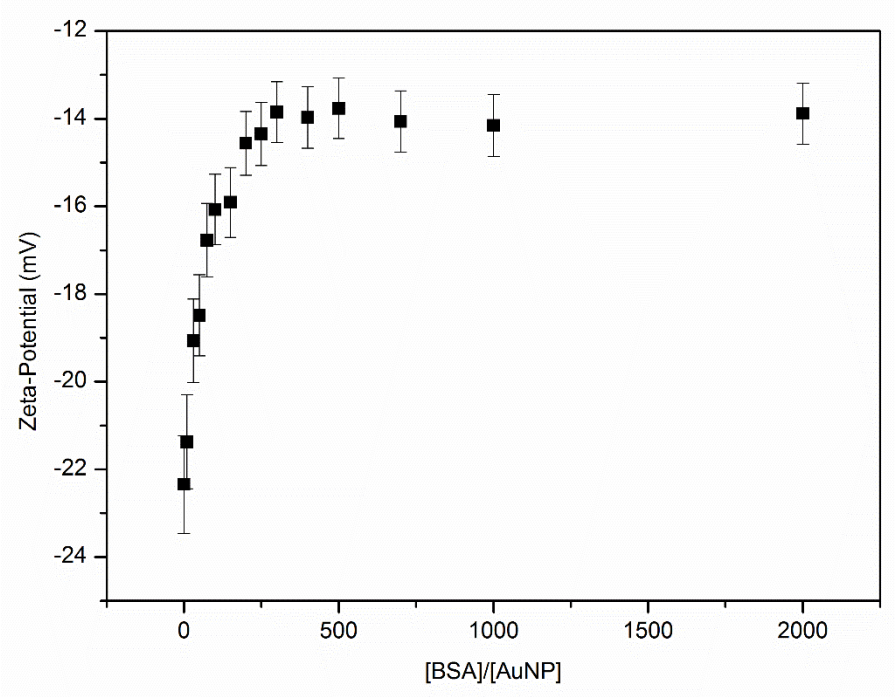

Figure 4.56. Estimated Zeta-Potential values for different molar ratios for BSA conjugation of AuNP-MUA samples.

Although the experimental Zeta-Potential values differ from the available literature [93, 94, 95] the curve depicts a decrease of negative global charge (increase of positive charge), corresponding to the charge neutralization by the less negative (or more positive) protein residues available at the surface of the bionanoconjugate. The Zeta-Potential values obtained by the Fergusson Plot Analysis should be used merely as a comparison tool between different protein conjugations, like the BSA and Fib presented in this work, relative to the respective non-conjugated samples in the same experimental conditions. Light dispersion techniques are more accurate and could be used to test the validity of the estimated results by the Fergusson plot analysis. Zeta-Potential values are in a previously discussed ± 30 mV colloid instability range, where repulsive forces are superseded by the attractive forces, without triggering an aggregation reaction. This is mainly due to the functionalization layer and protein corona providing aggregation resistance by steric effects.

The retardation coefficient (K_R), corresponds to the slowing effect on sample migration as gel concentration increases and therefore the gel pore radius diminishes. Sample hydrodynamic size affects the respective diffusion on a media. Two different sized samples will be affected by a gel concentration increase differently and this is observed on different sized AuNPs (e.g. Non-conjugated AuNP vs. Fully conjugated AuNP). If the surface charge is similar regardless of particle size, by maintaining the same type of synthesis, functionalization and other conditions, different band migrations are influenced only by the size and gel concentration.

Based on the Equation 4.6, l and r are the gel fiber length per unit mass and radius, respectively which are intrinsic properties of the gel, Equation 4.7 can be derived where A' and B are constants. The effective hydrodynamic diameter is represented by D_{eff}.

$$\sqrt{K_R} = A\left(\sqrt{\pi l}\frac{D_{eff}}{2} + \sqrt{\pi l}r\right)$$

Equation 4.6

$$\sqrt{K_R} = A'\left(\frac{D_{eff}}{2}\right) + B$$

Equation 4.7

From this new equation, a $\sqrt{K_R}$ vs. Hydrodynamic radius (D_{eff} / 2) linear fitting will construct a possible calibration curve, where sample size can be estimated based on the retardation coefficient depending on the gel concentration. Also, K_R values will be higher for larger sized AuNPs as these are affected at a higher extend to an increase in gel concentration, as stated before.

The constants A' and B however, need to be determined in order to obtain the desired D_{eff} value. This is obtained by constructing a size calibration curve, using AuNP samples with specific sizes. Since the previous experiment with BSA conjugation has no size calibration, the estimated bionanoconjugate size is impossible to obtain.

To overcome this problem, a new Fergusson plot analysis was performed combining the bionanoconjugated samples and the size standards, in a range of 15-39 nm in diameter. Figure 4.57 exhibits the AGE results for different AuNP-MUA sizes, used for the size calibration curve, and samples of fully conjugated AuNP-MUA with BSA and Fib at increasing gel concentrations.

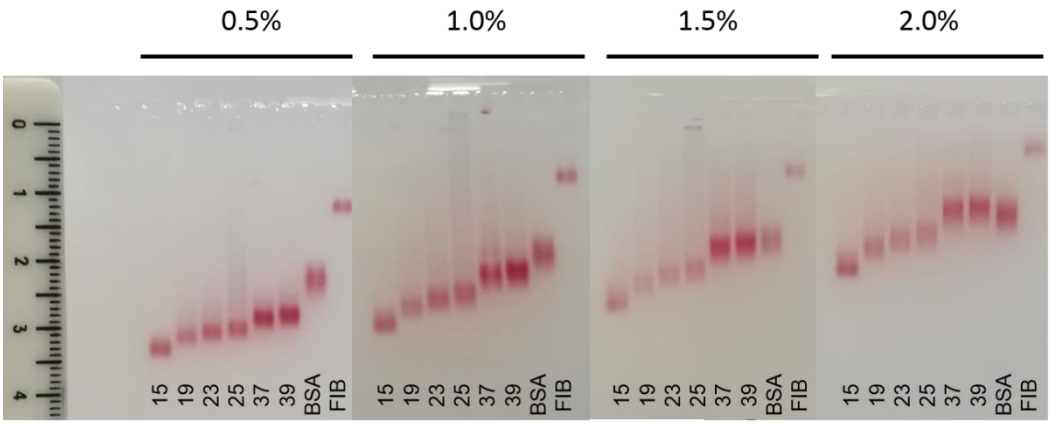

Figure 4.57. Agarose gel electrophoresis results of different sized (15-39 nm) AuNP-MUA and fully conjugated 15 nm AuNP samples with BSA and Fib at different gel concentrations (0.5-2.0%).

The major difference, of band migration for every sample in all gel results, is the BSA-conjugated sample migration distance to the 37 nm and 39nm AuNP-MUA samples. At lower gel concentrations (e.g. 0.5%), the BSA-conjugated sample migrates less than any other AuNP-MUA, of any size, being almost a $^1/_2$ centimeter apart from the 37 nm and 39 nm sized AuNP-MUA samples. However, when increasing the gel concentration, all bands obviously migrate less, but at the 2.0% gel concentration, the distance between the 37 nm and 39 nm AuNP-MUA samples and the BSA-conjugated sample is almost zero. This is due to the higher retardation effect, as gel concentration increases, of larger sized particles, suggesting that AuNPs, fully conjugated with BSA, have possibly a smaller hydrodynamic size than 37-39 nm. Plotting the logarithmized Electrophoretic mobilities ($Log_{10}M$) of the AGE results vs. Gel concentration (T) allows a better interpretation of the size related effects.

From the Figure 4.58, the slope is a direct indicator of the K_R value of each sample. As AuNP-MUA sizes increase, the slope increases, and when superimposed with the conjugated samples, the slope for the BSA conjugated sample it is similar to the 23-25 nm samples, while for the Fib conjugated sample, the slope is higher than any other AuNP-MUA size, giving a possible hint of a size surpassing the 39 nm. As for the interception, it correlates to the free electrophoretic migration (M_0), confirming that conjugated samples have less negative Zeta-Potential values, in particular the Fib conjugation.

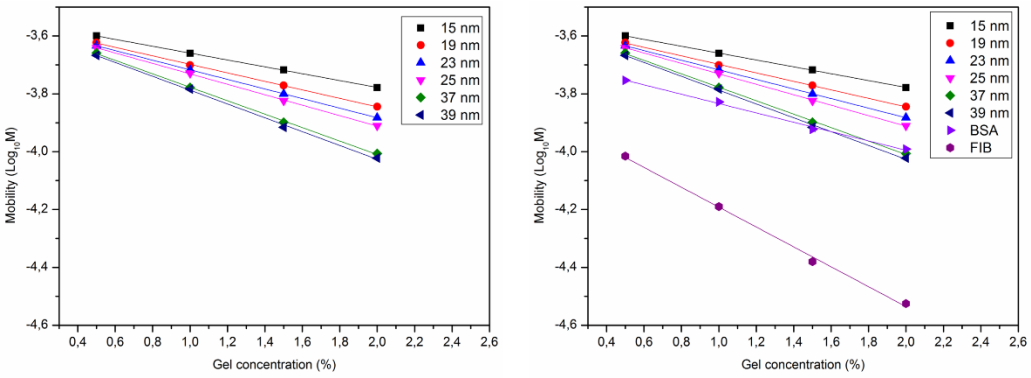

Figure 4.58. Fergusson plot analysis of AGE results. Multiple sized samples of AuNP-MUA (left) and comparison with fully conjugated 15 nm AuNP-MUA with Fib and BSA (right).

From the Fergusson plots in Figure 4.58, the values for $Log_{10}M_0$ and K_R were estimated and are presented in Table 4.16 4.17.

Table 4.16. Results from the Fergusson plot analysis. The 15-39 nm AuNPs used for the size calibration in blue, and the fully conjugated with BSA and Fib samples in green.

	$Log_{10}M_0$	K_R
15 nm	-3.540 ± 0.001	0.119 ± 0.001
19 nm	-3.551 ± 0.003	0.147 ± 0.002
23 nm	-3.551 ± 0.001	0.166 ± 0.001
25 nm	-3.550 ± 0.003	0.181 ± 0.002
37 nm	-3.544 ± 0.006	0.232 ± 0.004
39 nm	-3.548 ± 0.009	0.239 ± 0.007
BSA	-3.672 ± 0.010	0.161 ± 0.007
Fib	-3.848 ± 0.018	0.344 ± 0.013

It was estimated the size for the conjugated samples, from the size calibration curve in Figure 4.59 that provides the values for the *A'* and *B* constants of Equation 4.7, converting correspondent K_R values into Hydrodynamic radius ($D_{eff}/2$), and sequentially the Effective Diameter (D_{eff}).

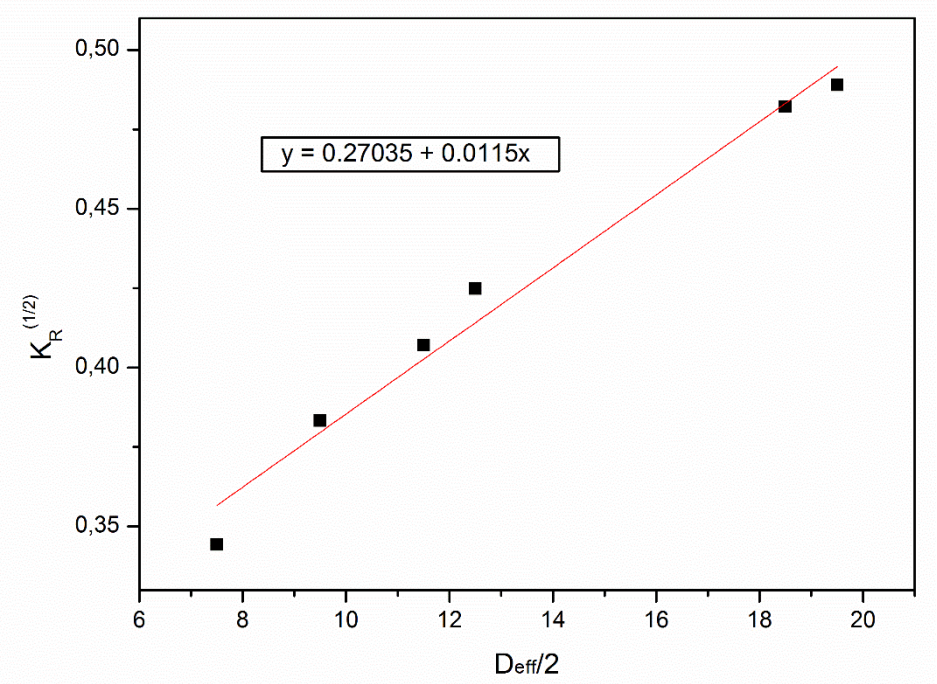

Figure 4.59. Size determination calibration equation derived from the Fergusson Plot Analysis

From the previous determined equation and the K_R values in Table 4.18, diameters of 22.5 nm for BSA-AuNP and 52.5 nm for Fib-AuNP were estimated. Since the retardation coefficient of Fib conjugated samples is higher than the size calibration curve range, any attempts on estimating sizes of that magnitude is prone to error.

Table 4.17. Diameter estimation of conjugated samples of 15nm AuNP-MUA with BSA and Fib.

Sample	K_R	Radius ($D_{eff}/2$)	Diameter (D_{eff})
BSA conjugation	0.40	11.25 nm	22.50 nm
Fib conjugation	0.58	26.25 nm	52.50 nm

Another possible issue of calculating sizes of bionanoconjugates is the fact that a nanoparticle of 22.5 nm migrates in the gel as a 22.5 nm bionanoconjugate. Obviously the bionanoconjugate will have more flexibility due to the outer layer being composed of proteins while the core is metallic, meanwhile a 22.5nm nanoparticle is, ignoring the surface functionalization, a full metallic particle which confer less flexibility while traversing a porous media.

With all the previously stated data, in the Fergusson Plot Analysis, the hydrodynamic diameter estimations point an increase of around 7.5 nm and 37.5 nm for BSA and Fib conjugation of 15nm AuNPs. Checking referenced dimensions, BSA is evaluated as a 7.5 x 6.5 x 4.0 nm protein and Fib as a 46 x 3 x 6 nm protein. [96]

Assuming as a sphere BSA of an average of 6 nm in diameter, the conjugation final diameter would increase to a maximum of 27 nm as seen in Figure 4.60. However, to get an increase of only 7.5 nm, each BSA would contribute 3.75 nm to the resulting total diameter. According to referenced values [96], BSA and HSA conjugation on various types of nanoparticles increased diameters by 4-10 nm (2-5 nm in radius).

From this study and other references, acknowledging the error associated with hydrodynamic size estimation, size increases suggest a surface adsorption of BSA as demonstrated in Figure 4.60, where upon adsorption a more compact conformation is present, allowing more contact points to the surface and stronger interactions.

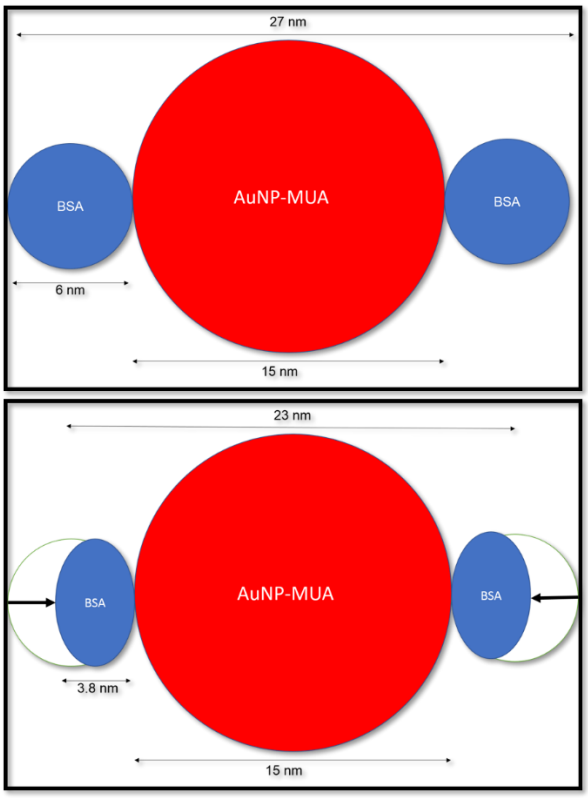

Figure 4.60. Ball depiction of AuNP-MUA and BSA conjugation.

As for Fib, a linear form must be assumed of around 46 nm. For an increase of 37.5 nm in diameter for the conjugate various theories and models can be executed to explain the possibility of this phenomenon. Assuming that at physiological conditions, Fib is in a semi-collapsed formation as depicted in Figure 4.61, where the different charges from the overall global negative 46 nm linear fibrinogen and the positive extensions of the alpha chains could entrap a 15nm AuNP and assume a more compact conformation.

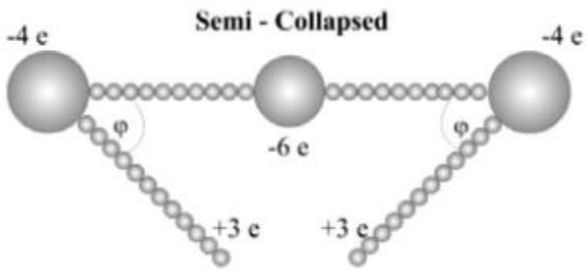

Figure 4.61. Semi-Collapsed formation of Fibrinogen at physiological conditions. The lower positive arms correspond to the extension of the alpha-chain. Adapted from [10].

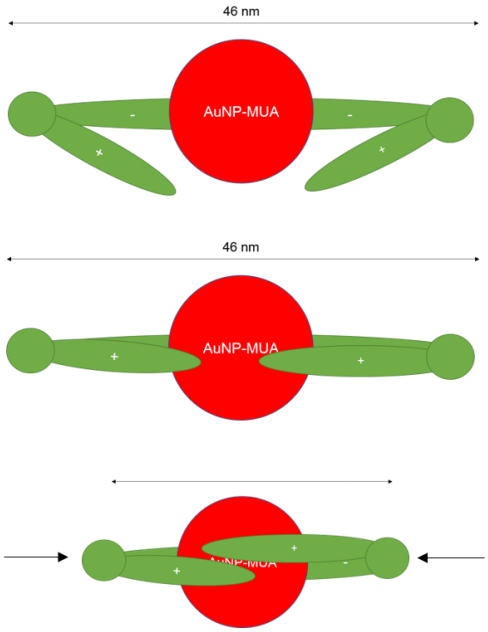

Figure 4.62. Image depiction of AuNP-MUA and Semi-collapsed Fib conjugation.

The compact conformation as seen in Figure 4.62 would assume a semi-spherical conformation but reducing the total hydrodynamic diameter, making a 52.5 nm diameter impossible. So, assuming that the size estimation is correct, this form of adsorption would not correspond to the reality.

However, if multiple AuNPs would adsorb to a single Fib a more feasible model would be applied. In Figure 4.63, although total hydrodynamic diameter remains under 50 nm due to the linearity of the bionanoconjugate, it could explain the retardation coefficient increase, misleading the of the Fergusson plot analysis results into an increase of diameter.

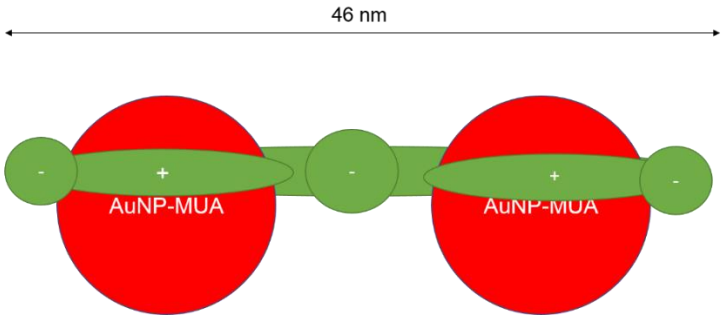

Figure 4.63. Image depiction of two AuNP-MUA and Semi-collapsed Fib conjugation.

This conformation would possibly lead to incomplete conjugation due to lack of accessibility of Fib around both nanoparticles leading to irreversible aggregation processes unless incomplete coverage would be counteracted with steric effects by Fib.

Another model is possible by allowing partial conjugation by each Fib on the globular end of Beta and Gamma chains and the extended arms of the Alpha Chain. This conformation would allow multiple Fib molecules to adsorb to the AuNP and augment the total diameter by a considerable amount as seen in Figure 4.64. The multiple Fib molecules would probably assume a more compact conformation to maximize surface adsorption.

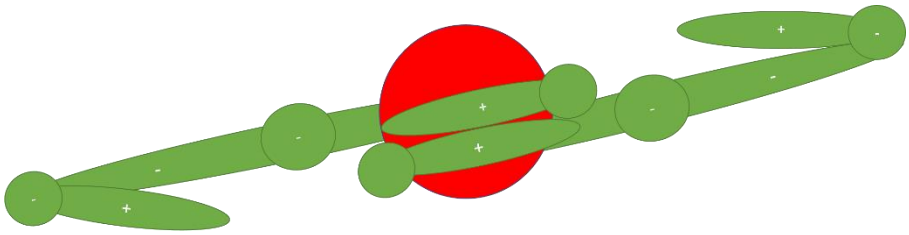

Figure 4.64. Image depiction of an AuNP-MUA and two Semi-collapsed Fib conjugation.

As for the Zeta-Potential, the bar chart in Figure 4.65 states all estimated values. All non-conjugated samples have a value of approximately -24 mV, possibly due to the type of surface functionalization with MUA, which is close to the ELS results for the non-conjugated 40 nm AuNP sample of -27.3 mV. These two different methods of obtaining the Zeta-Potential values should be futher studied to check the validity of the Fergusson Plot Analysis The conjugated samples have, as expected, a less negative Zeta-Potential, due to the absorption of less electronegative, compared to the AuNP-MUA surface, protein molecules.

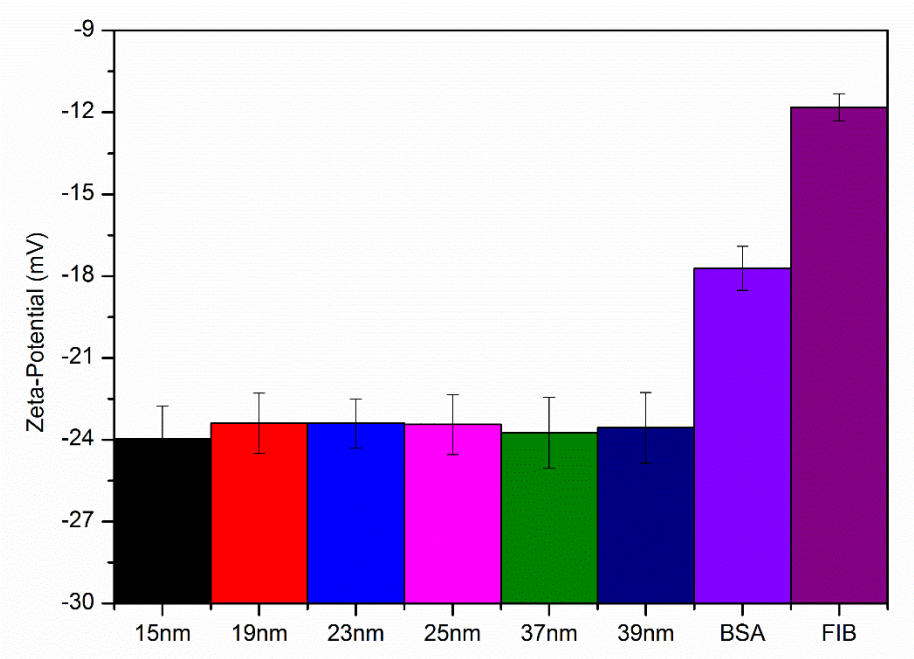

Figure 4.65. Zeta-Potential values for the different sized (15-39 nm) AuNP-MUA samples and the fully conjugated 15 nm AuNP-MUA samples (BSA and Fib).

4.7 Electrophoresis Video Analysis

The novel way of evaluating the electrophoretic behavior by extracting valuable information from recorded video results, instead of the classic final image, was tested using the second component of the eReuss software. The band intensity per area is an important parameter to optimize since the band contrast and concentration are directly related and should always be considered to check for sample saturation.

Analyzing the obtained total Intensity plot vs. time in Figure 4.66, it is possible to verify the saturation effect on the total intensity increase in the initial period, between 0 and 5 minutes, and the continuous increase in intensity after the 5-minute mark, indicating that, even with band smearing across the gel, the total intensity increased with time. To reduce this effect sample dilution must be performed. However, the right dilution has to be optimized as band contrast will be lost in subsequent dilutions, and consequently information and sensitivity to the band location, especially in the multi-band cases, will diminish.

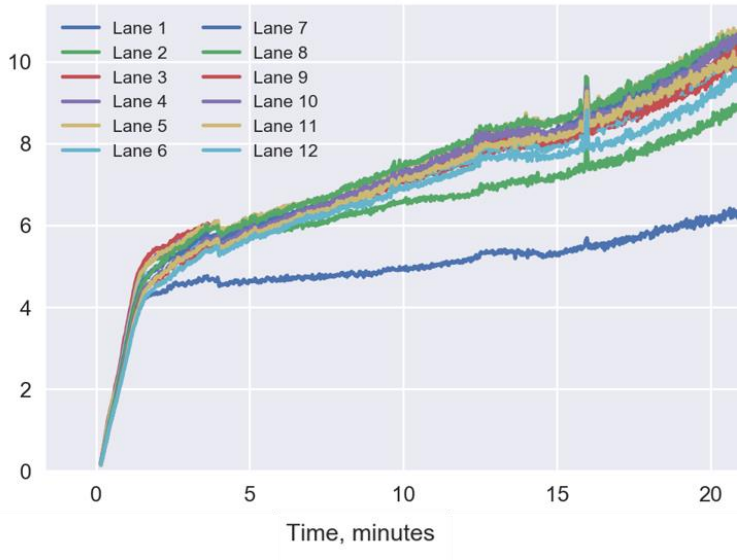

Figure 4.66. Intensity values for each Lane (1-12) along the recorded duration. Results past the 20-minute mark have been omitted due to video quality issues.

A dilution optimization step was performed, and the results are demonstrated in Figure 4.67. An experimental error is visible between 3 and 9 minutes, which was a consequence of the camera focus. Although the gap on the video analysis results, the intensity profiles seem to stabilize earlier with sequential dilutions, diminishing the saturation effect.

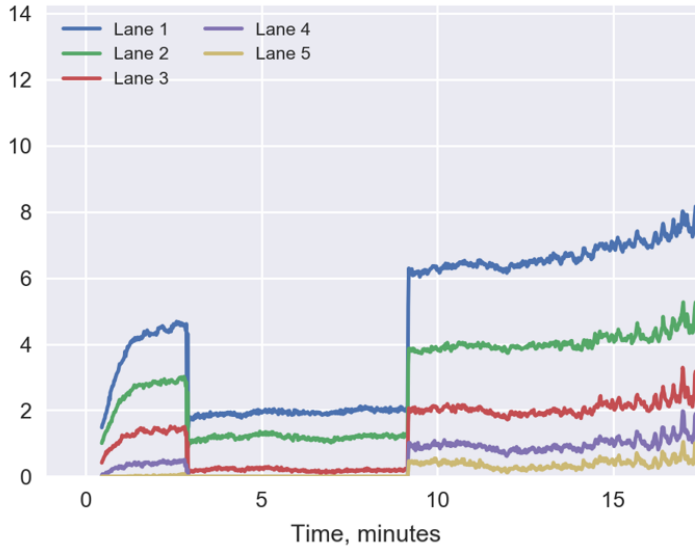

Figure 4.67. Dilution optimization for eReuss Video Analysis. Intensity various dilutions corresponding to 1:1 (Lane 1), 1:2 (Lane 2), 1:4 (Lane 3), 1:8 (Lane 4) and 1:16 (Lane 5).

However, as previously stated, the sample dilution has a side-effect on the information availability. Checking the lane profiling based on intensity, time and position, from Figure 4.68, it is possible to verify the higher background light/contrast noise on the most diluted samples. Also,

the intensity peaks, represented by the gaussians, are affected by the excessive dilution, disallowing the detection of the bands in the gel.

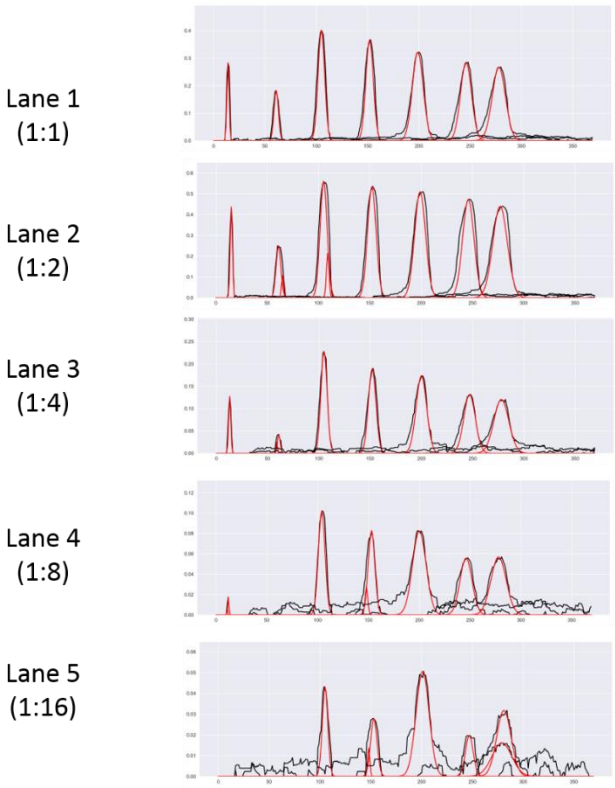

Figure 4.68. eReuss video analysis of the dilution optimization step. Band intensity of each lane captured in specific time frames from the whole video duration.

From all the previously discussed information, new AGE runs were tested in order to apply the video analysis process, with a 1:2 dilution pre-sample application on the gel. From Figure 4.69 a clear improvement in the total intensity, is observed.

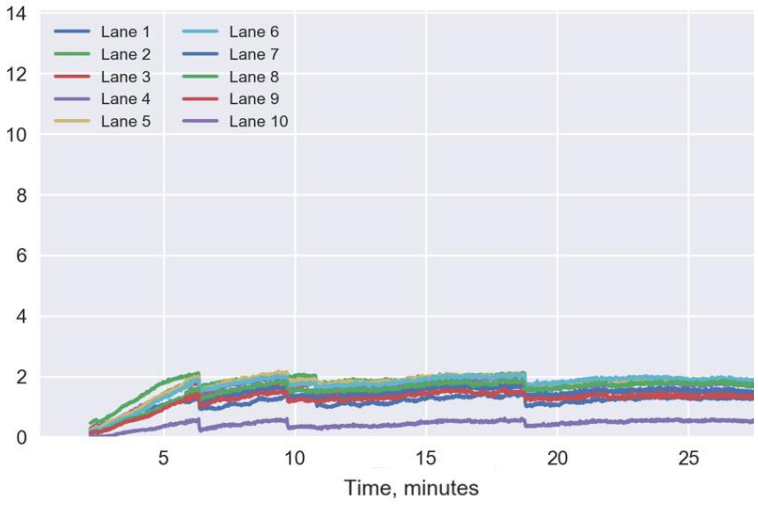

Figure 4.69. Total Intensity values for each Lane (1-10) along the recorded duration for the diluted samples.

When analyzing the band intensity profiles for the previously mentioned samples in Figure 4.70, it is visible that the bands are clearly detected by the eReuss software, even with the dilution effect. These results show that the quality of the results will depend on the previous optimization of light/contrast conditions and sample concentration.

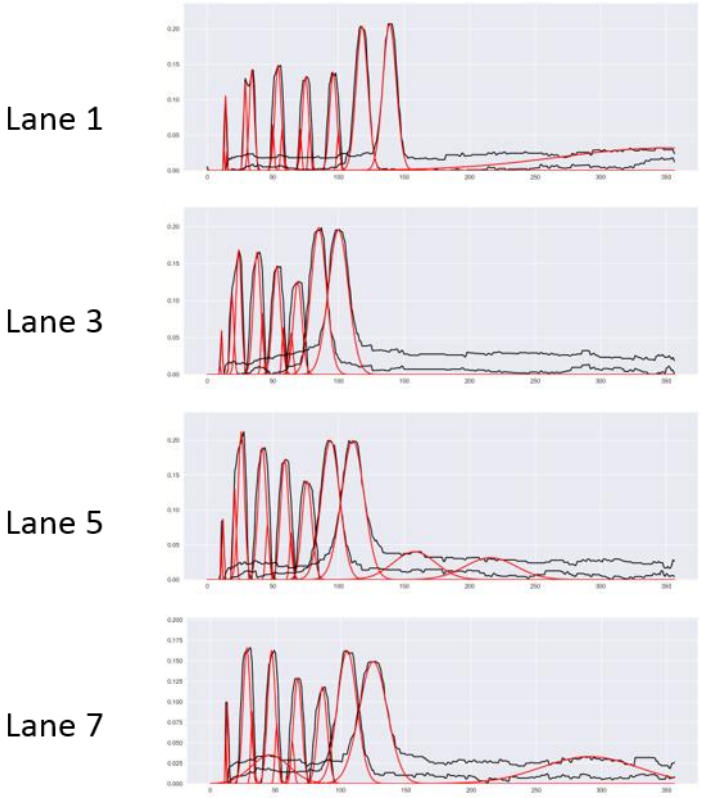

Figure 4.70. eReuss video analysis of the diluted samples. Band intensity of each lane captured in specific time frames from the whole video duration. Only the Lanes 1, 3, 5 and 7 were selected for this representation out of the ten total lanes.

As for the next step in the development of the eReuss software, the electrophoretic mobility variation with time will be a crucial data to exploit from these recorded results. This information will give insight on the variation of adsorbed proteins (quantity) and electric field during an electrophoresis run.

5 Conclusion and future perspectives

The objective of this work was to study the interaction of blood proteins with gold nanoparticles, giving insight on colloidal stability and the formation of a Protein Corona around the nanoparticles.

In the synthesis process, of 15 nm AuNPs, two methods were tested, based on the addition order of the reagents, having resulted in lower monodispersed particle sizes for the inverse order. Both methods were easy and fast to perform. As for stability, the particles had low to none signs of aggregation and remained usable even after months of synthesis.

The Surface Plasmon Resonance effect was confirmed as an accurate and useful tool for UV-Vis spectroscopy characterization of metallic nanoparticles. Size and concentration determination were consistent as different synthesized particle samples had similar conjugation ratios and color contrast after dilution to the desired concentration. The SPR effect, verified by UV-VIS spectroscopy, also allowed to perform quality control based on signs of aggregation at longer wavelengths (600-900 nm) and to confirm successful surface functionalization by a SPR peak red-shift of 5 nm.

Functionalization of the nanoparticle surface lead to significant improvements in colloidal stability at increased salt concentrations for the CALNN functionalization with an estimated aggregation mid-point at 1080 mM of salt, followed by MUA at 277 mM, and finally the non-functionalized AuNPs at 28 mM. As for acidic induced aggregation, the citrate and CALNN AuNPs proved to be more resilient to low pH, with estimated pKa values of 2.7 and 2.9, respectively, and MUA was less resilient, with an estimated pKa value of 3.9. In *in vivo* conditions MUA and CALNN AuNPs should be considered as ideal candidates for further studies. Another advantageous property of surface functionalization was the fact of Citrate-AuNPs were unable to migrate in Agarose Gel Electrophoresis, being impossible to perform a Langmuir Isotherm fitting to the Protein:AuNP conjugation ratio curve.

The attempted positive charged functionalization with AUT was unsuccessful resulting in aggregated samples, although the inversed functionalization method reduced significantly the aggregation effect. However, this type of charge reversal might prove, if stable in the tested conditions, to be more effective at adsorbing protein than the negative charged counterparts, as the tested proteins have a highly negative global net charge at pH 7.4, possibly augmenting the electrostatic attraction and thus the Protein-Corona formation, requiring less protein concentration to fully conjugate or/and increasing the stability of the first outer layer, increasing the hard-corona status, and facilitating the formation of the second outer layer, the theorized reversible soft-corona.

Upon conclusion that Human and Bovine blood proteins have high degrees of homology, both sequential and structural, Bovine proteins were used in this study due to higher availability and lower cost. As for the selection of Albumin and Fibrinogen, both proteins are relatively highly

abundant in plasma, with reported values of around 58% and 4% respectively, and both proteins have different shapes, namely albumin is globular, and fibrinogen is rod-shaped.

Bioconjugation of blood proteins with gold nanoparticles was successful for different nanoparticle sizes, varying from 15 nm to 40 nm, and functionalization with MUA and CALNN. With the Electrophoretic studies adsorption constants were estimated using data of electrophoretic mobility loss with increasing protein layer formation. This data was fitted to a Langmuir Isotherm curve or to a Hill Equation curve, which results had similar orders of magnitude and cooperativity factors of 1.0 and 0.8, respectively. As for the adsorption constants, estimated by the Langmuir Isotherm fitting, for the 15 nm AuNPs the values were of $(1.5 \pm 0.1) \times 10^{-2}$ (AuNP-MUA) for BSA, $(51.2 \pm 4.7) \times 10^{-2}$ (AuNP-CALNN), and $(34.3 \pm 1.2) \times 10^{-2}$ (AuNP-MUA) for Fib conjugation, while the CALNN-BSA interaction lead to band smearing, not allowing constant determination. These values assure that Fib has higher adsorption affinity towards the negative charged AuNP relatively to BSA, while both protein conjugations have similar affinity towards the two types of functionalization. In the case of the 40 nm AuNPs, only the Fib conjugation was tested, and results pointed for two adsorption constants, possibly corresponding to the formation of multi-layers of protein, with values of $(3 \pm 0.7) \times 10^{-2}$ and $(9.7 \pm 2.2) \times 10^{-4}$, respectively, that show that the two layers form at distant ratios of conjugation.

Light scattering studies also showed detection of the protein layer formation, by detecting increasing diameter of the bionanoconjugates in solution with increasing protein concentration used in their formation. In the future, both Electrophoretic and Light Scattering results should be compared, for hydrodynamic diameter and zeta-potential, in order to study if the results are similar and to test the Fergusson Plot Analysis results validity. The multi-band effect of the bioconjugation of Fib with 15 nm AuNPs showed that near equal size or larger sized proteins, relative to the nanoparticles, have an interesting interaction behavior that requires further studying. As for the bioconjugation of Fib with the 40 nm AuNPs, both AGE and Light Scattering results seem to indicate that two (or more) curves of conjugation, possibly resulting in the formation of multiple protein layers. These results might give a hint on how the formation of multiple layers, of differing binding affinities, is directly influenced by the size nanoparticle and how it could affect the Protein-Corona.

In this particular work, BSA and Fib were the proteins tested, which are just a small portion of the innumerous proteins present in plasma samples, each with individual properties and binding affinities, that will present a need for testing. As for these two proteins, Fib outshines BSA in binding affinity due to the advantageous larger size. Other individual proteins with similar shapes yet different sizes and also complete plasma samples should be tested. The immunoglobulins, for example, have a distinct Y-shaped format, and are also highly abundant in plasma: IgG, for example, occurs in a concentration in plasm that is 11 times that of Fibrinogen.

Finally, I propose a diagnostic or protein composition profiling tool to study the different nanoparticle and protein properties:

a) Adsorbed protein composition at three different separated surface charged nanoparticle samples (negative, positive and neutral). Differently charged proteins, in a plasma sample, would probably adsorb preferentially to a specific type of nanoparticle.
b) Different sized AuNPs, ranging from 10-15 nm to 100 nm, following the reasoning of the possibility that surface curvature and area availability influences the two layered (hard and soft) Protein-Corona formation.
c) Other proteins with similar structures (globular and rod-shaped) of differing molecular weights (e.g. the globular IgG of 150 kDa).
d) Find evidence on the impact of non-functionalized NP-Protein interaction, compared to the “biological friendly” functionalized electrostatic interactions, on protein structural integrity and bioactivity upon adsorption.

6 References

[1] M. Andaç and A. Denizli, “Affinity-recognition-based polymeric cryogels for protein depletion studies,” *RSC Adv.*, vol. 4, no. 59, pp. 31130–31141, 2014.

[2] M. J. Hajipour *et al.*, “Personalized disease-specific protein corona influences the therapeutic impact of graphene oxide,” *Nanoscale*, vol. 7, no. 19, pp. 8978–8994, 2015.

[3] M. J. Hajipour, S. Laurent, A. Aghaie, F. Rezaee, and M. Mahmoudi, “Personalized protein coronas: A ‘key’ factor at the nanobiointerface,” *Biomater. Sci.*, vol. 2, no. 9, pp. 1210–1221, 2014.

[4] K. C. Dee, D. A. Puleo, and R. Bizios, “Protein-Surface Interactions,” *An Introd. To Tissue-Biomaterial Interact.*, pp. 37–52, 2003.

[5] R. Franco and E. Pereira, “Gold Nanoparticles and Proteins, Interaction,” *Encycl. Met.*, pp. 908–915, 2013.

[6] D. H. Tsai *et al.*, “Adsorption and conformation of serum albumin protein on gold nanoparticles investigated using dimensional measurements and in situ spectroscopic methods,” *Langmuir*, vol. 27, no. 6, pp. 2464–2477, 2011.

[7] P. Lakshmi, M. Mondal, K. Ramadas, and S. Natarajan, “Molecular interaction of 2 , 4 - diacetylphloroglucinol (DAPG) with human serum albumin (HSA) : The spectroscopic , calorimetric and computational investigation,” *Spectrochim. Acta Part A Mol. Biomol. Spectrosc.*, vol. 183, no. April, pp. 90–102, 2017.

[8] H. Côté, S. Lord, and K. Pratt, “The Journal of The American Society of Hematology,” vol. 94, no. 3, pp. 837–845, 2017.

[9] K. C. Dee and D. a Puleo, “The Immune System and Inflammation,” *Blood Cells*, vol. 4, pp. 109–126, 2002.

[10] Z. Adamczyk, B. Cichocki, M. L. Ekiel-Jezewska, A. Słowicka, E. Wajnryb, and M. Wasilewska, “Fibrinogen conformations and charge in electrolyte solutions derived from DLS and dynamic viscosity measurements,” *J. Colloid Interface Sci.*, vol. 385, no. 1, pp. 244–257, 2012.

[11] R. Chang and B. Cruickshank, “Colóides,” in *Química*, 8th ed., Madrid: McGraw-Hill, Interamericana de España, 2005, pp. 514–515.

[12] R. C. Plumb, “Chemical principles exemplified,” *J. Chem. Educ.*, vol. 47, no. 3, p. 175, 1970.

[13] D. R. Tobergte and S. Curtis, “Rayleigh scattering,” *J. Chem. Inf. Model.*, vol. 53, no. 9, pp. 1689–1699, 2013.

[14] X. Fan, W. Zheng, and D. J. Singh, “Light scattering and surface plasmons on small spherical particles,” *Light Sci. Appl.*, vol. 3, no. 6, p. e179, 2014.

[15] Malvern, “Dynamic Light Scattering: An Introduction in 30 Minutes,” *URL http//www. malvern. com/malvern/kbase. nsf/ …*, no. MRK656-01, pp. 1–8, 2013.

[16] J. Bodycomb, “Method Development for Dynamic Light Scattering.” [Online]. Available: https://www.slideshare.net/HORIBA/method-development-for-dynamic-light-scattering. [Accessed: 21-Jul-2018].

[17] N. C. Santos and M. A. R. B. Castanho, “Teaching light scattering spectroscopy: The dimension and shape of tobacco mosaic virus,” *Biophys. J.*, vol. 71, no. 3, pp. 1641–1650, 1996.

[18] J. G. Mehtala and A. Wei, “Nanometric Resolution in the Hydrodynamic Size Analysis of Ligand- Stabilized Gold Nanorods,” *Langmuir*, vol. 30, pp. 13737–13743, 2014.

[19] V. Filipe, A. Hawe, and W. Jiskoot, “Critical evaluation of nanoparticle tracking analysis (NTA) by NanoSight for the measurement of nanoparticles and protein aggregates,” *Pharm. Res.*, vol. 27, no. 5, pp. 796–810, 2010.

[20] A. E. James and J. D. Driskell, “Monitoring gold nanoparticle conjugation and analysis of biomolecular binding with nanoparticle tracking analysis (NTA) and dynamic light scattering (DLS),” *Analyst*, vol. 138, no. 4, pp. 1212–1218, 2013.

[21] U. Nobbmann, “DLS or NTA which is better suited for nanoparticle size?” [Online]. Available: http://www.materials-talks.com/blog/2016/09/15/nta-or-dls/. [Accessed: 12-Jul-2018].

[22] S. Schlücker, “Surface-enhanced raman spectroscopy: Concepts and chemical applications,” *Angew. Chemie - Int. Ed.*, vol. 53, no. 19, pp. 4756–4795, 2014.

[23] L. M. Liz-marz, “Nanometals :,” no. February, pp. 26–31, 2004.

[24] S. K. Ghosh and T. Pal, “Interparticle Coupling Effect on the Surface Plasmon Resonance of Gold Nanoparticles: From Theory to Applications,” *Chem. Rev.*, vol. 107, no. 11, pp. 4797–4862, 2007.

[25] M. P. De Almeida and P. V Baptista, *Gold Nanoparticles as (Bio) Chemical Sensors*. 2014.

[26] P. M. Todebush, J. Camden, J. Roden, and G. C. Schatz, “Theoretical Analysis of Gold Nanoparticles.”

[27] S. Peiris, J. McMurtrie, and H. Y. Zhu, “Metal nanoparticle photocatalysts: Emerging processes for green organic synthesis,” *Catal. Sci. Technol.*, vol. 6, no. 2, pp. 320–338, 2016.

[28] D. B. Pedersen and E. J. S. Duncan, “Surface Plasmon Resonance Spectroscopy of Gold Nanoparticle- Coated Substrates,” *Tech. Rep.*, vol. 109, no. August, pp. 1–46, 2005.

[29] W. Haiss, N. T. K. Thanh, J. Aveyard, and D. G. Fernig, “Determination of Size and Concentration of Gold Nanoparticles from UV − Vis Spectra Determination of Size and Concentration of Gold Nanoparticles from UV - Vis Spectra,” vol. 79, no. October, pp. 4215–4221, 2015.

[30] D. J. Shaw, “Introduction to Colloid and Surface Chemistry,” *Elsevier Sci. LTD.*, vol. Oxford, UK, pp. 61–65, 69–73, 79, 84–89, 1992.

[31] B. V. Enüstün and J. Turkevich, “Coagulation of Colloidal Gold,” *J. Am. Chem. Soc.*, vol. 85, no. 21, pp. 3317–3328, 1963.

[32] D. Kopeliovich, “Stabilization of colloids [SubsTech].” [Online]. Available: http://www.substech.com/dokuwiki/doku.php?id=stabilization_of_colloids. [Accessed: 20-Jul-2018].

[33] NPTEL, “Module 8 : " Stability of Colloids ",” 2012. [Online]. Available: https://nptel.ac.in/courses/103104045/pdf_version/lecture37.pdf. [Accessed: 28-Jul-2018].

[34] M. Khoshnevisan, K. & Barkhi, “Zeta potential,” *Malvern Instruments Ltd*, no. May, pp. 1–9, 2015.

[35] J. W. Swan and E. M. Furst, “A simpler expression for Henry’s function describing the electrophoretic mobility of spherical colloids,” *J. Colloid Interface Sci.*, vol. 388, no. 1, pp. 92–94, 2012.

[36] P. H. Wiersema, A. L. Loeb, and J. T. G. Overbeek, “Calculation of the electrophoretic mobility of a spherical colloid particle,” *J. Colloid Interface Sci.*, vol. 22, no. 1, pp. 78–99, 1966.

[37] K. Makino and H. Ohshima, “Electrophoretic mobility of a colloidal particle with constant

surface charge density," *Langmuir*, vol. 26, no. 23, pp. 18016–18019, 2010.

[38] H. Ohshima, "Modified henry function for the electrophoretic mobility of a charged spherical colloidal particle covered with an ion-penetrable uncharged polymer layer," *J. Colloid Interface Sci.*, vol. 252, no. 1, pp. 119–125, 2002.

[39] A. Kitanovski, J. Tušek, U. Tomc, U. Plaznik, M. Ožbolt, and A. Poredoš, *Magnetocaloric Energy Conversion*. 2015.

[40] M. Peixoto De Almeida *et al.*, "Measurement of adsorption constants of laccase on gold nanoparticles to evaluate the enhancement in enzyme activity of adsorbed laccase," *Phys. Chem. Chem. Phys.*, vol. 20, no. 24, pp. 16761–16769, 2018.

[41] "Agarose gel electrophoresis for DNA samples." [Online]. Available: https://orbitbiotech.com/agarose-gel-electrophoresis-for-dna-samples-gel-electrophoresis-macro-molecules-edta-tris-glacial-acetic-acid-gel-loading-agarose-dye-buffer-gel-case-tae-glycerol-etbr/. [Accessed: 02-Aug-2018].

[42] F. R. Weaver, "Molecular Biology," vol. 12, no. 2, pp. 1–8, 2008.

[43] P. Y. Lee, J. Costumbrado, C.-Y. Hsu, and Y. H. Kim, "Agarose Gel Electrophoresis for the Separation of DNA Fragments," *J. Vis. Exp.*, no. 62, 2012.

[44] S. Park and K. Hamad-Schifferli, "Evaluation of hydrodynamic size and zeta-potential of surface-modified Au nanoparticle-DNA conjugates via ferguson analysis," *J. Phys. Chem. C*, vol. 112, no. 20, pp. 7611–7616, 2008.

[45] BIO-RAD, "A Guide to Polyacrylamide Gel Electrophoresis and Detection," p. 47, 2012.

[46] O. V Gorkun, Y. I. Veklich, J. W. Weisel, and S. T. Lord, "The conversion of fibrinogen to fibrin: recombinant fibrinogen typifies plasma fibrinogen.," *Blood*, vol. 89, no. 12, pp. 4407–14, 1997.

[47] D. Deeb, X. Gao, H. Jiang, A. S. Arbab, S. A. Dulchavsky, and S. C. Gautam, "Growth inhibitory and apoptosis-inducing effects of xanthohumol, a prenylated chalone present in hops, in human prostate cancer cells," *Anticancer Res.*, vol. 30, no. 9, pp. 3333–3339, 2010.

[48] I. Khan, K. Saeed, and I. Khan, "Nanoparticles: Properties, applications and toxicities," *Arab. J. Chem.*, 2017.

[49] K. Alaqad and T. A. Saleh, "Gold and Silver Nanoparticles: Synthesis Methods, Characterization Routes and Applications towards Drugs," *J. Environ. Anal. Toxicol.*, vol. 6, no. 4, 2016.

[50] T. Mori and T. Hegmann, "Determining the composition of gold nanoparticles: a compilation of shapes, sizes, and calculations using geometric considerations," *J. Nanoparticle Res.*, vol. 18, no. 10, pp. 1–36, 2016.

[51] S. Kumar, K. S. Gandhi, and R. Kumar, "Modeling of Formation of Gold Nanoparticles by Citrate Method †," *Ind. Eng. Chem. Res.*, vol. 46, no. 10, pp. 3128–3136, 2007.

[52] M. E. Diemer, "Aurous chloride," *J. Am. Chem. Soc.*, vol. 35, no. 5, pp. 552–559, 1913.

[53] "Citrate Synthesis of Gold Nanoparticles – MRSEC Education Group – UW–Madison." [Online]. Available: https://education.mrsec.wisc.edu/citrate-synthesis-of-gold-nanoparticles/. [Accessed: 07-May-2018].

[54] E. Pensa, E. Corte, M. H. Fonticelli, G. Benítez, A. Rubert, and R. C. Salvarezza, "The Chemistry of the Sulfur À Gold Interface : In Search of a Unified Model," *Acc. Chem. Res.*, vol. 45, no. 8, pp. 1183–1192, 2012.

[55] A. M. Alkilany *et al.*, "Colloidal stability of citrate and mercaptoacetic acid capped gold nanoparticles upon lyophilization: Effect of capping ligand attachment and type of cryoprotectants," *Langmuir*, vol. 30, no. 46, pp. 13799–13808, 2014.

[56] D. Graham and M. Boeckl, “Self-Assembled Monolayers: Advantages of Pure Alkanethiols | Sigma-Aldrich,” 2006. [Online]. Available: https://www.sigmaaldrich.com/technical-documents/articles/material-matters/self-assembled-monolayers.html. [Accessed: 08-Aug-2018].

[57] R. Lévy *et al.*, “Rational and combinatorial design of peptide capping ligands for gold nanoparticles,” *J. Am. Chem. Soc.*, vol. 126, no. 32, pp. 10076–10084, 2004.

[58] H. Hinterwirth, S. Kappel, T. Waitz, T. Prohaska, W. Lindner, and M. Lämmerhofer, “Quantifying thiol ligand density of self-assembled monolayers on gold nanoparticles by inductively coupled plasma-mass spectrometry,” *ACS Nano*, vol. 7, no. 2, pp. 1129–1136, 2013.

[59] W. A. Marmisollé, D. A. Capdevila, E. De La Llave, F. J. Williams, and D. H. Murgida, “Self-assembled monolayers of NH2-terminated thiolates: Order, pKa, and specific adsorption,” *Langmuir*, vol. 29, no. 17, pp. 5351–5359, 2013.

[60] S. H. De Paoli Lacerda *et al.*, “Interaction of gold nanoparticles with common human blood proteins,” *ACS Nano*, vol. 4, no. 1, pp. 365–379, 2010.

[61] E. Casals, T. Pfaller, A. Duschl, G. J. Oostingh, and V. Puntes, “Time evolution of the nanoparticle protein corona,” *ACS Nano*, vol. 4, no. 7, pp. 3623–3632, 2010.

[62] M. Lundqvist, J. Stigler, G. Elia, I. Lynch, T. Cedervall, and K. A. Dawson, “Nanoparticle size and surface properties determine the protein corona with possible implications for biological impacts.,” *Proc. Natl. Acad. Sci. U. S. A.*, vol. 105, no. 38, pp. 14265–70, Sep. 2008.

[63] I. Lynch and K. A. Dawson, “Protein-nanoparticle interactions,” *Nano Today*, vol. 3, no. 1–2, pp. 40–47, 2008.

[64] P. H. J. Turkevich, John; Cooper, “A study of the nucleation and growth process in the synthesis of colloidal gold,” *Discuss. Faraday Soc.*, vol. 55, no. c, pp. 55–75, 1951.

[65] J. Kimling, M. Maier, B. Okenve, V. Kotaidis, H. Ballot, and A. Plech, “Turkevich Method for Gold Nanoparticle Synthesis Revisited.pdf,” *J. Phys. Chem. B*, vol. 110, no. 95 mL, pp. 15700–15707, 2006.

[66] I. Ojea-Jiménez, N. G. Bastús, and V. Puntes, “Influence of the sequence of the reagents addition in the citrate-mediated synthesis of gold nanoparticles,” *J. Phys. Chem. C*, vol. 115, no. 32, pp. 15752–15757, 2011.

[67] “ffmpeg tool.” FFmpeg Developers, 2016.

[68] A. Bateman *et al.*, “UniProt: The universal protein knowledgebase,” *Nucleic Acids Res.*, vol. 45, no. D1, pp. D158–D169, 2017.

[69] H. M. Berman *et al.*, “The Protein Data Bank,” *Struct. Bioinforma.*, vol. 28, no. 1, pp. 181–198, 2005.

[70] S. F. Altschul, W. Gish, W. Miller, E. W. Myers, and D. J. Lipman, “Basic local alignment search tool,” *J. Mol. Biol.*, vol. 215, no. 3, pp. 403–410, 1990.

[71] A. Prlić *et al.*, “Pre-calculated protein structure alignments at the RCSB PDB website,” *Bioinformatics*, vol. 26, no. 23, pp. 2983–2985, 2010.

[72] S.-Y. Lin, Y.-T. Tsai, C.-C. Chen, C.-M. Lin, and C. Chen, “Two-Step Functionalization of Neutral and Positively Charged Thiols onto Citrate-Stabilized Au Nanoparticles,” *J. Phys. Chem. B*, vol. 108, no. 7, pp. 2134–2139, 2004.

[73] W. R. Carmody, “Easily prepared wide range buffer series,” *J. Chem. Educ.*, vol. 38, no. 11, p. 559, 1961.

[74] I. Gomes *et al.*, “Controlled adsorption of cytochrome c to nanostructured gold surfaces,” *J. Nanoparticle Res.*, vol. 14, no. 12, 2012.

[75] J. Cortez *et al.*, “Bionanoconjugates of tyrosinase and peptide-derivatised gold nanoparticles for biosensing of phenolic compounds,” *J. Nanoparticle Res.*, vol. 13, no. 3, pp. 1101–1113, 2011.

[76] M. C. Leopold, J. A. Black, and E. F. Bowden, “Influence of gold topography on carboxylic acid terminated self-assembled monolayers,” *Langmuir*, vol. 18, no. 4, pp. 978–980, 2002.

[77] D. Lide, *Handbook of Chemistry and Physics*, 72th ed. 1991.

[78] K. P. Browne and B. A. Grzybowski, “Controlling the properties of self-assembled monolayers by substrate curvature,” *Langmuir*, vol. 27, no. 4, pp. 1246–1250, 2011.

[79] C. Wolfenstein-Todel and M. W. Mosesson, “Human plasma fibrinogen heterogeneity : Evidence for an extended carboxyl-terminal sequence in a normal y chain variant (y ’),” *Proc. Natl. Acad. Sci. U. S. A.*, vol. 77, no. 9, pp. 5069–5073, 1980.

[80] “Bovine Serum Albumins - Albumin | Sigma-Aldrich.” [Online]. Available: https://www.sigmaaldrich.com/life-science/biochemicals/biochemical-products.html?TablePage=103994915&gclid=Cj0KCQjw6MHdBRCtARIsAEigMxFzDl3yP_IMP2cFQY9lA6hj8tocFCAJqW-jUOS9vMERfneHQoYDYRgaAsvGEALw_wcB. [Accessed: 13-Jul-2018].

[81] “Fibrinogen from bovine plasma Type I-S, 65-85% protein (≥75% of protein is clottable) | Sigma-Aldrich.” [Online]. Available: https://www.sigmaaldrich.com/catalog/product/sigma/f8630?lang=pt&region=PT. [Accessed: 13-Jul-2018].

[82] “Pierce BCA Protein Assay Kit - Thermo Fisher Scientific.” [Online]. Available: https://www.thermofisher.com/order/catalog/product/23225. [Accessed: 15-Jul-2018].

[83] P. K. Smith *et al.*, “Measurement of protein using bicinchoninic acid,” *Anal. Biochem.*, vol. 150, no. 1, pp. 76–85, 1985.

[84] J. Fassler and P. Cooper, “BLAST Glossary,” 2011.

[85] S. Chatterjee and T. K. Mukherjee, “Spectroscopic investigation of interaction between bovine serum albumin and amine-functionalized silicon quantum dots,” *Phys. Chem. Chem. Phys.*, vol. 16, no. 18, pp. 8400–8408, 2014.

[86] M. Lundqvist, J. Stigler, G. Elia, I. Lynch, T. Cedervall, and K. A. Dawson, “Nanoparticle size and surface properties determine the protein corona with possible implications for biological impacts,” *Proc. Natl. Acad. Sci.*, vol. 105, no. 38, pp. 14265–14270, 2008.

[87] W. Liu, J. Rose, S. Plantevin, M. Auffan, J.-Y. Bottero, and C. Vidaud, “Protein corona formation for nano materials and proteins of a similar size: hard or soft corona?,” *Optoelectron. Adv. Mater. Rapid Commun.*, vol. 4, no. 8, pp. 1166–1169, 2010.

[88] K. Siriwardana, A. Wang, M. Gadogbe, W. E. Collier, N. C. Fitzkee, and D. Zhang, “Studying the Effects of Cysteine Residues on Protein Interactions with Silver Nanoparticles.,” *J. Phys. Chem. C. Nanomater. Interfaces*, vol. 119, no. 5, pp. 2910–2916, 2015.

[89] M. Martinez, J. Weisel, and H. Ischiropoulos, “Functional impact of oxidative post-translational modifications on fibrinogen and fibrin clots,” vol. 8, no. 9, pp. 1385–1395, 2014.

[90] H. Gronbeck, A. Curioni, and W. Andreoni, “Thiols and Disulfides on the Au (111) Surface: The Headgroup - Gold Interaction,” *J. Am. Chem. Soc.*, vol. 122, no. 16, pp. 3839–3842, 2000.

[91] S. Köhler, F. Schmid, and G. Settanni, “The Internal Dynamics of Fibrinogen and Its Implications for Coagulation and Adsorption,” *PLoS Comput. Biol.*, vol. 11, no. 9, pp. 1–19, 2015.

[92] P. Roach, D. Farrar, and C. C. Perry, “Surface tailoring for controlled protein adsorption:

Effect of topography at the nanometer scale and chemistry," *J. Am. Chem. Soc.*, vol. 128, no. 12, pp. 3939–3945, 2006.

[93] J. Hühn *et al.*, "Dissociation coefficients of protein adsorption to nanoparticles as quantitative metrics for description of the protein corona: A comparison of experimental techniques and methodological relevance," *Int. J. Biochem. Cell Biol.*, vol. 75, pp. 148–161, 2016.

[94] A. Elbakry, A. Zaky, R. Liebl, R. Rachel, A. Goepferich, and M. Breunig, "Layer-by-layer assembled gold nanoparticles for siRNA delivery.," *Nano Lett.*, vol. 9, no. 5, pp. 2059–64, 2009.

[95] E. D. Kaufman *et al.*, "Probing protein adsorption onto mercaptoundecanoic acid stabilized gold nanoparticles and surfaces by quartz crystal microbalance and ζ-potential measurements," *Langmuir*, vol. 23, no. 11, pp. 6053–6062, 2007.

[96] H. P. Erickson, "Size and shape of protein molecules at the nanometer level determined by sedimentation, gel filtration, and electron microscopy," *Biol. Proced. Online*, vol. 11, no. 1, pp. 32–51, 2009.

Appendix

I. Gold nanoparticle Characterization

Table I.1. Estimated values for the molar extinction coefficients of gold nanoparticles of size between 2 and 100 nm in diameter.

d/ nm	ε_{450} / $M^{-1}cm^{-1}$	*d*/ nm	ε_{450} / $M^{-1}cm^{-1}$	*d*/ nm	ε_{450} / $M^{-1}cm^{-1}$
2	4.25E+05	35	3.21E+09	68	2.50E+10
3	1.49E+06	36	3.52E+09	69	2.61E+10
4	3.62E+06	37	3.84E+09	70	2.71E+10
5	7.20E+06	38	4.18E+09	71	2.82E+10
6	1.26E+07	39	4.54E+09	72	2.93E+10
7	2.03E+07	40	4.92E+09	73	3.05E+10
8	3.07E+07	41	5.32E+09	74	3.16E+10
9	4.43E+07	42	5.74E+09	75	3.28E+10
10	6.15E+07	43	6.18E+09	76	3.40E+10
11	8.27E+07	44	6.65E+09	77	3.52E+10
12	1.09E+08	45	7.13E+09	78	3.64E+10
13	1.39E+08	46	7.65E+09	79	3.77E+10
14	1.76E+08	47	8.18E+09	80	3.89E+10
15	2.18E+08	48	8.74E+09	81	4.02E+10
16	2.67E+08	49	9.32E+09	82	4.14E+10
17	3.24E+08	50	9.92E+09	83	4.27E+10
18	3.87E+08	51	1.06E+10	84	4.40E+10
19	4.60E+08	52	1.12E+10	85	4.53E+10
20	5.41E+08	53	1.19E+10	86	4.65E+10
21	6.31E+08	54	1.26E+10	87	4.78E+10
22	7.31E+08	55	1.33E+10	88	4.91E+10
23	8.42E+08	56	1.41E+10	89	5.04E+10
24	9.64E+08	57	1.48E+10	90	5.17E+10
25	1.10E+09	58	1.57E+10	91	5.30E+10
26	1.24E+09	59	1.65E+10	92	5.43E+10
27	1.40E+09	60	1.73E+10	93	5.56E+10
28	1.58E+09	61	1.82E+10	94	5.69E+10
29	1.76E+09	62	1.91E+10	95	5.82E+10
30	1.96E+09	63	2.00E+10	96	5.94E+10
31	2.18E+09	64	2.10E+10	97	6.07E+10
32	2.41E+09	65	2.19E+10	98	6.19E+10
33	2.66E+09	66	2.29E+10	99	6.31E+10
34	2.93E+09	67	2.40E+10	100	6.44E+10

II. Protein Homology Results

a) Fibrinogen

NW Score	Identities	Positives	Gaps
1574	383/877(44%)	451/877(51%)	273/877(31%)

```
Query  1    MFSVRDLCLVLSLVGAIKTEDGSDPPSGDFLTEGGGVRGPRLVERQQSACKETGWPFCSD  60
            MFS+R +CLVLS+VG   T D  +   GDFL EGGGVRGPR+VER QSACK++ WPFCSD
Sbjct  1    MFSMRIVCLVLSVVGTAWTADSGE---GDFLAEGGGVRGPRVVERHQSACKDSDWPFCSD  57

Query  61   EDWNTKCPSGCRMKGLIDEVDQDFTSRINKLRDSLFNYQKNSKDSNTLTKNIVELMRGDF  120
            EDWN KCPSGCRMKGLIDEV+QDFT+RINKL++SLF YQKN+KDS++LT NI+E++RGDF
Sbjct  58   EDWNYKCPSGCRMKGLIDEVNQDFTNRINKLKNSLFEYQKNNKDSHSLTTNIMEILRGDF  117

Query  121  AKANNNDNTFKQISEDLRSRIEILRRKVIEQVQRIKVLQKNVRDQLVDMKRLEVDIDIKI  180
            + ANN DNT+ ++SEDLRSRIE+L+RKVIE+VQ I++LQKNVR QLVDMKRLEVDIDIKI
Sbjct  118  SSANNRDNTYNRVSEDLRSRIEVLKRKVIEKVQHIQLLQKNVRAQLVDMKRLEVDIDIKI  177

Query  181  RSCKGSCSRALEHKVDLEDYKNQQKQLEQVIAINLLPSRDIQYLPLIKMSTITGPVPREF  240
            RSC+GSCSRAL  +VDL+DY++QQKQLEQVIA +LLPSRD Q+LPLIKM  +   VP  F
Sbjct  178  RSCRGSCSRALAREVDLKDYEDQQKQLEQVIAKDLLPSRDRQHLPLIKMKPVPDLVPGNF  237

Query  241  KSQLQEAPLEWKALLEMQQTKMVLETFGGDGHARGDSVSQGTGLAPGSPRKPGTSSIGNV  300
            KSQLQ+ P EWKAL +M Q +M LE  GG+   RG S S GTG    SPR P  SS G+
Sbjct  238  KSQLQKVPPEWKALTDMPQMRMELERPGGNEITRGGSTSYGTGSETESPRNP--SSAGSW  295

Query  301  NPGSYGPGSSGTWNPGRPEPGSAGTWNPGRPEPGSAGTWNPGRPEPGSAGTWNPGRPEPG  360
            N GS GPGS+G  NPG    G   TW PG   PGS G+WN G    GS G  NPG P PG
Sbjct  296  NSGSSGPGSTGNRNPGSSGTGGTATWKPGSSGPGSTGSWNSGSSGTGSTGNQNPGSPRPG  355

Query  361  SAGTWNPGRPEPGSAGTWNT-----GSSG-----SSSFRPDSSGHGNIRPSSPDWGTFRE  410
            S GTWNPG  E GSAG W +     GS+G     S SFRPDS G GN RP++PDWGTF E
Sbjct  356  STGTWNPGSSERGSAGHWTSESSVSGSTGQWHSESGSFRPDSPGSGNARPNNPDWGTFEE  415

Query  411  -EGSVSSGTKQEFHTGKLVTTKGDKELLIDNEKVTSGHTTTTRRSCSKVITKTVTNADGR  469
              G+VS GT++E+HT KLVT+KGDKEL    EKVTSG TTTTRRSCSK +TKTV   DG
Sbjct  416  VSGNVSPGTRREYHTEKLVTSKGDKELRTGKEKVTSGSTTTTRRSCSKTVTKTVIGPDGH  475

Query  470  TETTKEVVKSEDGSDCGDA-DFDWHHTFPSRGNLDDFFHRDKDD---------------F  513
             E TKEVV SEDGSDC +A D     T    G LD F HR  D+               F
Sbjct  476  KEVTKEVVTSEDGSDCPEAMDLG---TLSGIGTLDGFRHRHPDEAAFFDTASTGKTFPGF  532

Query  514  FTRSSHEF----DGRTGLAPEFAALGESGS---------SSSKTSTHSKQFVSSSTTVNR  560
            F+    EF    + R   +  F    ES S         S  K+S++SKQF +SST+ NR
Sbjct  533  FSPMLGEFVSETESRGSESGIFTNTKESSSHHPGIAEFPSRGKSSSYSKQF-TSSTSYNR  591

Query  561  GGSAIESKHFKMEDEAESLEDLGFKGAHGTQKGHTKARPARG----IHTSPLG-------  609
            G S  ESK +KM DEA S  D   +G H T++GH K+RP R     + T P G
Sbjct  592  GDSTFESKSYKMADEAGSEAD--HEGTHSTKRGHAKSRPVRDCDDVLQTHPSGTQSGIFN  649

Query       ------------------------------------------------------------

Sbjct  650  IKLPGSSKIFSVYCDQETSLGGWLLIQQRMDGSLNFNRTWQDYKRGFGSLNDEGEGEFWL  709

Query       ------------------------------------------------------------

Sbjct  710  GNDYLHLLTQRGSVLRVELEDWAGNEAYAEYHFRVGSEAEGYALQVSSYEGTAGDALIEG  769

Query       ------------------------------------------------------------

Sbjct  770  SVEEGAEYTSHNNMQFSTFDRDADQWEENCAEVYGGGWWYNNCQAANLNGIYYPGGSYDP  829

Query  610  --------------------------------EPSLTP  615
                                            P +T
Sbjct  830  RNNSPYEIENGVVWVSFRGADYSLRAVRMKIRPLVTQ  866
```

Figure II.1. Global Alignment of the Fibrinogen Alpha-chain (Bovine and Human).

Score	Expect	Method	Identities	Positives	Gaps
610 bits(1574)	0.0	Compositional matrix adjust.	367/655(56%)	430/655(65%)	79/655(12%)

```
Query  1    MFSVRDLCLVLSLVGAIKTEDGSDPPSGDFLTEGGGVRGPRLVERQQSACKETGWPFCSD  60
            MFS+R +CLVLS+VG   T D  +   GDFL EGGGVRGPR+VER QSACK++ WPFCSD
Sbjct  1    MFSMRIVCLVLSVVGTAWTADSGE---GDFLAEGGGVRGPRVVERHQSACKDSDWPFCSD  57

Query  61   EDWNTKCPSGCRMKGLIDEVDQDFTSRINKLRDSLFNYQKNSKDSNTLTKNIVELMRGDF  120
            EDWN KCPSGCRMKGLIDEV+QDFT+RINKL++SLF YQKN+KDS++LT NI+E++RGDF
Sbjct  58   EDWNYKCPSGCRMKGLIDEVNQDFTNRINKLKNSLFEYQKNNKDSHSLTTNIMEILRGDF  117

Query  121  AKANNNDNTFKQISEDLRSRIEILRRKVIEQVQRIKVLQKNVRDQLVDMKRLEVDIDIKI  180
            + ANN DNT+ ++SEDLRSRIE+L+RKVIE+VQ I++LQKNVR QLVDMKRLEVDIDIKI
Sbjct  118  SSANNRDNTYNRVSEDLRSRIEVLKRKVIEKVQHIQLLQKNVRAQLVDMKRLEVDIDIKI  177

Query  181  RSCKGSCSRALEHKVDLEDYKNQQKQLEQVIAINLLPSRDIQYLPLIKMSTITGPVPREF  240
            RSC+GSCSRAL  +VDL+DY++QQKQLEQVIA +LLPSRD Q+LPLIKM  +   VP  F
Sbjct  178  RSCRGSCSRALAREVDLKDYEDQQKQLEQVIAKDLLPSRDRQHLPLIKMKPVPDLVPGNF  237

Query  241  KSQLQEAPLEWKALLEMQQTKMVLETFGGDGHARGDSVSQGTGLAPGSPRKP--------  292
            KSQLQ+ P EWKAL +M Q +M LE  GG+   RG S S GTG    SPR P
Sbjct  238  KSQLQKVPPEWKALTDMPQMRMELERPGGNEITRGGSTSYGTGSETESPRNPSSAGSWNS  297

Query  293  ---GTSSIGNVNPGSYGPGSSGTWN-------------PGRPEPGSAGTWNPGRPEPGSA  336
               G  S GN NPGS G G + TW                 G    GS G  NPG P PGS
Sbjct  298  GSSGPGSTGNRNPGSSGTGGTATWKPGSSGPGSTGSWNSGSSGTGSTGNQNPGSPRPGST  357

Query  337  GTWNPGRPEPGSAGTWNPGRPEPGSAGTWNPGRPEPGSAGTWNTGSSGSSSFRPDSSGHG  396
            GTWNPG  E GSAG W       GS G W+                S S SFRPDS G G
Sbjct  358  GTWNPGSSERGSAGHWTSESSVSGSTGQWH---------------SESGSFRPDSPGSG  401

Query  397  NIRPSSPDWGTFRE-EGSVSSGTKQEFHTGKLVTTKGDKELLIDNEKVTSGHTTTTRRSC  455
            N RP++PDWGTF E  G+VS GT++E+HT KLVT+KGDKEL    EKVTSG TTTTRRSC
Sbjct  402  NARPNNPDWGTFEEVSGNVSPGTRREYHTEKLVTSKGDKELRTGKEKVTSGSTTTTRRSC  461

Query  456  SKVITKTVTNADGRTETTKEVVKSEDGSDCGDA-DFDWHHTFPSRGNLDDFFHRDKDD--  512
            SK +TKTV   DG  E TKEVV SEDGSDC +A D     T    G LD F HR  D+
Sbjct  462  SKTVTKTVIGPDGHKEVTKEVVTSEDGSDCPEAMDLG---TLSGIGTLDGFRHRHPDEAA  518

Query  513  -------------FFTRSSHEF----DGRTGLAPEFAALGESGS---------SSSKTST  546
                         FF+    EF    + R   +  F    ES S          S  K+S+
Sbjct  519  FFDTASTGKTFPGFFSPMLGEFVSETESRGSESGIFTNTKESSSHHPGIAEFPSRGKSSS  578

Query  547  HSKQFVSSSTTVNRGGSAIESKHFKMEDEAESLEDLGFKGAHGTQKGHTKARPAR  601
            +SKQF +SST+ NRG S  ESK +KM DEA S  D   +G H T++GH K+RP R
Sbjct  579  YSKQF-TSSTSYNRGDSTFESKSYKMADEAGSEAD--HEGTHSTKRGHAKSRPVR  630
```

Range 2: 733 to 763 Graphics Next Match Previous Match First Match

Score	Expect	Method	Identities	Positives	Gaps
18.9 bits(37)	1.1	Compositional matrix adjust.	10/31(32%)	16/31(51%)	2/31(6%)

```
Query  561  GGSAIESKHFKMEDEAE--SLEDLGFKGAHG  589
            G  A    HF++  EAE  +L+   ++G  G
Sbjct  733  GNEAYAEYHFRVGSEAEGYALQVSSYEGTAG  763
```

Figure II.2. Local Alignment of the Fibrinogen Alpha-chain (Bovine and Human).

NW Score	Identities	Positives	Gaps
2098	381/492(77%)	421/492(85%)	25/492(5%)

```
Query  1    Q-----------------------FPTDYDEGQDDRPKVGLGARGHRPYDKKKEEAPSL  36
                                    F     +G +D  +    ARGHRP DKK+EEAPSL
Sbjct  1    MKRMVSWSFHKLKTMKHLLLLLLCVFLVK-SQGVNDNEEGFFSARGHRPLDKKREEAPSL  59

Query  37   RPVPPPISGGGYRARPATATVGQKKVERKPPDADGCLHADPDLGVLCPTGCKLQDTLVRQ  96
            RP PPISGGGYRARPA A   QKKVERK PDA GCLHADPDLGVLCPTGC+LQ+ L++Q
Sbjct  60   RPAPPPISGGGYRARPAKAAATQKKVERKAPDAGGCLHADPDLGVLCPTGCQLQEALLQQ  119

Query  97   ERPIRKSIEDLRNTVDSVSRTSSSTFQYITLLKNMWKGRQNQVQDNENVVNEYSSHLEKH  156
            ERPIR S+++L N V++VS+TSSS+FQY+ LLK++W+ RQ QV+DNENVVNEYSS LEKH
Sbjct  120  ERPIRNSVDELNNNVEAVSQTSSSSFQYMYLLKDLWQKRQKQVKDNENVVNEYSSELEKH  179

Query  157  QLYIDETVKNNIPTKLRVLRSILENLRSKIQKLESDVSTQMEYCRTPCTVTCNIPVVSGK  216
            QLYIDETV +NIPT LRVLRSILENLRSKIQKLESDVS QMEYCRTPCTV+CNIPVVSGK
Sbjct  180  QLYIDETVNSNIPTNLRVLRSILENLRSKIQKLESDVSAQMEYCRTPCTVSCNIPVVSGK  239

Query  217  ECEKIIRNEGETSEMYLIQPEDSSKPYRVYCDMKTEKGGWTVIQNRQDGSVDFGRKWDPY  276
            ECE+IIR  GETSEMYLIQP+ S KPYRVYCDM TE GGWTVIQNRQDGSVDFGRKWDPY
Sbjct  240  ECEEIIRKGGETSEMYLIQPDSSVKPYRVYCDMNTENGGWTVIQNRQDGSVDFGRKWDPY  299

Query  277  KQGFGNIATNAEGKKYCGVPGEYWLGNDRISQLTNMGPTKLLIEMEDWKGDKVTALYEGF  336
            KQGFGN+ATN +GK YCG+PGEYWLGND+ISQLT MGPT+LLIEMEDWKGDKV A Y GF
Sbjct  300  KQGFGNVATNTDGKNYCGLPGEYWLGNDKISQLTRMGPTELLIEMEDWKGDKVKAHYGGF  359

Query  337  TVQNEANKYQLSVSKYKGTAGNALIEGASQLVGENRTMTIHNSMFFSTYDRDNDGWKTTD  396
            TVQNEANKYQ+SV+KY+GTAGNAL++GASQL+GENRTMTIHN MFFSTYDRDNDGW T+D
Sbjct  360  TVQNEANKYQISVNKYRGTAGNALMDGASQLMGENRTMTIHNGMFFSTYDRDNDGWLTSD  419

Query  397  PRKQCSKEDGGGWWYNRCHAANPNGRYYWGGAYTWDMAKHGTDDGVVWMNWQGSWYSMKK  456
            PRKQCSKEDGGGWWYNRCHAANPNGRYYWGG YTWDMAKHGTDDGVVWMNW+GSWYSM+K
Sbjct  420  PRKQCSKEDGGGWWYNRCHAANPNGRYYWGGQYTWDMAKHGTDDGVVWMNWKGSWYSMRK  479

Query  457  MSMKIRPYFPEQ  468
            MSMKIRP+FP+Q
Sbjct  480  MSMKIRPFFPQQ  491
```

Figure II.3. Global Alignment of the Fibrinogen Beta-chain (Bovine and Human).

Score	Expect	Method	Identities	Positives	Gaps
822 bits(2123)	0.0	Compositional matrix adjust.	380/461(82%)	420/461(91%)	0/461(0%)

```
Query  8    EGQDDRPKVGLGARGHRPYDKKKEEAPSLRPVPPPISGGGYRARPATATVGQKKVERKPP  67
            +G +D  +    ARGHRP DKK+EEAPSLRP PPPISGGGYRARPA A   QKKVERK P
Sbjct  31   QGVNDNEEGFFSARGHRPLDKKREEAPSLRPAPPPISGGGYRARPAKAAATQKKVERKAP  90

Query  68   DADGCLHADPDLGVLCPTGCKLQDTLVRQERPIRKSIEDLRNTVDSVSRTSSSTFQYITL  127
            DA GCLHADPDLGVLCPTGC+LQ+ L++QERPIR S+++L N V++VS+TSSS+FQY+ L
Sbjct  91   DAGGCLHADPDLGVLCPTGCQLQEALLQQERPIRNSVDELNNNVEAVSQTSSSSFQYMYL  150

Query  128  LKNMWKGRQNQVQDNENVVNEYSSHLEKHQLYIDETVKNNIPTKLRVLRSILENLRSKIQ  187
            LK++W+ RQ QV+DNENVVNEYSS LEKHQLYIDETV +NIPT LRVLRSILENLRSKIQ
Sbjct  151  LKDLWQKRQKQVKDNENVVNEYSSELEKHQLYIDETVNSNIPTNLRVLRSILENLRSKIQ  210

Query  188  KLESDVSTQMEYCRTPCTVTCNIPVVSGKECEKIIRNEGETSEMYLIQPEDSSKPYRVYC  247
            KLESDVS QMEYCRTPCTV+CNIPVVSGKECE+IIR  GETSEMYLIQP+ S KPYRVYC
Sbjct  211  KLESDVSAQMEYCRTPCTVSCNIPVVSGKECEEIIRKGGETSEMYLIQPDSSVKPYRVYC  270

Query  248  DMKTEKGGWTVIQNRQDGSVDFGRKWDPYKQGFGNIATNAEGKKYCGVPGEYWLGNDRIS  307
            DM TE GGWTVIQNRQDGSVDFGRKWDPYKQGFGN+ATN +GK YCG+PGEYWLGND+IS
Sbjct  271  DMNTENGGWTVIQNRQDGSVDFGRKWDPYKQGFGNVATNTDGKNYCGLPGEYWLGNDKIS  330

Query  308  QLTNMGPTKLLIEMEDWKGDKVTALYEGFTVQNEANKYQLSVSKYKGTAGNALIEGASQL  367
            QLT MGPT+LLIEMEDWKGDKV A Y GFTVQNEANKYQ+SV+KY+GTAGNAL++GASQL
Sbjct  331  QLTRMGPTELLIEMEDWKGDKVKAHYGGFTVQNEANKYQISVNKYRGTAGNALMDGASQL  390

Query  368  VGENRTMTIHNSMFFSTYDRDNDGWKTTDPRKQCSKEDGGGWWYNRCHAANPNGRYYWGG  427
            +GENRTMTIHN MFFSTYDRDNDGW T+DPRKQCSKEDGGGWWYNRCHAANPNGRYYWGG
Sbjct  391  MGENRTMTIHNGMFFSTYDRDNDGWLTSDPRKQCSKEDGGGWWYNRCHAANPNGRYYWGG  450

Query  428  AYTWDMAKHGTDDGVVWMNWQGSWYSMKKMSMKIRPYFPEQ  468
             YTWDMAKHGTDDGVVWMNW+GSWYSM+KMSMKIRP+FP+Q
Sbjct  451  QYTWDMAKHGTDDGVVWMNWKGSWYSMRKMSMKIRPFFPQQ  491
```

Figure II.4. Local Alignment of the Fibrinogen Beta-chain (Bovine and Human).

NW Score	Identities	Positives	Gaps
1994	363/455(80%)	404/455(88%)	5/455(1%)

```
Query  1    MSWSSHPPSVI--FYILSLLSSACLAYVATRDNCCILDERFGSYCPTTCGIADFLNNYQT  58
            MSWS HP ++I  FY L  LSS C+AYVATRDNCCILDERFGSYCPTTCGIADFL+ YQT
Sbjct  1    MSWSLHPRNLILYFYALLFLSSTCVAYVATRDNCCILDERFGSYCPTTCGIADFLSTYQT  60

Query  59   SVDKDLRTLEGILYQVENKTSEARELVKAIQISYNPDQPSKPNNIESATKNSKSMMEEIM  118
             VDKDL++LE IL+QVENKTSE ++L+KAIQ++YNPD+ SKPN I++AT  S+ M+EEIM
Sbjct  61   KVDKDLQSLEDILHQVENKTSEVKQLIKAIQLTYNPDESSKPNMIDAATLKSRKMLEEIM  120

Query  119  KYETLISTHESTIRFLQEVYNSNSQKIVNLRDKVVQLEANCQEPCQDTVKIHDVTGRDCQ  178
            KYE  I TH+S+IR+LQE+YNSN+QKIVNL++KV QLEA CQEPC+DTV+IHD+TG+DCQ
Sbjct  121  KYEASILTHDSSIRYLQEIYNSNNQKIVNLKEKVAQLEAQCQEPCKDTVQIHDITGKDCQ  180

Query  179  DVANKGAKESGLYFIRPLKA-KQFLVYCEIDGSGNGWTVFQKRLDGSLDFKKNWIQYKEG  237
            D+ANKGAK+SGLYFI+PLKA +QFLVYCEIDGSGNGWTVFQKRLDGS+DFKKNWIQYKEG
Sbjct  181  DIANKGAKQSGLYFIKPLKANQQFLVYCEIDGSGNGWTVFQKRLDGSVDFKKNWIQYKEG  240

Query  238  FGHLSPTGTGNTEFWLGNEKIHLISTQSSIPYVLRIQLEDWNGRTSTADYASFKVTGEND  297
            FGHLSPTGT  TEFWLGNEKIHLISTQS+IPY LR++LEDWNGRTSTADYA FKV  E D
Sbjct  241  FGHLSPTGT--TEFWLGNEKIHLISTQSAIPYALRVELEDWNGRTSTADYAMFKVGPEAD  298

Query  298  KYRLTYAYFIGGDAGDAFDGYDFGDDSSDKFFTSHNGMQFSTWDSDNDKYDGNCAEQVGI  357
            KYRLTYAYF GGDAGDAFDG+DFGDD SDKFFTSHNGMQFSTWD+DNDK++GNCAEQ G
Sbjct  299  KYRLTYAYFAGGDAGDAFDGFDFGDDPSDKFFTSHNGMQFSTWDNDNDKFEGNCAEQDGS  358

Query  358  GWWMNKCHAGHLNGVYYQGGTYSKTSTPNGYDNGIIWATWKSRWYSMKKTTMKIIPLNRL  417
            GWWMNKCHAGHLNGVYYQGGTYSK STPNGYDNGIIWATWK+RWYSMKKTTMKIIP NRL
Sbjct  359  GWWMNKCHAGHLNGVYYQGGTYSKASTPNGYDNGIIWATWKTRWYSMKKTTMKIIPFNRL  418

Query  418  AIGEGQQHQLGGAKQVGVEHHVEIEYD          444
             IGEGQQH LGGAKQV  EH  E EYD
Sbjct  419  TIGEGQQHHLGGAKQVRPEHPAETEYDSLYPEDDL  453
```

Figure II.5. Global Alignment of the Fibrinogen Gamma-chain (Bovine and Human).

Score	Expect	Method	Identities	Positives	Gaps
776 bits(2004)	0.0	Compositional matrix adjust.	363/447(81%)	404/447(90%)	5/447(1%)

```
Query  1    MSWSSHPPSVI--FYILSLLSSACLAYVATRDNCCILDERFGSYCPTTCGIADFLNNYQT  58
            MSWS HP ++I  FY L  LSS C+AYVATRDNCCILDERFGSYCPTTCGIADFL+ YQT
Sbjct  1    MSWSLHPRNLILYFYALLFLSSTCVAYVATRDNCCILDERFGSYCPTTCGIADFLSTYQT  60

Query  59   SVDKDLRTLEGILYQVENKTSEARELVKAIQISYNPDQPSKPNNIESATKNSKSMMEEIM  118
             VDKDL++LE IL+QVENKTSE ++L+KAIQ++YNPD+ SKPN I++AT  S+ M+EEIM
Sbjct  61   KVDKDLQSLEDILHQVENKTSEVKQLIKAIQLTYNPDESSKPNMIDAATLKSRKMLEEIM  120

Query  119  KYETLISTHESTIRFLQEVYNSNSQKIVNLRDKVVQLEANCQEPCQDTVKIHDVTGRDCQ  178
            KYE  I TH+S+IR+LQE+YNSN+QKIVNL++KV QLEA CQEPC+DTV+IHD+TG+DCQ
Sbjct  121  KYEASILTHDSSIRYLQEIYNSNNQKIVNLKEKVAQLEAQCQEPCKDTVQIHDITGKDCQ  180

Query  179  DVANKGAKESGLYFIRPLKA-KQFLVYCEIDGSGNGWTVFQKRLDGSLDFKKNWIQYKEG  237
            D+ANKGAK+SGLYFI+PLKA +QFLVYCEIDGSGNGWTVFQKRLDGS+DFKKNWIQYKEG
Sbjct  181  DIANKGAKQSGLYFIKPLKANQQFLVYCEIDGSGNGWTVFQKRLDGSVDFKKNWIQYKEG  240

Query  238  FGHLSPTGTGNTEFWLGNEKIHLISTQSSIPYVLRIQLEDWNGRTSTADYASFKVTGEND  297
            FGHLSPTGT  TEFWLGNEKIHLISTQS+IPY LR++LEDWNGRTSTADYA FKV  E D
Sbjct  241  FGHLSPTGT--TEFWLGNEKIHLISTQSAIPYALRVELEDWNGRTSTADYAMFKVGPEAD  298

Query  298  KYRLTYAYFIGGDAGDAFDGYDFGDDSSDKFFTSHNGMQFSTWDSDNDKYDGNCAEQVGI  357
            KYRLTYAYF GGDAGDAFDG+DFGDD SDKFFTSHNGMQFSTWD+DNDK++GNCAEQ G
Sbjct  299  KYRLTYAYFAGGDAGDAFDGFDFGDDPSDKFFTSHNGMQFSTWDNDNDKFEGNCAEQDGS  358

Query  358  GWWMNKCHAGHLNGVYYQGGTYSKTSTPNGYDNGIIWATWKSRWYSMKKTTMKIIPLNRL  417
            GWWMNKCHAGHLNGVYYQGGTYSK STPNGYDNGIIWATWK+RWYSMKKTTMKIIP NRL
Sbjct  359  GWWMNKCHAGHLNGVYYQGGTYSKASTPNGYDNGIIWATWKTRWYSMKKTTMKIIPFNRL  418

Query  418  AIGEGQQHQLGGAKQVGVEHHVEIEYD  444
             IGEGQQH LGGAKQV  EH  E EYD
Sbjct  419  TIGEGQQHHLGGAKQVRPEHPAETEYD  445
```

Figure II.6. Local Alignment of the Fibrinogen Gamma-chain (Bovine and Human).

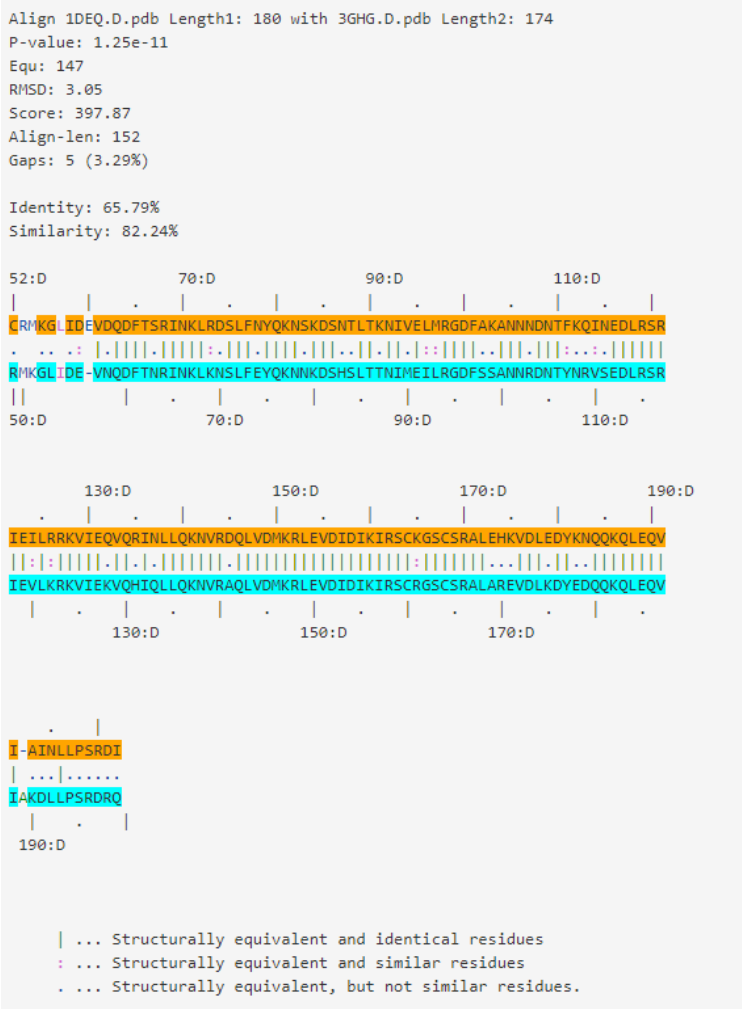

Figure II.7. Rigid Alignment of the PDB files of the Fibrinogen Alpha-chain (Bovine and Human).

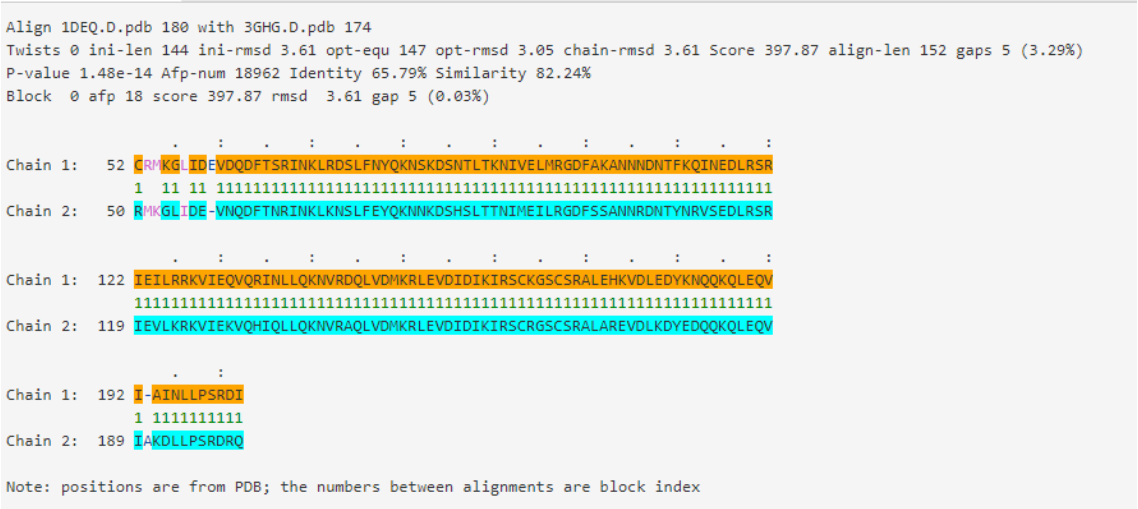

Figure II.8. Flexible Alignment of the PDB files of the Fibrinogen Alpha-chain (Bovine and Human).

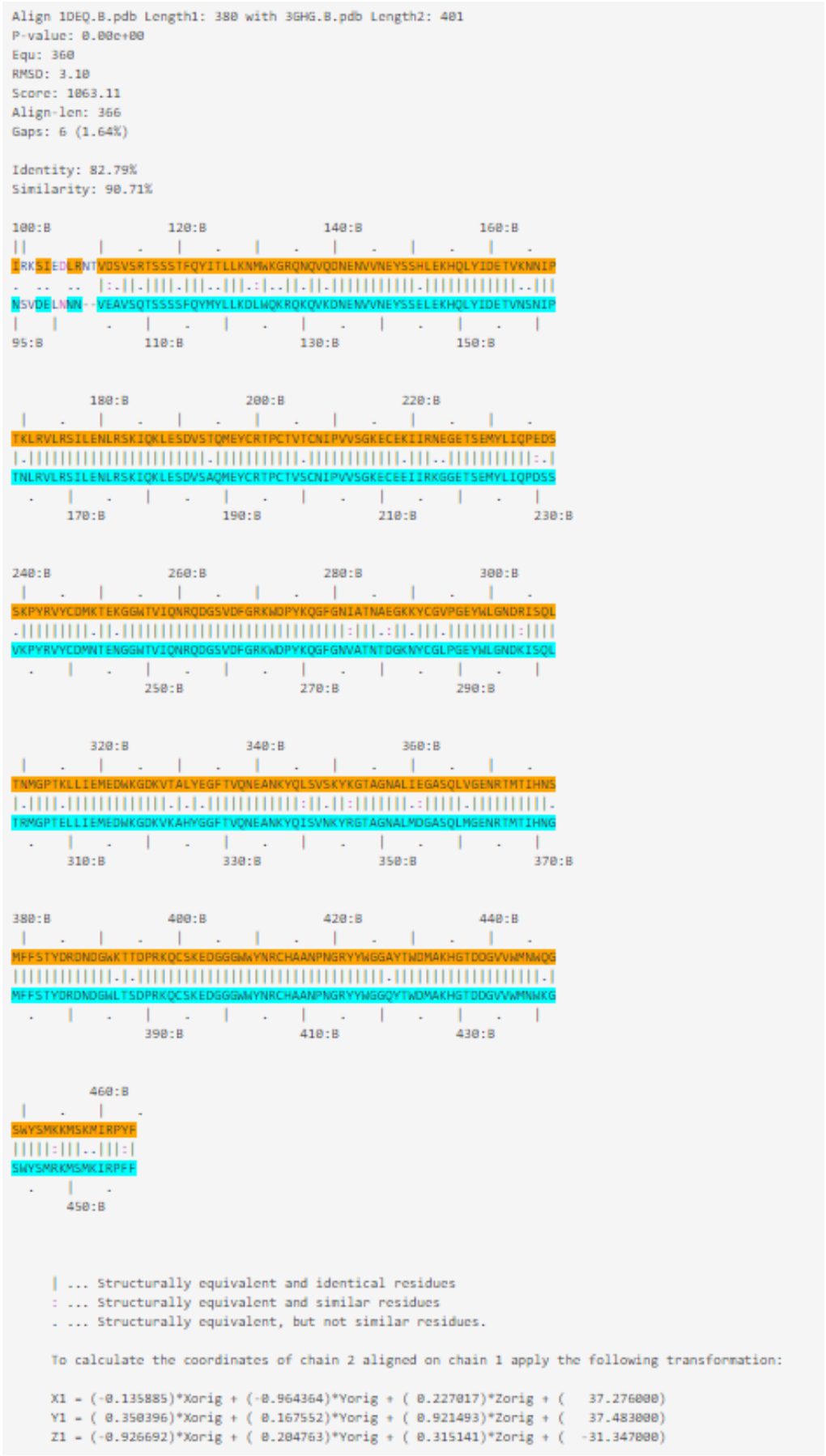

Figure II.9. Rigid Alignment of the PDB files of the Fibrinogen Beta-chain (Bovine and Human).

```
Align 1DEQ.B.pdb 380 with 3GHG.B.pdb 401
Twists 1 ini-len 368 ini-rmsd 2.40 opt-equ 378 opt-rmsd 2.33 chain-rmsd 4.13 Score 1063.11 align-len 378 gaps 0 (0.00%)
P-value 0.00e+00 Afp-num 47917 Identity 83.33% Similarity 92.59%
Block  0 afp  4 score 93.15 rmsd  1.31 gap 0 (0.00%)
Block  1 afp 42 score 973.81 rmsd  2.27 gap 5 (0.01%)

                .    :    .    :    .    :    .    :    .    :    .    :    .    :
Chain 1:   88 KLQDTLVRQERPIRKSIEDLRNTVDSVSRTSSSTFQYITLLKNMWKGRQNQVQDNENVVNEYSSHLEKHQ
              1111111111111111111111111111111111122222222222222222222222222222222222
Chain 2:   81 QLQEALLQQERPIRNSVDELNNNVEAVSQTSSSSFQYMYLLKDLWQKRQKQVKDNENVVNEYSSELEKHQ

                .    :    .    :    .    :    .    :    .    :    .    :    .    :
Chain 1:  158 LYIDETVKNNIPTKLRVLRSILENLRSKIQKLESDVSTQMEYCRTPCTVTCNIPVVSGKECEKIIRNEGE
              2222222222222222222222222222222222222222222222222222222222222222222222
Chain 2:  151 LYIDETVNSNIPTNLRVLRSILENLRSKIQKLESDVSAQMEYCRTPCTVSCNIPVVSGKECEEIIRKGGE

                .    :    .    :    .    :    .    :    .    :    .    :    .    :
Chain 1:  228 TSEMYLIQPEDSSKPYRVYCDMKTEKGGWTVIQNRQDGSVDFGRKWDPYKQGFGNIATNAEGKKYCGVPG
              2222222222222222222222222222222222222222222222222222222222222222222222
Chain 2:  221 TSEMYLIQPDSSVKPYRVYCDMNTENGGWTVIQNRQDGSVDFGRKWDPYKQGFGNVATNTDGKNYCGLPG

                .    :    .    :    .    :    .    :    .    :    .    :    .    :
Chain 1:  298 EYWLGNDRISQLTNMGPTKLLIEMEDWKGDKVTALYEGFTVQNEANKYQLSVSKYKGTAGNALIEGASQL
              2222222222222222222222222222222222222222222222222222222222222222222222
Chain 2:  291 EYWLGNDKISQLTRMGPTELLIEMEDWKGDKVKAHYGGFTVQNEANKYQISVNKYRGTAGNALMDGASQL

                .    :    .    :    .    :    .    :    .    :    .    :    .    :
Chain 1:  368 VGENRTMTIHNSMFFSTYDRDNDGWKTTDPRKQCSKEDGGGWWYNRCHAANPNGRYYWGGAYTWDMAKHG
              2222222222222222222222222222222222222222222222222222222222222222222222
Chain 2:  361 MGENRTMTIHNGMFFSTYDRDNDGWLTSDPRKQCSKEDGGGWWYNRCHAANPNGRYYWGGQYTWDMAKHG

                .    :    .    :    .
Chain 1:  438 TDDGVVWMNWQGSWYSMKKMSKMIRPYF
              22222222222222222222222222
Chain 2:  431 TDDGVVWMNWKGSWYSMRKMSMKIRPFF

Note: positions are from PDB; the numbers between alignments are block index
```

Figure II.9. Flexible Alignment of the PDB files of the Fibrinogen Beta-chain (Bovine and Human). Results show two blocks of aligned structures.

Figure II.10. Rigid Alignment of the PDB files of the Fibrinogen Gamma-chain (Bovine and Human).

```
Align 1DEQ.C.pdb 370 with 3GHG.C.pdb 381
Twists 0 ini-len 360 ini-rmsd 3.85 opt-equ 354 opt-rmsd 3.10 chain-rmsd 3.85 Score 1038.70 align-len 360 gaps 6 (1.67%)
P-value 0.00e+00 Afp-num 45430 Identity 81.67% Similarity 90.56%
Block  0 afp 45 score 1038.70 rmsd  3.85 gap 6 (0.02%)

                .   :   .   :   .   :   .   :   .   :   .   :   .   :
Chain 1:   37 DKDLRTLEG--ILYQVENKTSEARELVKAIQISYNPDQPSKPNNIESATKNSKSMMEEIMKYETLISTHE
              11  1  11  1111111111111111111111111111111111111111111111111111111111
Chain 2:   35 KVDKDLQSLEDILHQVENKTSEVKQLIKAIQLTYNPDESSKPNMIDAATLKSRKMLEEIMKYEASILTHD

                .   :   .   :   .   :   .   :   .   :   .   :   .   :
Chain 1:  105 STIRFLQEIYNSNSQKIVNLRDKVVQLEANCQEPCQDTVKIHDVTGRDCQDVANKGAKESGLYFIRPLKA
              1111111111111111111111111111111111111111111111111111111111111111111111
Chain 2:  105 SSIRYLQEIYNSNNQKIVNLKEKVAQLEAQCQEPCKDTVQIHDITGKDCQDIANKGAKQSGLYFIKPLKA

                .   :   .   :   .   :   .   :   .   :   .   :   .   :
Chain 1:  175 KQQFLVYCEIDGSGNGWTVFQKRLDGSLDFKKNWIQYKEGFGHLSPTGNTEFWLGNEKIHLISTQSTIPY
              1111111111111111111111111111111111111111111111111111111111111111111111
Chain 2:  175 NQQFLVYCEIDGSGNGWTVFQKRLDGSVDFKKNWIQYKEGFGHLSPTGTTEFWLGNEKIHLISTQSAIPY

                .   :   .   :   .   :   .   :   .   :   .   :   .   :
Chain 1:  245 VLRIQLEDWNGRTSTADYASFKVTGENDKYRLTYAYFIGGDAGDAFDGYDFGDDSSDKFFTSHNGMQFST
              1111111111111111111111111111111111111111111111111111111111111111111111
Chain 2:  245 ALRVELEDWNGRTSTADYAMFKVGPEADKYRLTYAYFAGGDAGDAFDGFDFGDDPSDKFFTSHNGMQFST

                .   :   .   :   .   :   .   :   .   :   .   :   .   :
Chain 1:  315 WDSDNDKYDGNCAEQDGSGWWMNKCHAGHLNGVYYQGGTYSKTSTPNGYDNGIIWATWKSRWYSMKKTTM
              1111111111111111111111111111111111111111111111111111111111111111111111
Chain 2:  315 WDNDNDKFEGNCAEQDGSGWWMNKCHAGHLNGVYYQGGTYSKASTPNGYDNGIIWATWKTRWYSMKKTTM

                .   :
Chain 1:  385 KIIPLNRLAI
              1111111111
Chain 2:  385 KIIPFNRLTI

Note: positions are from PDB; the numbers between alignments are block index
```

Figure II.11. Flexible Alignment of the PDB files of the Fibrinogen Gamma-chain (Bovine and Human).

NW Score	Identities	Positives	Gaps
1844	385/615(63%)	389/615(63%)	0/615(0%)

```
Query  1                      EDGSDPPSGDFLTEGGGVRGPRLVERQQSACKETGWPFCSD  41
                              EDGSDPPSGDFLTEGGGVRGPRLVERQQSACKETGWPFCSD
Sbjct  1    MFSVRDLCLVLSLVGAIKTEDGSDPPSGDFLTEGGGVRGPRLVERQQSACKETGWPFCSD  60

Query  42   EDWNTKCPSGCRMKGLIDEVDQDFTSRINKLRDSLFNYQKNSKDSNTLTKNIVELMRGDF  101
            EDWNTKCPSGCRMKGLIDEVDQDFTSRINKLRDSLFNYQKNSKDSNTLTKNIVELMRGDF
Sbjct  61   EDWNTKCPSGCRMKGLIDEVDQDFTSRINKLRDSLFNYQKNSKDSNTLTKNIVELMRGDF  120

Query  102  AKANNNDNTFKQINEDLRSRIEILRRKVIEQVQRINLLQKNVRDQLVDMKRLEVDIDIKI  161
            AKANNNDNTFKQI+EDLRSRIEILRRKVIEQVQRI +LQKNVRDQLVDMKRLEVDIDIKI
Sbjct  121  AKANNNDNTFKQISEDLRSRIEILRRKVIEQVQRIKVLQKNVRDQLVDMKRLEVDIDIKI  180

Query  162  RSCKGSCSRALEHKVDLEDYKNQQKQLEQVIAINLLPSRDIQYLPILKMSTITGPVPREF  221
            RSCKGSCSRALEHKVDLEDYKNQQKQLEQVIAINLLPSRDIQYLP++KMSTITGPVPREF
Sbjct  181  RSCKGSCSRALEHKVDLEDYKNQQKQLEQVIAINLLPSRDIQYLPLIKMSTITGPVPREF  240

Query  222  KSQLQEAPLEWKALLEMQQTKMVLETFGGDGHARGDSVSQGTGLAPGSPRKPGTSSIGNV  281
            KSQLQEAPLEWKALLEMQQTKMVLETFGGDGHARGDSVSQGTGLAPGSPRKPGTSSIGNV
Sbjct  241  KSQLQEAPLEWKALLEMQQTKMVLETFGGDGHARGDSVSQGTGLAPGSPRKPGTSSIGNV  300

Query  282  NPGSYGPGSSGTWNPGRPEPGSAGTWNPGRPEPGSAGTWNPGRPEPGSAGTWNPGRPEPG  341
            NPGSYGPGSSGTWNPGRPEPGSAGTWNPGRPEPGSAGTWNPGRPEPGSAGTWNPGRPEPG
Sbjct  301  NPGSYGPGSSGTWNPGRPEPGSAGTWNPGRPEPGSAGTWNPGRPEPGSAGTWNPGRPEPG  360

Query  342  SAGTWNPGRPEPGSAGTWNTGSSGSSSFRPDSSGHGNIRPSSPDWGTFR             390
            SAGTWNPGRPEPGSAGTWNTGSSGSSSFRPDSSGHGNIRPSSPDWGTFR
Sbjct  361  SAGTWNPGRPEPGSAGTWNTGSSGSSSFRPDSSGHGNIRPSSPDWGTFREEGSVSSGTKQ  420

Sbjct  421  EFHTGKLVTTKGDKELLIDNEKVTSGHTTTTRRSCSKVITKTVTNADGRTETTKEVVKSE  480

Sbjct  481  DGSDCGDADFDWHHTFPSRGNLDDFFHRDKDDFFTRSSHEFDGRTGLAPEFAALGESGSS  540

Sbjct  541  SSKTSTHSKQFVSSSTTVNRGGSAIESKHFKMEDEAESLEDLGFKGAHGTQKGHTKARPA  600

Sbjct  601  RGIHTSPLGEPSLTP  615
```

Figure II.12. Global Alignment of the PDB file with the UniProt sequence for the Alpha-Chain (Bovine).

NW Score	Identities	Positives	Gaps
2157	406/468(87%)	406/468(86%)	0/468(0%)

```
Sbjct  1    QFPTDYDEGQDDRPKVGLGARGHRPYDKKKEEAPSLRPVPPPISGGGYRARPATATVGQK  60

Query  1    KVERKPPDADGCLHADPDLGVLCPTGCKLQDTLVRQERPIRKSIEDLRNTVDSVSRTSSS  60
            KVERKPPDADGCLHADPDLGVLCPTGCKLQDTLVRQERPIRKSIEDLRNTVDSVSRTSSS
Sbjct  61   KVERKPPDADGCLHADPDLGVLCPTGCKLQDTLVRQERPIRKSIEDLRNTVDSVSRTSSS  120

Query  61   TFQYITLLKNMWKGRQNQVQDNENVVNEYSSHLEKHQLYIDETVKNNIPTKLRVLRSILE  120
            TFQYITLLKNMWKGRQNQVQDNENVVNEYSSHLEKHQLYIDETVKNNIPTKLRVLRSILE
Sbjct  121  TFQYITLLKNMWKGRQNQVQDNENVVNEYSSHLEKHQLYIDETVKNNIPTKLRVLRSILE  180

Query  121  NLRSKIQKLESDVSTQMEYCRTPCTVTCNIPVVSGKECEKIIRNEGETSEMYLIQPEDSS  180
            NLRSKIQKLESDVSTQMEYCRTPCTVTCNIPVVSGKECEKIIRNEGETSEMYLIQPEDSS
Sbjct  181  NLRSKIQKLESDVSTQMEYCRTPCTVTCNIPVVSGKECEKIIRNEGETSEMYLIQPEDSS  240

Query  181  KPYRVYCDMKTEKGGWTVIQNRQDGSVDFGRKWDPYKQGFGNIATNAEGKKYCGVPGEYW  240
            KPYRVYCDMKTEKGGWTVIQNRQDGSVDFGRKWDPYKQGFGNIATNAEGKKYCGVPGEYW
Sbjct  241  KPYRVYCDMKTEKGGWTVIQNRQDGSVDFGRKWDPYKQGFGNIATNAEGKKYCGVPGEYW  300

Query  241  LGNDRISQLTNMGPTKLLIEMEDWKGDKVTALYEGFTVQNEANKYQLSVSKYKGTAGNAL  300
            LGNDRISQLTNMGPTKLLIEMEDWKGDKVTALYEGFTVQNEANKYQLSVSKYKGTAGNAL
Sbjct  301  LGNDRISQLTNMGPTKLLIEMEDWKGDKVTALYEGFTVQNEANKYQLSVSKYKGTAGNAL  360

Query  301  IEGASQLVGENRTMTIHNSMFFSTYDRDNDGWKTTDPRKQCSKEDGGGWWYNRCHAANPN  360
            IEGASQLVGENRTMTIHNSMFFSTYDRDNDGWKTTDPRKQCSKEDGGGWWYNRCHAANPN
Sbjct  361  IEGASQLVGENRTMTIHNSMFFSTYDRDNDGWKTTDPRKQCSKEDGGGWWYNRCHAANPN  420

Query  361  GRYYWGGAYTWDMAKHGTDDGVVWMNWQGSWYSMKKMSKMIRPYFPEQ  408
            GRYYWGGAYTWDMAKHGTDDGVVWMNWQGSWYSMKKMS  IRPYFPEQ
Sbjct  421  GRYYWGGAYTWDMAKHGTDDGVVWMNWQGSWYSMKKMSMKIRPYFPEQ  468
```

Figure II.13. Global Alignment of the PDB file with the UniProt sequence for the Beta-Chain (Bovine).

NW Score	Identities	Positives	Gaps
2114	403/445(91%)	405/445(91%)	3/445(0%)

```
Query  1                          YVATRDNCCILDERFGSYCPTTCGIADFLNNYQTSV  36
                                  YVATRDNCCILDERFGSYCPTTCGIADFLNNYQTSV
Sbjct  1    MSWSSHPPSVIFYILSLLSSACLAYVATRDNCCILDERFGSYCPTTCGIADFLNNYQTSV  60

Query  37   DKDLRTLEGILYQVENKTSEARELVKAIQISYNPDQPSKPNNIESATKNSKSMMEEIMKY  96
            DKDLRTLEGILYQVENKTSEARELVKAIQISYNPDQPSKPNNIESATKNSKSMMEEIMKY
Sbjct  61   DKDLRTLEGILYQVENKTSEARELVKAIQISYNPDQPSKPNNIESATKNSKSMMEEIMKY  120

Query  97   ETLISTHESTIRFLQEIYNSNSQKIVNLRDKVVQLEANCQEPCQDTVKIHDVTGRDCQDV  156
            ETLISTHESTIRFLQE+YNSNSQKIVNLRDKVVQLEANCQEPCQDTVKIHDVTGRDCQDV
Sbjct  121  ETLISTHESTIRFLQEVYNSNSQKIVNLRDKVVQLEANCQEPCQDTVKIHDVTGRDCQDV  180

Query  157  ANKGAKESGLYFIRPLKAKQQFLVYCEIDGSGNGWTVFQKRLDGSLDFKKNWIQYKEGFG  216
            ANKGAKESGLYFIRPLKAKQ FLVYCEIDGSGNGWTVFQKRLDGSLDFKKNWIQYKEGFG
Sbjct  181  ANKGAKESGLYFIRPLKAKQ-FLVYCEIDGSGNGWTVFQKRLDGSLDFKKNWIQYKEGFG  239

Query  217  HLSPTG--NTEFWLGNEKIHLISTQSTIPYVLRIQLEDWNGRTSTADYASFKVTGENDKY  274
            HLSPTG  NTEFWLGNEKIHLISTQS+IPYVLRIQLEDWNGRTSTADYASFKVTGENDKY
Sbjct  240  HLSPTGTGNTEFWLGNEKIHLISTQSSIPYVLRIQLEDWNGRTSTADYASFKVTGENDKY  299

Query  275  RLTYAYFIGGDAGDAFDGYDFGDDSSDKFFTSHNGMQFSTWDSDNDKYDGNCAEQDGSGW  334
            RLTYAYFIGGDAGDAFDGYDFGDDSSDKFFTSHNGMQFSTWDSDNDKYDGNCAEQ G GW
Sbjct  300  RLTYAYFIGGDAGDAFDGYDFGDDSSDKFFTSHNGMQFSTWDSDNDKYDGNCAEQVGIGW  359

Query  335  WMNKCHAGHLNGVYYQGGTYSKTSTPNGYDNGIIWATWKSRWYSMKKTTMKIIPLNRLAI  394
            WMNKCHAGHLNGVYYQGGTYSKTSTPNGYDNGIIWATWKSRWYSMKKTTMKIIPLNRLAI
Sbjct  360  WMNKCHAGHLNGVYYQGGTYSKTSTPNGYDNGIIWATWKSRWYSMKKTTMKIIPLNRLAI  419

Query  395  GEGQQHQLGGAKQAGDV          411
            GEGQQHQLGGAKQ G
Sbjct  420  GEGQQHQLGGAKQVGVEHHVEIEYD  444
```

Figure II.14. Global Alignment of the PDB file with the UniProt sequence for the Gamma-Chain (Bovine).

NW Score	Identities	Positives	Gaps
2668	562/866(65%)	562/866(64%)	0/866(0%)

```
Query  1                      ADSGEGDFLAEGGGVRGPRVVERHQSACKDSDWPFCSDEDW  41
                              ADSGEGDFLAEGGGVRGPRVVERHQSACKDSDWPFCSDEDW
Sbjct  1    MFSMRIVCLVLSVVGTAWTADSGEGDFLAEGGGVRGPRVVERHQSACKDSDWPFCSDEDW  60

Query  42   NYKCPSGCRMKGLIDEVNQDFTNRINKLKNSLFEYQKNNKDSHSLTTNIMEILRGDFSSA  101
            NYKCPSGCRMKGLIDEVNQDFTNRINKLKNSLFEYQKNNKDSHSLTTNIMEILRGDFSSA
Sbjct  61   NYKCPSGCRMKGLIDEVNQDFTNRINKLKNSLFEYQKNNKDSHSLTTNIMEILRGDFSSA  120

Query  102  NNRDNTYNRVSEDLRSRIEVLKRKVIEKVQHIQLLQKNVRAQLVDMKRLEVDIDIKIRSC  161
            NNRDNTYNRVSEDLRSRIEVLKRKVIEKVQHIQLLQKNVRAQLVDMKRLEVDIDIKIRSC
Sbjct  121  NNRDNTYNRVSEDLRSRIEVLKRKVIEKVQHIQLLQKNVRAQLVDMKRLEVDIDIKIRSC  180

Query  162  RGSCSRALAREVDLKDYEDQQKQLEQVIAKDLLPSRDRQHLPLIKMKPVPDLVPGNFKSQ  221
            RGSCSRALAREVDLKDYEDQQKQLEQVIAKDLLPSRDRQHLPLIKMKPVPDLVPGNFKSQ
Sbjct  181  RGSCSRALAREVDLKDYEDQQKQLEQVIAKDLLPSRDRQHLPLIKMKPVPDLVPGNFKSQ  240

Query  222  LQKVPPEWKALTDMPQMRMELERPGGNEITRGGSTSYGTGSETESPRNPSSAGSWNSGSS  281
            LQKVPPEWKALTDMPQMRMELERPGGNEITRGGSTSYGTGSETESPRNPSSAGSWNSGSS
Sbjct  241  LQKVPPEWKALTDMPQMRMELERPGGNEITRGGSTSYGTGSETESPRNPSSAGSWNSGSS  300

Query  282  GPGSTGNRNPGSSGTGGTATWKPGSSGPGSTGSWNSGSSGTGSTGNQNPGSPRPGSTGTW  341
            GPGSTGNRNPGSSGTGGTATWKPGSSGPGSTGSWNSGSSGTGSTGNQNPGSPRPGSTGTW
Sbjct  301  GPGSTGNRNPGSSGTGGTATWKPGSSGPGSTGSWNSGSSGTGSTGNQNPGSPRPGSTGTW  360

Query  342  NPGSSERGSAGHWTSESSVSGSTGQWHSESGSFRPDSPGSGNARPNNPDWGTFEEVSGNV  401
            NPGSSERGSAGHWTSESSVSGSTGQWHSESGSFRPDSPGSGNARPNNPDWGTFEEVSGNV
Sbjct  361  NPGSSERGSAGHWTSESSVSGSTGQWHSESGSFRPDSPGSGNARPNNPDWGTFEEVSGNV  420

Query  402  SPGTRREYHTEKLVTSKGDKELRTGKEKVTSGSTTTTRRSCSKTVTKTVIGPDGHKEVTK  461
            SPGTRREYHTEKLVTSKGDKELRTGKEKVTSGSTTTTRRSCSKTVTKTVIGPDGHKEVTK
Sbjct  421  SPGTRREYHTEKLVTSKGDKELRTGKEKVTSGSTTTTRRSCSKTVTKTVIGPDGHKEVTK  480

Query  462  EVVTSEDGSDCPEAMDLGTLSGIGTLDGFRHRHPDEAAFFDTASTGKTFPGFFSPMLGEF  521
            EVVTSEDGSDCPEAMDLGTLSGIGTLDGFRHRHPDEAAFFDTASTGKTFPGFFSPMLGEF
Sbjct  481  EVVTSEDGSDCPEAMDLGTLSGIGTLDGFRHRHPDEAAFFDTASTGKTFPGFFSPMLGEF  540

Query  522  VSETESRGSESGIFTNTKESSSHHPGIAEFPSRGKSSSYSK                      562
            VSETESRGSESGIFTNTKESSSHHPGIAEFPSRGKSSSYSK
Sbjct  541  VSETESRGSESGIFTNTKESSSHHPGIAEFPSRGKSSSYSKQFTSSTSYNRGDSTFESKS  600

Sbjct  601  YKMADEAGSEADHEGTHSTKRGHAKSRPVRDCDDVLQTHPSGTQSGIFNIKLPGSSKIFS  660

Sbjct  661  VYCDQETSLGGWLLIQQRMDGSLNFNRTWQDYKRGFGSLNDEGEGEFWLGNDYLHLLTQR  720

Sbjct  721  GSVLRVELEDWAGNEAYAEYHFRVGSEAEGYALQVSSYEGTAGDALIEGSVEEGAEYTSH  780

Sbjct  781  NNMQFSTFDRDADQWEENCAEVYGGGWWYNNCQAANLNGIYYPGGSYDPRNNSPYEIENG  840

Sbjct  841  VVWVSFRGADYSLRAVRMKIRPLVTQ  866
```

Figure II.15. Global Alignment of the PDB file with the UniProt sequence for the Alpha-Chain (Human).

NW Score	Identities	Positives	Gaps
2484	461/491(94%)	461/491(93%)	0/491(0%)

```
Query  1    QGVNDNEEGFFSARGHRPLDKKREEAPSLR  30
            QGVNDNEEGFFSARGHRPLDKKREEAPSLR
Sbjct  1    MKRMVSWSFHKLKTMKHLLLLLLCVFLVKSQGVNDNEEGFFSARGHRPLDKKREEAPSLR  60

Query  31   PAPPPISGGGYRARPAKAAATQKKVERKAPDAGGCLHADPDLGVLCPTGCQLQEALLQQE  90
            PAPPPISGGGYRARPAKAAATQKKVERKAPDAGGCLHADPDLGVLCPTGCQLQEALLQQE
Sbjct  61   PAPPPISGGGYRARPAKAAATQKKVERKAPDAGGCLHADPDLGVLCPTGCQLQEALLQQE  120

Query  91   RPIRNSVDELNNNVEAVSQTSSSSFQYMYLLKDLWQKRQKQVKDNENVVNEYSSELEKHQ  150
            RPIRNSVDELNNNVEAVSQTSSSSFQYMYLLKDLWQKRQKQVKDNENVVNEYSSELEKHQ
Sbjct  121  RPIRNSVDELNNNVEAVSQTSSSSFQYMYLLKDLWQKRQKQVKDNENVVNEYSSELEKHQ  180

Query  151  LYIDETVNSNIPTNLRVLRSILENLRSKIQKLESDVSAQMEYCRTPCTVSCNIPVVSGKE  210
            LYIDETVNSNIPTNLRVLRSILENLRSKIQKLESDVSAQMEYCRTPCTVSCNIPVVSGKE
Sbjct  181  LYIDETVNSNIPTNLRVLRSILENLRSKIQKLESDVSAQMEYCRTPCTVSCNIPVVSGKE  240

Query  211  CEEIIRKGGETSEMYLIQPDSSVKPYRVYCDMNTENGGWTVIQNRQDGSVDFGRKWDPYK  270
            CEEIIRKGGETSEMYLIQPDSSVKPYRVYCDMNTENGGWTVIQNRQDGSVDFGRKWDPYK
Sbjct  241  CEEIIRKGGETSEMYLIQPDSSVKPYRVYCDMNTENGGWTVIQNRQDGSVDFGRKWDPYK  300

Query  271  QGFGNVATNTDGKNYCGLPGEYWLGNDKISQLTRMGPTELLIEMEDWKGDKVKAHYGGFT  330
            QGFGNVATNTDGKNYCGLPGEYWLGNDKISQLTRMGPTELLIEMEDWKGDKVKAHYGGFT
Sbjct  301  QGFGNVATNTDGKNYCGLPGEYWLGNDKISQLTRMGPTELLIEMEDWKGDKVKAHYGGFT  360

Query  331  VQNEANKYQISVNKYRGTAGNALMDGASQLMGENRTMTIHNGMFFSTYDRDNDGWLTSDP  390
            VQNEANKYQISVNKYRGTAGNALMDGASQLMGENRTMTIHNGMFFSTYDRDNDGWLTSDP
Sbjct  361  VQNEANKYQISVNKYRGTAGNALMDGASQLMGENRTMTIHNGMFFSTYDRDNDGWLTSDP  420

Query  391  RKQCSKEDGGGWWYNRCHAANPNGRYYWGGQYTWDMAKHGTDDGVVWMNWKGSWYSMRKM  450
            RKQCSKEDGGGWWYNRCHAANPNGRYYWGGQYTWDMAKHGTDDGVVWMNWKGSWYSMRKM
Sbjct  421  RKQCSKEDGGGWWYNRCHAANPNGRYYWGGQYTWDMAKHGTDDGVVWMNWKGSWYSMRKM  480

Query  451  SMKIRPFFPQQ  461
            SMKIRPFFPQQ
Sbjct  481  SMKIRPFFPQQ  491
```

Figure II.16. Global Alignment of the PDB file with the UniProt sequence for the Beta-Chain (Human).

NW Score	Identities	Positives	Gaps
2161	408/453(90%)	409/453(90%)	16/453(3%)

```
Query  1    YVATRDNCCILDERFGSYCPTTCGIADFLSTYQT  34
            YVATRDNCCILDERFGSYCPTTCGIADFLSTYQT
Sbjct  1    MSWSLHPRNLILYFYALLFLSSTCVAYVATRDNCCILDERFGSYCPTTCGIADFLSTYQT  60

Query  35   KVDKDLQSLEDILHQVENKTSEVKQLIKAIQLTYNPDESSKPNMIDAATLKSRKMLEEIM  94
            KVDKDLQSLEDILHQVENKTSEVKQLIKAIQLTYNPDESSKPNMIDAATLKSRKMLEEIM
Sbjct  61   KVDKDLQSLEDILHQVENKTSEVKQLIKAIQLTYNPDESSKPNMIDAATLKSRKMLEEIM  120

Query  95   KYEASILTHDSSIRYLQEIYNSNNQKIVNLKEKVAQLEAQCQEPCKDTVQIHDITGKDCQ  154
            KYEASILTHDSSIRYLQEIYNSNNQKIVNLKEKVAQLEAQCQEPCKDTVQIHDITGKDCQ
Sbjct  121  KYEASILTHDSSIRYLQEIYNSNNQKIVNLKEKVAQLEAQCQEPCKDTVQIHDITGKDCQ  180

Query  155  DIANKGAKQSGLYFIKPLKANQQFLVYCEIDGSGNGWTVFQKRLDGSVDFKKNWIQYKEG  214
            DIANKGAKQSGLYFIKPLKANQQFLVYCEIDGSGNGWTVFQKRLDGSVDFKKNWIQYKEG
Sbjct  181  DIANKGAKQSGLYFIKPLKANQQFLVYCEIDGSGNGWTVFQKRLDGSVDFKKNWIQYKEG  240

Query  215  FGHLSPTGTTEFWLGNEKIHLISTQSAIPYALRVELEDWNGRTSTADYAMFKVGPEADKY  274
            FGHLSPTGTTEFWLGNEKIHLISTQSAIPYALRVELEDWNGRTSTADYAMFKVGPEADKY
Sbjct  241  FGHLSPTGTTEFWLGNEKIHLISTQSAIPYALRVELEDWNGRTSTADYAMFKVGPEADKY  300

Query  275  RLTYAYFAGGDAGDAFDGFDFGDDPSDKFFTSHNGMQFSTWDNDNDKFEGNCAEQDGSGW  334
            RLTYAYFAGGDAGDAFDGFDFGDDPSDKFFTSHNGMQFSTWDNDNDKFEGNCAEQDGSGW
Sbjct  301  RLTYAYFAGGDAGDAFDGFDFGDDPSDKFFTSHNGMQFSTWDNDNDKFEGNCAEQDGSGW  360

Query  335  WMNKCHAGHLNGVYYQGGTYSKASTPNGYDNGIIWATWKTRWYSMKKTTMKIIPFNRLTI  394
            WMNKCHAGHLNGVYYQGGTYSKASTPNGYDNGIIWATWKTRWYSMKKTTMKIIPFNRLTI
Sbjct  361  WMNKCHAGHLNGVYYQGGTYSKASTPNGYDNGIIWATWKTRWYSMKKTTMKIIPFNRLTI  420

Query  395  GEGQQHHLGGAKQA----------------GDV  411
            GEGQQHHLGGAKQ                  D+
Sbjct  421  GEGQQHHLGGAKQVRPEHPAETEYDSLYPEDDL  453
```

Figure II.17. Global Alignment of the PDB file with the UniProt sequence for the Gamma-Chain (Human).

b) Albumin

NW Score	Identities	Positives	Gaps
2553	465/609(76%)	536/609(88%)	1/609(0%)

```
Query  1    MKWVTFISLLLLFSSAYSRGVFRRDTHKSEIAHRFKDLGEEHFKGLVLIAFSQYLQQCPF  60
            MKWVTFISLL LFSSAYSRGVFRRD HKSE+AHRFKDLGEE+FK LVLIAF+QYLQQCPF
Sbjct  1    MKWVTFISLLFLFSSAYSRGVFRRDAHKSEVAHRFKDLGEENFKALVLIAFAQYLQQCPF  60

Query  61   DEHVKLVNELTEFAKTCVADESHAGCEKSLHTLFGDELCKVASLRETYGDMADCCEKQEP  120
            ++HVKLVNE+TEFAKTCVADES   C+KSLHTLFGD+LC VA+LRETYG+MADCC KQEP
Sbjct  61   EDHVKLVNEVTEFAKTCVADESAENCDKSLHTLFGDKLCTVATLRETYGEMADCCAKQEP  120

Query  121  ERNECFLSHKDDSPDLPKL-KPDPNTLCDEFKADEKKFWGKYLYEIARRHPYFYAPELLY  179
            ERNECFL HKDD+P+LP+L +P+ + +C  F  +E+ F  KYLYEIARRHPYFYAPELL+
Sbjct  121  ERNECFLQHKDDNPNLPRLVRPEVDVMCTAFHDNEETFLKKYLYEIARRHPYFYAPELLF  180

Query  180  YANKYNGVFQECCQAEDKGACLLPKIETMREKVLASSARQRLRCASIQKFGERALKAWSV  239
            +A +Y   F ECCQA DK ACLLPK++ +R++  ASSA+QRL+CAS+QKFGERA KAW+V
Sbjct  181  FAKRYKAAFTECCQAADKAACLLPKLDELRDEGKASSAKQRLKCASLQKFGERAFKAWAV  240

Query  240  ARLSQKFPKAEFVEVTKLVTDLTKVHKECCHGDLLECADDRADLAKYICDNQDTISSKLK  299
            ARLSQ+FPKAEF EV+KLVTDLTKVH ECCHGDLLECADDRADLAKYIC+NQD+ISSKLK
Sbjct  241  ARLSQRFPKAEFAEVSKLVTDLTKVHTECCHGDLLECADDRADLAKYICENQDSISSKLK  300

Query  300  ECCDKPLLEKSHCIAEVEKDAIPENLPPLTADFAEDKDVCKNYQEAKDAFLGSFLYEYSR  359
            ECC+KPLLEKSHCIAEVE D +P +LP L ADF E KDVCKNY EAKD FLG FLYEY+R
Sbjct  301  ECCEKPLLEKSHCIAEVENDEMPADLPSLAADFVESKDVCKNYAEAKDVFLGMFLYEYAR  360

Query  360  RHPEYAVSVLLRLAKEYEATLEECCAKDDPHACYSTVFDKLKHLVDEPQNLIKQNCDQFE  419
            RHP+Y+V +LLRLAK YE TLE+CCA  DPH CY+ VFD+ K LV+EPQNLIKQNC+ FE
Sbjct  361  RHPDYSVVLLLRLAKTYETTLEKCCAAADPHECYAKVFDEFKPLVEEPQNLIKQNCELFE  420

Query  420  KLGEYGFQNALIVRYTRKVPQVSTPTLVEVSRSLGKVGTRCCTKPESERMPCTEDYLSLI  479
            +LGEY FQNAL+VRYT+KVPQVSTPTLVEVSR+LGKVG++CC  PE++RMPC EDYLS++
Sbjct  421  QLGEYKFQNALLVRYTKKVPQVSTPTLVEVSRNLGKVGSKCCKHPEAKRMPCAEDYLSVV  480

Query  480  LNRLCVLHEKTPVSEKVTKCCTESLVNRRPCFSALTPDETYVPKAFDEKLFTFHADICTL  539
            LN+LCVLHEKTPVS++VTKCCTESLVNRRPCFSAL  DETYVPK F+ + FTFHADICTL
Sbjct  481  LNQLCVLHEKTPVSDRVTKCCTESLVNRRPCFSALEVDETYVPKEFNAETFTFHADICTL  540

Query  540  PDTEKQIKKQTALVELLKHKPKATEEQLKTVMENFVAFVDKCCAADDKEACFAVEGPKLV  599
             + E+QIKKQTALVEL+KHKPKAT+EQLK VM++F AFV+KCC ADDKE CFA EG KLV
Sbjct  541  SEKERQIKKQTALVELVKHKPKATKEQLKAVMDDFAAFVEKCCKADDKETCFAEEGKKLV  600

Query  600  VSTQTALA   607
             ++Q AL
Sbjct  601  AASQAALGL  609
```

Figure II.18. Global Alignment of Albumin (Bovine and Human).

Score	Expect	Method	Identities	Positives	Gaps
984 bits(2545)	0.0	Compositional matrix adjust.	465/608(76%)	536/608(88%)	1/608(0%)

```
Query  1    MKWVTFISLLLLFSSAYSRGVFRRDTHKSEIAHRFKDLGEEHFKGLVLIAFSQYLQQCPF  60
            MKWVTFISLL LFSSAYSRGVFRRD HKSE+AHRFKDLGEE+FK LVLIAF+QYLQQCPF
Sbjct  1    MKWVTFISLLFLFSSAYSRGVFRRDAHKSEVAHRFKDLGEENFKALVLIAFAQYLQQCPF  60

Query  61   DEHVKLVNELTEFAKTCVADESHAGCEKSLHTLFGDELCKVASLRETYGDMADCCEKQEP  120
            ++HVKLVNE+TEFAKTCVADES   C+KSLHTLFGD+LC VA+LRETYG+MADCC KQEP
Sbjct  61   EDHVKLVNEVTEFAKTCVADESAENCDKSLHTLFGDKLCTVATLRETYGEMADCCAKQEP  120

Query  121  ERNECFLSHKDDSPDLPKL-KPDPNTLCDEFKADEKKFWGKYLYEIARRHPYFYAPELLY  179
            ERNECFL HKDD+P+LP+L +P+ + +C  F  +E+ F  KYLYEIARRHPYFYAPELL+
Sbjct  121  ERNECFLQHKDDNPNLPRLVRPEVDVMCTAFHDNEETFLKKYLYEIARRHPYFYAPELLF  180

Query  180  YANKYNGVFQECCQAEDKGACLLPKIETMREKVLASSARQRLRCASIQKFGERALKAWSV  239
            +A +Y   F ECCQA DK ACLLPK++ +R++  ASSA+QRL+CAS+QKFGERA KAW+V
Sbjct  181  FAKRYKAAFTECCQAADKAACLLPKLDELRDEGKASSAKQRLKCASLQKFGERAFKAWAV  240

Query  240  ARLSQKFPKAEFVEVTKLVTDLTKVHKECCHGDLLECADDRADLAKYICDNQDTISSKLK  299
            ARLSQ+FPKAEF EV+KLVTDLTKVH ECCHGDLLECADDRADLAKYIC+NQD+ISSKLK
Sbjct  241  ARLSQRFPKAEFAEVSKLVTDLTKVHTECCHGDLLECADDRADLAKYICENQDSISSKLK  300

Query  300  ECCDKPLLEKSHCIAEVEKDAIPENLPPLTADFAEDKDVCKNYQEAKDAFLGSFLYEYSR  359
            ECC+KPLLEKSHCIAEVE D +P +LP L ADF E KDVCKNY EAKD FLG FLYEY+R
Sbjct  301  ECCEKPLLEKSHCIAEVENDEMPADLPSLAADFVESKDVCKNYAEAKDVFLGMFLYEYAR  360

Query  360  RHPEYAVSVLLRLAKEYEATLEECCAKDDPHACYSTVFDKLKHLVDEPQNLIKQNCDQFE  419
            RHP+Y+V +LLRLAK YE TLE+CCA  DPH CY+ VFD+ K LV+EPQNLIKQNC+ FE
Sbjct  361  RHPDYSVVLLLRLAKTYETTLEKCCAAADPHECYAKVFDEFKPLVEEPQNLIKQNCELFE  420

Query  420  KLGEYGFQNALIVRYTRKVPQVSTPTLVEVSRSLGKVGTRCCTKPESERMPCTEDYLSLI  479
            +LGEY FQNAL+VRYT+KVPQVSTPTLVEVSR+LGKVG++CC  PE++RMPC EDYLS++
Sbjct  421  QLGEYKFQNALLVRYTKKVPQVSTPTLVEVSRNLGKVGSKCCKHPEAKRMPCAEDYLSVV  480

Query  480  LNRLCVLHEKTPVSEKVTKCCTESLVNRRPCFSALTPDETYVPKAFDEKLFTFHADICTL  539
            LN+LCVLHEKTPVS++VTKCCTESLVNRRPCFSAL  DETYVPK F+ + FTFHADICTL
Sbjct  481  LNQLCVLHEKTPVSDRVTKCCTESLVNRRPCFSALEVDETYVPKEFNAETFTFHADICTL  540

Query  540  PDTEKQIKKQTALVELLKHKPKATEEQLKTVMENFVAFVDKCCAADDKEACFAVEGPKLV  599
             + E+QIKKQTALVEL+KHKPKAT+EQLK VM++F AFV+KCC ADDKE CFA EG KLV
Sbjct  541  SEKERQIKKQTALVELVKHKPKATKEQLKAVMDDFAAFVEKCCKADDKETCFAEEGKKLV  600

Query  600  VSTQTALA  607
             ++Q AL
Sbjct  601  AASQAALG  608
```

Figure II.19. Global Alignment of Albumin (Bovine and Human).

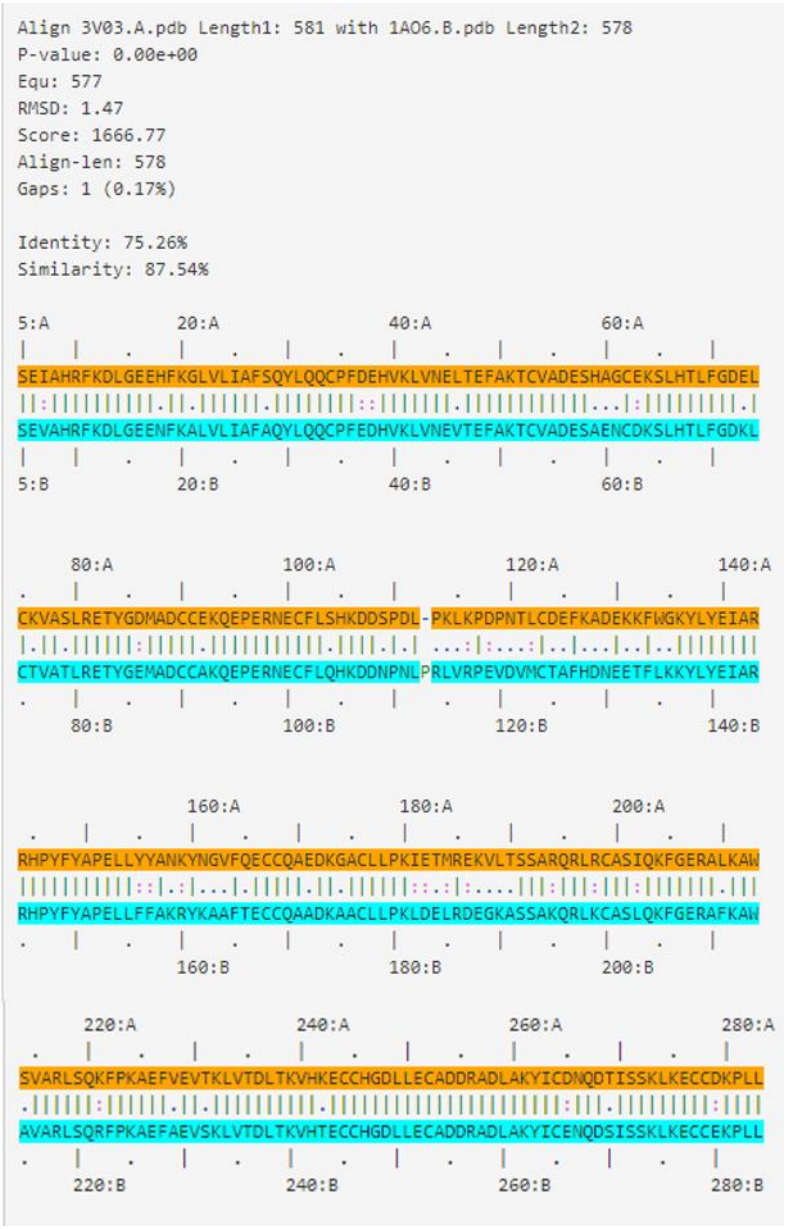

Figure II.20. First part of the Rigid Alignment of the PDB files of Albumin (Bovine and Human).

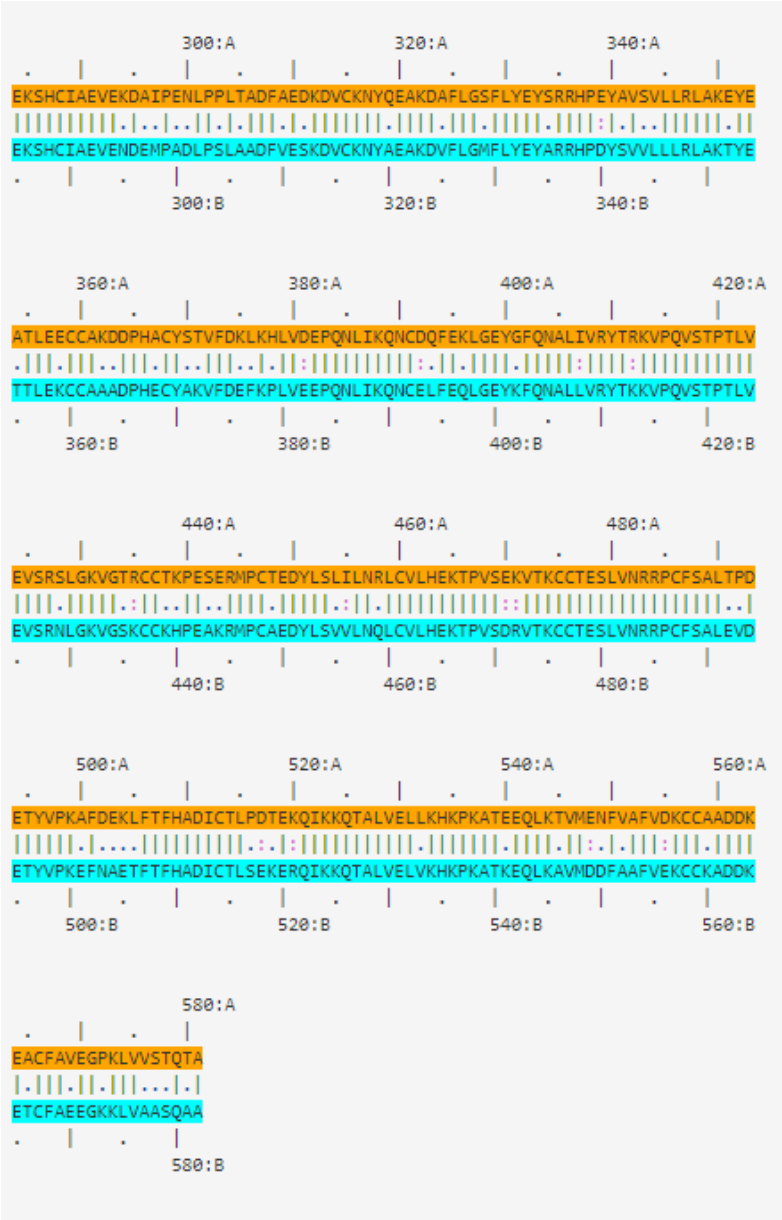

Figure II.21. Second part of the Rigid Alignment of the PDB files of Albumin (Bovine and Human).

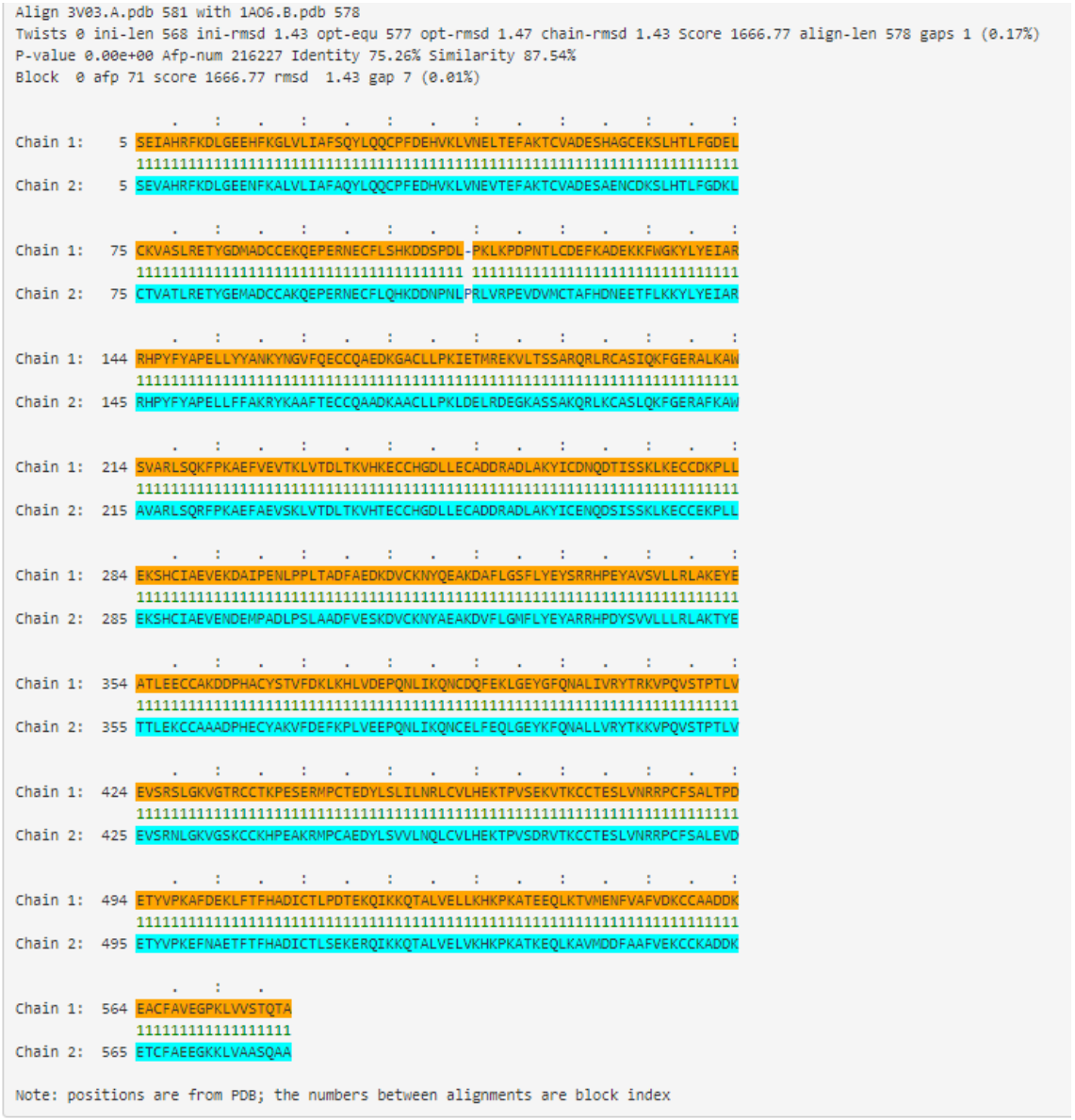

```
Align 3V03.A.pdb 581 with 1AO6.B.pdb 578
Twists 0 ini-len 568 ini-rmsd 1.43 opt-equ 577 opt-rmsd 1.47 chain-rmsd 1.43 Score 1666.77 align-len 578 gaps 1 (0.17%)
P-value 0.00e+00 Afp-num 216227 Identity 75.26% Similarity 87.54%
Block  0 afp 71 score 1666.77 rmsd  1.43 gap 7 (0.01%)

                .    :    .    :    .    :    .    :    .    :    .    :    .    :
Chain 1:    5 SEIAHRFKDLGEEHFKGLVLIAFSQYLQQCPFDEHVKLVNELTEFAKTCVADESHAGCEKSLHTLFGDEL
              1111111111111111111111111111111111111111111111111111111111111111111111
Chain 2:    5 SEVAHRFKDLGEENFKALVLIAFAQYLQQCPFEDHVKLVNEVTEFAKTCVADESAENCDKSLHTLFGDKL

                .    :    .    :    .    :    .    :    .    :    .    :    .    :
Chain 1:   75 CKVASLRETYGDMADCCEKQEPERNECFLSHKDDSPDL-PKLKPDPNTLCDEFKADEKKFWGKYLYEIAR
              1111111111111111111111111111111111111 1111111111111111111111111111111
Chain 2:   75 CTVATLRETYGEMADCCAKQEPERNECFLQHKDDNPNLPRLVRPEVDVMCTAFHDNEETFLKKYLYEIAR

                .    :    .    :    .    :    .    :    .    :    .    :    .    :
Chain 1:  144 RHPYFYAPELLYYANKYNGVFQECCQAEDKGACLLPKIETMREKVLTSSARQRLRCASIQKFGERALKAW
              1111111111111111111111111111111111111111111111111111111111111111111111
Chain 2:  145 RHPYFYAPELLFFAKRYKAAFTECCQAADKAACLLPKLDELRDEGKASSAKQRLKCASLQKFGERAFKAW

                .    :    .    :    .    :    .    :    .    :    .    :    .    :
Chain 1:  214 SVARLSQKFPKAEFVEVTKLVTDLTKVHKECCHGDLLECADDRADLAKYICDNQDTISSKLKECCDKPLL
              1111111111111111111111111111111111111111111111111111111111111111111111
Chain 2:  215 AVARLSQRFPKAEFAEVSKLVTDLTKVHTECCHGDLLECADDRADLAKYICENQDSISSKLKECCEKPLL

                .    :    .    :    .    :    .    :    .    :    .    :    .    :
Chain 1:  284 EKSHCIAEVEKDAIPENLPPLTADFAEDKDVCKNYQEAKDAFLGSFLYEYSRRHPEYAVSVLLRLAKEYE
              1111111111111111111111111111111111111111111111111111111111111111111111
Chain 2:  285 EKSHCIAEVENDEMPADLPSLAADFVESKDVCKNYAEAKDVFLGMFLYEYARRHPDYSVVLLLRLAKTYE

                .    :    .    :    .    :    .    :    .    :    .    :    .    :
Chain 1:  354 ATLEECCAKDDPHACYSTVFDKLKHLVDEPQNLIKQNCDQFEKLGEYGFQNALIVRYTRKVPQVSTPTLV
              1111111111111111111111111111111111111111111111111111111111111111111111
Chain 2:  355 TTLEKCCAAADPHECYAKVFDEFKPLVEEPQNLIKQNCELFEQLGEYKFQNALLVRYTKKVPQVSTPTLV

                .    :    .    :    .    :    .    :    .    :    .    :    .    :
Chain 1:  424 EVSRSLGKVGTRCCTKPESERMPCTEDYLSLILNRLCVLHEKTPVSEKVTKCCTESLVNRRPCFSALTPD
              1111111111111111111111111111111111111111111111111111111111111111111111
Chain 2:  425 EVSRNLGKVGSKCCKHPEAKRMPCAEDYLSVVLNQLCVLHEKTPVSDRVTKCCTESLVNRRPCFSALEVD

                .    :    .    :    .    :    .    :    .    :    .    :    .    :
Chain 1:  494 ETYVPKAFDEKLFTFHADICTLPDTEKQIKKQTALVELLKHKPKATEEQLKTVMENFVAFVDKCCAADDK
              1111111111111111111111111111111111111111111111111111111111111111111111
Chain 2:  495 ETYVPKEFNAETFTFHADICTLSEKERQIKKQTALVELVKHKPKATKEQLKAVMDDFAAFVEKCCKADDK

                .    :    .
Chain 1:  564 EACFAVEGPKLVVSTQTA
              11111111111111111
Chain 2:  565 ETCFAEEGKKLVAASQAA

Note: positions are from PDB; the numbers between alignments are block index
```

Figure II.22. Flexible Alignment of the PDB files of Albumin (Bovine and Human).

NW Score	Identities	Positives	Gaps
3086	582/607(96%)	582/607(95%)	0/607(0%)

```
Query  1                                                DTHKSEIAHRFKDLGEEHFKGLVLIAFSQYLQQCPF  36
                                                        DTHKSEIAHRFKDLGEEHFKGLVLIAFSQYLQQCPF
Sbjct  1    MKWVTFISLLLLFSSAYSRGVFRRDTHKSEIAHRFKDLGEEHFKGLVLIAFSQYLQQCPF  60

Query  37   DEHVKLVNELTEFAKTCVADESHAGCEKSLHTLFGDELCKVASLRETYGDMADCCEKQEP  96
            DEHVKLVNELTEFAKTCVADESHAGCEKSLHTLFGDELCKVASLRETYGDMADCCEKQEP
Sbjct  61   DEHVKLVNELTEFAKTCVADESHAGCEKSLHTLFGDELCKVASLRETYGDMADCCEKQEP  120

Query  97   ERNECFLSHKDDSPDLPKLKPDPNTLCDEFKADEKKFWGKYLYEIARRHPYFYAPELLYY  156
            ERNECFLSHKDDSPDLPKLKPDPNTLCDEFKADEKKFWGKYLYEIARRHPYFYAPELLYY
Sbjct  121  ERNECFLSHKDDSPDLPKLKPDPNTLCDEFKADEKKFWGKYLYEIARRHPYFYAPELLYY  180

Query  157  ANKYNGVFQECCQAEDKGACLLPKIETMREKVLTSSARQRLRCASIQKFGERALKAWSVA  216
            ANKYNGVFQECCQAEDKGACLLPKIETMREKVL SSARQRLRCASIQKFGERALKAWSVA
Sbjct  181  ANKYNGVFQECCQAEDKGACLLPKIETMREKVLASSARQRLRCASIQKFGERALKAWSVA  240

Query  217  RLSQKFPKAEFVEVTKLVTDLTKVHKECCHGDLLECADDRADLAKYICDNQDTISSKLKE  276
            RLSQKFPKAEFVEVTKLVTDLTKVHKECCHGDLLECADDRADLAKYICDNQDTISSKLKE
Sbjct  241  RLSQKFPKAEFVEVTKLVTDLTKVHKECCHGDLLECADDRADLAKYICDNQDTISSKLKE  300

Query  277  CCDKPLLEKSHCIAEVEKDAIPENLPPLTADFAEDKDVCKNYQEAKDAFLGSFLYEYSRR  336
            CCDKPLLEKSHCIAEVEKDAIPENLPPLTADFAEDKDVCKNYQEAKDAFLGSFLYEYSRR
Sbjct  301  CCDKPLLEKSHCIAEVEKDAIPENLPPLTADFAEDKDVCKNYQEAKDAFLGSFLYEYSRR  360

Query  337  HPEYAVSVLLRLAKEYEATLEECCAKDDPHACYSTVFDKLKHLVDEPQNLIKQNCDQFEK  396
            HPEYAVSVLLRLAKEYEATLEECCAKDDPHACYSTVFDKLKHLVDEPQNLIKQNCDQFEK
Sbjct  361  HPEYAVSVLLRLAKEYEATLEECCAKDDPHACYSTVFDKLKHLVDEPQNLIKQNCDQFEK  420

Query  397  LGEYGFQNALIVRYTRKVPQVSTPTLVEVSRSLGKVGTRCCTKPESERMPCTEDYLSLIL  456
            LGEYGFQNALIVRYTRKVPQVSTPTLVEVSRSLGKVGTRCCTKPESERMPCTEDYLSLIL
Sbjct  421  LGEYGFQNALIVRYTRKVPQVSTPTLVEVSRSLGKVGTRCCTKPESERMPCTEDYLSLIL  480

Query  457  NRLCVLHEKTPVSEKVTKCCTESLVNRRPCFSALTPDETYVPKAFDEKLFTFHADICTLP  516
            NRLCVLHEKTPVSEKVTKCCTESLVNRRPCFSALTPDETYVPKAFDEKLFTFHADICTLP
Sbjct  481  NRLCVLHEKTPVSEKVTKCCTESLVNRRPCFSALTPDETYVPKAFDEKLFTFHADICTLP  540

Query  517  DTEKQIKKQTALVELLKHKPKATEEQLKTVMENFVAFVDKCCAADDKEACFAVEGPKLVV  576
            DTEKQIKKQTALVELLKHKPKATEEQLKTVMENFVAFVDKCCAADDKEACFAVEGPKLVV
Sbjct  541  DTEKQIKKQTALVELLKHKPKATEEQLKTVMENFVAFVDKCCAADDKEACFAVEGPKLVV  600

Query  577  STQTALA  583
            STQTALA
Sbjct  601  STQTALA  607
```

Figure II.23. Global Alignment of the PDB file with the UniProt sequence for Albumin (Bovine).

NW Score	Identities	Positives	Gaps
3068	585/609(96%)	585/609(96%)	0/609(0%)

```
Query  1                                                    DAHKSEVAHRFKDLGEENFKALVLIAFAQYLQQCPF  36
                                                            DAHKSEVAHRFKDLGEENFKALVLIAFAQYLQQCPF
Sbjct  1    MKWVTFISLLFLFSSAYSRGVFRRDAHKSEVAHRFKDLGEENFKALVLIAFAQYLQQCPF  60

Query  37   EDHVKLVNEVTEFAKTCVADESAENCDKSLHTLFGDKLCTVATLRETYGEMADCCAKQEP  96
            EDHVKLVNEVTEFAKTCVADESAENCDKSLHTLFGDKLCTVATLRETYGEMADCCAKQEP
Sbjct  61   EDHVKLVNEVTEFAKTCVADESAENCDKSLHTLFGDKLCTVATLRETYGEMADCCAKQEP  120

Query  97   ERNECFLQHKDDNPNLPRLVRPEVDVMCTAFHDNEETFLKKYLYEIARRHPYFYAPELLF  156
            ERNECFLQHKDDNPNLPRLVRPEVDVMCTAFHDNEETFLKKYLYEIARRHPYFYAPELLF
Sbjct  121  ERNECFLQHKDDNPNLPRLVRPEVDVMCTAFHDNEETFLKKYLYEIARRHPYFYAPELLF  180

Query  157  FAKRYKAAFTECCQAADKAACLLPKLDELRDEGKASSAKQRLKCASLQKFGERAFKAWAV  216
            FAKRYKAAFTECCQAADKAACLLPKLDELRDEGKASSAKQRLKCASLQKFGERAFKAWAV
Sbjct  181  FAKRYKAAFTECCQAADKAACLLPKLDELRDEGKASSAKQRLKCASLQKFGERAFKAWAV  240

Query  217  ARLSQRFPKAEFAEVSKLVTDLTKVHTECCHGDLLECADDRADLAKYICENQDSISSKLK  276
            ARLSQRFPKAEFAEVSKLVTDLTKVHTECCHGDLLECADDRADLAKYICENQDSISSKLK
Sbjct  241  ARLSQRFPKAEFAEVSKLVTDLTKVHTECCHGDLLECADDRADLAKYICENQDSISSKLK  300

Query  277  ECCEKPLLEKSHCIAEVENDEMPADLPSLAADFVESKDVCKNYAEAKDVFLGMFLYEYAR  336
            ECCEKPLLEKSHCIAEVENDEMPADLPSLAADFVESKDVCKNYAEAKDVFLGMFLYEYAR
Sbjct  301  ECCEKPLLEKSHCIAEVENDEMPADLPSLAADFVESKDVCKNYAEAKDVFLGMFLYEYAR  360

Query  337  RHPDYSVVLLLRLAKTYETTLEKCCAAADPHECYAKVFDEFKPLVEEPQNLIKQNCELFE  396
            RHPDYSVVLLLRLAKTYETTLEKCCAAADPHECYAKVFDEFKPLVEEPQNLIKQNCELFE
Sbjct  361  RHPDYSVVLLLRLAKTYETTLEKCCAAADPHECYAKVFDEFKPLVEEPQNLIKQNCELFE  420

Query  397  QLGEYKFQNALLVRYTKKVPQVSTPTLVEVSRNLGKVGSKCCKHPEAKRMPCAEDYLSVV  456
            QLGEYKFQNALLVRYTKKVPQVSTPTLVEVSRNLGKVGSKCCKHPEAKRMPCAEDYLSVV
Sbjct  421  QLGEYKFQNALLVRYTKKVPQVSTPTLVEVSRNLGKVGSKCCKHPEAKRMPCAEDYLSVV  480

Query  457  LNQLCVLHEKTPVSDRVTKCCTESLVNRRPCFSALEVDETYVPKEFNAETFTFHADICTL  516
            LNQLCVLHEKTPVSDRVTKCCTESLVNRRPCFSALEVDETYVPKEFNAETFTFHADICTL
Sbjct  481  LNQLCVLHEKTPVSDRVTKCCTESLVNRRPCFSALEVDETYVPKEFNAETFTFHADICTL  540

Query  517  SEKERQIKKQTALVELVKHKPKATKEQLKAVMDDFAAFVEKCCKADDKETCFAEEGKKLV  576
            SEKERQIKKQTALVELVKHKPKATKEQLKAVMDDFAAFVEKCCKADDKETCFAEEGKKLV
Sbjct  541  SEKERQIKKQTALVELVKHKPKATKEQLKAVMDDFAAFVEKCCKADDKETCFAEEGKKLV  600

Query  577  AASQAALGL  585
            AASQAALGL
Sbjct  601  AASQAALGL  609
```

Figure II.24. Global Alignment of the PDB file with the UniProt sequence for Albumin (Human).

III. Fergusson Analysis Results

Table III.1. Fergusson Plot Analysis results from the BSA conjugation of AuNP-MUA samples at various Agarose gel concentrations.

[BSA]/[AuNP]	$Log_{10}M_0$	K_R
0	-3.57 ± 0.01	0.22 ± 0.01
10	-3.59 ± 0.01	0.22 ± 0.01
30	-3.64 ± 0.02	0.21 ± 0.01
50	-3.65 ± 0.02	0.23 ± 0.01
75	-3.69 ± 0.03	0.22 ± 0.02
100	-3.71 ± 0.04	0.22 ± 0.02
150	-3.72 ± 0.02	0.24 ± 0.01
200	-3.76 ± 0.02	0.23 ± 0.01
250	-3.76 ± 0.01	0.24 ± 0.01
300	-3.78 ± 0.03	0.23 ± 0.02
400	-3.78 ± 0.03	0.24 ± 0.02
500	-3.78 ± 0.01	0.24 ± 0.01
700	-3.78 ± 0.01	0.26 ± 0.01
1000	-3.77 ± 0.01	0.27 ± 0.01
2000	-3.78 ± 0.01	0.27 ± 0.01

IV. DLS and NTA results for the 40 nm AuNPs

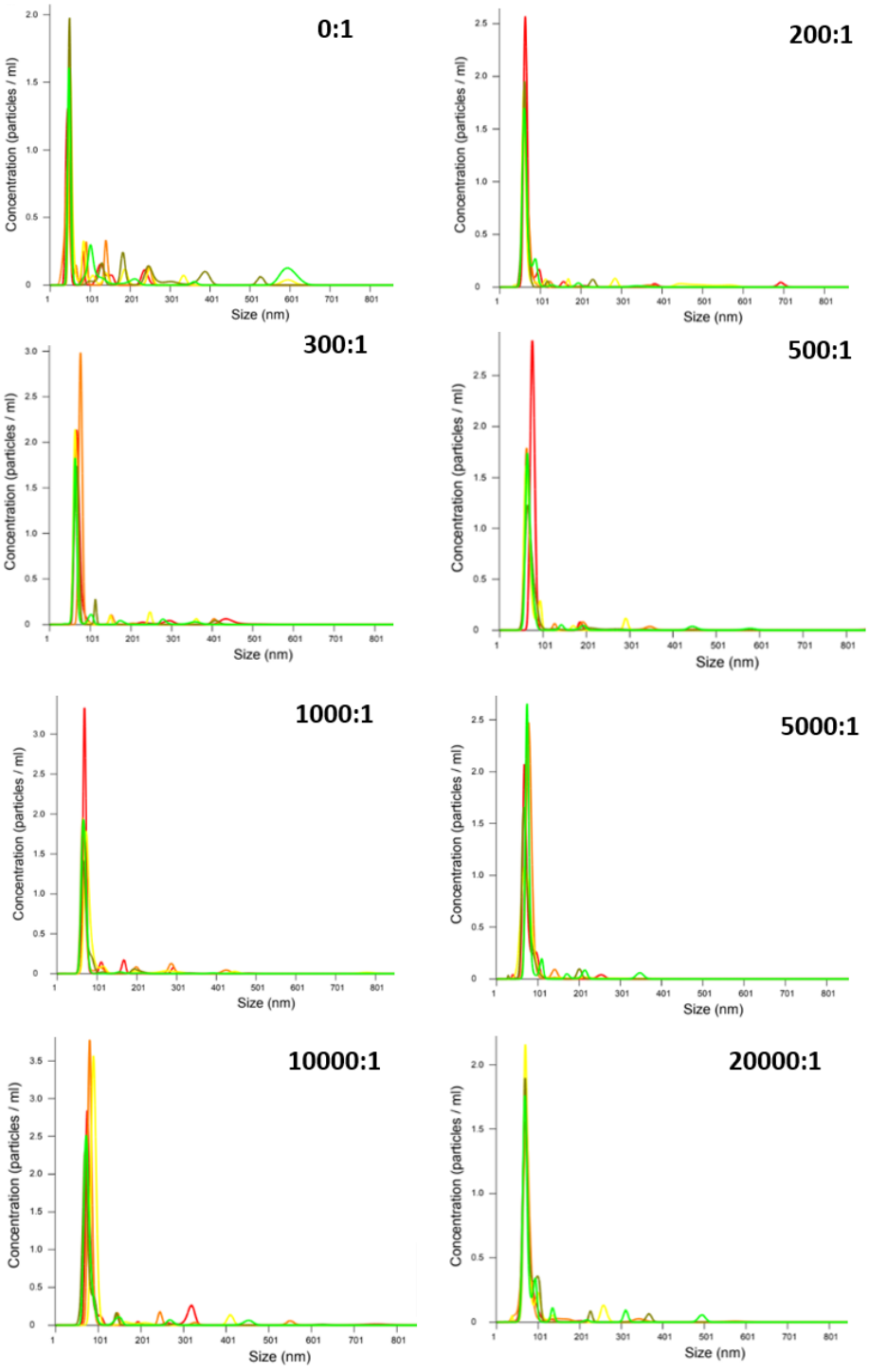

Figure IV.1. NTA results of the Bioconjugation of Fib with the 40 nm AuNPs.

Table IV.1. Summary of the DLS and NTA results of the bioconjugation of Fib with 40 nm AuNPs.

		DLS		NTA	
Sample #	**[Fib]/ [AuNP]**	**Mean Diameter by Intensity (nm)**	**Mean Diameter by Number (nm)**	**Mean Diameter (nm)**	**SD (nm)**
1	0	58.7 ± 0.2	24.5 ± 0.3	68.2 ± 4.6	60.9 ± 10.6
2	40	63.1 ± 0.2	30.6 ± 1.2	126.7 ± 71.0	94.1 ± 33.3
3	60	80.4 ± 0.2	29.7 ± 2.9	206.5 ± 62.5	96.1 ± 21.7
4	100	62.0 ± 0.2	41.4 ± 0.5	157.2 ± 59.9	48.1 ± 10.9
5	200	71.0 ± 0.1	38.5 ± 0.1	68.9 ± 1.3	39.8 ± 7.5
6	300	81.1 ± 0.7	33.4 ± 2.6	74.3 ± 2.1	36.6 ± 3.9
7	500	73.6 ± 0.8	40.6 ± 0.5	73.0 ± 1.7	35.3 ± 4.4
8	1000	74.3 ± 0.1	46.6 ± 0.3	75.4 ± 2.8	32.2 ± 6.4
9	5000	79.3 ± 0.2	47.5 ± 0.3	77.0 ± 1.9	22.6 ± 3.1
10	10000	84.5 ± 0.2	43.6 ± 1.8	85.4 ± 3.6	38.0 ± 5.2
11	20000	89.0 ± 0.6	49.7 ± 0.4	76.6 ± 1.1	30.1 ± 4.7
12	30000	103.6 ± 0.8	59.0 ± 0.6	117.5 ± 26.4	61.7 ± 17.9

V. List of Reagents and Instruments

Table V.1. List of proteins.

Protein	Description	Supplier
Low range molecular weight standards	Unstained SDS-PAGE Standards, low range	BIO-RAD
Albumin	Bovine serum lyophilized powder, ≥96%, 66 kDa	Sigma
Fibrinogen	Bovine serum fraction I, Type I-S, 71%, 340 kDa	Sigma
CALNN (Cys-Ala-Leu-Asr-Asr)	533.61 Da	Caslo
Protein standard	1 mg/ml Bovine serum Albumin	Sigma

Table V.2. List of Chemical Reagents.

Chemical Reagents	Description	Supplier
Gold(III) chloride trihydrate	≥99.9% , 393.83 Da	Sigma
Sodium citrate tribasic dihydrate	294.10 Da	Sigma
Dodecyl Sulphate Sodium Salt	288.38 Da	Panreac
Acrylamide/Bis-acrylamide	30% (w/w) acrylamide/bis-acrylamide solution	Sigma
N,N,N',N'-Tetramethylethylenediamine (TEMED)	Ultrapure solution, 116.20 Da	Sigma

Ammonium Persulfate	≥98% , 228.20 Da	Sigma
Agarose	Ultrapure	Sigma
Tris(hydroxymethyl)-aminomethane	≥99.8% , 121.14 Da	Sigma
Potassium phosphate dibasic	174.18 Da	Riedel-de Haen
Potassium phosphate monobasic	136.09 Da	Riedel-de Haen
Acetic acid	60.05 Da	Scharlau
Brilliant Blue R-250	854.02 Da	Sigma
Methanol	32.04 Da	Fisher
Glycine	75.07 Da	Sigma
Bromophenol Blue	669.96 Da	Panreac
Glycerol	87%	Panreac
	99.5%	Sigma
2-mercaptoethanol	78.13 Da	Sigma
Tris-acetate-EDTA	50X (40 mM Tris, 20 mM acetic acid, 1 mM EDTA)	Sigma
Copper(II) Sulfate Pentahydrate Solution	4% (w/v) copper(II) sulfate pentahydrate	Sigma
Bicinchoninic acid solution	Bicinchoninic acid, sodium carbonate, sodium tartrate, sodium bicarbonate	Sigma
Sodium chloride	99% , 58.44 Da	Scharlau
Sodium hydroxide	39.99 Da	Sigma
Hydrochloric Acid	98%	Sigma
11-Amino-1-undecanethiol hydrochloride (AUT)	239.85 Da	Sigma
11-mercaptoundecanoic acid (MUA)	218.36 Da	Sigma

Table V.3. List of Instruments.

Instruments	**Model**	**Supplier**
pH Electrode	Basic 20+	Crison
Centrifuge	K3 Series , BRK5424 rotor	Centurion Scientific
Vertical electrophoresis Cell	Mini-PROTEAN Tetra Cell	BIO-RAD
Horizontal electrophoresis Cell	Mini-Sub Cell GT Cell	BIO-RAD
Electrophoresis power supply	PowerPac™ Basic Power Supply	BIO-RAD
Thermo-shaker	TS-100	Biosan
UV-Vis Spectrophotometer	Varian Cary® 50	Varian
Cuvette cell	Quartz , 10 mm	Zuzi

Analytical Balance	AS 220/C/2	Radwag
Zetasizer (DLS and ELS)*	Panaltyical Zetasizer ZS	Malvern
Capillary cell (DLS)*	DTS1070	Malvern
NanoSight (NTA)*	Panaltyical NanoSight NS300	Malvern